Siam Photon

THAI
SYNCHROTRON
NATIONAL LAB

SLRI
Annual Review
2018 - 2019

ISSN 0911-5730

Message from Chairman

In the last decade of SLRI, we have been developing cutting-edge technologies related to synchrotron science and basic knowledge of synchrotron techniques not only for Thai community but also for for regions, especially the ASEAN. It is well known that synchrotron facilities have been one of the most important scientific infrastructures for human society since the first synchrotron machine was built in 1949. Nowadays, there are over 50 synchrotron sources in operation around the world.

In Thailand, the synchrotron source so-called the “Siam Photon Source” has served researchers from academia and industries for more than 20 years. We are proud to be part of the society development under the late Rama the 9th King’s scheme of sustainable development.

Assoc. Prof. Dr.Soranit Siltharm, M.D.
Chairman of the Board of SLRI

Message from CEO

The year of 2018 marking the 10th SLRI Anniversary was another successful year of SLRI in many aspects including increased number of publications by users and number of young generation participated in trainings and workshops organized by the institute. We have created and received trust from industrial partners which is clearly proven by the number of industrial projects carried out at our laboratories. Since 2008, the first year as a governmental public organization, SLRI has played a vital role as a strong scientific platform to strengthen research collaboration in ASEAN. Currently, we are fully accepted as an international infrastructure.

In term of regional aspect, in 2018, SLRI shared a full collaboration in establishment of an ASEAN network so-called "ASEAN Large Nuclear and Synchrotron Facilities Network – LNSN". The network aims to support utilization of large radiation facilities such as synchrotron, neutron and other possible facilities in the Southeast Asia for doing research, developing a regional capacity building and connecting people using scientific tools in the region.

For the next decade to come, SLRI strongly believes that we will open another successful chapter for our contribution. We promise to continue moving forward for progressive growth and strength of the science community in response to the ASEAN motto:

'One vision, One Identity, One Community'.

Prof. Wng. Cmdr. Dr. Sarawut Sujitjorn
Chief Executive Officer

Message from Editor

Dear Readers,

Since the last decade of service, the number of foreign users especially from South East Asia has raised. This is due to the fact that the number of research implemented at SLRI has increased, and we are doing more advanced research. Advanced research requires advanced tools such as synchrotron facility. To communicate with the international user community, SLRI therefore has introduced an annual review in the English version since 2016.

In this 2nd issue of the annual review (2018-2019), it contains our latest development at the facility both for the source and the beamlines such as a linear accelerator for industrial applications, a new XAS beamline and an in-house vacuum brazing oven in the first section. For research activities section, thanks to SLRI users, there are some results from their research using synchrotron radiation. A new section in the issue is the Industrial Applications aiming to show some research cases of how to use the facility to help industries solving problems or develop new products.

We do believe that since the previous decade, we have played a vital role in the research community. We are going to continue our role as a scientific platform in the next decade to come.

Dr.Somchai Tancharakorn
Editor

CONTENT

FACILITY : CURRENT STATUS

RESEARCH ACTIVITIES

INDUSTRIAL APPLICATIONS

USER STATISTICS

FACILITIES: CURRENT STATUS

INSTALLATION AND COMMISSIONING OF BL1.1W:MXT X-RAY DIFRACTION END-STATION

P. Chirawatkul[*], C. Saiyasombat, S. Wannapaiboon, S. Pongampai,
P. Tarawarakarn, S. Srichan, N. Wongprachanukul, and N. Suwanta
Synchrotron Light Research Institute (Public Organization) 111 University Avenue, Muang District,
Nakhon-Ratchasima 30000, Thailand

ABSTRACT

The setups for newly added x-ray diffraction, XRD, end-station at BL1.1W:MXT, their support structures, alignment scheme, and control software are described. Flexibility to performing experiments in 1D-XRD or 2D-XRD setups and possibility of measurements in grazing incident or transmission geometry are proposed. The capability in obtaining diffraction patterns with high angular resolution is demonstrated. The peak FWHM of 0.03° in 2θ from the measurement of NIST standard LaB_6 SRM 660a using the 1D-XRD setup was achieved.

INTRODUCTION

The XRD end-station has been added to the BL1.1W-MXT. Along with the existing x-ray absorption spectroscopy, XAS, and x-ray fluorescence, XRF, end-stations, the three techniques can be used complementarily for structure characterization. The XRD station is equipped with two position sensitive detectors, an array of strip detectors and a 2D image plate. The strip detector is employed where a long range of scattering angles, e.g. up to 150°, and higher resolution diffraction patterns are required. The image plate is used in the case where the structures of samples contain orientations, or the samples are not well crystalized. The BL1.1W-MXT upgraded end-stations are shown in Figure 1.

The report is organized as follows. In the next section, the setups for the 1D and 2D XRD are described. The installation of the 1D detector system and control software are outlined in the Installing MYTHEN 6K and Control Software sections. Currently measurements can be made only in transmission configuration and at room temperature. The results of those measurements are shown in the Commissioning Results section. Summary is given in the last section.

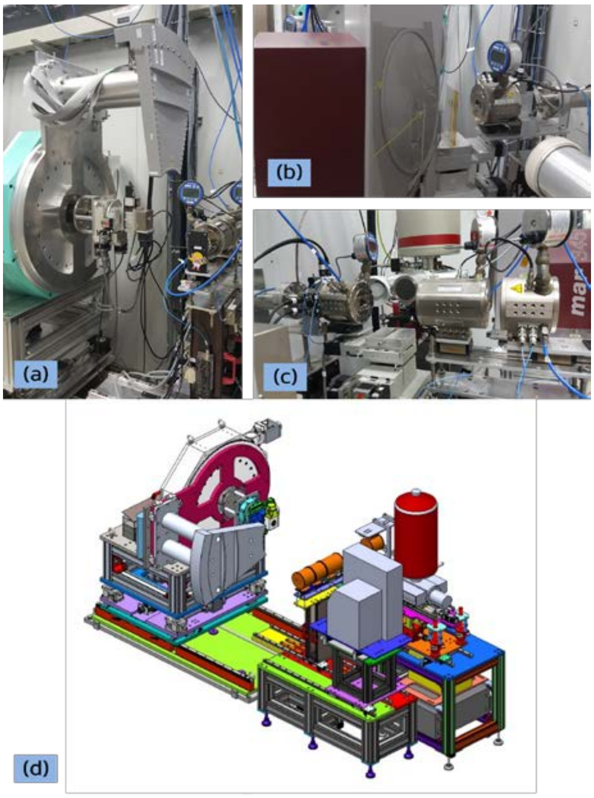

Figure 1: BL1.1W upgraded end-stations. The 1D-XRD (a) setup, 2D-XRD setup (b), and XAS and XRF end-stations (c) were installed on movable support structures (d) enabling the stations to be moved in and out of the beam.

THE END-STATION

1D-XRD

MYTHEN 6K is employed as a 1D-XRD detector. It was chosen because of its large 24-bit dynamic range, high frame rate and zero noise attributes [1]. The 6 modules of the MYTHEN 6K were aligned in an arc of a circle with a radius of curvature of 760 mm and an angular coverage of approximately 30°. The detector is installed on a support structure optimized for powder diffraction measurements, allowing detector movements to cover scattering angles up to 150°.

Measurements will be made primarily in a transmission mode where samples are filled in capillaries with inner diameters of 0.3 or 0.5 mm. The sample stage is also equipped with a spinner capable of rotating the capillary with the speed of at least 10 Hz. This way, measurements can be made without the effect of preferred orientation and quantitative analysis such as Rietveld could be reliably performed.

It is also possible to perform experiments in a grazing incident (GI) geometry, suitable for thin films or slab samples. A GI stage can be placed on the main sample stage of the XAS end-station which can be aligned to the center of rotation of the MYTHEN 6K. Samples prepared for 1D-XRD and 2D-XRD transmission geometry, and a GI stage are shown in Figure 2.

2D-XRD

MAR345 image plate is used as a 2D detector. The detector has a reasonable 16-bit dynamic range with considerably large active area of 345 mm in diameter. The detector is placed on two slide guides, one for movements across the beam direction (*x*-axis) used to move the detector in and out of the beam and another for movements along the beam direction (*y*-axis) used to adjust sample-to-detector distances. Powder samples can be filled in plastic frames, Figure 2(b), for transmission measurements. Experiments in a GI geometry using the same GI stage as the 1D-XRD setup can also be performed. The measurements will allow in-plane as well as out-of-plane structures to be investigated.

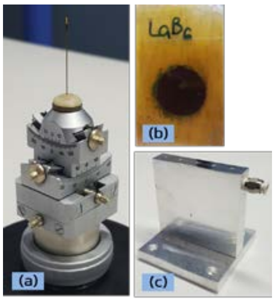

Figure 2: Samples filled in a Kapton® capillary for 1D-XRD measurements in transmission mode (a), sample filled in a plastic frame with Kapton® windows for 2D-XRD measurements in transmission mode (b) and a grazing incident (GI) stage for 1D and 2D XRD measurements (c).

Usable x-ray energies for both the 1D and 2D XRD setups are 8, 12, and 15 keV. As the fluxes for 12 keV x-rays are the highest, measurements will mainly be made at this energy. In the case where lower or higher scattering angles are required 8 or 15 keV x-rays can be used. Estimated angular coverage for measurements made using MAR345 at 8, 12, and 15 keV x-rays along with the angular range covered by the MYTHEN 6K are presented in Table 1.

Table 1: Estimated angular coverage of XRD measurements at BL1.1W-MXT using MYTHEN 6K and MAR345.

Detector	Energy (keV)	Estimated angular coverage (Cu K$_{\alpha1}$ equivalence) (2θ)
MYTHEN 6K	8, 12, 15	10°-150°
MAR345	8	6°-49°
	12	9°-75°
	15	12°-100°

INSTALLING MYTHEN 6K

Figure 3 shows engineering drawings of the MYTHEN 6K support structure and the XRD sample stage. The support structure contains 3 movable axes, namely, support-x, support-z and main θ. The support-x movement is used to move the detector in and out of the beam. The support-z movement is used to move the rotation center of the main θ movement to the beam height. The detector rotation along the scattering angles is made using the main θ movement.

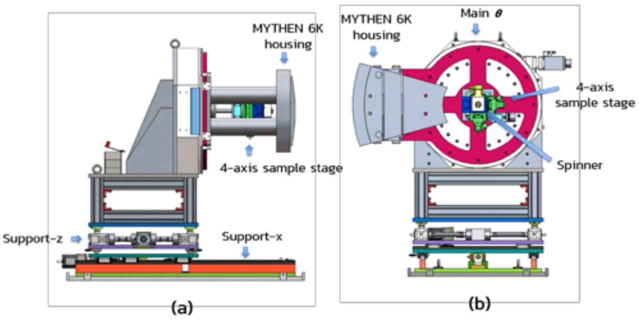

Figure 3: Engineering drawings of the MYTHEN 6K support structure. The view along the beam direction (a) and across the beam direction (b) are shown. Arrows indicate 3 motorized stages for support-x, support-z and main θ movements, the housing of the MYTHEN 6K, a 4-axis motorized sample stage and a spinner.

The XRD sample stage is placed at the center of rotation of the main θ stage. It is a 4-axis goniometer with movements across the beam direction (*x*-axis), along the beam direction (*y*-axis), vertical (*z*-axis), and the pitch rotation. The *y* and *z* movements are used to fine tune the sample position to the rotation center of the detector. The *x* movement is used to select part of the samples exposed to the beam. And pitch movement is used for future development of XRD measurements in reflection geometry.

A crucial aspect to aligning the support structure is the alignment of the main θ stage and the sample pitch rotations to a common rotation center at the center of the detector array curvature and the sample position, as shown in Figure 4a. Portable coordinate measuring machines (CMMs) was used to assist the assemble of the support structure, Figure 4b. The final check showed that the center of the detector array curvature was misaligned from the rotation center of the main θ stage by 0.028 mm horizontally and 0.108 mm vertically which are less than the diameter of the sample capillary of 0.3 mm and acceptable. The misalignment of the rotation center of the sample pitch and the sample position to the rotation center of the main θ stage was around 0.8 mm and considered significant. The support of the sample stage is therefore needed to be redesigned to allow more assemble flexibility. The sample stage *y* and *z* movements were temporarily used to compensate the misalignment.

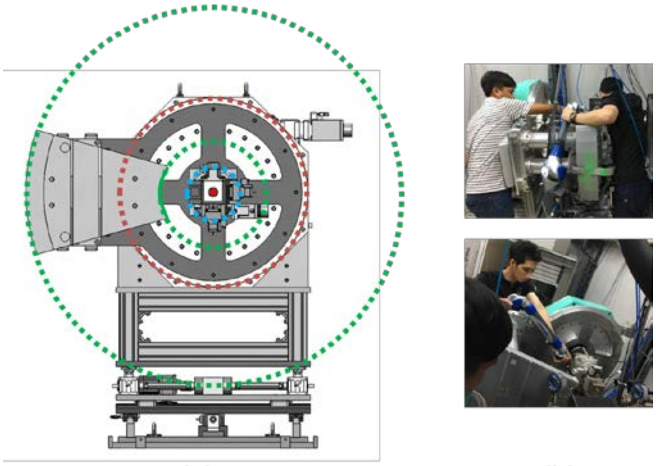

(a) (b)

Figure 4: 1D-XRD support structure assemble scheme (a). The rotation center of the main θ stage (brown) and the sample stage pitch (blue) were aligned to the sample position (red) and the center of the detector array curvature (green). The concentricity of the stages was checked using the FARO portable coordinate measuring machines (CMMs) (b).

CONTROL SOFWARE

For the 2D-XRD measurement, the mar345 program provided by the marXperts GmbH could be used for user service. Because the 1D-XRD measurements are configuration dependent, a dedicated control software was in-housed developed.

Screenshots of the XRD Measurement System and Alignment XRD support applications developed for 1D-XRD experiments are shown in Figure 5. The Alignment XRD support application was written for control of the support-x, support-z and main θ movements and the XRD Measurement System application was written for control of the experiments. The XRD Measurement System application is divided into calibration section, which includes calibration and global offset determination, and measurement section, shown as tabs in the application window. The calibration section was designed for measurements of standard materials at a series detector angular positions to obtain a relation between detector's channel numbers and actual scattering angles. The calibration method used follows the outline given in [1] of which the relation is represented in terms of angular offsets for each module and a global offset for all modules.

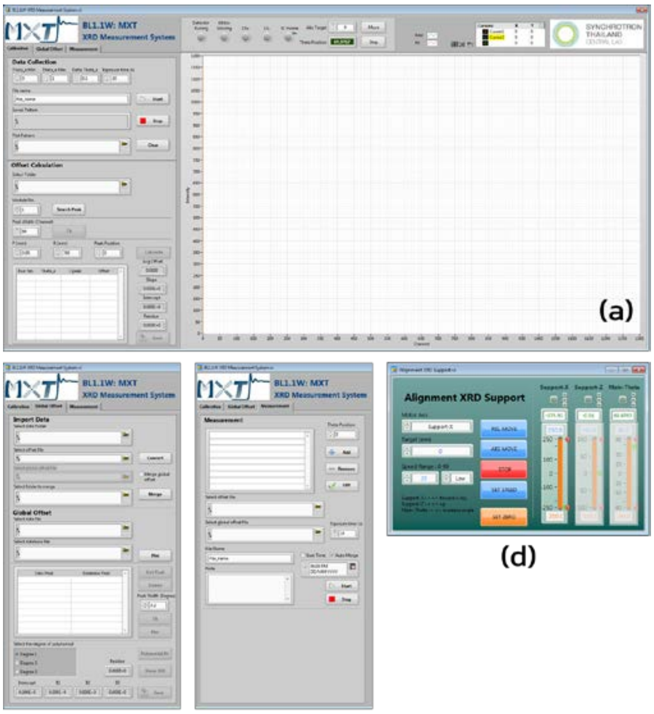

(b) (c)

Figure 5: Screenshots of XRD Measurement System and Alignment XRD Support applications. The Calibration (a) and Global offset (b) tabs are used for determining the relation between detector's channel numbers and actual scattering angles. Measurements are made by adjusting measurement parameters in the Measurement tab (c). The x, z and main θ movements of the support structure are control using the Alignment XRD Support application (d).

Because there are gaps between neighboring detector modules, which introduces gaps of 0.17° in the diffraction pattern, measurements need to be made at least twice at shifted detector angular positions to avoid data loss. In the Measurements section, a list of measurements at specific detector angular positions can be compiled. The measured patterns with overlapped scattering angles are then merged, and the output is one complete diffraction pattern.

COMMISSIONING RESULTS

A NIST standard LaB_6 SRM 660a [2] was used to determine angular resolutions of the obtained diffraction patterns. The XRD patterns of the SRM 660a measured using the MYTHEN 6K and the MAR345 are shown in Figure 6(a) and 6(b), respectively. The vertical beam size used in both setups was 0.3 mm. Also shown in Figure 6, are the FWHM of the (110) peaks. As seen from the figure, the FWHM of the (110) peak measured using the MYTHEN 6K is around 0.03° in 2θ, which is almost one order of magnitude lower than that measured using the MAR345 and approximately half a typical peak width obtained from a benchtop diffractometer.

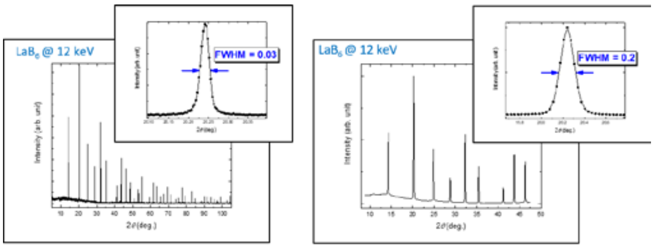

(a) (b)

Figure 6: XRD patterns of NIST standard LaB_6 SRM 660a measured using the MYTHEN 6K (a) and the MAR345 (b). The (110) peak at 20.245° is plotted to emphasize the peak width of 0.03° in 2θ obtained from the MYTHEN 6K and the peak width of 0.2° in 2θ obtained from the MAR345.

Although the angular resolution of the patterns measured using the 2D-XRD system is not as good, it is essential to note that both the 1D and 2D XRD setups can be used complementarily. If the structure contains orientations, it can only be measured using a 2D detector. And for poorly crystallized samples, the crystallinity can be determined from 2D diffraction patterns.

Depending on scattering power of elements in the samples, exposure time to obtain reasonably good signal-to-noise ratio can vary from 120 seconds to 600 seconds for each diffraction pattern of the MAR345 and for each scan of the MYTHEN 6K.

SUMMARY

The development of the XRD end-station has been described. The in-house constructed support structures and developed software were outlined. Experiments were successfully performed using both the 1D-XRD and 2D-XRD setups. Higher angular resolution was achieved using the 1D-XRD setup while the 2D-XRD setup can be an alternative for measurements of samples with orientated structures or poorly crystalline materials.

ACKNOWLEDGEMENTS

Many components of the end-station have been designed and fabricated in-house including the electronics and control systems. The work would not be possible without great contributions from SLRI supporting staffs.

REFERENCES

[1] A. Bergamaschi, A. Cervellino, R. Dinapoli, F. Gozzo, B. Henrich, I. Johnson, P. Kraft, A. Mozzanica, B. Schmitt, X. Shi, "The MYTHEN detector for X-ray powder diffraction experiments at the Swiss Light Source", J. Synchrotron Rad., vol 17, pp. 653-668, 2010.

[2] SRM 660a; Lanthanum Hexaboride Powder; National Institute of Standards and Technology OR National Bureau of Standards; U.S. Department of Commerce: Gaithersburg, MD (13 September 2000).

CONTACT

*Prae Chirawatkul, tel: +66 44217040 ext. 1624, 1471; prae@slri.or.th

X-RAY TOMOGRAPHIC MICROSCOPY BEAMLINE AT SIAM PHOTON LABORATORY

C. Rojviriya[*]*, P. Pakawanit, and C. Phoovasawat*

Synchrotron Light Research Institute (Public Organization) 111 University Avenue, Muang District,
Nakhon-Ratchasima 30000, Thailand

ABSTRACT

A new beamline dedicated to X-raytomographic microscopy(XTM) has been installed at Siam Photon Laboratory (SPL), Synchrotron Light Research Institute (SLRI). This XTM beamline is aimed to provide the submicron resolution X-ray imaging. The synchrotron radiation associated with 2T multipole wiggler has offered the photon intensity and working energy of 5 – 20 keV that benefits X-ray imaging for life science research. With an upgrade of monochromatic system in the near future, the XTM beamline will be enabled energy subtraction tomographic imaging that brings along the scientific opportunities in materials science.

INTRODUCTION

Synchrotron radiation X-ray tomographic microscopy (SRXTM) is a powerful non-destructive technique that enables 3D visualization of opaque samples. Combining a microscopic lens system, the optical performance can achieve submicron details for millimeter-sized sample. The internal structure can be revealed from tomographic datasets reconstructed from radiographic projections. These are acquired while the sample is rotated in between a stationary X-ray source and an X-ray sensitive detector or a scintillator screen that converts X-rays into visible light, which is then recorded by a CMOS camera. The tomographic data is derived from the differential X-ray absorption contributed by the attenuation coefficient, density, and sample thickness with respect to the Beer-Lambert law [1]. The high brilliance of synchrotron lights from the 1.2 GeV Siam Photon Source (SPS) enables the rapid acquisition of X-ray projections as compared to more traditional X-ray laboratory instruments. The X-ray beam collimation providing the parallel beam simplifies the tomographic reconstruction algorithm. In addition, the X-ray energy is tunable to a narrow energy band. This eliminates the issue of energy dependence on X-ray absorption (as known as beam hardening artifacts) and allows for energy-specific quantitative analysis.

The SRXTM facility has been installed at Beamline 1.2W (BL1.2W: XTM), Siam Photon Laboratory (SPL) aiming to provide high-resolution X-ray tomographic imaging facility for local needs and international users. The installation was finished in 2016 and was open to public users for the first time in November 2017. The XTM beamline utilizes synchrotron radiation associated with 2T multipole wiggler at the minimum gap of 23.5 mm, which provides the critical energy of 2 keV. Optical elements are simplified to maintain the homogeneity of beam profile as well as to minimize the loss of photon intensity for quality X-ray imaging. The end-station supports the standard absorption-contrast microtomography, propagation phase-contrast microtomography, and laminography setups. The SRXTM is available in filtered polychromatic beam operation at energy of 5 – 20 keV. With an upgrade of monochromatic system in the near future, the XTM beamline will be enabled tomographic imaging with energy subtraction that brings it the scientific opportunities in materials science.

Here, the article describes the details of XTM beamline including source, beamline, end-station, and its optical performance, enclosed with some applications potential for the 3D inspection and quality assessment in medical research.

PHOTON SOURCE

XTM beamline was installed at the Siam Photon Source (SPS), which operates at 1.2 GeV, 150 mA. The 5-period multipole wiggler (MPW) with a magnetic field of 2T and K factor of 45 was used as the radiation source. The effective source size is 944 µm x 116 µm in horizontal and in vertical, respectively. At the minimum gap of 23.5 mm, MPW generates the synchrotron radiation with the critical energy of 2 keV. Total power associated with the wiggler source is approximately 714 W. Plot of partial flux as a function of photon energy ranging from 2 to 20 keV is showed in Figure 1. The key source parameters [2] are summarized in Table 1.

Table 1: Key parameters of photon source.

Source parameters	
Electron energy	1.2 GeV
Current	150 mA
Effective source size (H, V)	944 µm,116 µm (60.77 µrad, 40.87 µrad)
Multipole wiggler	
Peak field	2.2 T
Period length	22 cm
Number of periods	5
Minimum magnet gap	23.5 mm
Critical energy	2.087 keV
Total power at 150mA	714 W
Photon source size (H, V)	2.77 mm, 0.27 mm (9mrad, 0.25mrad)

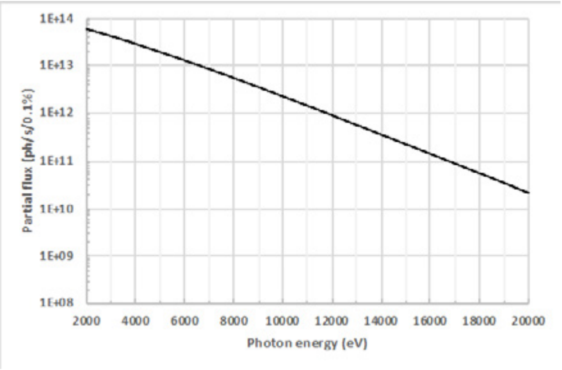

Figure 1: Partial flux of MPW source for the photon energy ranging 2 – 20 keV. The calculation was carried out at a minimum gap of 23.5 mm with SPS parameters, using SPECTRA program [2].

The MPW radiation is utilized by three beamlines. The XTM beamline has taken the center of fan beam radiation as opted for photon flux and intensity. Flanked on either side by ±7.5 mrad is the multiple X-ray techniques beamline (BL1.1: MXT) and the small-angled X-ray scattering beamline (BL1.3: SAXS). Photon source size for XTM beamline is 2.77 mm x 0.27 mm. The horizontal and vertical divergences are 9 mrad and 0.25 mrad, respectively. The beam profile of photon source is shown in Figure 3.

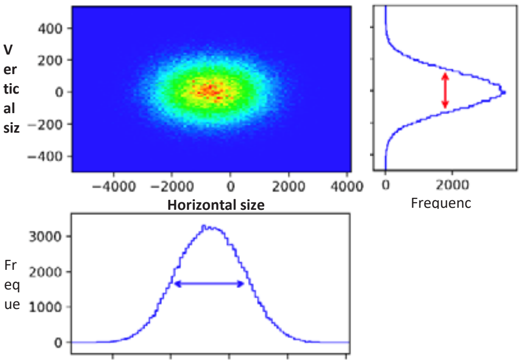

Figure 2: Photon source ofMPW. Horizontal and vertical source size is 2.77 mm and 0.27 mm, respectively. The beam profile was generated on SHADOWOui [3].

XTM BEAMLINE DESCRIPTION

Real space, full-field imaging, and in particular tomography needs a homogeneous and stable beam profileto perform optimal background corrections. Therefore, the XTM beamline is aimed to simplify the optics by minimizing the number of optical elements. This would also help in reducing the intensity loss and possibility to introduce aberration due to roughness.

In XTM beamline, two main optical components are involved in the beam conditioning; a focusing mirror (FM) to collimate the X-ray beam, and a fixed-exit double crystal monochromator (DCM) to provide monochromatic X-ray beam. The schematic diagram of XTM beamline is illustrated in Figure 3. The FM is located at 8900 mmfrom the wiggler source. This is a toroidal mirror with a sagittal radius of 46.05 mm and tangential radius of 5081202 mm to collimate the X-ray beam towards the sample position. The mirror is coated with a layer of Rh with 50 Å thickness on top of a Pt with 250 Å thickness. At the grazing angle of 3.5 mrad, the bilayer coating can optimize the X-ray energy by more than 90% reflectivity. The DCM, which was recently installed in the beamline, is located at 33250 mm from the source. It is in the XTM experimental station due to the hindrance of sister beamlines (as shown in Figure 4). The DCM is the fixed-exit type with the Ge (111) crystals pair employed to produce monochromatic X-ray beam ranging from 5 to 20 keV.The monochromatic X-ray is 25 mm offset from the optical path. The *SHADOWOUi* raytracing program[3] suggested that DCM could give the energy resolution of 10^{-4} although the partial photon flux at the sample position (34 m from source) is varied between 10^{9} - 10^{12} photon/s/0.1% (Table 2). The commission of the DCM is in progress.

For some experiments that require white beam, the DCM can opt for polychromatic X-ray beam. The first crystal can be evacuated from the beam path to allow white beam to pass through to the sample position. Along the XTM beamline, the low energy bandpass (< 2 keV) is filtered by Be windows. For further filtering, the attenuator (18730 mm from the source) can provide acombination of filter choices depending on the imaging experiment.

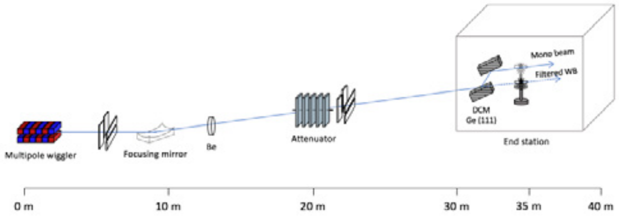

Figure 3: Schematic layout of XTM beamline.

Table 2: Energy resolution and photon flux for X-rays energy range of 5 – 20 keV expected from Ge (111) crystals [2].

Photon energy (keV)	Energy resolution (dE/E)	Intensity (ph/s/0.1%BW)
5	3.80×10^{-4}	3.77×10^{12}
8	3.80×10^{-4}	2.17×10^{12}
10	4.00×10^{-4}	6.94×10^{11}
15	5.40×10^{-4}	5.64×10^{10}
20	9.60×10^{-4}	2.52×10^{9}

END-STATION

The XTM end station is designed for standard absorption-contrast microtomography (micro-CT) and propagation phase contrast micro-CT that mainly utilize the partially parallel beam. As demonstrated in Figure 4, the end station is basically equipped with a sample holder that is situated on a rotary stage, scintillator-coupling X-ray microscopy, and a 5.5 megapixels scientific CMOS camera (PCO.edge, 2560 x 2160 pixels). The sampleis placed at 34 m from the source. A 6-axis goniometer provides total motion control of the sample including X/Y/Z translation, X/Y tilting, and Z rotation for tomographic imaging. The sample centering is associated with additional XY stage on top of the rotary stage. The end-station is mainly controlled by LabVIEW (National Instruments).

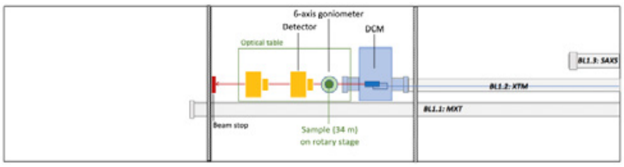

Figure 4: End station of XTM beamline in top view.

As shown in Figure 5, the key components such as the sample goniometer, the precision rotary stage, and the x-ray imaging detector are placed on an optical table. The detector can get either as close as reasonably achievable to the sample to obtain absorptioncontrast for a standard tomography, or it can be translated as far as 1 m from the sample to providepropagation-based phase contrast as needed. For the laminate sample, the goniometer can be tilted up to 15 degrees with respect to the detector for laminographic imaging experiment [4].

The tomographic data can be automatically acquired via *XIMAC* (X-ray Imaging Acquisition), a user-friendly GUI written at SLRI. Associated with on-the-fly control, the data acquisition for a typical scan of 1801 projections takes 16 minutes. The CT reconstruction and segmentation analysis are carried out on *Octopus Reconstruction* software (Inside Matters).

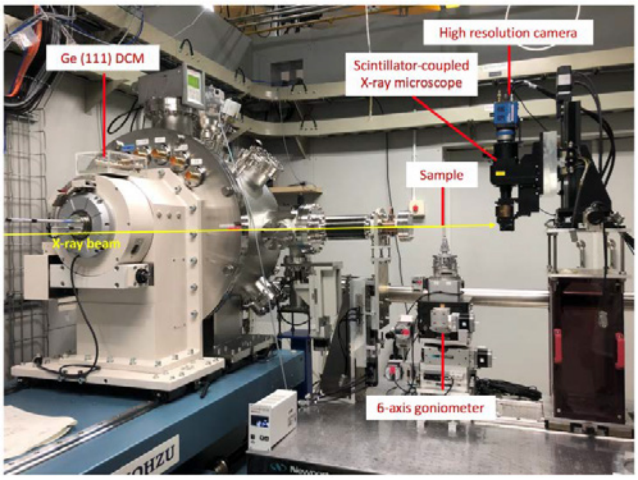

Figure 5: Experimental setup for X-ray microtomography in the end-station of XTM beamline.

OPTICAL PERFORMANCE

Pixel size and spatial resolution of the XTM station is relied on the performance of detection system, which comprises the scintillator-coupled microscope and the high-resolution scientific CMOS camera (2560 x 2160 pixels). Combining magnifying lens system, the optical performance can achieve submicron details for millimeter-sized sample. At 10X magnification, this detection systemcan generate images with isotropic voxel size as small as 0.72 µm with a spatial resolution of less than 2 µm (determined from JIMA resolution pattern in Figure 6). The magnifying lens are available at 2X, 5X, and 10X. Given the magnification, the field of view (FOV) and corresponding pixel sizes are listed in Table 3.

Table 3: Optical performance of XTM detection

PCO.edges CMOS chip	Magnifying lens		
(2560 x 2160 pixels)	2X	5X	10X
Horizontal field of view (mm)	9.24	3.70	1.85
Vertical field of view (mm)	7.80	3.14	1.56
Pixel size (µm)	3.61	1.44	0.72
Maximum resolution (µm)	5	3	1.5

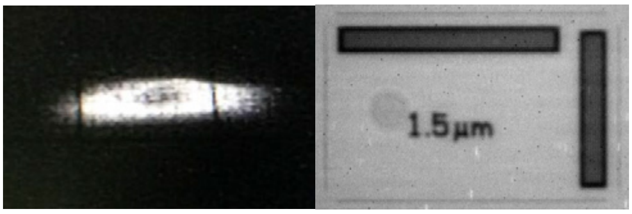

Figure 6: X-ray beam at the sample position (34 m from MPW source) and its X-ray projection of the JIMA resolution pattern taken from the XTM end-station.

Given the optical performance, the microstructure of bone can be visualized in 3D at submicron resolution. Figure 7 and 8 demonstrate the wide application potential for the 3D inspection and quality assessment in bone research. Recently, the XTM beamline has contributed in the impairment of bone microstructure in spontaneously hypertensive rats [5]. The SRXTM of the femoral heads in Figure 7 clearly shows the osteoporosis remarkably increased in spontaneous hypertensive rats relative to wild-type rats. This finding will pave a way to the development of novel therapeutic interventions that concomitantly target hypertension and osteoporosis in the reduction of unwanted outcomes, such as bone fractures, in elderly patients.Furthermore, optical performance of XTM beamline provides capability of visualizing and analyzing porosity quantitatively for compact bone, which is invisible by laboratory CT scanner. Application of XTM beamline in bone researches was also noted in finding a new treatment on diabetic bone porosity for non-obese type 2 diabetic (T2DM) patients [6]. More contribution was made to the research and development of phytoestrogens from Thai herbs for postmenopausal osteoporosis and ovariectomy osteoporosis treatment. Figure 8 demonstrates the microstructure of femur and tibia in normal, ovariectomized, and estradiol-treated ovariectomized mice.

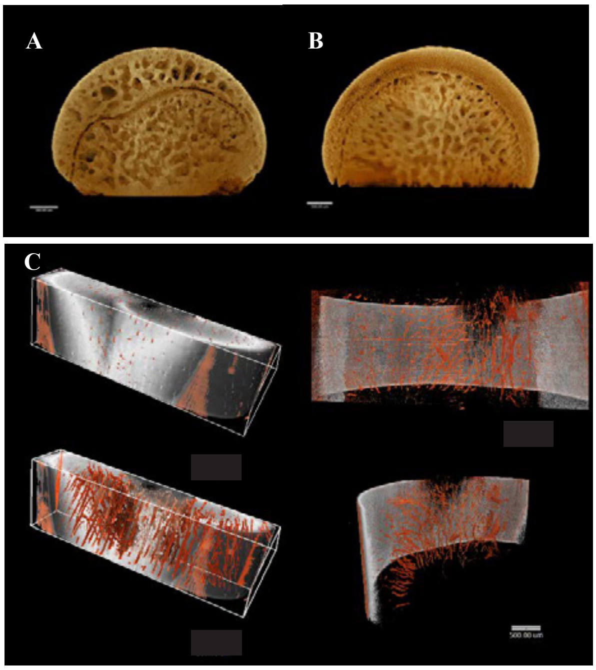

Figure 7: Microstructures of rat bones. (A) femoral head from spontaneous hypertensive rats and (B) wild-type rats [5]. (C) Compact bone from high salt induced hypertensive rats with the network of blood vessels (Harversian canels) represented in red color.

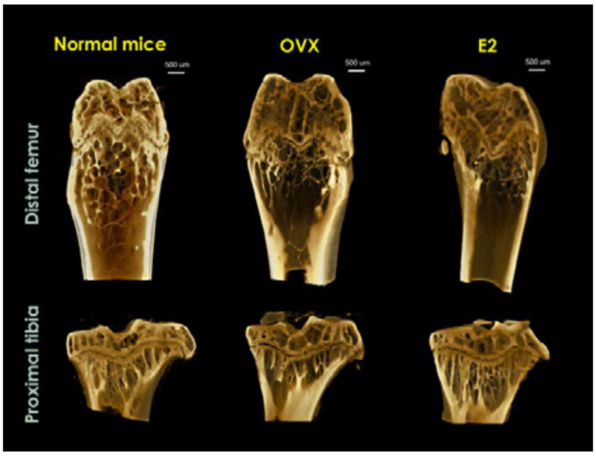

Figure 8: Microstructrure of femur and tibia from normal, ovariectomized (OVX) and Estradiol-treated ovariectomized (E2) mice.

CURRENT STATUS & FUTURE DEVELOPMENT

The XTM beamline is operated in (filtered) polychromatic beam mode. Working energy, expressed in terms of mean energy, is available between 5 – 20 keV by a selection of filters. The X-ray beam at the sample position measured at 34 m from source is approximately 10 x 4 cm without tailoring aperture. The end-station equips the 6-axis goniometer for rotation, translation, and tilting sample, to supports SRXTM imaging setups such as the standard absorption-contrast microtomography, the propagation phase-contrast microtomography, and the laminographic imaging. The DCM with Ge (111) crystal pair has been installed in the beamline recently. The commission will be finished in 2020. With an upgrade of monochromatic system in the near future, the beam hardening artefacts will be reduced thus enhancing the quality of data. In addition, the XTM beamline will be enabled energy subtractiontomography bringing along the scientific opportunities in materials science. Technical specification of XTM beamline is summarized in Table 4.

Table 4: Technical specification of XTM beamline

Specification	
Source	Multipole wiggler, 2T
Energy range	5 – 20 keV
Operation	Monochromatic beam: Ge (111): 5 – 20 keV (approx.10^{12}ph/s/0.1% BW @8 keV) White beam (filtered)
Beam size	Unfocused, (H) 10 mm x (V) 4 mm (untailoredbeam)
Detection	Scintillator-coupled X-ray microscope (Optique Peter, France)

	2560x2160 pixels sCMOS camera (PCO.edge 5.5)
Resolution	1.5 μm spatial resolution 0.72 μm pixel size
Imaging mode	Absorption-contrastmicrotomography Propagation-based phase contrast microtomography Laminography

SUMMARY

The X-ray tomographic beamline (BL1.2W: XTM) was successfully installed at Siam Photon Laboratory in November 2016 and was open to public users in November 2017.The beamline is available in filtered polychromatic X-ray beam operation at the working energy between 5 – 20 keV. The X-ray imaging is based on microscopy platform that can offer a spatial resolution of 1.5 um and isotropic voxel size up to 0.72 um. The optical performance of the XTM beamline has demonstratedthe application potential in bone research. With an upgrade of monochromatic system in the near future, the XTM beamline willbe improved in data qualityand also enabled energy-specific tomographic imaging the scientific opportunities in materials science.

ACKNOWLEDGEMENTS

The authors would like toexpress the gratitude to Supagorn Rugmai for the beamline design and also Somchai Tancharakorn for his support. Many thanks to Siriwat Soontranon and Prae Jariyawatkul, and BL1 members for their assistance that has always been contributed to beamline installation. Our deep appreciation for all the hard work and dedication is offered to all SLRI engineers and supporting staffs.

REFERENCES

[1] D. F. Swinehart, “The Beer-Lambert Law”, *J. Chem. Educ.* vol. 39 (7), p. 333, 1962.
[2] T. Tanaka and H. Kitamura, “SPECTRA: a synchrotron radiation calculation code”, *J. Synchrotron Rad,* vol.8, pp. 1221-1228, 2001.
[3] L. Rebuffi and M. Sanchez del Rio, "ShadowOui: A new visual environment for X-ray optics and synchrotron beamline simulations”, *J. Synchrotron Rad.*vol. 23 pp. 1357-1367, 2016.
[4] L. Helfen,*et al.*,“On the implementation of computed laminography using synchrotron radiation”, *Rev. Sci.Instrum.*vol. 82, 063702, 2011.
[5] W. Tiyasatkulkovit,*et al.*, “Impairment of bone microstructure and upregulation of osteoclastogenic markers in spontaneously hypertensive rats”, *Sci. Rep.*vol. 9, 12293, 2019.
[6] P. Adulyaritthikul*et al.,* “The effect of metformin and P38 MAPK inhibitor on diabetic bone porosity in non-obese type 2 diabetic rats” *J. Appl. Pharm. Sci.* vol. 9(07), pp 082-090, 2019.

CONTACT

*Catleya Rojviriya; tel: +66-44 217040 ext 1431; catleya@slri.or.th

DEVELOPMENT AND CURRENT STATUS OF SAXS/WAXS STATION AT BL1.3W: SAXS/WAXS OF SLRI

*S. Soontaranon, N. Kamonsutthipaijit, S. Chio-Srichan, C. Keawhan and S. Rugmai**
Synchrotron Light Research Institute (Public Organization) 111 University Avenue, Muang District,
Nakhon-Ratchasima 30000, Thailand

ABSTRACT

This report presents the development and current status of Small and Wide Angle X-ray Scattering (SAXS/WAXS) station at beamline 1.3W: SAXS/WAXS of the Synchrotron Light Research Institute (SLRI). The experimental station has capability for simultaneous SAXS/WAXS measurements optimized for studies of nano and semi-crystalline structures of materials. Capability for BioSAXS measurements to investigate low resolution macromolecular structures has also been established.

INTRODUCTION

Small and Wide X-ray Scattering (SAXS/WAXS) techniques have been available for users at Siam Photon Laboratory of SLRI since 2011 .The SAXS technique provides information on the size and shape of nanoparticles and nanostructures, whereas WAXS provides information on crystalline structure of the samples. At the beginning, the beamline optics was designed to deliver X-ray from a bending magnet (BM) source, and separate SAXS and WAXS setups were available to SLRI users [1]. In 2013, a 5-period multipole wiggler (MW) with an effective magnetic field of 2.2 T was installed. The beamline optics have been modified and relocated to utilize high intensity x-ray from the MW [2]. Since then, BL1.3W: SAXS/WAXS has been in operation and welcoming users from around the world.

In the past years, the SAXS/WAXS experimental station has been continuously improved to better served the user community. A simultaneous SAXS/WAXS, together with various in-situ capabilities have been established. To serve the growing macromolecular research community the capability of the station has also been expanded to BioSAXS technique. The development, current status and performance of the beamline are reported in this review.

SIMULTANEUS SAXS/WAXS SETUP AND STATUS

Nano and crystalline structures of material can be studied using combined SAXS and WAXS measurements. Several applications, especially in polymer and material sciences, found these two techniques to be very important structural characterization method. Although two separate measurements of SAXS and WAXS are useful, the drawback is that it cannot give the information at the exact same condition, especially when *in-situ* experiments such as heating or stretching of the sample are performed.

In order to overcome this problem, the capability to simultaneously measure SAXS and WAXS pattern has been developed at BL1.3W: SAXS/WAXS by incorporating two CCD detectors (Rayonix LX170HS and SX165). The WAXS detector LX170HS is specifically designed for synchrotron simultaneous SAXS/WAXS measurement by introducing a groove at the long edge of the detector allowing the SAXS signal with the scattering angle less than 1.8 degree to pass through. The simultaneous SAXS/WAXS setup as shown in Figure 1 allows the SAXS sample-to-detector distance to vary between 2 to 4.5 m. This corresponds to the q-range of 0.2 nm^{-1} to 1.8 nm^{-1} and 0.08 nm^{-1} to 0.8 nm^{-1}, respectively. Simultaneously, the WAXS detector can cover the 2θ range of 8 to 40 degree. The control system has been developed to synchronize the operation of the two detectors. The in-house developed data processing software, SAXSIT [3], was modified to support the data obtained from both detectors. Together with the simultaneous measurement setup, various *in-situ* measurement apparatus, such as heating and stretching, has also been developed. Several user groups especially from polymer sciences are beneficial from this new apparatus due to the improvement on both the accuracy of the measured data and the reduction of the experimental time.

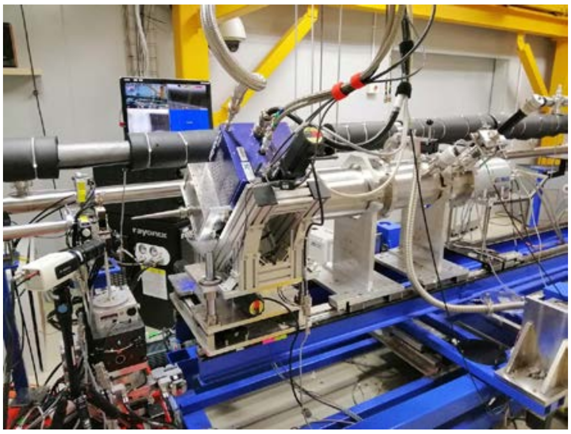

Figure 1: Simultaneous SAXS/WAXS setup at the BL1.3W.

BIOSAXS STATUS

The use of small angle scattering for structural characterizations of biological macromolecules in solution has seen a dramatic increase over the last decade. To respond to the needs of the growing user community, BioSAXS at BL1.3W: SAXS/WAXS has been developed with newly designed sample environment, sample cell, experimental setup and data analysis.

Sample environment

Sudden elevation in temperature can cause proteins to aggregate or denature. The cooling unit system at SAXS beamline has been prepared and can be adjusted at any desired temperature from 10 to 25 °C . For the study of heating effect on proteins, we also provide a heating stage to increase the temperature up to 200 °C.

Sample cell

Two copper blocks of 28 × 40 × 5 mm^3 are used as the caps with PTFE insertion (28 × 40 × 1.5 mm^3), which is inert to chemicals and biological samples in between. Kapton tape with 125 μm thickness was used as windows. Four small bolts were used for cell tightening. The sample cell has an opening to the X-ray beam of 10 × 4 mm^2. Sample cell volume required is 60 μl in air.

Experimental setup

Since the scattering pattern from protein in solution is isotropic, the q-range can be increased with the same Rayonix SX165 detector by off-setting the detector position as shown in Figure 2.

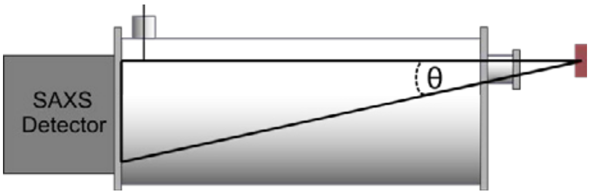

Figure 2: A section of the flight tube. The SAXS detector, the sample cell and the vacuum tube are shown. The triangle represents the accessible range for SAXS.

Data analysis

Initial data processing, which includes calibration, data reduction of the 2D scattering pattern to a 1D scattering curve and background subtraction, occurs at the beamline. Those pre-processing data steps will be done by BioXTAS software [4]. Further processing is performed by the ATSAS package available from EMBL, Hamburg [5]. Both BioXTAS and ATSAS are available for both Windows and OS X.

BioSAXS user base

The statistics of the number of proposals in protein research at BL 1.3W is demonstrated in Figure 3. Since 2013, the first protein SAXS users starts to use beamline. In 2017, number of BioSAXS proposals increased to 10, and then 21 in 2018 when the number of protein proposals equaled the ones from polymer and materials science. The first BioSAXS paper was published in 2018 which draws attentions from the protein researchers to our beamline more [6].

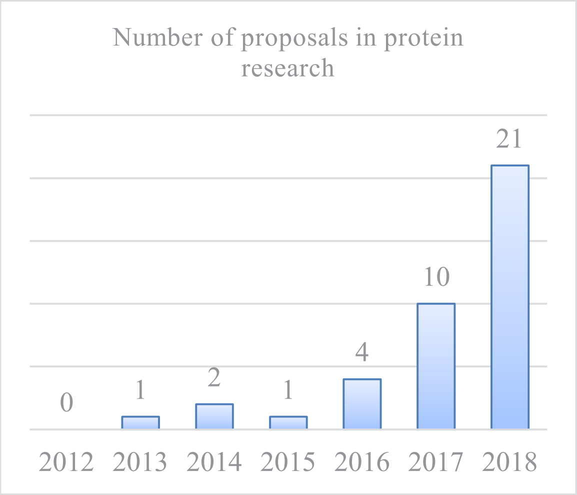

Figure 3: Growth in protein SAXS proposals in the last seven years of BL 1.3W.

CONCLUSION

BL1.3W: SAXS/WAXS has been successfully developed simultaneous SAXS/WAXS measurement to expand its capability in electron density fluctuation detection for material characterization for its users. Moreover, BioSAXS user community is becoming bigger and stronger. The beamline has been accepting proposals from users and supports users from multidisciplinary research. Development projects will be based on user requirements.

ACKNOWLEDGEMENTS

This development has been continuously supported by Technical support group.

REFERENCES

[1] S. Soontaranon and S. Rugmai. "Small Angle X-ray Scattering at Siam Photon Laboratory", Chinese Journal of Physics, vol. 50, pp. 204-210, 2012.

[2] R. Phinjaroenphan, S. Soontaranon, P. Chirawatkul, J. Chaiprapa, W. Busayaporn, S. Pongampai, S. Lapboonreung and S. Rugmai. "SAXS/WAXS Capability and Absolute Intensity Measurement Study at the SAXS Beamline of the Siam Photon Laboratory", *Journal of Physics*: Conference series 425 (2013): 132019.

[3] Rugmai, S. and Soontaranon S. Beamline 1.3W: SAXS (Small Angle X-ray Scattering) [online] Available at: https://www.slri.or.th/en/bl13w-saxs.html [Accessed 1 Apr 2019].

[4] J. B Hopkins, R. E. Gillilan, and S. Skou. “BioXTAS RAW: improvements to a free open- source program for small-angle X-ray scattering data reduction and analysis”, Journal of Applied Crystallography, vol. 50, pp. 1545-1553, 2017.

[5] D. Franke, M.V. Petoukhov, P.V. Konarev, A. Panjkovich, A. Tuukkanen, H.D.T. Mertens, A.G. Kikhney, N.R. Hajizadeh, J.M. Franklin, C.M. Jeffries, and D.I. Svergun, “ATSAS 2.8: a comprehensive data analysis suite for small-angle scattering from macromolecular solutions”, *Journal of Applied Crystallography*, vol. 50, pp. 1212-1225, 2017.

[6] Yuenyao, A, Petchyam, N., Kamonsutthipaijit, N., Chaiyen, P. and Pakotiprapha, D., “Crystal structure of the Flavin reductase of Acinetobacter baumannii p-hydroxyphenylacetate 3-hydroxylase (HPAH) and identification of amino acid residues underlying its regulation by aromatic ligands”. *Archives of Biochemistry and Biophysics,* vol. 653, pp. 24-38,2018.

CONTACT

*Supagorn Rugmai, tel: +66-44 217040 ext 1655; supagorn@slri.or.th

THE CAPABILITY OF BL7.2W: MX BEAMLINE AT SLRI FOR INVESTIGATION OF CRYSTALLINITY OF BIOLOGICAL AND MATERIAL SAMPLES

C. Songsiriritthigul[1*]*, N. Mothong*[1]*, M. Phanak*[1]*, J. Attarataya*[1]*, M. Sripakdee*[2] *and S. Ngamsomrit*[2]

[1]Synchrotron Light Research Institute (Public Organization),111 University Avenue, Muang District,
Nakhon Ratchasima, 30000, Thailand

[2]School of Physics, Suranaree University of Technology, 111 University Avenue, Muang District,
Nakhon Ratchasima, 30000, Thailand

ABSTRACT

This work presents the beamline alignment and the commissioning results of BL7.2W: Macromolecular Crystallography (MX) recently operated on the upgraded 6.5 Tesla Superconducting Wavelength Shifter (SWLS) at the 1.2 GeV Siam Photon Source of the Synchrotron Light Research Institute (SLRI), Thailand. Report of the improvement of measured photon flux will be compared with that of the previous 4.09 Tesla SWLS. Demonstration of capability for the BL7. 2W : MX diffraction beamline at SLRI for investigation of crystallinity of biological and material samples will be also discussed herein.

INTRODUCTION

The operation of 1. 2 GeV storage ring in user mode of operation has been performed since 2016 and the maximum beam current was 150 mA. The two new IDs (a 2.4 Tesla Multipole Wiggler (MPW) and a 6.5 Tesla Superconducting Wavelength Shifter (SWLS) are advantageously utilized for BL7.2W: Macromolecular Crystallography (MX), BL1.1W: Multiple X-ray Techniques (MXT), BL1.2W: X-ray Imaging and X-ray Tomographic Microscopy (XTM) and BL1.3 W: Small/Wide Angle X-ray Scattering (SAXS/WAXS) as reported [1].

Before October 2017, the beamline BL7.2W: MX utilized hard X-rays from the 4.09 Tesla SWLS. The installation of the new RF system has provided the operation the SWLS at its maximum magnetic field of 6. 5 Tesla and consequently increased both the flux and the photon energy delivered to end-station as shown in Figure 1. Flux density at 6.5 T of magnet in SPS storage ring (8 keV) was approximately two times compared to that of 4.09 T.

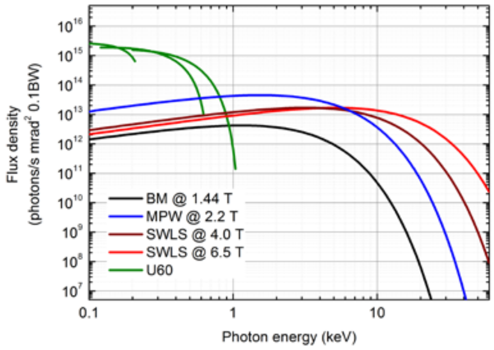

Figure 1: The Siam Photon Source spectral flux densities.

COMMISSIONING RESULTS AND PERFORMANCE

The major optical elements of the BL7.2W: MX beamline are a cylindrical collimating mirror (CM), a double-crystal monochromator (DCM) and a toroidal focusing mirror (FM) as formerly described [2].

In late October, 2016, commercial DCM from Kohzu; model TSR-2DCM, which maintained fixed-exit beam by adopting two cam stages, was installed and commissioned. A simple transmission-mode X-ray Absorption Spectroscopy (XAS) equipment was installed to the downstream of beamline for energy calibration using standard metal foil and photon flux measurement.

The photon flux measurement was carried out to evaluate beamline performance from the commissioning which utilized the upgraded 6.50 T SWLS. The photon flux is in the range of 3.95×10^{11} - 9.75×10^{11} (phs/s/100 mA), depending on the photon energy.

Partial flux calculation for a 4.09 T SWLS at photon energy 8 keV with opening angle of 2.0 mrad (hor) x 0.42 mrad (ver) was 4.49×10^{11} (phs/s/100 mA) whereas that of the 6.50 T SWLS at same energy is 9.75×10^{11} (phs/s/100 mA) as shown in Figure 2.

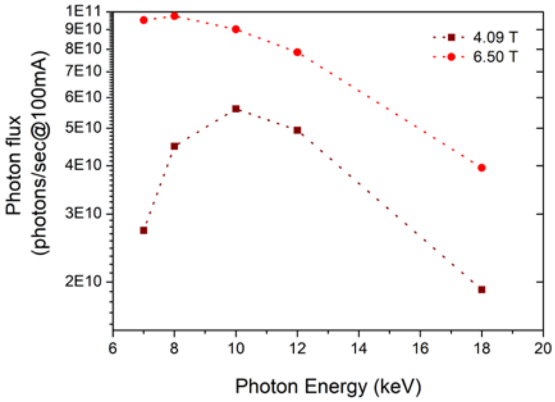

Figure 2: Photon flux at XAS station generated from a 4.09 Tesla and 6.5 Tesla superconducting wavelength shifter. Flux was calculated at sample position of XAS. Vertical opening: 0.42 mrad, Horizontal opening: 2.0 mrad.

From commissioning tests of the 6.50 T SWLS, energy can be selectable within the range of 5 to 20 keV (Table 1). The experimental station of BL7.2W: MX is comprised of a MarDTB diffractometer with a 2theta offset up to 30° and a MarCCD 165 mm detector (Table 1). The crystal cooling to temperature of 100 K is obtained with an Oxford cryostream 700 series. The detector-to-crystal distances can be varied between 45 to 390 mm.

*Table 1***:** *Beamline specification*

Technique	X-ray diffraction (Biological & Material samples)
Source type	Superconducting wavelength shifter 6.50 Tesla
Ring Current	150 mA
Photon Energy	5-20 keV
Optics	Cylindrical Collimating Mirror (Rh/Pt coated) Fixed Exit Double Crystal Si(111) Monochromator Toroidal Focusing Mirror(Rh/Pt coated)
Beam divergence **Beam size**	2.0 mrad x 0.42 mrad at DCM 32.32 mm (h) x 4.09 mm (v) at DCM
Flux	9.75 x 10^{10} phs/s/100mA after FM @8 keV
Goniometer	MarDTB Goniometer system
Xtal-detector Distance	45-390 mm
Detector	MarCCD® with 165mm in diameter
2theta Range	0-30°
Cryo Capability	Oxford cryostream 700 series (working temperature 100 K)
Softwares	iMOSFLM, CCP4 & SAXSIT

The capability of BL7.2W :MX for biological samples

In Thailand, there are researchers from various institutions (Chiang Mai University, Chulalongkorn University, Kasetsart University, Mahidol University, Prince of Songkla University, Suranaree University of Technology, National Science and Technology Development Agency and Synchrotron Light Research Institute) who have been conducting research in structural biology. Since 2014, the result of our users which was successfully submitted to Protein Data Bank is triosephosphate isomerase from *Leishmania siamensis* (PDB code 5CG7) [3]. Moreover, data collection from C-terminal half of gelsolin was accomplished [4]. Up till now, there are two international publications from X-ray diffraction screening experiments using BL7.2W: MX produced by the 4.09 Tesla SWLS [5 & 6].

The capability of BL7.2W :MX for material samples

This is due to limited capability of X-rays produced by the 6.50 Tesla wavelength shifter of the beamline operated on the SPS 1.2 GeV storage ring. As we know, MX users in Thailand have regularly performed experiments at the third-generation light sources such as Spring-8 (Japan), TPS (Taiwan), and Diamond (UK), since they deliver photon flux in the order of 10^{11}-10^{13} photons/sec. Therefore, our remaining beamtime is allocated for material samples.

Image processing program called SAXSIT developed by BL1.3W:SAXS/WAXS team can be used to process the 2D scattering patterns for further analyses. 4-bromo benzoic acid is used as calibration standard for determining the accurate sample to detector distance. Measuring at a sample-to-detector distance of 100 mm gives a clear view on the 2nd, 3rd and 4th order peak, thus corresponding to 4.72, 3.74 and 3.31 Å, respectively as shown in Figure 3a and b.

.

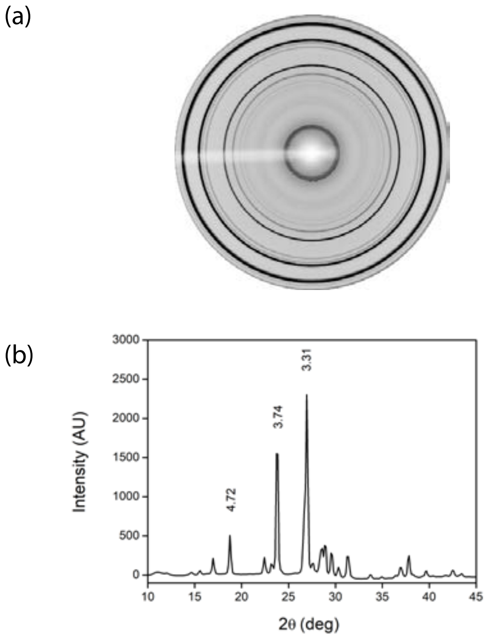

Figure 3: Results from 4- bromo benzoic acid standard at BL7.2W: MX (a) X-ray Diffraction pattern (b) Radially averaged scattering pattern.

Measurements of standard Mn and Bi were carried out as shown in Figure 4a and b, respectively.

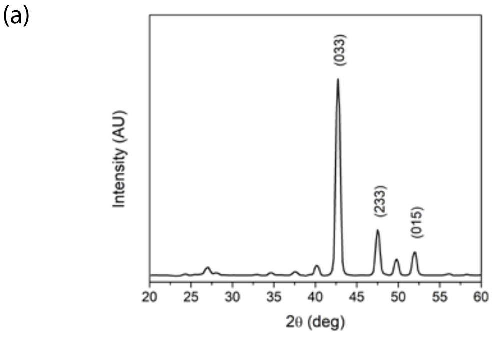

Figure 4: X-ray Diffraction pattern (a) Mn standard (b) Bi standard.

(b)

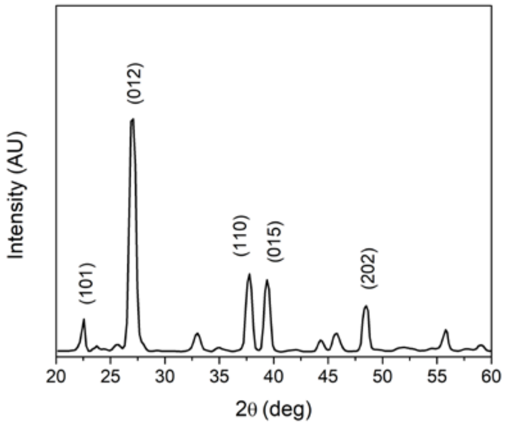

Figure 4: X-ray Diffraction pattern (a) Mn standard (b) Bi standard(continue).

A two-dimensional XRD system in transmission mode is also introduced to study of zeolite synthesized as shown in Figure 5.

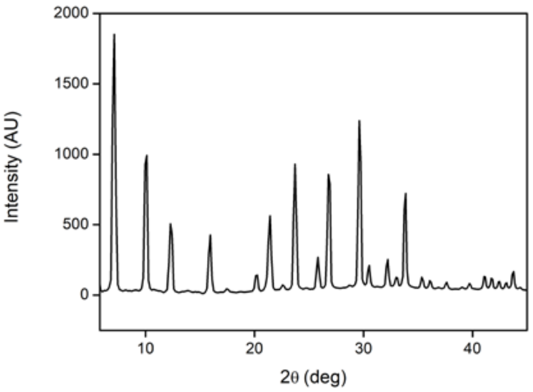

Figure 5: Radially averaged scattering patterns of zeolites synthesized.

Moreover, the modified geometrical setup was performed for grazing-incidence X-ray diffraction (GIXRD). Taking the advantage of accurate and fine controlling of phi-axis of MarDTB Goniometer system, users can employ small incident angles for the incoming X-ray beam. Therefore, diffraction can be made surface sensitive. The GIXRD was used for identifying crystalline structures in the iron nitride (FeN) films on silicon (100) substrate (unpublished data). Deposition of iron nitride (FeN) films on the substrate was prepared by reactive gas-timing dc magnetron sputtering technique. The nitrogen timing was 10, 15 or 20 sec, and the argon timing was fixed at 30 sec. Different Ar: N_2 gas-timing ratios cause the formation of different Fe-N phases of the as-deposited and annealed films. This may be due to the different concentrations of nitrogen in the deposited films leading to the variation of the mixture of Fe-N phases after annealing at the same temperature. In all cases, the results suggest that when the annealing temperature increases, there might be a reduction of nitrogen concentration. When the annealing is increased up to 500, only γ″-FeN and α-Fe were found.

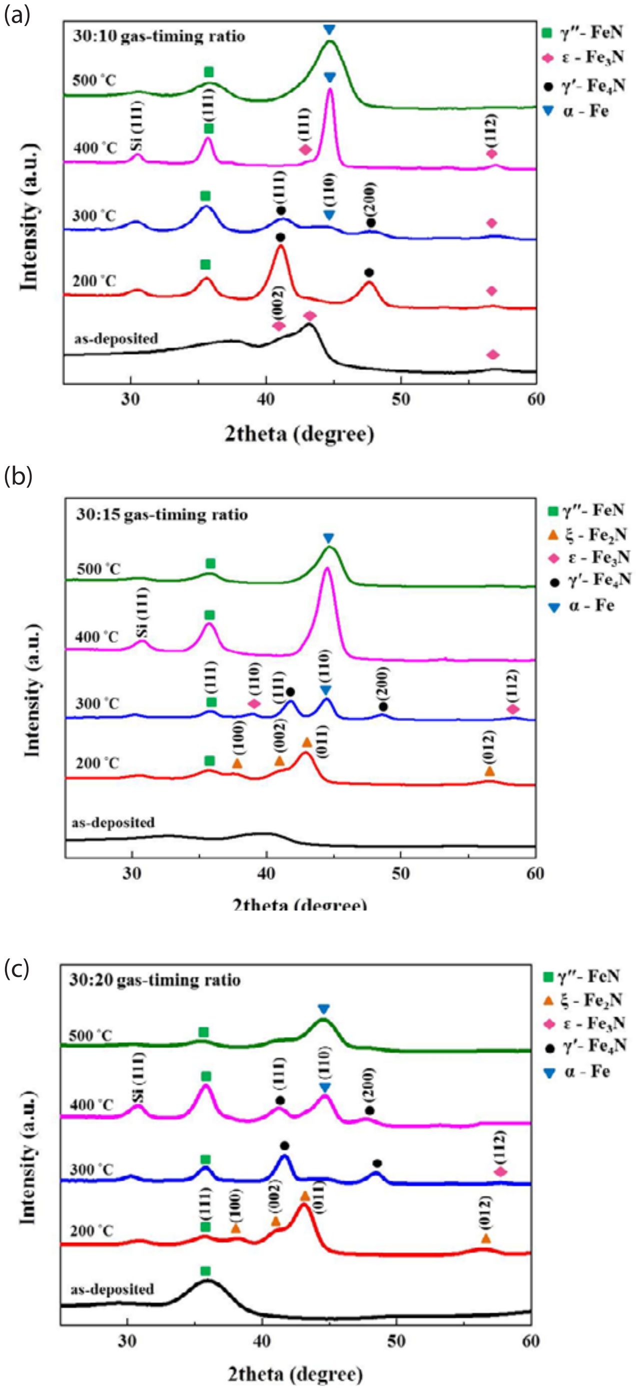

Figure 6: GIXRD patterns Fe-N films prepared by dc magnetron sputtering with Ar:N_2 gas-timing ratio of (a) 30:10, (b) 30:15 and (c) 30:20 before and after annealing at 200, 300, 400 and 500 °C.

SUMMARY

BL7.2W: MX has lately delivered hard X-rays from 6.5 T SWLS of the Siam Photon Storage Ring. Commissioning results show the performance enhancement of the BL7.2W: MX. At the present, BL7.2W: MX is proposedly dedicated to Macromolecular Crystallography. However, MarDTB Goniometer system installed at the end station gives a new possibility for new approaches, transmission XRD and GIXRD techniques.

ACKNOWLEDGEMENTS

We wish to thank other support staffs from Control System Section, Component Fabrication Section and Electronics & Information Support Section.

REFERENCES

[1] P. Klysubun, S. Boonsuya, N. Juntong, K. Kittimanapun, S. Kongtawong, S. Krainara, A. Kwankasem, T. Pulampong, P. Sudmuang and N. Suradet. Siam Photon Source: Present Machine Status and Future Upgrades, Proceedings of IPAC2017, May 14-19, 2017, Copenhagen, Denmark.

[2] W. Klysubun, M. Sophon, M. Phanak, N. Deethae, N. Wongprachanukul, A. Suthummapiwat, P. Cherdchoo and P. Songsiriritthigul. Development of a hard X-ray beamline for macromolecular crystallography at the Siam Photon Laboratory, The Fifth Asia Oceania Forum for Synchrotron Radiation Research (AOFSRR2010), July 5, 2010, POSCO International Center, Pohang, Korea.

[3] B. Kuaprasert, J. Attarataya, P. Riangrungroj, W. Pornthanakasem, W. Suginta, M. Mungthin, S. Leelayoova, K. Choowongkomon and U. Leartsakulpanich. Preliminary crystallographic analysis of *Leishmania siamensis* triosephosphate isomerase complexed with its novel inhibitor, *J. Sci. Technol.*, vol. 22(3), 285-293, 2015.

[4] S. Choknud, C. Songsiriritthigul and S. Chumnarnsilpa. The structural study of the C-terminal half of gelsolin. The 10th international Symposium of the Protein Society of Thailand, Bangkok, Thailand, July 15-17, 2015, pp. 167-172.

[5] J. Siritapetawee, C. Talabnin, J. Vanichtanankul, C. Songsiriritthigul, K. Thumanu, C-J. Chen and N. Komanasin. Characterization of the binding of a glycosylated serine protease from *Euphorbia* cf. lactea latex to human fibrinogen, *Biotechnol. Appl. Bioc.*, vol., 64(6), 862-870, 2017.

[6] K. Boonyapakron, A. Jaruwat, B. Liwnaree, T. Nimchua, V. Champreda, P. Chitnumsub, Structure-based protein engineering for thermostable and alkaliphilic enhancement of endo-β-1,4-xylanase for applications in pulp bleaching, *J .Biotechnol.*, vol 259, 95–102, 2017.

CONTACT

*Chomphunuch Songsiriritthigul, tel: +66-44 217040 Ext 1485; chomphunuch@slri.or.th

DEVELOPMENT OF ELECTRON-YIELD XANES AT BEAMLINE BL8

W. Klysubun, P. Amonpattaratkit, S. Chaichuay, and C. Cholsuk*
Synchrotron Light Research Institute (Public Organization) 111 University Avenue, Muang District,
Nakhon Ratchasima 30000, Thailand

ABSTRACT

The paper reports development of electron-yield (EY) mode X-ray absorption near-edge structure spectroscopy at the SLRI BL8 beamline. A new electron-yield detector was fabricated and tested at Mg, S, and Ni *K* edges. MgO, FeSO$_4$, and NiO were used as test samples. The detector was optimized using 150 V applied voltage on its Ni mesh, 5 mm distance between the Ni mesh and the sample, and the Ni mesh size of 484 mm^2. This results in high S/N ratios of the measured XANES spectra. The EY XANES data were also compared with those acquired in transmission and fluorescence-yield modes.

INTRODUCTION

The BL8 beamline at SLRI has been operated for synchrotron users to perform X-ray absorption spectroscopy (XAS) since 2006. It delivers a vertically-collimated, unfocused X-ray beam to a XAS station. The photon energy of the beamline ranges from 1.0 keV to 13.2 keV [1-2] covering *K*-edge absorption from sodium to selenium and L_3-edge absorption from bromine to lead. X-ray absorption near edge structure (XANES) and extended X-ray absorption fine structure (EXAFS) spectra can be acquired in transmission (TM), fluorescence-yield (FY) and electron-yield (EY) modes.

By comparison, EY experiments detect electrons rather than X-rays, and only electrons near surface region of the sample can escape and consequently counted by a detector. Therefore, EY is a surface probe. Previously, an in-house EY detector was made, but it was not often used because of the difficulty of mounting a sample and connecting electrical wires. A simple EY setup consists of a metal mesh of positive voltage and a grounded conductive sample holder as shown in Fig. 1. When an X-ray beam irradiates the sample in vacuum, emitted Auger electrons are easily drawn by the mesh, resulting in electron currents in picoampere range, which can be measured with a current amplifier. In this report, a new user-friendly EY detector designed by Klysubun and Chaichuay [3] were tested at the Mg *K*-edge, S *K*-edge, and Ni *K*-edge.

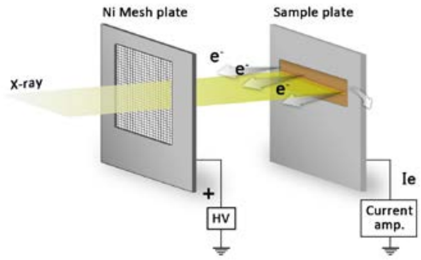

Figure 1: Schematic drawing of the electron-yield detector.

EXPERIMENTS

Figure 2 shows the new EY detector, which can be easily connected to the sample chamber of the XAS station with an ISO DN100 flange. The sample chamber was evacuated to a pressure of 1 mbar during the following experiments.

At the Mg *K* edge (1250 eV), MgO powder was used as a test sample. It was ground into fine particles and homogeneously pasted on copper conductive tape (Ted Pella, Inc.) on the stainless-steel sample holder of the EY detector (Fig 3). The BL8 double crystal monochromator was equipped with beryl(10-10) crystals for photon energy scanning, and the I_0 chamber was filled with nitrogen gas (5 mbar) for recording incident photon intensity (I_0). The electron currents from the I_0 and EY detectors were amplified at 10^8 V/A and 10^{10} V/A, respectively, using Keithley 428 current amplifiers, then converted to frequency at 0.1MHz/V and finally counted. XANES spectra of MgO were measured as a function of applied voltage on the Ni mesh, distance between the mesh and the sample, and mesh size. Absorption (μ) was determined from I_e/I_0. A signal-to-noise ratio (S/N) was measured by $N_s/(N_s+N_b)^{1/2}$ where N_s and N_b are the counts of the signal and the background of I_e, respectively [4].

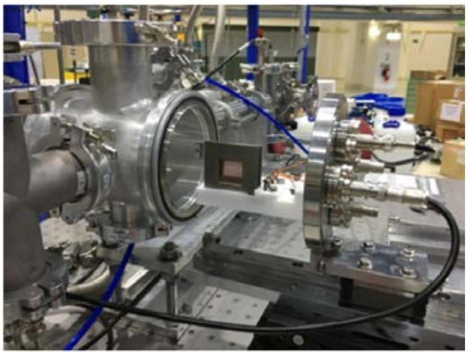

Figure 2: Photograph of the new electron-yield detector.

Figure 3: Sample preparation for the EY experiments.

At S *K* edge (2472 eV) and Ni *K* edge (8333 eV), $FeSO_4$ and NiO were used as test samples, respectively; they were similarly prepared as described for MgO. The $FeSO_4$ experiment employed InSb(111) crystals, 37 mbar nitrogen in the I_0 chamber, and the 10^7 V/A for I_e amplifying; the NiO experiment, Ge(220) crystals, 61 mbar Ar in the I_0 chamber, and the 10^{10} V/A for I_e amplifying. Normalization of the XANES data were carried out using the Athena software [5].

RESULTS AND DISCUSSION

The S/N ratios were determined from the experimental Mg *K*-edge XANES spectra for all settings reported in Table 1. Figure 4 shows the MgO spectra of settings A and E, having the lowest S/N (120) and the highest (221) S/N, respectively. Obviously, the signal counts of I_e and S/N are linearly increased with the mesh voltage where the best spectrum was obtained at 150 V (Fig. 5). Using higher voltage might further increase the EY signal. Settings E and G compare the distances between the mesh and the sample, 5 mm and 10 mm, at 150 V; similarly, settings D and F compare the same distances at 125 V. The results indicate that the 5 mm distance yields better S/N. Settings D and H compare the mesh sizes, 484 mm^2 and 1225 mm^2; the smaller one results in better S/N. Optimization of the EY detector is therefore crucial to obtain the best spectral quality.

Table 1: Settings of the new EY detector and S/N of the MgO XANES spectra

Setting	Voltage (V)	Distance (mm)	Mesh size (mm^2)	S/N
A	50	5	484	120
B	75	5	484	138
C	100	5	484	157
D	125	5	484	197
E	150	5	484	221
F	125	10	484	166
G	150	10	484	200
H	125	5	1225	157

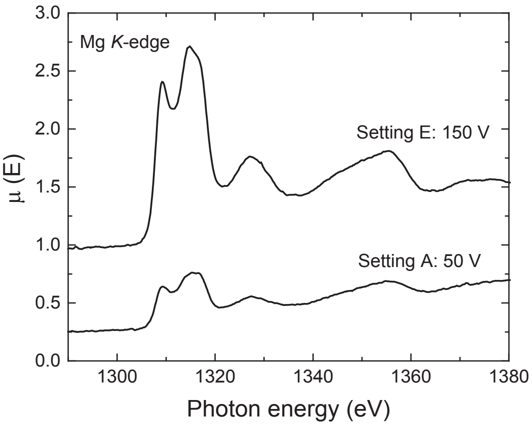

Figure 4: Mg K-edge XANES spectra of MgO measured with settings A and E, comparing the mesh voltages of 50 V and 150 V.

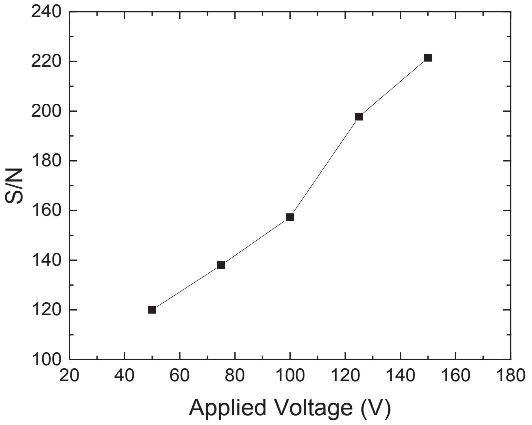

Figure 5: S/N ratio as a function of applied voltage on the Ni mesh.

XANES spectra collected from the EY mode are free of self-absorption effect [6]. This can be seen in Fig. 6 comparing the EY MgO spectra with that recorded in FY mode by a 7-element Si drift detector at BL8. Additionally, the EY S/N is much higher resulting in shorter measurement time. The observed MgO XANES characteristic peaks are consistent with those reported by Aritani *et. al.* [7] and Takata *et. al.* [8]. It should be noted that the TM mode is also not affected by self absorption, but it is difficult to prepare the sample as the X-ray attenuation length in MgO is very short, i.e. 0.7 μm at the Mg *K* edge.

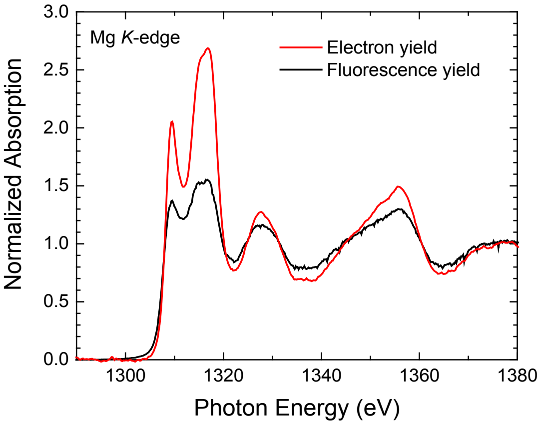

Figure 6: Mg K-edge XANES spectra of MgO measured in electron-yield and fluorescence-yield modes.

Although EY deceases as atomic number increases, Auger electrons from S and Ni can be effectively detected in our measurements. Shown in Fig. 7 are an S *K*-edge XANES spectra measured with the EY detector and a transmission spectrum. The EY S/N is 40. The white-line peak seen in the EY data is much stronger than that of the TM data; this discrepancy is not yet explainable. Additional experiments shall be performed on other S compounds to investigate this unknown behavior. On the contrary, XANES spectra of NiO measured from the EY and TM modes are in good agreement as illustrated in Fig. 8. The EY S/N is 381.

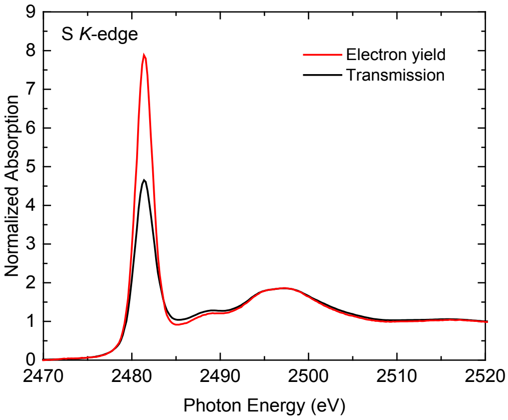

Figure 7: S K-edge XANES spectra of $FeSO_4$ measured in electron-yield and transmission modes.

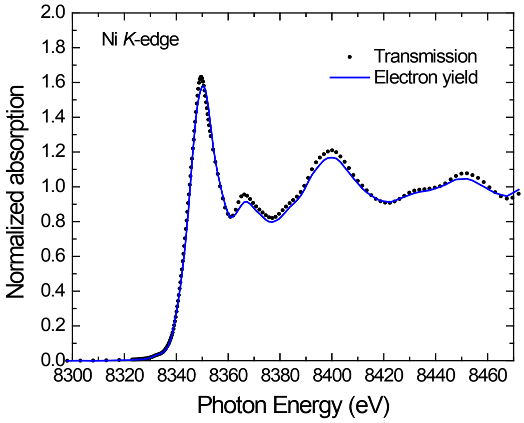

Figure 8: Ni K-edge XANES spectra of NiO measured in electron-yield and transmission modes.

CONCLUSION

A new electron-yield detector was tested at the beamline BL8 at the Mg, S, and Ni *K* edges. Presently, the detector has been optimized using an applied voltage on the Ni mesh, 150V; distance between the Ni mesh and the sample, 5 mm; and the Ni mesh size, 484 mm^2. High S/N ratios were achieved in the experimental XANES data of MgO, $FeSO_4$, and NiO used as test samples. The EY XANES technique at BL8 was successfully developed to support surface-science studies in the future.

ACKNOWLEDGEMENTS

We would like to thank Garnet Hoyes for his recommendation and discussion on the EY detector. Ladawan Prakhamthong and Supanun Lapboonrueng are acknowledged for experimental supports.

REFERENCES

[1] W. Klysubun, P. Tarawarakarn, N. Thamsanong, P. Amonpattaratkit, C. Cholsuk, S. Lapboonrueng, S. Chaichuay, W. Wongtepa, "Upgrade of SLRI BL8 Beamline for XAFS spectroscopy in a photon energy range of 1-13 keV", *Radiat. Phys. Chem.*, in press, 2019.

[2] W. Klysubun, P. Sombunchoo, W. Deenan, C. Kongmark, "Performance and status of Beamline BL8 at SLRI for x-ray absorption spectroscopy", *J. Synchrotron Rad.*, vol. 19, pp. 930-936, 2012.

[3] W. Klysubun, S. Chaichuay, "Design of an EY detector", Thailand patent application, in preparation.
[4] H. Abe, G. Aquilanti, R. Boada, B. Bunker, P. Glatzel, M. Nachtegaal, S. Pascarelli, "Improving the quality of XAFS data. *J. Synchrotron Rad.* 25, 972-980, 2018.
[5] B. Ravel, M. Newville, "ATHENA, ARTEMIS, HEPHAESTUS: Data analysis for X-ray absorption spectroscopy using IFEFFIT", *J. Synchrotron Rad*. 12, 537-541.
[6] W. Calvin, *XAFS for everyone*, CRC Press, 2013.
[7] H. Aritani, H. Yamada, T. Yamamoto, T. Tanaka, S. Imamura, *J. Synchrotron Rad*. **8**, 593-595, 2001.
[8] Takata, Y., Shigemasa, E., Kosugi, N. (2001). *J. Synchrotron Rad.* **8**, 351-353.

CONTACT

*Wantana Klysubun, tel: +66-44-217040 ext. 1490; wantana@slri.or.th

ASEAN BEAMLINE AT SIAM PHOTON LABORATORY: PROGRESS REPORT

S. Tancharakorn, S. Srichan, R. Supruangnet, N. Jearnaikoon, K. Sitisard and P. Sanwong*
Synchrotron Light Research Institute (Public Organization) 111 University Avenue, Muang District,
Nakhon Ratchasima 30000, Thailand

ABSTRACT

A beamline so-called ASEAN is one of X-ray absorption spectroscopy beamlines at Siam Photon Laboratory (SPL), and will be in operation in the mid-2020. The beamline utilises synchrotron radiation from a 3.5T superconducting multipole wiggler (SMPW) which can provide synchrotron radiation with energy up to 30 keV. Beamsize at sample position is 1 mm in diameter with photon flux of 10^{12} ph/s at 10 keV. A Si(Li) detector supported by IAEA will be installed by the end of 2020. A paraboloidal mirror lens will later be installed allowing the beam to be focused down to 10 μm in diameter and μ-XAS technique can be performed. Currently, the beamline construction and installation has already been completed. The SMPW will be commissioned in the mid-2019 followed by the test of the ASEAN beamline.

INTRODUCTION

Siam Photon Laboratory (SPL) has operated synchrotron light source since 2003. So far, 10 beamlines including 4 XAS beamlines are available for users. [1] There are some differences among these XAS beamlines as shown in Table 1.

Table 1: List of XAS beamlines at SPL

BL	Source	Energy range (keV)	Beamsize (HxV) mm²
BL1.1W	MPW(2.2T)	4-18	5x2.5
BL2.2*	BM	4-12	1x2
BL5.2	BM	1.25-12	10x1
BL8	BM	1.25-11	13x2.5

*BL2.2: Time Resolved XAS
MPW: Multipole Wiggler
BM: Bending Magnet

The ASEAN beamline will utilise synchrotron radiation from a new insertion device so-called a superconducting multipole wiggler (SMPW) designed and constructed by National Synchrotron Radiation Research Center (NSRRC) [2], Taiwan. It has been installed into the storage ring since July 2018. The new source can provide synchrotron energy from 5 to 25 keV. In comparison with other XAS beamlines, it gives users an advantage for studying K_α edge of heavy elements such as Cd. The ASEAN beamline will mainly be dedicated for users from South-East Asia in hoping to strengthen regional collaboration using science and technology. One thing should be mentioned that this beamline is also partly supported by the International Atomic Energy Agency (IAEA).

BEAMLINE DESIGN

The design of ASEAN beamline is similar to a regular X-ray beamline in many synchrotron radiation facilities. It consists of a collimating mirror (CM), a double-crystal monochromator (DCM) and a focusing mirror (FM). The optical layout of ASEAN beamline is shown in Figure 1.

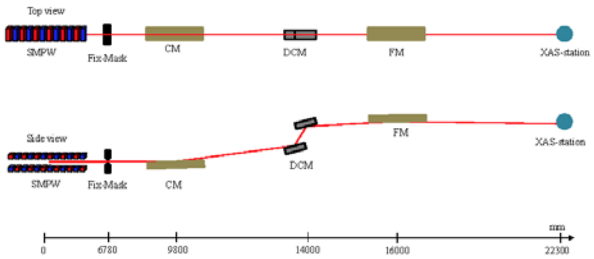

Figure 1: Optical layout of ASEAN beamline

After the water-cooled mask in front-end section, the central beam is vertically collimated by a water-cooled collimating mirror (CM) located at 9.8 m from the source. A double crystal monochrotmator (DCM) with a pair of Si(111) or Si(311) crystals is located at 14 m. The beam is then focused using toroidal mirror at 16 m with the focus point at sample position of XAS experiments situated 22.3 m away from the synchrotron radiation source. The cut-off energy of a grazing incident angle of 2.5 mrad on the Pt-coated CM and FM around 33 keV. The reflectivity of Pt coating is mostly greater than 85% in the photon energy up to 30 keV. The calculated photon flux and the expected beam size at the sample position as shown in Figure 2 and 3, respectively.

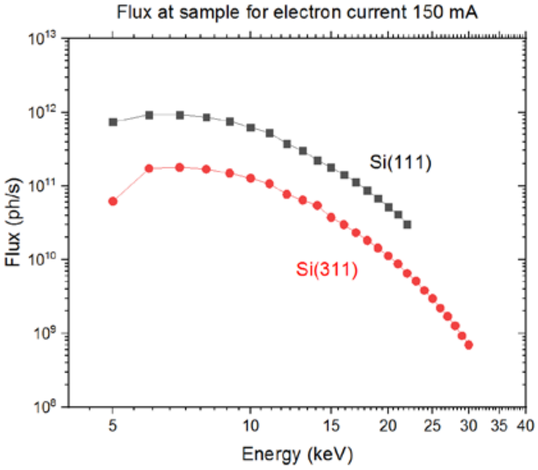

Figure 2: Calculated photon flux at sample position.

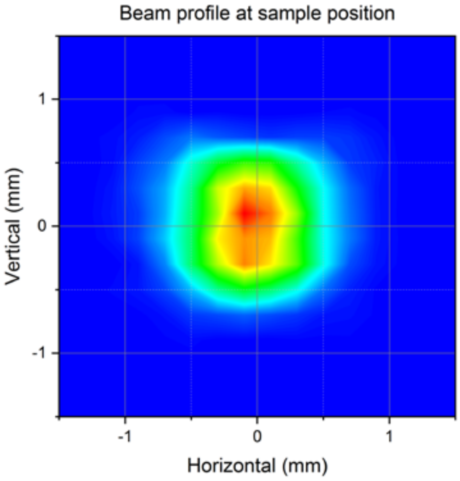

Figure 3: Expected beam size at sample position.

CONSTRUCTION AND INSTALLATION

Some beamline components such as chambers for bending magnet, front-end, collimating mirror and focusing mirror have been constructed in-house at SLRI. Figure 4 shows 2D drawing of ASEAN beamline. The ASEAN beamline is connected to BM5 chamber which has already been occupied by BL5.2 and BL5.3. Therefore, a new bending chamber has to be re-designed to accommodate at least 3 beamlines at different angles. [1] For ASEAN beamline, front-end chamber consists of photon beam position monitor (PBPM) and three water-cooled masks to divide synchrotron beam into 3 branches; A, B and C. The ASEAN beamline is assigned to 5.1WB, where W stands for wiggler and B is for central line. The DCM is purchased from TOYAMA, Japan. To cover energy range from 5 – 25 keV, a pair of Si(111) crystals will be installed. They can be replaced with Si(311) for higher energy range.

CURRENT STATUS AND FUTURE PLAN

In 2018, SMPW and cryogenic transfer lines (LHe and LN_2 lines) were successfully installed during machine shutdown in July and August followed by the installation of front end and collimating mirror chamber. DCM was later installed in October. In 2019, radiation shielding hutch will be finished in January. Focusing mirror chamber and end-station will be installed in the February. The beamline commissioning will be carried out in May and June before the annual maintenance in July. The 4-element Si(Li) detector from IAEA will be installed by October. The first user is expected to perform an experiment at the ASEAN beamline by the end of 2019. In the late 2020, a paraboloidal mirror lens will be installed for μ-XAS and μ-XRF techniques.

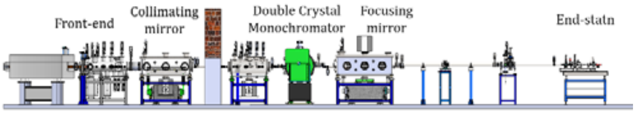

Figure 4: A 2D drawing of the ASEAN beamline.

ACKNOWLEDGEMENTS

We would like to acknowledge NSRRC, Taiwan for helping us with the design and construction of SMPW as well as other technical supports. We would like to thank IAEA for SDD detector and financial support for training. This project could not be possible without support from SLRI engineering teams.

REFERENCES

[1] S. Tancharakorn, 2018, The Siam Photon Laboratory, a high brilliant light source in South-East Asia, *SLRI Annual Review 2016-17*, 10-13.

[2] J. C. Jan et al, "Design of a 3.5 T Superconducting Multipole Wiggler", *Proc. IPAC'17*, pp. 3564-3567, 2017.

CONTACT

*Somchai Tancharakorn, tel: +66-44-217040 ext 1477; somchai@slri.or.th

---

[1] See article "Design, fabrication and installation of vacuum chamber for bending magnet at Siam Photon Source" for more detail.

SUPERCONDUCTING MULTIPOLE WIGGLER FOR ASEAN BEAMLINE

P. Sunwong[*]*, A. Kwankasem, V. Sooksrimuang, C. Dhammatong, N. Suradet, C. Preecha, S. Boonsuya, S. Srichan, K. Sittisard, S. Chaichuay, T. Pulampong, T. Chanwattana, P. Sudmuang, R. Supruangnet and S. Tancharakorn*

Synchrotron Light Research Institute (Public Organization) 111 University Avenue, Muang District, Nakhon-Ratchasima 30000, Thailand

ABSTRACT

A new insertion device, Superconducting Multipole Wiggler (SMPW) with the peak field strength of 3.5 T, was installed in the storage ring of Siam Photon Source as a radiation source for a new hard X-ray beamline. Cool-down process, as well as magnet training, was performed with careful tuning of liquid helium filling procedure for efficient management of liquid helium supply. The SMPW was successfully tested with electron beam and commissioning results show that the effects on beam dynamics are as expected. They can be compensated for using quadrupole magnets and horizontal/vertical correctors installed at the upstream and downstream. The SMPW is planned for operation and providing the beam service for beamline commissioning in 2019.

INTRODUCTION

A Superconducting Multipole Wiggler (SMPW) was designed and manufactured by the National Synchrotron Radiation Research Center (NSRRC) [1] as a radiation source for a so-called ASEAN beamline, a new beamline of the Siam Photon Source. The beamline will utilize hard X-ray radiation with the photon energy between 5 – 30 keV for X-ray Absorption Spectroscopy (XAS) technique. With the capability of liquid helium liquefaction system at the Synchrotron Light Research Institute (SLRI) and the available space of 1,660 mm in the storage ring, a superconducting insertion device with the peak field strength at least 3.5 T and the number of periods at least 5 was chosen. This manuscript presents the SMPW design specification, the performance in terms of magnetic field quality and operation, cryogenics operation details and commissioning results.

SUPERCONDUCTING MULTIPOLE WIGGLER

Detailed specification and requirement of the SMPW are summarized in Table 1. The minimum peak field strength is 3.5 T, the minimum number of periods is 5 and the period length is ~77 mm. The good field region, where the field homogeneity is better than 0.5%, is ± 25 mm. The static heat load should be less than 3.0 W or 4.2 L/hr. The final design values are also listed in the table.

Figure 1 shows an overall drawing of the SMPW including the extended Beam Position Monitors (BPMs) at the upstream and downstream. In addition, a pair of horizontal/vertical correctors and magic fingers were also designed and manufactured for correction of electron trajectory and integral multipole errors. The magic fingers are, however, not used because the measured dynamic field integral of the SMPW is small (13.0 G·cm).

Table 1: Specification and requirement of SMPW.

SMPW parameters	Requirement	Design value
Peak field strength (T)	≥ 3.5	3.55
Period length (mm)	~77	77
Number of periods	≥ 5	6
Pole gap (mm)	~22	22.5
Clearance aperture (mm × mm)	15 × 106	15 × 106
Good field region (mm), $\Delta B/B \le 0.5\%$	± 25	± 25
Static heat load (W)	< 3.0	1.54
Superconducting wire	NbTi	NbTi
Beam duct material	Aluminum	Aluminum

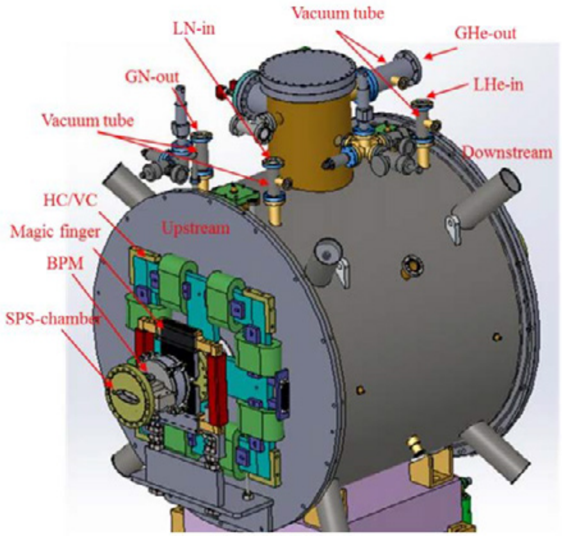

Figure 1: Overall drawing of SMPW, extended BPMs and correctors.

The calculated flux density obtained from 3.5 T SMPW is 2×10^{13} photons/s/mrad^2/0.1BW at the photon energy of 10 keV, the beam energy of 1.2 GeV and the beam current of 150 mA as presented in Figure 2. Total power of photons radiated from the SMPW is 1.05 kW with the radiation fan size of 10.8 mrad and 0.43 mrad in horizontal and vertical directions, respectively. The calculated deflection parameter is 25. Figure 3 is the calculated linear power density along the horizontal direction. Two horizontal photon absorbers were installed at the SMPW downstream to absorb photon energy at the angle larger than 8.6 mrad so the heat load on the bending chamber is minimized. Photon energy depositing on the downstream straight chamber is less than 1 W, therefore the existing chamber can be used without modification.

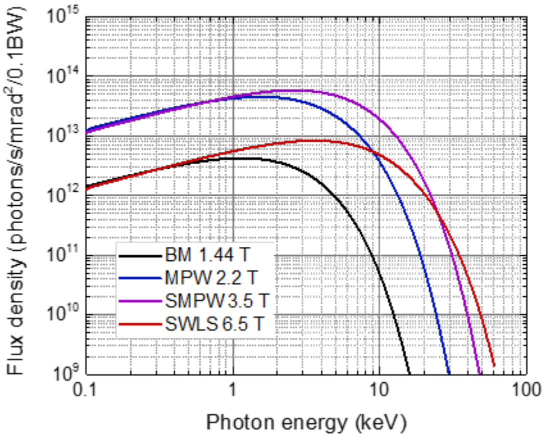

Figure 2: Radiation spectrum of 3.5 T SMPW and other insertion devices and bending magnet of Siam Photon Source for the beam energy of 1.2 GeV and the beam current of 150 mA.

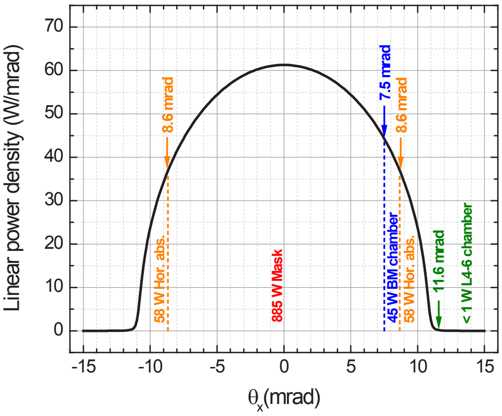

Figure 3: Linear power density along the horizontal radiation angle of 3.5 T SMPW for the beam energy of 1.2 GeV and the beam current of 150 mA.

Performance

The SMPW was tested at NSRRC to evaluate the performance such as superconducting and cool-down behaviors, static heat load and magnetic field quality. During the first cool-down with liquid helium at NSRRC, the maximum training current achieved is 269 A. The second cool-down was done at SLRI before the site acceptance test with the maximum training current of 266 A, which is 5% above the nominal current of 253 A for the peak field strength of 3.5 T. Training performance of the SMPW tested at SLRI is shown in Figure 4. Temperatures of the cryostat, magnet arrays and current leads were also monitored and confirm a consistency between the two cool-downs. Static heat load of the SMPW is 2.23 W measured at NSRRC and 1.99 W measured at SLRI. These are corresponding to an approximated liquid helium consumption of 3.1 and 2.8 L/hr, respectively.

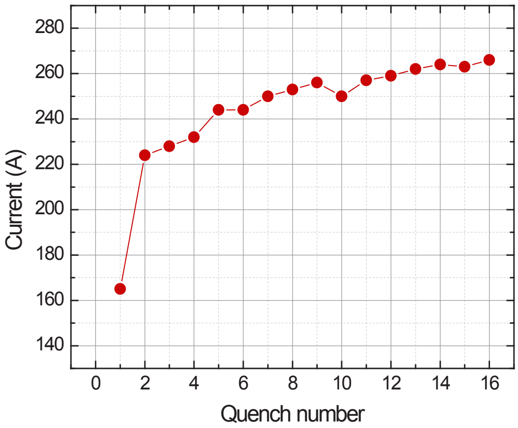

Figure 4: Training performance of SMPW.

A complete set of magnetic field measurement was obtained during the factory acceptance test at NSRRC only. The measurement was performed using a Hall sensor scan and a stretch wire system. Longitudinal magnetic field distribution of the SMPW at the applied current of 258 A is plotted in Figure 5(a) and the excitation curve is plotted in Figure 5(b). Table 2 shows the measured field integrals of the SMPW at the applied current of 258 A. All magnetic field integrals are within the requirement, with the exception of the vertical first field integral (dipole integral) which is 211.8 G·cm while the requirement is ≤ 100 G·cm. The provided horizontal/vertical correctors can be used to compensate for this field integral. In a combine mode, the corrector capacity is 80 G·cm/A. The maximum excitation current of the correctors is 10 A, therefore the dipole field integral can be corrected.

Figure 5(c) shows the transverse field homogeneity measured by the Hall sensor scan. During the measurement, a dummy chamber with external heaters was inserted into the 100 K beam duct to provide a 300 K environment for the Hall sensor. The sensor scan was limited to ± 5 mm due to the size of the chamber. Results of the Hall sensor scan from the vertical test performed in a test Dewar were thus included to allow a justification of the good field region where the field homogeneity must be better than 0.5%.

Table 2: Magnetic field quality of SMPW.

Parameters	**Requested**	**Measured**
Hor. 1st field integral (G·cm)	≤ 100	34.3
Ver. 1st field integral (G·cm)	≤ 100	211.8
Hor. 2nd field integral (G·cm^2)	$\leq 2\times10^4$	1080
Ver. 2nd field integral (G·cm^2)	$\leq 2\times10^4$	5730
Dipole integral (G·cm)	≤ 100	211.8
Quadrupole integral (G)	≤ 100	25.5
Sextupole integral (G/cm)	≤ 100	49.8
Octupole integral (G/cm^2)	≤ 100	13.9
Dynamic field integral (G·cm)	≤ 50	13.0

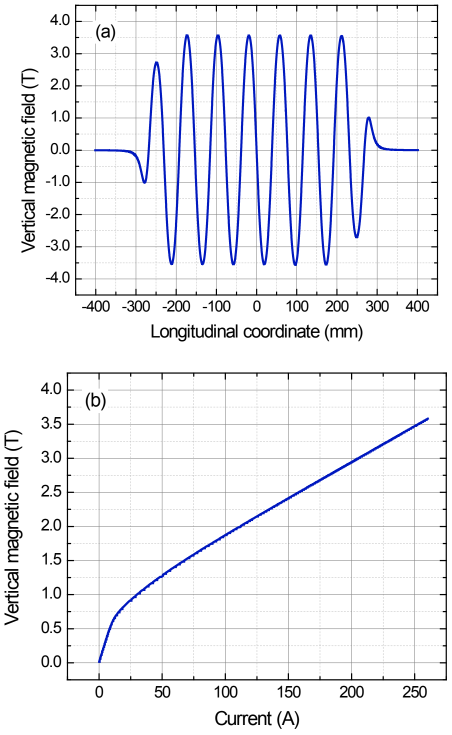

Figure 5(a,b): Measured magnetic field of SMPW: longitudinal magnetic field distribution at 258 A (a), excitation curve (b).

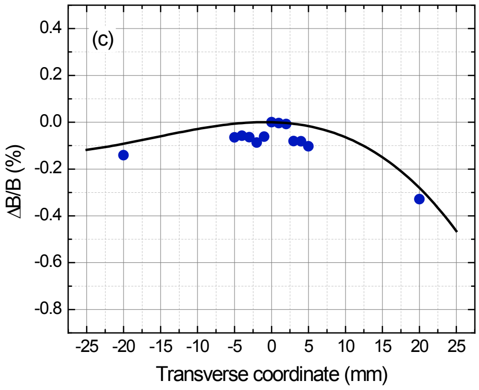

Figure 5(c): Measured magnetic field of SMPW: transverse field homogeneity at the applied current of 258 A (c).

INSTALLATION AND OPERATION

The SMPW, extended BPMs and correctors were installed in the storage ring of the Siam Photon Source at the center of straight section between the bending magnets BM04 and BM05. The process after installation includes (1) pumping and purge of liquid helium and liquid nitrogen vessels, (2) pumping the 300 K vacuum vessel to 1×10^{-4} torr or lower, (3) particle cleaning of the liquid helium vessel with continuous flow of nitrogen gas and (4) repeating pumping and purge for at least three times. The SMPW is then cooled-down with liquid nitrogen first, followed by liquid helium to 4.2 K. Temperature and pressure behaviors of the SMPW during the cool-down process are illustrated in Figure 6. The temperatures T1 – T4 are measured at the bottom of liquid helium vessel, the magnet arrays and the protection diodes which should be immersed in liquid helium when the SMPW is in operation. The temperatures T5 and T6 are measured below the Nb_3Sn/Cu bus bar and the temperatures T7 and T8 are measured below the vapor-cooled current leads.

In order to safely operate the vapor-cooled current leads, temperature and voltage across the current lead are monitored and added to the interlock system. The voltage across the current lead must be less than 0.15 V and the temperature at the bottom end must be lower than 25 K. This is also to ensure that the Nb_3Sn/Cu bus bar between the current lead and the magnet arrays is operating in the superconducting state. Process for filling of liquid helium has been optimized and it was found that the maximum current lead temperature at the bottom end can be controlled below 25 K and the maximum voltage rise across the current lead is below 10 μV at the nominal current of 253 A. The filling process is set to start when liquid helium level falls below 80% and stop when the level reaches 98%.

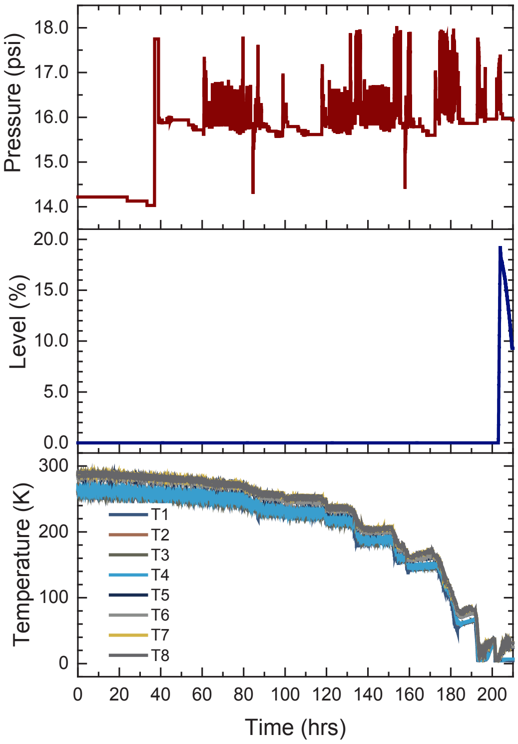

Figure 6: Liquid helium vessel pressure, liquid helium level and temperature of SMPW during the cool-down process.

Helium liquefaction system (HELIAL 1000) for Siam Photon Source has liquefaction capacity of 20 L/hr without liquid nitrogen pre-cool. It is feasible to supply liquid helium to two superconducting insertion devices; the existing Superconducting Wavelength Shifter (SWLS) and the new SMPW. CRYOFLEX® transfer line with 4-tube design (CERN type) is chosen to transfer liquid helium from liquid helium distributor to the SMPW because it has a low value of heat loss and it is easy to install. Heat loss of the CRYOFLEX® transfer line is approximately 40 mW/m, not including the loss at couplings and joints. Total length of the transfer line is 30 m. The transfer line uses liquid nitrogen as thermal shielding so additional liquid nitrogen line was installed, besides the liquid nitrogen line for SMPW. In operation, the SWLS operated at 308 A needs liquid helium filling every 15 hours while the SMPW operated at 253 A needs liquid helium filling every 10 hours.

COMMISSIONING

Before installation in the storage ring of Siam Photon Source, effects of the SMPW on electron beam dynamics were investigated using an angular kick map calculated by Elleaume's method [2]. It was found that the calculated vertical tune shift at the maximum SMPW current is 0.07, while there is no change in the horizontal tune. Since the SMPW is installed in the middle of the straight section, the perturbed optics is symmetric. Two independent quadrupole power supplies (for quadrupole magnets adjacent to the SMPW) will be sufficient for linear optics compensation. The betatron function and betatron tune can be restored to the original unperturbed values without any difficulty.

Particle tracking was also performed to investigate the effects of SMPW on the dynamic aperture. The simulation result shows that the dynamics aperture drastically decreases in vertical plane as seen in Figure 7 due to the limitation of physical aperture of the vacuum chamber. Nevertheless, this does not affect the momentum aperture which is wide enough for beam injection. The SMPW was successfully installed in August 2018 and the commissioning was performed at 1.2 GeV full energy injection. The process is not difficult compared to the commissioning of 6.5 T SWLS and 2.2 T Multipole Wiggler in 2013 [3]. The beam can be injected at the nominal SMPW field of 3.5 T without any effect on the injection efficiency.

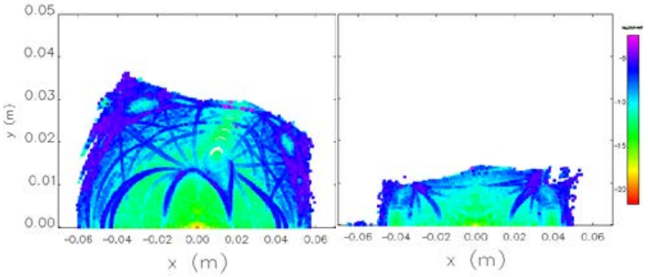

Figure 7: Dynamic aperture of the bare ring (left) and with the SMPW (right).

Influence of the SMPW on electron beam dynamics was also measured. The betatron tune shift was observed as shown in Figure 8 where the vertical tune increases as a function of the SMPW current as expected, and there is almost no change in the horizontal tune. By adjusting the magnetic field of quadrupole magnets in the matching cell near the SMPW together with the two main quadrupole families, the beta beating and betatron tune shift were minimized. The close orbit distortion was also observed. Minimization can be achieved in both horizontal and vertical planes by using the horizontal/vertical correctors installed at the upstream and downstream of the SMPW.

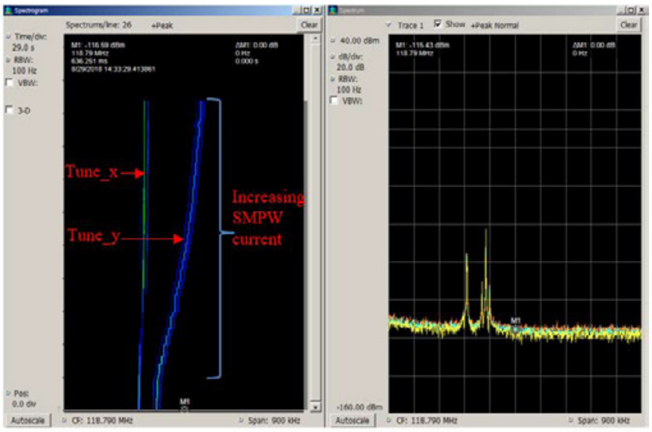

Figure 8: Measured betatron tune shift when increasing the SMPW current.

ACKNOWLEDGEMENTS

The authors are particularly grateful to NSRRC team, J. C. Jan, H. H. Chen, F. Y. Lin, C. H. Chang, C. S. Hwang and G. H. Luo, for the great collaboration and support throughout the project. In addition, thanks to SLRI team for the good teamwork during installation and commissioning.

REFERENCES

[1] J. C. Jan et al, “Design of a 3.5 T Superconducting Multipole Wiggler”, *Proc. IPAC’17*, pp. 3564-3567, 2017.
[2] P. Elleaume, “A New Approach to the Electron Beam Dynamics in Undulators and Wigglers”, *Proc. EPAC’92*, pp. 661, 1992.
[3] P. Sudmuang et al, “Commissioning of the 2.4 T Multipole Wiggler and the 6.5 T Superconducting Wavelength Shifter at Siam Photon Source”, *Proc. IPAC’14*, pp. 1192-1194, 2014.

CONTACT

**Prapaiwan Sunwong, tel: +6644217040 ext.1528; prapaiwan@slri.or.th*

DESIGN, FABRICATION AND INSTALLATION OF VACUUM CHAMBER FOR BENDING MAGNET AT SIAM PHOTON SOURCE

**S. Srichan, K. Sittisard, P. Pruekthaisong, P. Sunwong, R. Supruangnet, N. Jearanaikoon and S. Tancharakorn*
Synchrotron Light Research Institute (Public Organization) 111 University Avenue, Muang District,
Nakhon-Ratchasima 30000, Thailand

ABSTRACT

A new vacuum chamber for bending magnet for the 1.2 GeV Siam Photon Source at Synchrotron Light Research Institute has been designed, constructed and successfully installed to the bending magnet no. 5 (BM5). This vacuum chamber so-called bending chamber is made of stainless steel SUS316L and is approximately 2.2 m in length in the direction of electron trajectory with two exit ports for photon beams. The chamber was tested at vacuum level of 10^{-10} mbar with distributed ion pump (DIP) and 500 l/sec sputtering ionization pump. This article presents details of its design, fabrication and installation.

INTRODUCTION

Siam Photon Source (SPS) is a 1.2 GeV synchrotron radiation source with circumference of 81.3 m. It is operated by Synchrotron Light Research Institute (SLRI). The SPS storage ring consists of 8 bending magnets (BMs) and 4 straight sections as shown in Figure 1. In 2015, three insertion devices (IDs) were installed into each straight sections, only one remained available between BM4 and BM5. At that time, the number of proposals were increased to over 300 per year. More than 80 percent requested for X-ray beamlines. Due to such high demand, a hard X-ray beamline was considered to be built with higher energy and flux comparing to other available beamlines. A new superconducting ID was therefore considered to be installed to the storage ring. In 2016, a new project so-called the 'ASEAN beamline' was started. This beamline connecting to the exit port of the BM5 utilizes synchrotron radiation from a superconducting multipole wiggler (SMPW) designed and constructed by National Synchrotron Radiation Research Center (NSRRC) [1], Taiwan. However, the BM5 had only one exit port and was occupied by BL5.2:SUT-NANOTEC-SLRI beamline. Therefore, a new bending chamber to accommodate at least 2 beamlines must be installed. The project of design and fabrication of a new bending chamber started in the beginning of 2016.

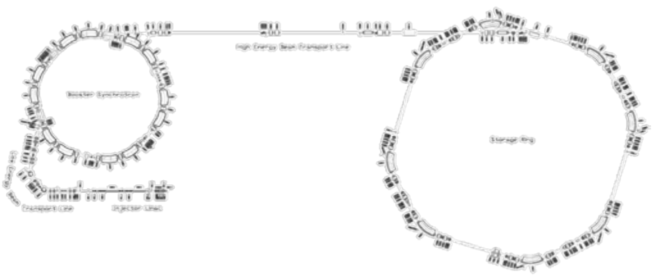

Figure 1: A schematic diagram of Siam Photon Source

DESIGN AND FABRICATION

Design concept and Finite Element Analysis

The new bending chamber design was aimed to meet three important requirements including two available exit photon ports for accommodating two beamlines, working vacuum level at 10^{-11} mbar and the compatibility between the entrance and exit ports for electron beam of the new chamber and storage ring. Based on experience, stainless steel (SUS316L) with electro-polishing surface was selected to be a main material for the bending chamber due to the fact that SUS316L is non-magnetic material. It has also been used at SLRI facility for many years giving us strong confidence in using this material for the new chamber. The drawing of the bending chamber is shown in Figure 2. Components and internal details are shown in Figure 3. The bending chamber consists of two exit ports for photon beam, entrance and exit ports of electron with elliptical shapes matching to the electron ports of storage ring. A sputtering ionization pump can be installed either on top or below of the exit photon ports. The length of the electron track is 2.2 meters.

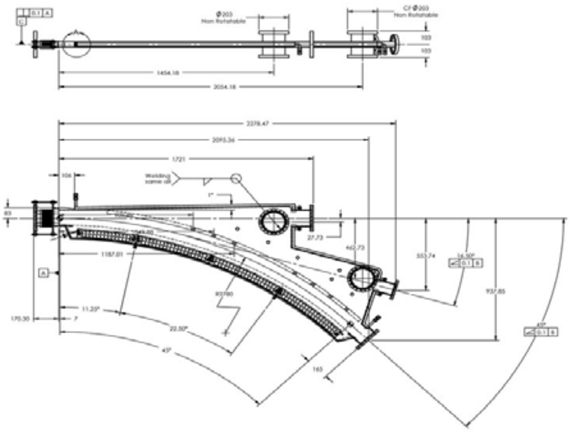

Figure 2: Dimensional drawing of bending chamber.

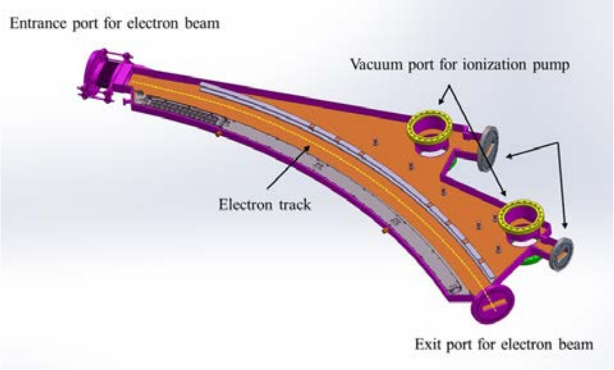

Figure 3: 3D model of the new bending chamber showing internal details.

Prior the fabrication of the bending chamber, deformation analysis under effects of ultrahigh vacuum environment and gravity has been carried out using ANSYS® package. The thickness for both top and bottom plates is 3 mm with total weight of 120 kg. Result shows the maximum deformation of about 1.455 mm as shown in Figure 4 which is considered to be acceptable.

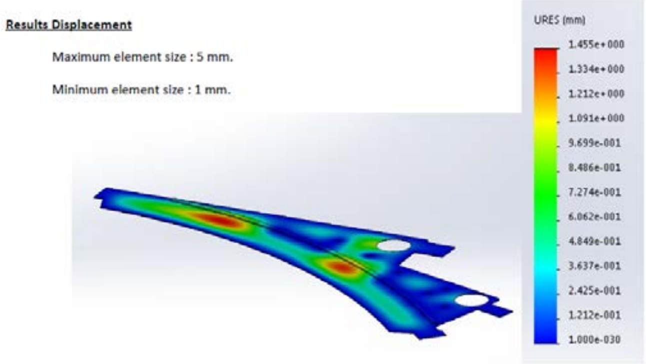

Figure 4: Deformation analysis of bending chamber under vacuum and gravity loads.

Fabrication process

The most important and critical process of the bending chamber fabrication is the preparation of the top and bottom plates because its own size and weight may cause the distortion. Firstly, therefore, a laser cutting machine was used to cut a thick stainless steel. Laser cutting technique gives a precision of about 0.1 mm depending on cutting speed. When all parts were ready, they were then brought for welding process in a clean room. They were then welded using tungsten inert gas welding (TIG) technique. The parallelism of two plates is also vital. The heat at the welded spot may cause the plate misshaped. In order to avoid accumulated heat at the area near the welded spot, technician had to occasionally change the welding position. A dual gauge was used to monitor the distance between two plates to ensure the parallelism. Figure 5 shows the welding process in class 1000 clean room.

Figure 5: TIG welding in clean room and controlling deflection of top and bottom plates.

GEOMETRY INSPECTION AND TEST

Geometry inspection is a vital process to ensure that all mechanical dimensions of component are correct within acceptant tolerance according to the design. Using a portable coordinate measuring machine, our engineer can inspect dimensions of the finished component as shown in Figure 6 with high accuracy of ±0.027 mm.

Figure 6: Dimension inspected by portable coordinate measuring machine.

When the geometry inspection process was done, the next process was a vacuum related tests including vacuum leak test, performance of a distribution ionization pump (DIP) and ultrahigh vacuum (UHV) test. All tests were carried out in a mechanical laboratory. The chamber has finally reached UHV level.

Figure 7: Ultra high vacuum test.

INSTALLATION AND COMMISSIONING

The installation work was done in June, 2017 during the annual machine shutdown. The following steps were done for the installation of bending chamber (see Figure 8);

- Turn off the bending magnet power supply and disconnect all electrical connectors,
- Remove the top part of the bending magnet,
- Disconnect the bending chamber and the storage ring,
- Remove the existing bending chamber,
- Place the new bending chamber on top of the bottom part of bending magnet,
- Connect the new chamber to the storage ring,
- Install the sputtering ionization chamber,
- Install the top part of the bending magnet and connect all electrical connectors,
- Start vacuum backing and
- Test the bending chamber by storing electrons.

Figure 8: The bending chamber installed on top of the bottom part of bending magnet.

After the installation, the new bending chamber was tested by running the storage ring at full electron current of 150 mA. Parameters including vacuum level and surface temperature were carefully observed. The results were satisfied.

CONCLUSIONS

The new bending chamber has been carefully designed and fabricated in-house. Since June 2017, it has been successfully installed into the SPS storage ring and operated under ultrahigh vacuum.

ACKNOWLEDGEMENTS

The authors would like to acknowledge members of Mechanical System Division, SLRI for their hard working on this project.

REFERENCES

[1] J. C. Jan et al, “Design of a 3.5 T Superconducting Multipole Wiggler”, *Proc. IPAC’17*, pp. 3564-3567, 2017.

CONTACT

*Supawan Srichan, Tel: +6644217040 Ext. 1307;
supawan@slri.or.th

COMPUTATIONAL MATERIALS PHYSICS PROJECT AT SYNCHROTRON LIGHT RESEARCH INSTITUTE

W. Busayaporn[1], J. T-Thienprasert[2], I. Fongkaew[3], W. Sailuam[4], M. Chotsawat[1], A. Banjongkan[5], S. Tancharakorn[1] and P. Phothongkam[1]*

[1]Synchrotron Light Research Institute (Public Organization), 111 University Avenue, Muang District, Nakhon Ratchasima 30000, Thailand

[2]Department of Physics, Faculty of Science, Kasetsart University, 50 Ngam Wong Wan Road, Chatuchak, Bangkok 10900, Thailand

[3]School of Physics, Suranaree University of Technology, 111 University Avenue, Muang District, Nakhon Ratchasima 30000, Thailand

[4]Department of Applied Physics, Faculty of Engineering, Rajamangala University of Technology ISAN (Khon Kaen Campus), Khon Kaen, 40000, Thailand

[5]School of Engineering, Suranaree University of Technology, 111 University Avenue, Muang District, Nakhon Ratchasima 30000, Thailand

ABSTRACT

This article given report and update of the SLRI-High Performance Computer 1 and 2 (SLRI-HPC1 and SLRI-HPC2) operated at the Synchrotron Light Research Institute (SLRI) under the Computational Materials Physics (CMP) project. Main objectives of facilities are providing further support to experiment using Synchrotron Radiation in term of investigate structures of materials down into atomic scale and also playing important role on prediction of structures and properties of materials before conducting the experiment. The article also demonstrates examples of work done by SLRI-HPCs both of the first principle calculations for structural prediction and supportive role to gain higher understanding of various materials in the experiment at SLRI.

INTRODUCTION

In 2010, SLRI has established the High Performance Computer 1 (SLRI-HPC1) to deliver services on the first principle calculation and support calculation to gain understanding of atomic structures and mechanisms using Synchrotron Radiation(SR). The SLRI-HPC1 has been fully operated in 2012 up to now. In addition, SLRI-HPC2 also established in 2017 under the Computational Materials Physics (CMP) project to strengthen the role of computational modeling supported SR usage at SLRI. Nowadays, SLRI-HPC1 and 2 providing scope of work from atomic structures, molecular dynamics to the protein docking reactions.

FACILITIES AND SOFTWARE

The current status of SLRI-HPC1 is composed of 504 cores of DellPowerEdge with AMD Opteron^{TM} 2.2-2.6 GHz processors at each core. Data storage for this system has been installed with 4.5TB capacity providing R_{max} at 3.5 TFLOPS. Similarly, the SLRI-HPC2 initially established with 72 cores of Lenovo ThinkSystem with Intel® Xeon Silver 4116 2.1 GHz processors at newer architecture. In addition, 60 TB data storage has been installed with promising possibility to extend the capacity in near future. Performance of the SLRI-HPC2 has been estimated at R_{max} = 1.7 TFLOPS with lower number of CPU processors. The SLRI-HPCs have been installed with various computational packages to calculate material structures ranged from atomic scale up to molecular dynamics such as VASP, CRYSTAL, GAUSSIAN, FEFF, QE, LMTO, LAMMPI, Phonopy, Abinit, SATLEED, Xcrysden, DLV, Vesta, GROMACS and GOLD. Works of SLRI-HPCs can be accomplished in structural and properties prediction of materials as the first principle calculation implemented Density Functional Theory (DFT) and also supportive role for experimental technique such as X-ray Absorption Spectroscopy (XAS), X-ray Photoemission Electron Spectroscopy (XPS), Quantitative Low-energy Electron Diffraction (LEED-IV), IV-Low-energy Emission Electron Microscopy (IV-LEEM). The calculation also accomplishes to reveal the chemical path reaction for catalyst via DFT or even finding effective ligands in macromolecular investigation via Molecular Docking. Since 2012 to present, SLRI-HPCs taking part in number of publications more than 30 articles. Recent fiscal year (FY2018), SLRI-HPCs provided service up to nearly 3-million CPU hours to users.

Figure 1: Images of (a) SLRI-HPC1 and (b) SLRI-HPC2.

RESEARCH HIGHLIGHTS

First Principle Calculation: Phase and Vibrational Prediction for 2-Dimensional Graphene under High Pressure [1]

The phase stabilities and intrinsic properties of two structures of hydrogenated diamondized bilayer graphenes (H-BLGs) were theoretically investigated via first principle calculation. These two hydrogenated structures are 2-dimensional materials adopting the crystal structures of diamond and of lonsdaleite so called H-diamondene and H-lonsdaleitene. Our simulations demonstrate these H-BLGs are thermodynamically stable with respect to bilayer graphene and hydrogen molecule at 0 GPa, and additionally they are found to withstand the physical change in structure up to at least 1000 K, ensuring their dynamical and thermal stabilities. The studied H-BLGs are predicted not only to behave as direct and wide band gap semiconductors, but also to have a remarkably high resistance to in-plane plastic deformation induced by indentation as implied by their high in-plane elastic constants comparable to those of diamond and of lonsdaleite. The mechanical stability of the materials is investigated using the fulfilment of the Born stability criteria. Finally, the analysis of phonon vibrational modes of frequencies in BLGs has been conducted. The result reveals possible Raman and IR active modes, which are found to be distinctly different from those of hydrogenated diamond-like amorphous carbon and defective graphene. This calculation exhibits as it could be used as a fingerprint for future experimental characterization of the materials for identification of the carbon-based materials.

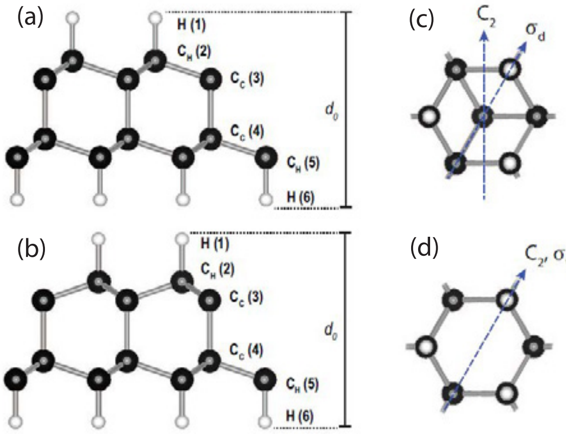

Figure 2: Ball and stick model of H-diamondene in (a)[100]direction and (b)[001]direction perpendicular to the page and H-lonsdaleitene in (c)[100]direction and (d)[001]direction perpendicular to the page. Denoted numbers (1)-(6) represented number of atomic layers while d_0 is the effective layer of material to calculate the elastic properties.

Local structure of stoichiometric and oxygen-deficient $A_2Ti_6O_{13}$(A= Li, Na, and K studied by X-ray absorption spectroscopy and first-principles calculations[2]

Oxygen vacancy defects (V_O)in Ti-based oxides is one of major defects in oxide materials and well-known as they play important roles in intrinsic properties such as catalytic processes. However, knowledge of their formations and related properties are limited. Here, the use of X-ray absorption spectroscopy (XAS) measurements to compare the relative proportion of V_O defects in as-grown alkali hexatitanate $A_2Ti_6O_{13}$(A=Li, Na, K) are demonstrated. Both X-ray absorption near edge structure (XANES) and extended X-ray absorption fine structure (EXAFS) techniques were studied to reveal the local structure of the material. The XANES spectra of Ti K-edge in all samples indicates the presence of $(Ti^{+4})O_6$ units in good agreement with reported X-ray diffraction(XRD) results. The small influence of cations A was observed and can be reconstructed in the simulated spectra. In addition, the oxygen-deficiency in the structure has been semi-quantitatively determined in $K_2Ti_6O_{1-3x}$ by the *in situ* time-resolved XAS measurements under reducing conditions

(10%H_2/Ar, 50-650 ^{O}C). The *in situ* XANES measurements indicate that the oxidation state of bulk Ti remains the same as the as-grown sample, i.e., 4+, at elevated temperatures. Meanwhile the level of V_O increasing as of higher temperature and reach to the maximum at 550 ˚C then slightly decrease after this point indicated by EXAFS spectra. Furthermore, first-principles calculation using Density Functional Theory (DFT) has been applied to confirm the formation of V_O defects. The calculation has been carried out for a 126-atom $K_2Ti_6O_{13}$ supercell with V_O at various positions. Based on calculated EXAFS, the removal of the oxygen atom nearest to the tunnel, which is the lowest energy structure, provides a good match to the experimental spectra.

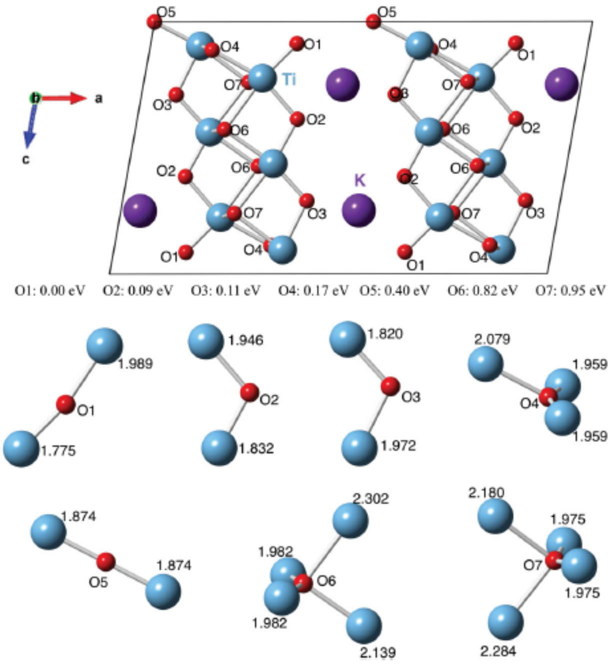

Figure 3: (top)Structure of crystallographically inequivalent O site for the calculations of V_O defects labelled as O1-O7. Energies used to create such type of equivalent defect have been mentioned and relatively sorted from lowest energy as O1. (Bottom)The bond lengths of all inequivalent defects have been shown in the unit of angstrom.

Nearly-free-electron system of monolayer Na on the surface of single-crystal $HfSe_2$[3]

The electronic structure of a single Na monolayer on the surface of single-crystal $HfSe_2$ is investigated using angle-resolved photoemission spectroscopy. We find that this system exhibits an almost perfect "nearly-free electron" behavior with an extracted effective mass of ~$1m_e$, in contrast to heavier masses found previously for alkali-metal monolayers on other substrates. Our density-functional-theory calculations indicate that this is due to the large lattice constant, causing both exchange and correlation interactions to be suppressed, and to the weak hybridization between the over layer and the substrate. This is therefore an ideal model system for understanding the properties of two-dimensional materials.

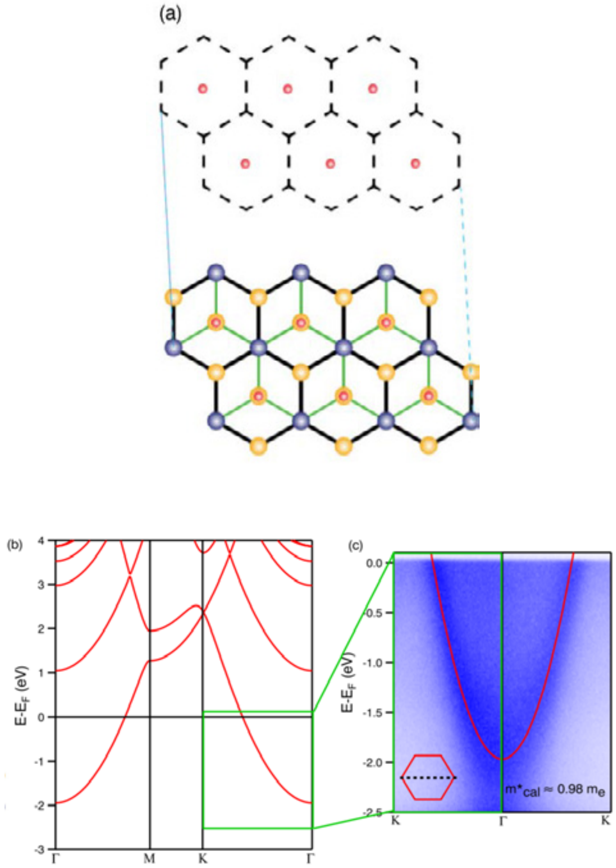

Figure 4: (a)(top)Atomic structures of bare monolayer of Na and (a) (bottom)atomic structure of monolayer Na on $HfSe_2$which is used for calculating the band structures. (b)and (c)The band structures and inlet showed consistence of the calculation to the actual XPS experiment, respectively.

Low Energy Electron Microscopy Study of Tiered 'Wedding-cake' Island Formation of Bi-layer Graphene by Using Chemical Vapor Deposition Technique[4]

Mono-layer graphene shows zero-bandgap dispersion relation which differ from bi-and multi-layer graphene that open up its energy bandgap. Therefore, bi- and multi-layer graphene are more preferable in electronics and photonics applications. In this work, Chemical Vapor Deposition (CVD) technique has been used as it is recognized for producing high-quality graphene. The main objective of this fabrication is the challenge of producing a large area bi-layer graphene. Here, we report a study of the mechanism of uniform tiered 'wedding-cake' graphene island growth by using copper oxide nanoparticle as a nucleation seeds. The stacking order of the multi-layer graphene island is clearly depicted through Low Energy

Electron Microscopy (LEEM). The growth can be controlled by changing the hydrogen flow rate which affects the etching of graphene edges. By implying the vapor trapping mechanism, the seeding can be done simultaneously with the bi-layer graphene growth by using a novel single-step CVD fabrication process. After that, Intensities-Voltages mode of Low Energy Electron Microscopy(IV-LEEM) experiment has been conducted to identify the localized distribution of layers' numbers of graphene. Graphical User Interface (GUI) has been developed and analyzed using computational source under CMP project. All of IV-LEEM plots can indicate numbers of layers of graphene at localized area. Then all data has been plotted in color-code to demonstrate the distribution and quantitatively indicate the bi-layers graphene on the surface.

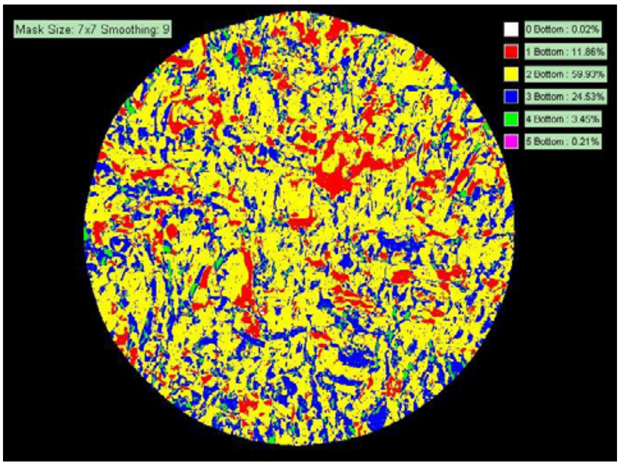

Figure 5: The color coding of 10 sccm H_2 flow rate sample in 7.5 µm FOV. The dominant yellow color resembles the preferable bi-layer graphene with the coverage up to ~60% of total area.

REFERENCES

[1] T. Pakornchotea, A. Ektarawong, B. Alling, U. Pinsook, S. Tancharakorn, W. Busayaporn, T. Bovornratanaraks, Carbon 13892 (2019).

[2] J. Kanchanawarin, W. Limphirat, P. Promchana, T. Sooknoi, T. Maluangnont, K. Simalaotao, A. Boonchun, P. Reunchan , S. Limpijumnong, and J. TThienprasert, J.Appl.Phys.124, 155101 (2018).

[3] T. Eknapakul, I. Fongkaew, S. Siriroj, R. Vidyasagar, J.D. Denlinger, L. Bawden, S-K. Mo, P.D.C. King, H. Takagi, S. Limpijumnong, and W. Meevasana, Phys.Rev.**B** 94, 201121(R)(2016).

[4] S.M. Hafiz, S.A.A. Kamal, W. Busayaporn, L.H. Ngee, i-SAMN2018, PUTRAJAYA e-Proceeding, (2018).

CONTACT

*Wutthikrai Busayaporn, tel: +66-44-217040 ext. 1451; wutthikrai@slri.or.th

OPERATION OF SPS WITH FULL ENERGY INJECTION

T. Chanwattana[*], T. Pulampong, P. Sudmuang*
Synchrotron Light Research Institute (Public Organization), 111 University Avenue, Muang District,
Nakhon Ratchasima 30000, Thailand

ABSTRACT

Full energy injection was studied and implemented at Siam Photon Source (SPS). An electron beam is accelerated to 1.2 GeV full energy in the booster synchrotron. The beam is transferred injected into the storage ring. The full energy injection is simpler and takes shorter injection than the original injection because the beam energy ramping in the storage ring is no longer needed. The full energy injection makes machine commission to be done easier and quicker. Upgrades of the SPS machine and commissioning of SPS for full energy injection were finished in 2018 and SPS has been operated with the full energy injection for user service since May 2018.

INTRODUCTION

Without electron beam in a storage ring, synchrotron radiation cannot be produced for users to conduct any experiments and research. The electron beam gets into the storage ring by electron beam injection from an injector system of the synchrotron light source. The injection procedure of a light source, therefore, determines quality of the light source's performance.

The SPS injector consists of an electron gun, a linear accelerator (linac) and a booster synchrotron. The SPS storage ring operates at 1.2 GeV in decay mode with beam injection twice a day. Original injection procedure of SPS starts from producing an electron beam by the thermionic DC electron gun. The linac increases the beam energy to 40 MeV. The 40-MeV beam is transferred through low-energy beam transport line (LBT) to the booster synchrotron where the beam energy is boosted to 1 GeV. The 1-GeV beam is transferred to the storage ring (STR) by high-energy beam transport line (HBT) as shown in Figure 1. The electron beam energy is ramped up to 1.2 GeV by an RF cavity in the storage ring. Since the energy of the injected beam and that of the stored beam are different, electron beam injection or refill to increase beam current in the storage ring has to be done after disposal of remaining stored beam. The injection procedure begins with dumping the stored beam and proceeds with setting magnet parameters of the storage ring for storing 1-GeV beam, injecting fresh 1-GeV beam and ramping the beam energy together with setting the storage ring parameters for storing 1.2-GeV beam simultaneously. This injection procedure takes almost 50 minutes until the beam is ready for user service. This long-time procedure also results in large variation of temperature of various instruments in both accelerator system and beamlines and it reduces accuracy and efficiency of the instruments. In order to enhance the performance of SPS, a more efficient injection procedure is required.

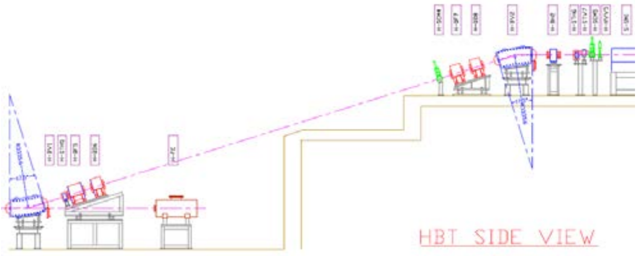

Figure 1: Side view of high energy beam transport line (HBT) of SPS.

FULL ENERGY INJECTION

The new injection procedure is known as full energy injection. The booster synchrotron accelerates the beam to full energy of 1.2 GeV instead of 1.0 GeV. The beam from the booster is transferred and then injected to the storage ring. As the beam enters the storage ring at the same beam energy as the stored beam, dumping of the existing stored beam prior to beam injection and energy ramping in the storage ring are no longer needed. Therefore, the full energy injection is simpler than the original injection. Procedure of the full energy injection is done in following steps:

- Stop slow orbit feedback (SOFB)
- Open multipole wiggler (MPW) gap
- Set the storage ring magnet parameters for beam injection
- Transfer electron beam to the booster and accelerate the beam to 1.2 GeV
- Inject the 1.2 GeV beam to the storage ring until the beam current is 150 mA
- Set the storage ring magnet parameters to store the beam
- Close MPW gap
- Run SOFB

Since the SPS injection system was originally designed for injection at 1 GeV, the SPS machine needs to be upgraded especially magnet power supplies in the booster, an extraction septum magnet (SMD) and HBT.

SPS MACHINE UPGRADE

In order to achieve the full energy injection, upgrades of the SPS machine have been done according to Table 1. An increase in the maximum beam energy in the booster to 1.2 GeV requires longer ramping time and higher maximum RF voltage but lower repetition rate. The horizontal and vertical betatron tunes were changed in order to increase efficiency of injection into the booster.

Table 1: Parameters of designed and upgraded booster synchrotron

	Designed	Upgraded
Lattice structure	FODO	
Number of periods	6	
Circumference	43.19 m	
Beam current	30 mA	
RF frequency	118 MHz	
Injection energy	40 MeV	
Maximum energy	1.0 GeV	1.2 GeV
Repetition rate	0.5 Hz	0.33 Hz
Ramping time	600 ms	1400 ms
Maximum RF voltage	60 kV	80 kV
Betatron tune (H/V)	2.25/1.25	2.22/1.41

The main changes of the SPS accelerator system were made in magnet power supplies, a timing system and beam diagnostic systems.

Magnet power supplies

Original magnet power supplies in the booster and HBT are not capable of supplying high enough electric current for handling the 1.2-GeV beam. The power supplies in the booster that were replaced are power supplies of bending magnets, quadrupole magnets and SMD. The power supplies in HBT that were replaced are power supplies of horizontal bending magnets (H-BH1 and H-BH2), vertical bending magnets (H-BV1 and H-BV2) and quadrupoles (H-QD1 and H-QF2). Table 2 shows a list of power supplies magnets and their maximum current. The installations of the new power supplies in the booster and HBT were finished in 2015 and 2018, respectively.

Table 2: Comparisons of original and upgraded power supplies

Magnet type	Original	Upgraded
Booster magnets		
Bending (BM)	1300 A	1700 A
Quadrupole (QD)	435 A	600 A
Septum (SMD)	600 V/5738 A	600 V/8250 A
HBT magnets		
Hor. bending (H-BH1 and H-BH2)	95 A	135 A
Ver. bending (H-BV1 and H-BV2)	620 A	900 A
Quadrupole (H-QD1 and H-QF2)	20 A	35 A

Timing system

Injection period was changed from 2 s to 3 s to compensate for reduction of repetition rate of the injection from 0.5 Hz to 0.33 Hz. Ramping pattern of the booster magnets were expanded to increase the beam energy in the booster from 1.0 GeV to 1.2 GeV. The maximum voltage of the RF cavity in the booster was increased from 60 kV to 80 kV. Figure 2 shows ramping pattern of bending and quadrupole magnets in the booster for original injection (1 GeV) and for full energy injection (1.2 GeV).

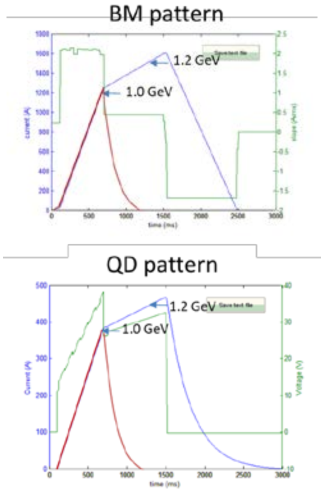

Figure 2: Ramping pattern of bending (BM) and quadrupole (QD) in the booster synchrotron.

Beam diagnostic systems

The beam diagnostic system of SPS was upgraded by improving tune measurement system in the booster synchrotron [1] and installing a turn-by-turn beam position monitoring (BPM) system in the storage ring. The tune measurement system is used for measuring horizontal and vertical tune in the booster. A layout of the tune measurement system is shown in Figure 3. The BPM system was upgraded using *Libera Spark ERXR BPMs* to monitor beam position in the storage ring on turn-by-turn basis. This information was used to indicate arrival of the injected beam to the storage ring and the number of turn that the beam can survive. An example of the turn-by-turn BPM station is shown in Figure 4.

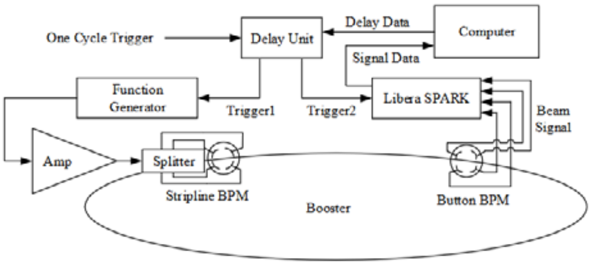

Figure 3: Layout of the booster tune measurement system.

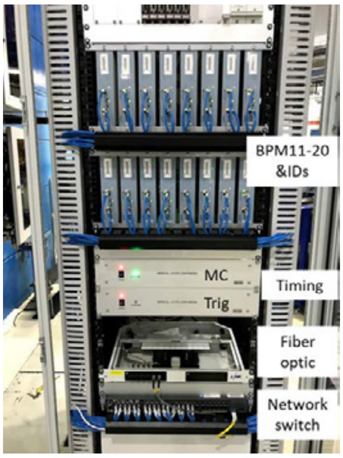

Figure 4: One of the stations for Libera Spark ERXR turn-by-turn BPMs recently installed.

COMMISSIONING

Magnet power supplies and acceleration of the beam energy to 1.2 GeV in the booster synchrotron were commissioned in 2015. Extraction of the 1.2-GeV beam from the booster and beam transfer through HBT were commissioned in 2018. Commissioning of full energy injection was done based on the procedure of preliminary full energy injection commissioning in 2015 [2]. The procedure is as follows:

- Set parameters of booster synchrotron to obtain 1.2-GeV electron beam in the booster
- Adjust current of SMD and kicker magnet in the booster for 1.2-GeV beam extraction
- Adjust current of the HBT magnets for beam transfer to the storage ring
- Adjust current of an injection septum (SMI), three bump magnets and magnets in the storage ring.

Screen monitors were used to check transverse beam profile and position from SMD through the end of HBT. Beam position on screen monitors corresponding to a case with high injection efficiency are shown in Figure 5. Wall current monitors were used to check whether the beam pass SMI. Signal from a photo multiplier tube (PMT) and the turn-by-turn BPMs in the storage ring were used to observe the beam in the storage ring as shown in Figure 6. Therefore, a machine configuration for the full energy injection with high injection efficiency can be obtained. Storage of 1.2-GeV beam from full energy injection was successful in March 2018.

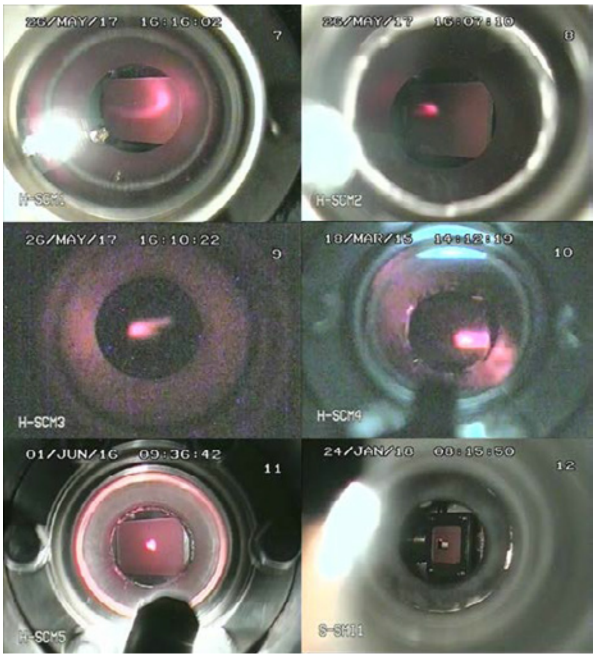

Figure 5: Screen monitors in HBT shows electron beam profile and position for beam injection with high injection efficiency.

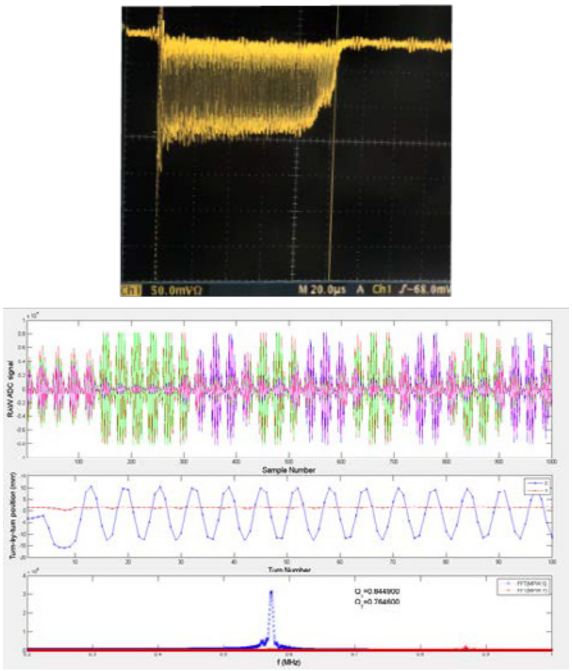

Figure 6: PMT signal indicates multi turn arrival of the beam at PMT (top). Signal Libera Spark signal shows that electron beam at 1.2 GeV is stored (bottom).

FULL ENERGY INJECTION IN ACTION

Full energy injection was approved for the user service mode and SPS has been operated with full energy injection since May 2018. The storage ring is refilled with 1.2-GeV beam twice a day and the whole injection procedure takes less than 20 minutes. The beam is dumped once a week on Monday morning. The SPS machine status of original injection and full energy injection can be seen in Figure 7.

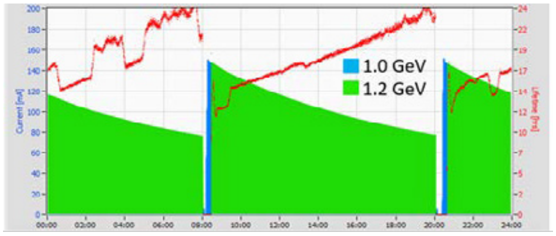

Injection at 1.0 GeV and ramping to 1.2 GeV

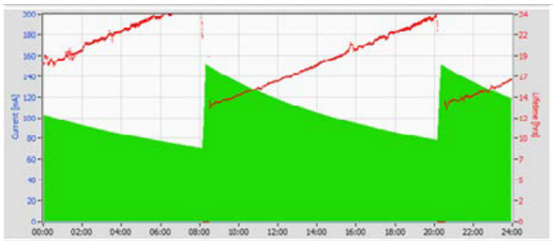

Full energy injection

Figure 7: SPS beam current profile in 24 hours with 1.0 GeV beam injection (top) and full energy injection (bottom).

Running SPS with full energy injection shortens injection time by reducing complexity injection procedure. This results in higher temperature stability of instruments in accelerator system and beamlines. The full energy injection allows machine commissioning to be done quicker and more effective. Recently, a superconducting multipole wiggler was installed in the SPS storage ring [3] and the commissioning was successful conveniently thanks to full energy injection.

Nowadays, worldwide synchrotron light sources have been operated in top-up mode which electron beam is injected to the storage ring regularly to keep beam current stable for the whole beam service. The full energy injection takes SPS one step closer to operation in the top-up mode. Studies and upgrades of radiation shielding and fast orbit feedback (FOFB) will be carried on further for the top-up mode.

ACKNOWLEDGEMENTS

The authors would like to thank and express our great appreciation to members of accelerator department, Source and Utility Maintenance and Operation (SUMO) team and other SLRI members including former members for their support and dedication of time and effort to make this project successful.

REFERENCES

[1] S. Kongtawong, P. Sudmuang, S. Krainara, P. Klysubun, “Improvement of Tune Measurement System at Siam Photon Source”, in *Proceedings of the 4th International Beam Instrumentation Conference (IBIC2015)*, Melbourne, Australia, September 13-17, 2015, pp. 184-186.

[2] Beam Dynamics Group and Source Utility Maintenance and Operation, “Preliminary Result for 1.2 GeV Full Energy Injection”, *SLRI Technical Note, SLRI-TN-2015/05*, 2015.

[3] P. Sunwong et al, *“Superconducting Multipole Wiggler for ASEAN Beamline”, SLRI Annual Review*, 2018.

CONTACT

*Thakonwat Chanwattana, tel: +66-44-217040 ext.1507; thakonwat@slri.or.th

MAGNET DEVELOPMENT FOR SIAM PHOTON SOURCE

P. Sunwong[*], *S. Prawanta, A. Kwankasem, V. Sooksrimuang, B. Boonwanna, C. Preecha and P. Sudmuang*

Synchrotron Light Research Institute (Public Organization) 111 University Avenue, Muang District,
Nakhon Ratchasima 30000, Thailand

ABSTRACT

Magnets for Siam Photon Source have been designed, manufactured and tested at the Synchrotron Light Research Institute (SLRI). Development of magnet prototype for Siam Photon Source II project is currently in progress. The magnet design process is conducted in-house for both engineering design and magnetic deign (magnetic field calculation). Magnet manufacturing was also completed in-house in the early state of magnet development and now being transferred to local manufacturing industries within the country. Magnetic field measurement and magnet testing is planned to follow the same strategy in order to get domestic industries ready for large-scale magnet production for the Siam Photon Source II project.

INTRODUCTION

Siam Photon Source is currently the only synchrotron light source in Thailand. It has been operated since 2003 with the beam energy of 1.2 GeV and the maximum beam current of 150 mA. The storage ring lattice is Double-Bend Achromat (DBA) lattice with the ring circumference of 81.3 m. There are currently 10 beamlines and 12 experimental stations utilizing a range of synchrotron radiation from bending magnets and insertion devices. With increasing number of users, Siam Photon Source II project is recently realized and the detailed design is in progress. The project aims to maximize industrial engagement within the country, especially for manufacturing of some components such as magnets and vacuum chambers. Nevertheless, domestic manufacturing industries have no experience in accelerator although they have potential and capability to produce high-precision machining parts. Existing magnet suppliers, on the other hand, only deal with industrial magnets where the precision and accuracy are not needed. It is a challenge for the Synchrotron Light Research Institute (SLRI) to develop skills, knowledge and experience for magnet design and fabrication, and cooperate with the industries to be able to manufacture and supply large-scale accelerator magnets for the Siam Photon Source II and for future projects of the country and around the world.

This manuscript presents detailed magnet development at SLRI including magnet design and simulation, magnet manufacturing and magnetic field measurement. Ongoing development of magnet prototype for Siam Photon Source II project, which is a half-cell prototype of Double Triple Bend Achromat (DTBA) lattice, is also discussed.

MAGNET DESIGN AND SIMULATION

Magnetic design and magnetic field calculation of accelerator magnets have long been done using either two-dimensional simulation softwares such as POISSON [1], or three-dimensional simulation softwares such as Radia [2] and Opera-3D [3]. In general, magnetic field of iron-dominated electromagnet is defined by the shape and geometry of the magnet poles. This was seen at the Siam Photon Source when the air-cooled coils of the sextupole magnets in the storage ring were replaced by the new water-cooled coils fabricated in-house [4]. The new coils consist of skew-quadrupole windings which are later used for electron beam coupling correction. Figure 1 illustrates some examples of preliminary magnet design for the Siam Photon Source II using Radia. Required magnetic field of the magnets is summarized in Table 1.

Magnetic field homogeneity required for accelerator magnets is typically in the range of 10^{-4} within the good field region. For instance, $\Delta B/B$ of the 0.87 T dipole magnet must be below 10^{-4} within ±17 mm along the transverse (x) coordinate. Magnetic field quality is also expressed in terms of multipole errors since any magnetic field can be represented by a multipole field expansion. It is usually emphasized during the magnet design process that requirement of the field quality is met and optimization of the pole profile will be iterated when necessary.

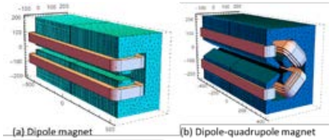
(a) Dipole magnet (b) Dipole-quadrupole magnet

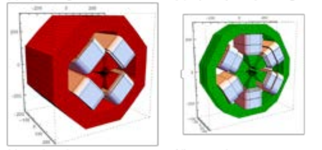
(c) Quadrupole magnet (d) Sextupole magnet

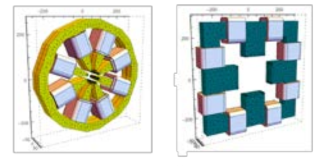
(e) Octupole magnet (f) Correcting magnet

Figure 1: Preliminary design of magnets for Siam Photon Source II using Radia.

Table 1: Required magnetic field of magnets for Siam Photon Source II.

Magnet type	Required magnetic field
Dipole magnet	0.87 T
Dipole-quadrupole magnet	0.6 T, 27.1 T/m
Quadrupole magnet	60 T/m
Sextupole magnet	2,030 T/m^2
Octupole magnet	72,000 T/m^3
Correcting magnet	0.008 T·m

Mechanical and engineering design of the magnets is carried out by taking into account the magnet manufacturing process, mechanical strength, assembly, alignment and space available at the installation site. Engineering design includes the use of pins and pole clamps for accuracy and repeatability of the assembly to be within the specified tolerance. It also includes the magnet coil design where the conductor size, coil connection, operating current and cooling parameters are optimized as far as practically possible for the best performance and low cost.

MAGNET MANUFACTURING

Magnet pole and yoke made of solid steel can be fabricated using Computer Numerical Control (CNC) multi-axis milling machine and Electrical Discharge Machining (EDM) wire cutting machine to be within the tolerance of 10 – 20 µm. Low-carbon steel is typically chosen due to superior magnetic properties, despite the degradation in mechanical properties and machinability. Standard AISI 1010 or JIS-S10C with the carbon content of 0.1% was long used for accelerator magnets but the lower-carbon steel such as AISI 1006 or even pure iron has become more popular.

Figure 2(a) shows the magnet poles made of AISI 1010 solid steel using the EDM wire cutting machine. By measuring with the Coordinate Measuring Machine (CMM), it was found that machining accuracy of the pole profile can be controlled within 10 µm while the accuracy of the assembled part is up to 50 µm with pins and pole clamps. It is therefore noted that number of parts for magnet assembly should be minimized as much as practically possible.

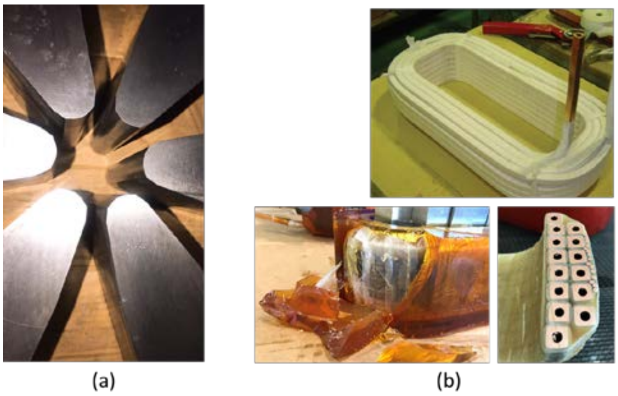

Figure 2: Magnet manufacturing; (a) magnet poles produced by EDM wire cutting machine and (b) magnet coil fabrication.

Figure 2(b) shows the fabrication process of the magnet coils. A copper hollow conductor (for water-cooled type) is first insulated using mica tape before being wound into a coil. The whole coil is then wrapped with Tedlar® polyvinyl fluoride film before the Vacuum Pressure Impregnation (VPI) process with epoxy. Detailed method of the VPI process is reported elsewhere [5]. The excess epoxy and the Tedlar® film can be removed easily after the epoxy is cured. Figure 2(b) demonstrates that air bubbles are completely eliminated and no void is found in the epoxy matrix between the conductors.

MAGNETIC FIELD MEASUREMENT

A Hall probe measurement system has been developed at SLRI, originally for magnetic field mapping of the insertion devices. The measurement system is presently employed for the field mapping of accelerator magnets, predominantly the magnet prototype for the Siam Photon Source II. The measurement system consists of a three-axis Hall probe installed on the support that can be controlled to move in three directions (x, y and z). Figure 3 shows the Hall probe measurement system measuring the magnetic field of a combined function dipole-quadrupole (DQ) magnet prototype developed at SLRI. The probe scanning, magnetic field measurement and data acquisition are controlled using LabVIEW program.

Figure 3: Magnetic field measurement of combined function DQ magnet prototype using Hall probe system.

Results of magnetic field measurement using the Hall probe measurement system are plotted in Figure 4 for the combined function DQ magnet prototype. Results from the simulation in Radia are also plotted for comparison. Deviation between the measurement and the simulation is within 1%, similar to the results reported in reference [6]. Quadrupole gradient derived from Figure 4 for the operating current of 220 A is normalized and plotted in Figure 5 where the measured data is also in agreement with the calculated one. For the combined function DQ magnet, the required field homogeneity (ΔG/G) is to be better than 10^{-2} within ±8 mm. Multipole error (B_n/B_2) of the magnetic field derived from the field mapping measurement in Figure 4 is also within 10^{-2}.

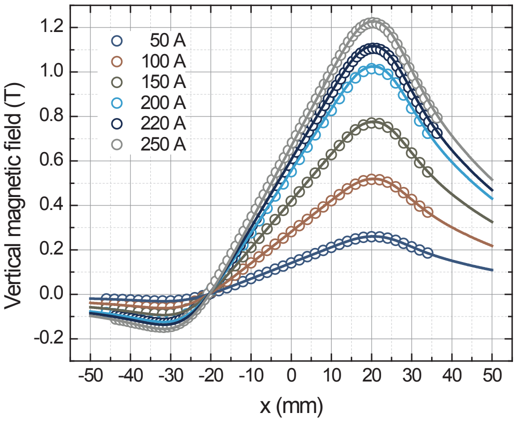

Figure 4: Vertical field component of combined function DQ magnet prototype along the horizontal coordinate obtained from Radia simulation (solid lines) and from measurement (open symbols).

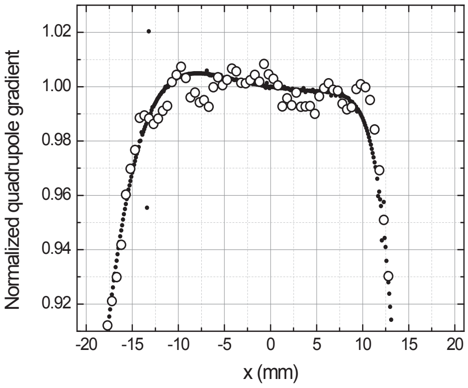

Figure 5: Normalized quadrupole gradient of combined function DQ magnet prototype along the horizontal coordinate. The open symbol is from the measurement and the solid symbol is from Radia simulation.

PROTOTYPE DEVELOPMENT AND PLAN

In order to prepare for the construction of Siam Photon Source II, full-scale prototype of DTBA lattice has been developed. The prototype does not only include the magnets, but also include the girders, supports, vacuum chambers, connection and wiring, vacuum pumps and all other components in a half-cell (depicted in Figure 6 where only magnets and part of vacuum chambers are shown). The prototype development is planned to be completed within 2022 before the procurement and construction of these components start.

Since all the magnet design is carried out by SLRI, local industries will be responsible only for manufacturing of the magnet prototype. Some magnets such as sextupole and correcting magnets will be made of laminated or electrical steel. Non-grain oriented electrical steel with the thickness of 1 mm and the maximum core loss of 12 W/kg is recently purchased from Thyssenkrupp Steel Europe AG. The lamination has Stabolit®70 coating which can act as an adhesive and bond the laminations together. Manufacturing technique, where the laminations are bonded into a bulk before machining, is planned and the appropriate process will be investigated.

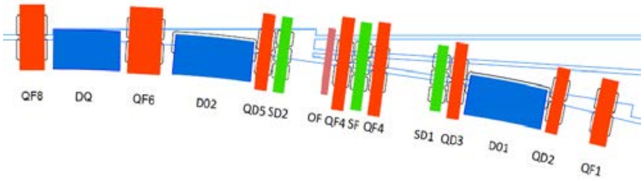

Figure 6: Drawing of a half-cell of DTBA lattice.

In fact, multipole field components of the magnets are best measured using a rotating coil system [7], a vibrating wire system [8] or a stretch wire system [9] because the measurement can be performed faster and more accurate with higher sensitivity to the higher-order multipole fields. Development of the multipole measurement system is currently in progress.

ACKNOWLEDGEMENTS

The authors would like to acknowledge all of the supporting staff from mechanical and production divisions at SLRI for their assistance with the engineering design and the production of components for the magnet prototype.

REFERENCES

[1] S. Humphries, "POISSON/SUPERFISH Codes for Personal Computers", *Linear Accelerator Conference*, Ottawa, Canada, pp. 778-780, 1992.

[2] O. Chubar et al, "A Three-dimensional Magnetostatics Computer Code for Insertion Devices", *J. Synchrotron Rad.*, vol. 5, pp. 481-484, 1998.

[3] "Opera Simulation Software", [Online]. Available: https://operafea.com

[4] P. Sunwong et al, *private communication*, SLRI, Thailand, 2015.

[5] A. Kwankasem et al, *private communication*, SLRI, Thailand, 2017.

[6] Andersson et al, "3D Calculations for the MAX II Lattice Magnets", *EPAC'98*, pp. 1207-1209, 1998.

[7] L. Walckiers, "The Harmonic Coil Method", *CERN Accelerator School on Magnetic Measurement and Alignment*, Montreux, Switzerland, pp. 138-166, 1992.

[8] P. Arpaia et al, "Magnetic Field Measurements on Small Magnets by Vibrating Wire Systems", *IEEE International Instrumentation and Measurement Technology Conference*, Binjiang, China, 2011.

[9] G. Le Bec et al, "Stretch Wire Measurement of Multipole Accelerator Magnets", *Phys. Rev. ST Accel. Beams,* vol. 15, pp. 022401, 2012.

CONTACT

*Prapaiwan Sunwong, tel: +6644217040 ext.1528; prapaiwan@slri.or.th

COUPLING CORRECTION

P. Sudmuang, T. Pulampong, and T. Chanwattana*
Synchrotron Light Research Institute (Public Organization) 111 University Avenue, Muang District,
Nakhon Ratchasima 30000, Thailand

ABSTRACT

The correction of the linear betatron coupling and the spurious vertical dispersion generated by magnet errors is an important issue related to the brilliance of the photon beam in synchrotron light source. This correction has been successfully performed in the SPS storage ring after modification of sextupole magnet coils with additional skew quadrupole component. Linear optic from close orbit (LOCO) together with the Robust Conjugate *Direction Search (RCDS) were employed to identify the* skew quadrupole gradient required for coupling reduction. Details of sextupole magnet coils modification as well as the results of coupling correction will be presented.

INTRODUCTION

Photon brilliance of synchrotron light source is inversely proportional to the product of the horizontal and vertical beam emittance. An increase in vertical emittance is mainly caused by linear betatron coupling and spurious vertical dispersion. The linear betatron coupling can also be caused by the skew quadrupole component of magnets through magnet error, misalignment (rolling) of quadrupoles and vertical orbit displacement of sextupoles. Spurious vertical dispersion can be generated by vertical steering magnet and coupling of the horizontal dispersion through skew quadrupole components in the dispersive region. The reduction of vertical emittance referred as coupling correction can be performed by using skew quadrupole magnets and reducing the vertical orbit in the sextupole magnets.

In the SPS storage ring, the skew quadrupole magnets did not exist since the beginning. The vertical emittance was reduced only by minimizing the vertical orbit. Since September 2017, the sextupole magnet coils have been modified and successfully installed into the storage ring. These new coils are capable of generating independent skew quadrupole field for coupling correction. Two algorithms: LOCO and RCDS were used to identify the skew quadrupole gradient needed for reducing the coupling error.

In this manuscript, the modification of sextupole magnet coils will be described in detail. A result of the coupling correction obtained from RCDS and LOCO is presented as well.

MODIFICATION OF SEXTUPOLE MAGNET COILS

There are sixteen sextupole magnets consist of two families: SF and SD installed in the SPS storage ring. These magnets are originally designed for controlling chromaticity at 1.0 GeV beam energy. When the storage ring has been upgraded to 1.2 GeV, all sextupole magnets need to be operated at higher than the specification up to 130%. This results in a dramatic increase in temperature rise in the coils.

In order to increase the magnetic field, reduce the coil temperature rise and generate the skew quadrupole field simultaneously, the sextupole magnet coils were modified. Existing magnets pole and yoke were used without any changing because it is sufficient to produce the magnetic field required for 1.2 GeV. Figure 1 shows the sextupole magnet before and after the modification.

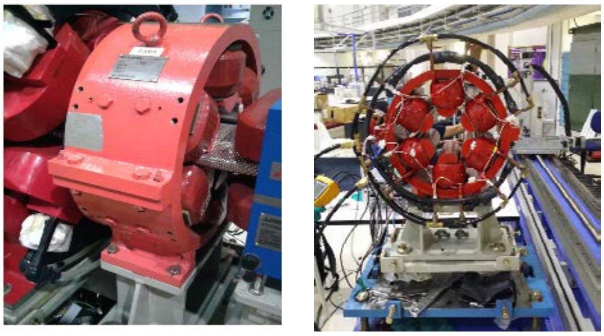

Figure 1: Sextupole magnet before (left) and after (right) modification.

The new coils are fabricated with the water-cooled coils made by a hollow conductor that has a cooling water channel inside [1]. Additional coils required for the skew quadrupole field were wound on top of main sextupole coils. The maximum field of 160 $T.m^{-2}$ and 0.64 $T.m^{-1}$ can be obtained from sextupole and skew quadrupole magnet coil, respectively. Table 1 summarizes the parameters of original and modification sextupole magnets.

Table 1: Specification of sextupole magnet coils.

Parameters	Original	Modification
Max. current (A)	12	250
Max. ampere turns (A.P)	1320	3500
Maximum field (T.m^{-2})	60	160
Number of turns	110	14
Cooling type	Air cooling	Water cooling
Temper rise (C) at 12 A	35	<3.0
Max. required skew quadrupole gradient (T.m^{-1})	-	0.64

COUPLING CORRECTION METHOD

There are several ways used to correct coupling. Traditional method, based on orbit response matrix called LOCO is widely used. LOCO is normally implemented in the storage ring in order to calibrate and correct the linear optic. It is also effective to find an optimal solution to eliminate the perturbation of high field insertion device. Another good way is to apply the online optimization techniques such as genetic algorithms [2], particle swarm optimization (PSO) [3] and robust conjugate direction search (RCDS) [4]. The RCDS method was proposed and demonstrated through simulation and experiments that it is much more efficient and robust [5]. Turn by Turn (TbT) beam position monitors (BPMs) can also be used for coupling correction [5]. This method has a great advantage compared to that LOCO and online optimization method because TbT data can be taken within seconds and with small perturbation to the storage beam. However, there is no TbT BPMs system available in the SPS storage ring at the moment. Details of coupling correction in this manuscript show only with the LOCO and RCDS algorithm.

LOCO algorithm

The optics calibration with the LOCO code is based on a fit between the model response matrix M_{mod} and the measured response matrix M_{meas}, obtained from measuring the orbit change while varying the corrector magnet excitation. Parameters such as quadrupole and skew quadrupole strengths, BPM gains and couplings, and corrector gains and couplings in the measurement system, are varied to minimize the chi-squared χ^2 difference between the model and measured response matrices:

$$\chi^2 = \sum_{i,j} \frac{\left(M_{\mathrm{mod},ij} - M_{\mathrm{meas},ij}\right)^2}{\sigma_i^2} \equiv \sum_{k=i,j} E_k^2, \qquad (1)$$

where σ_x is the measured noise level on the i^{th} BPM, and E_k the error vector.

To carry out the LOCO analysis, Matlab Middle Layer (MML) together with Accelerator Toolbox (AT) have been used to measure the necessary data and construct the LOCO data structure. The measured input data set, which includes the orbit response matrix, the dispersion functions, and the standard deviation of the BPM signals, requires accurate and well-calibrated BPMs. Therefore, the measurement was carried out after beam-based alignment and initial orbit correction had been performed. The whole measurement takes approximately 30 minutes.

A fully-coupled orbit response matrix containing 1120 elements was analyzed to determine the coupling and spurious vertical dispersion. A total of 208 parameters presented in the following table were varied in the fitting. These fitting parameters were determined from the parameter set that provides good agreement between the fitted model and measured orbit response matrices. Sufficiently accurate fit was obtained after 5 iterations, as observed by the chi-squared value and the distribution of residual differences between measured and fitted response matrices.

Table 2. Parameters varied in the linear optic analysis.

Fitting parameters	Number of elements
BPM gains	40
BPM couplings	40
Corrector strengths	28
Corrector tilts	28
Quadrupole gradients	28
Quadrupole tilts	28
Skew quadrupole gradients	16

The LOCO analysis has been successfully employed in the SPS storage ring since 2012 [6]. The linear optic parameters such as betatron tune, betatron function, and dispersion function have already corrected to the design vales. Therefore, only the skew quadrupole gradients are applied to storage ring.

RCDS algorithm

Online optimization used for beam coupling correction is based on Robust Conjugate Direction Search (RCDS) which was developed by X. Huang, SLAC [7]. The algorithm employs conjugate direction search method. Powell's conjugate direction relying on line search allows a search for better solutions in many different directions which are perpendicular to each other. The algorithm works on iterative basis to obtain better direction on the variable space for a local minimum of the set objective.

In RCDS, the line optimiser was modified to cope with measured noise according to the rms noise level. The algorithm will define a search zone (bracketing) that is sufficient to search for a local minimum solution. The two extremes of the zone are defined in each direction from the step that gives less objective value than 3× noise level of the previous solution. This makes the optimiser robust against the measured noise. Then within the valid range line optimiser should locate the local optimal with existing of noise by adjusting a uniform step size in the zone and applying parabolic curve fitting. From the reference quadratic curve, a bad measured data point, which is too far from the reference curve will be removed. Then fitting will be applied again, and points that error is larger than the average error of the centroid of the measured data set, will be rejected. Then the new minimum is found from the new fit. At the beginning of the first run, noise will be measured over several iterations and the rms value will be used as one of the input to the optimiser. The robustness of RCDS allows efficient online optimization for beam coupling minimization.

Moreover, the algorithm also uses normalised variables instead of the raw variables to allow well distribution of the values when the scale of variables is different.

COUPLING CORRECTION RESULTS

Optimum currents of both focusing skew quadrupole (SQF) and defocusing skew quadrupole (SQD) magnets used for coupling correction are shown in figure 2 and 3, respectively. A comparison of the results obtained with LOCO and RCDS are also presented in the same figure. It was found that there are some discrepancies at some locations, especially in SQD. This may properly due to the effect of SQD to the coupling are not significant.

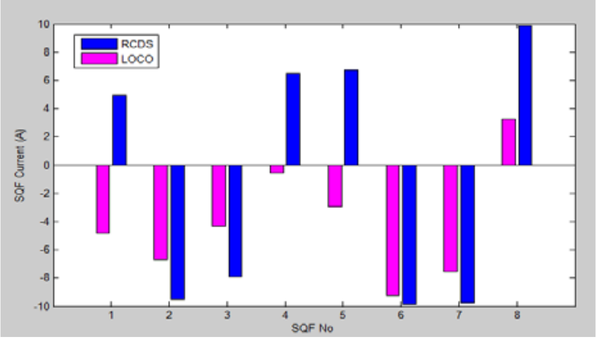

Figure 2: Comparison of the SQF skew quadrupole current obtained by LOCO and RCDS.

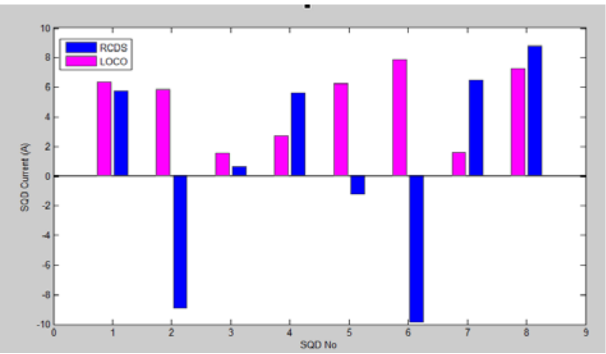

Figure 3: Comparison of the SQD skew quadrupole current obtained by LOCO and RCDS

After the above optimum current of skew quadrupole magnets were implemented, the related data consist of measured beam size and measured betatron coupling was studied. Table 3 shows a comparison of the measured beam size for two methods. It was found that the RCDS obtained the smallest vertical beam size. Thus, this method was chosen for normal operation.

Table 3: Comparison of the measured beam size.

Method	Measured beam size	
	Horizontal (mm)	Vertical (mm)
Before correction	0.3201	0.2822
LOCO	0.3183	0.2648
RCDS	0.3230	0.2330

The coupling measurement was performed by tune split method. The coupling ratio κ is calculated

$$\kappa = \frac{\varepsilon_y}{\varepsilon_x} = \frac{C^2}{C^2+2\Delta^2} \qquad (2)$$

where Δ is the difference between horizontal and vertical fraction tune, C is the minimum separation between the horizontal and vertical tune determined by changing the main quadrupole magnet current. The tune separation before and after correction with the RCDS method was measured and shown in figure 4. It was found that the measured coupling ratio was reduced to a factor 4 when all insertion devices are operated at the maximum filed. With the maximum field of skew quadrupole magnets of 0.64 T.m^{-1} the coupling ratio cannot be reduced to the target value at 1%.

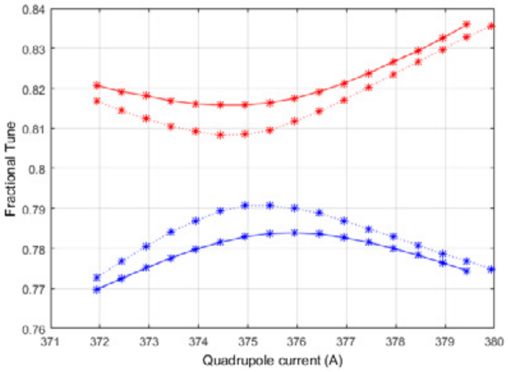

Figure 4: Comparison of the measured coupling before (solid line) and after correction (dotted line) by using RCDS method.

SUMMARY

The skew quadrupole magnets embedded in the sextupole magnet were successfully installed and implemented for coupling correction in the SPS storage ring. The optimum current of skew quadrupole magnets was optimized by using the LOCO and RCDS algorithm. The minimum vertical beam size of 0.2330 mm was archived, corresponding to a coupling ratio of 4%. When the insertion devices are completely operated, the target coupling ratio at 1% cannot be performed. It is due to the limitation of the skew quadrupole field and strong nonlinear effect generated from the multipole wiggler.

ACKNOWLEDGEMENTS

The authors would like to express appreciation to Source and Utility Maintenance and Operation (SUMO) team for their support and kindness.

REFERENCES

[1] A. Kwankasem *et al*, SLRI-TN-2017-01 New Water-Cooled coils for Sextupole *Magnets*, SLRI, Thailand, 2017.

[2] M. Borland, V. Sajaev, L. Emery, and A. Xiao, in Proceedings of PAC 2009, Vancouver, BC, Canada, 2009, p.3851.

[3] X. Huang and J. Safranek, Nuclear Instruments and Methods in Physics Research Section A: Accelerators, Spectrometers, Detectors and Associated Equipment757, 48, 2014.

[4] R. Bartolini, I. P. S. Martin, J. H. Rowland, P. Kuske, and F. Schmidt, Phys. Rev. ST Accel. Beams11, 104002

[5] X. Yang and X. Huang, BNL-112293-2016-JA, Brookhaven National Laboratory, 2016.

[6] P. Sudmuang, *et al.*, Improving Siam Photon Source Storage Ring Performance with Linear Optics Analysis, SRI, Lyon, France ,2012

[7] X. Huang and J. Safranek. Online optimization of storage ring nonlinear beam dynamics. Phys. Rev. ST Accel. Beams, 18:084001, Aug 2015.

CONTACT

*Porntip Sudmuang, tel: +66-44 217040 ext 1518; porntip@slri.or.th

STREAK CAMERA FOR BUNCH LENGTH MEASUREMENT

T. Pulampong, P. Sudmuang, and T. Chanwattana*
Synchrotron Light Research Institute (Public Organization) 111 University Avenue, Muang District,
Nakhon Ratchasima 30000, Thailand

ABSTRACT

Siam Photon Source (SPS) has one diagnostic beamline utilizing visible synchrotron light emitted from a dipole magnet. Since the beginning of the machine operation, diagnostic system has been continuously developed to extract the properties of the circulating electron beam. With the new streak camera, longitudinal properties of the beam can be observed for the first time using synchroscan unit. Then bunch length can be calculated from the collected profile data after post-processing step which also be compared with analytic calculation. Available slow single sweep unit can be utilized to reveal the bunch by bunch transverse beam profile.

INTRODUCTION

In an electron storage ring, longitudinal beam profile measurement is not trivial. Very fast instrument is required to extract the longitudinal properties of the beam. Streak camera combining a streak tube and phosphor screen allows us to see the electron beam longitudinally. Radiated synchrotron light is the only input for streak camera. To see the beam longitudinal profile, the beam has to be steered 90 degrees and be projected on a screen. Thus the input photon has to be converted to charged particle (electron in this case). A photocathode is employed as a converter thus electric field can be used to vertically sweep the produced electron as shown in Figure 1. Universal streak camera C10910 as shown in Figure 2 is used in SPS storage ring.

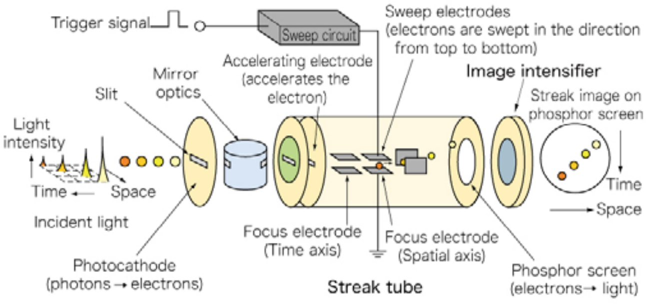

Figure 1: Working principle of a streak camera. [1]

Figure 2: Universal streak camera C10910.

STREAK CAMERA SET-UP

The requirement for the streak camera is that the measured light has to be focused on the photocathode. Small focused beam is more preferable for better signal to noise ratio. A simple optic setup has been prepared for the streak camera system as shown in Figure.3. Optic line on the table used for the streak camera is the last line close to beamline 4 experimental station. This allows easy access to the new streak camera system for alignment and operation. On the optical table, the system composes of a beam splitter then focusing lens, another beam splitter, a mirror, an ND filter and a vertical beam steerer. The beam steerer allows the light plane to be adjusted to the best position for streak camera. This arrangement brings the focused light to the streak camera.

Unlike transverse beam profile system to boost the resolution or the signal to noise ratio, low magnification is more preferable for streak camera. Thus very small bright light spot in front of the camera can be seen as shown in Figure 4. During commissioning and operation in focusing mode, bright light may cause dark spot on the CCD. Intensity level has to be carefully controlled by filter and shutter.

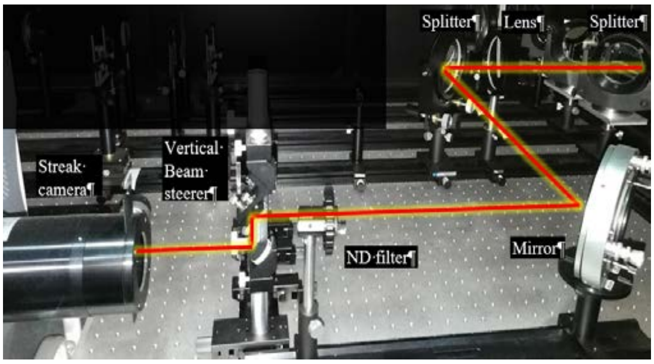

Figure 3: Optical alignment and light path.

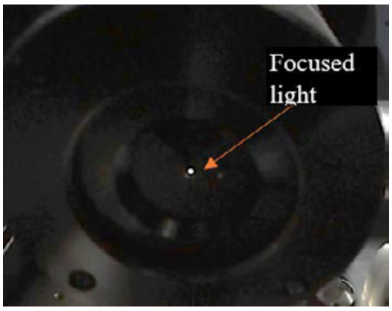

Figure 4: Focused light on streak camera.

OPERATION MODE

Two units are available for streak camera operation at SLRI. The first unit is synchroscan unit and the second one is slow speed single sweep unit. These allow us to investigate the bunch-by-bunch electron beam behavior in both longitudinal and transverse planes.

Synchroscan mode

This mode is the normal operation mode used for longitudinal beam profile measurement. The results can be processed into bunch length of electron bunches in the storage ring. Figure 5 shows the configuration of the input signal and the whole one turn bunches train seen on the screen. Vertical sweep with the RF frequency acts on each bunch to project the beam on the screen. The head of the bunch will appear on the top of CCD while the tail will end up on the bottom. Horizontal sweep is applied to separate each bunch profile on the CCD.

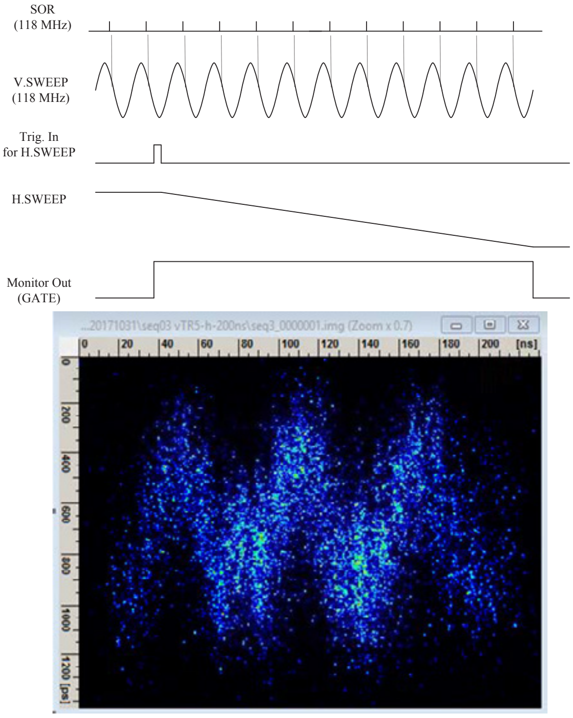

Figure 5: Configuration and profile from synchroscan mode.

Slow single sweep mode

To use slow single sweep unit, we have to turn off all the module and power supply of the streak camera. Then we carefully replace the synchroscan unit with the slow single seep unit on the side of the streak camera. Only vertical slow sweep will be applied in this mode. Operation with the slow single seep unit allows us to see the movement of the transverse beam profile of the whole train for one single turn as shown in Figure 6. Transverse beam oscillation can be observed.

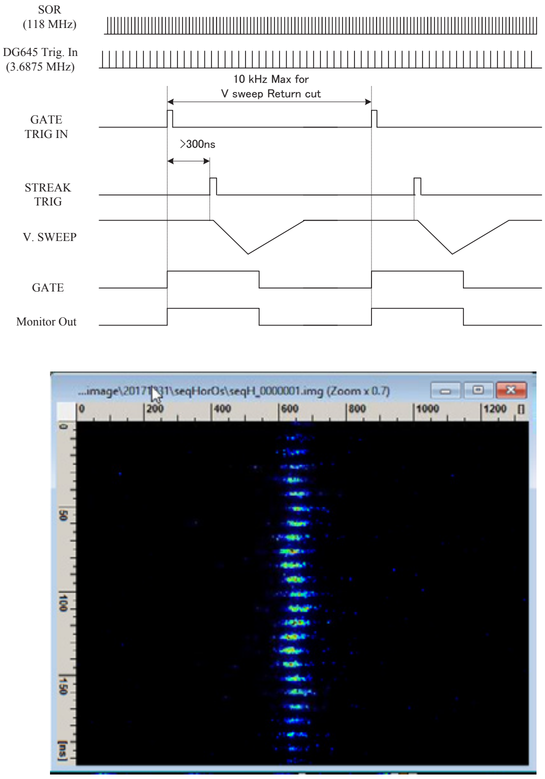

Figure 6: Configuration and profile from slow single sweep mode.

Post-processing for slow single sweep mode can be done to extract bunch-by-bunch beam centroid movement and beam size variation. However, in daily operation; the slow single sweep unit may not be used because we may be interested more in the fast longitudinal profile of the beam. Bunch length measurement is also one important to characterize the machine and need to be measured regularly.

Operation and post processing for bunch length

Data collection can be performed using the sequence command that allows continuous frame capturing from the CCD camera unit. The larger number of frame the longer acquisition time. To gain sufficient signal to noise ratio, the information of each captured frame has to be accumulated. This is similar to photography in a dark place which requires longer shutter time to see good detail of object.

Post processing for synchroscan mode, as the normal operation mode, will only be discussed here. Prior to data collection, delay unit may need some adjustment to bring the beam vertically to the center of the screen. This can be clearly seen using analog integration option in the acquisition control. Thus all the information can be captured sufficiently. The exposure time has to be 10 ms and the number of exposures of 50 should allow sufficient accumulation. This will define the maximum and minimum margin of the oscillating longitudinal beam profile. A good margin after adjustment can be seen in Figure 7. The integrated profile on the fast time scale should appear about on the middle of the available screen range.

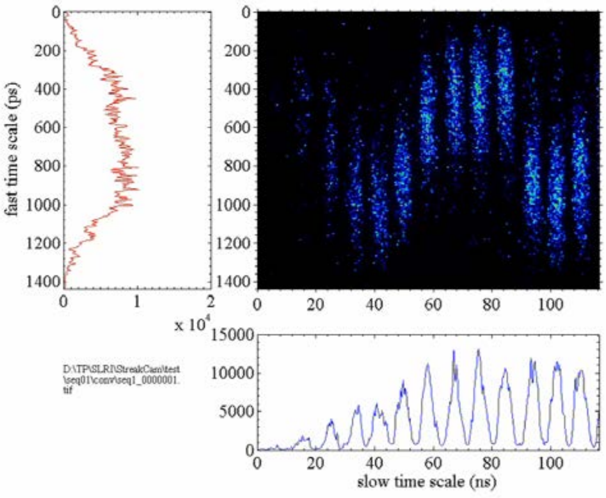

Figure 7: Projected intensity from CCD.

Post-processing

Post processing for bunch length calculation relates mainly to image processing on the sequence generated from the streak camera. The initial processing is to sum the RGB of each pixel as the light intensity projected on each axis. Then further analysis can be continued. The captured frame is composed of information from many electron bunches (~13-14 bunches) as shown in Figure 7. The projected intensity on each axis is also plotted. To further analyze the data, it is required to separate information of individual bunch. Bunch separation can be found by flipping the intensity peak (projected on horizontal axis) upside down and searching for peaks. The found peaks are the lowest intensity points that can be used as the bunches separation points as shown in Figure 8.

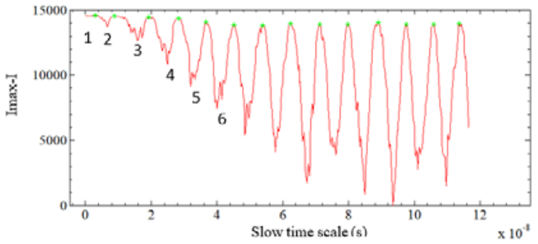

Figure 8: Bunch separation point from intensity.

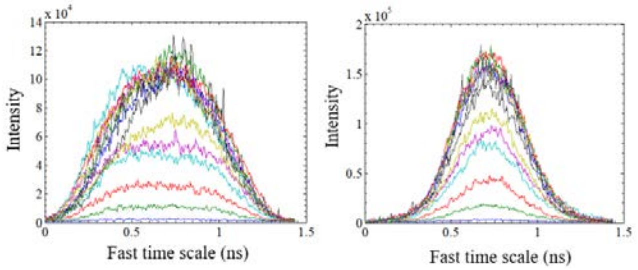

Figure 9: Accumulated intensity without (left) and with (right) profile re-centering.

In our case, it is observable that the longitudinal profile of each bunch oscillates on the fast time axis (vertical plane). This may be an indicator for collective instability. To find the true bunch profile from the captured sequence of figures, the oscillation need to be removed. In each frame, the center of each bunch was determined by Gaussian fit with centering and scaling option. Then the re-centered intensity profile of each bunch can be accumulated with the same reference (center) for the whole sequence. Re-centering can remove the effect of longitudinal oscillation. Figure 9 demonstrates the improvement of accumulating intensity profile after re-centering which provides more accurate Gaussian beam profile. The intensity profile depends strongly on the total number of frames taken in the sequence. Because signal to noise ratio increases with more number of frames. Background subtraction function was also applied to ensure cleaner bunch information.

After post processing of the acquired intensity, Figure 9 (right) gave us the true longitudinal profile of each bunch. Figure 9 (left) on the other hand, is the beam profile integrated with small movement (observable broader peaks) which implies overestimated bunch length. Bunch length calculation can be performed based on the corrected profile. The result of the first half of the bunches train can be seen in Figure 10. The fitted bunch length for individual bunch is plotted in blue and red is the error bar. It is obvious that the bunch length of the first few bunches (1-2) is too long and the error bar is larger compared to other bunches. It is caused by low current in the first few bunch which provides low intensity on the CCD as shown in Figure 7. To acquire the correct bunch length these large error values were excluded. Similar result can be found for the bunches at the tail of the train. From the result of 21 bunches, the calculated half bunch length (σ_l) was 188.63 ± 3.28 (ps).

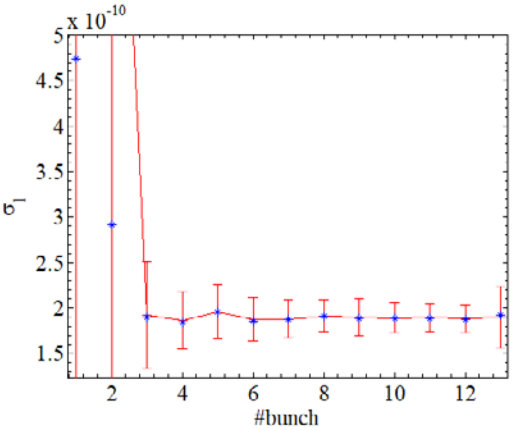

Figure 10: Measured bunch length for the first 13 bunches.

BUNCH LENGTH COMPARISON

To verify the measured bunch length value, the model bunch length was calculated. Theoretical formula for zero current bunch length (half) can be written as [2]

$$\sigma_l = \frac{\sqrt{2\pi}c}{\omega_{rev}}\sqrt{\frac{-\eta E_0}{heV_{rf}\cos(\phi_s)}}\,\frac{\sigma_u}{E_0} \qquad (1)$$

where η is the phase slip factor, φ_s is the synchronous phase given by $V_{rf}\ \sin(\varphi_s)$ =U0, ω_{rev} is the revolution frequency and h is the harmonic number.

The bunch length calculated from equation (1) is the natural bunch length which considers a bare ring condition without any insertion device and it is the bunch length at zero current. This is the equilibrium longitudinal dimension contributed by two conflicting effects: radiation damping and quantum excitation. In reality, in a storage ring, there are insertion devices and the operating beam current is not zero. The effect of strong field insertion device in a dispersive section will normally lengthen the bunch because of the dispersion generation which boost the excitation effect. Thus energy spread will be increased compared to the bare ring condition.

In SPS storage ring there is a strong field insertion device namely Super conducting Wavelength Shifter (SWLS). The operating magnetic peak field can reach 6.5 T at the supplied current of 308 A. Figure 11 shows the calculated energy spread ratio affected by the peak field of the SWLS. It is clear that the SWLS peak field more than 2 T can introduce energy spread growth. The growth ratio accelerates after the peak field is greater than about 4.5 T. Energy spread grows 25.6 % at the operating field of 6.5 T.

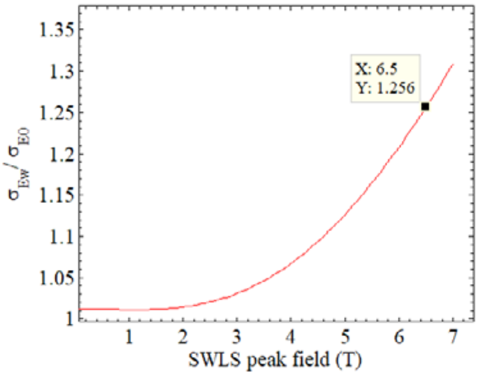

Figure 11: Energy spread ratio as a function of SWLS field.

Table 1: Bunch length comparison.

	Bunch length	
	(ps)	(mm)
Measurement	188.6	56.5
Analytic zero current	128.8	38.6
Analytic inc. SWLS	156.0	47.7

Calculated half bunch length including the effect from SWLS is 156 ps. It is worth noting that this is the zero current bunch length with the effect of SWLS only. The measured bunch length is longer than the calculated value due to the current depend effects. Table 1 summarizes the measured and calculated bunch length.

SUMMARY

The new Streak camera was assembled and installed successfully in the diagnostic beamline. The system fit nicely on the existing optical table. The system was commissioned and operation set up was performed. Longitudinal beam profile was observed for the first time since the beginning of SPS. A program used for data collection, post-processing and data analysis was written. User can conveniently operate the streak camera remotely to perform bunch length measurement with synchroscan unit. The measured bunch length was about 188 ps while the theoretical zero current bunch length including SWLS effect was about 156 ps. The discrepancy may emerge from current dependent effects.

Slow single sweep unit was also tested successfully. Horizontal beam centroid variation can be extract. Though, in normal operation we use only synchroscan unit for bunch length measurement.

ACKNOWLEDGEMENTS

The authors would like to express appreciation to Source and Utility Maintenance and Operation (SUMO) team for their support and kindness.

REFERENCES

[1] https://www.hamamatsu.com/jp/en/product/photometry-systems/streak-camera/operating-principle/index.html

[2] A. Chao et al., Handbook of Accelerator Physics and Engineering, 2nd Edition, World Scientific Publishing Co. Pet. Ltd. Singapore (2012)

CONTACT

*Thapakron Pulampong, tel: +66-44 217040 ext 1527; thapakron@slri.or.th

CURRENT STATUS OF THE SLRI-BEAM TEST FACILITY

K. Kittimanapun[1], N. Chanlek[1], C. Kobdaj[2], N. Laojamnongwong[2] and A. Lakrathok[2]*
[1] Synchrotron Light Research Institute (Public Organization) 111 University Avenue, Muang District,
Nakhon Ratchasima 30000, Thailand
[2] School of Physics, Institute of Science, Suranaree University,111 University Avenue, Muang District,
Nakhon Ratchasima 30000, Thailand

ABSTRACT

The Synchrotron Light Research Institute (SLRI) Beam Test Facility or SLRI-BTF has been developed to maximize usage of the Siam Photon Source injector and to increase diversity of research. Requested by users requiring electron beam to test and calibrate high-energy particle detectors and instrumentations, SLRI-BTF is capable of producing electron test beam with tunable energy ranging from 40 MeV – 1.2 GeV and with adjustable intensity up to millions of electrons per spill. The electron test beam has successfully been employed to investigate pixel sensor efficiency and more experiments has been planned for different types of measurement.

INTRODUCTION

A new experimental station, called a Beam Test Facility (BTF), has been built at the Synchrotron Light Research Institute (SLRI) to directly utilize high-energy electron beam produced from the Siam Photon Source (SPS) injector [1]. Benefiting from the injection scheme that fills electrons into the SPS storage ring twice daily, the SLRI-BTF beam time is available up to 11.5 hours per period or 23 hours a day. SLRI-BTF has been designed to provide electron test beam with energy that ranges from 40 MeV – 1.2 GeV by applying various acceleration time to a synchrotron booster. Depending on types of measurement and diagnostic instrumentations, the provided test beam intensity can be adjusted from a few electrons per spill suitable for testing tracking devices, such as pixel sensors, silicon drift detectors, etc., to millions of electrons per spill for studies of high-energy particle irradiation.

SLRI BEAM TEST FACIILITY

Including the electron gun, a linear accelerator, a low energy beam transport line (LBT), a synchrotron booster, and a high energy beam transport line (HBT), the components of the SPS injector are illustrated in Figure 1. The electron beam accelerated to 40 MeV by the coupled linac and to 1.2 GeV by the synchrotron booster is transported to HBT where the BTF experimental station locates next to the vertical bending magnet. Electron beam parameters at HBT are listed in Table 1. Without an intensity reduction system, the minimum test beam intensity is approximately 10^8 electrons per spill.

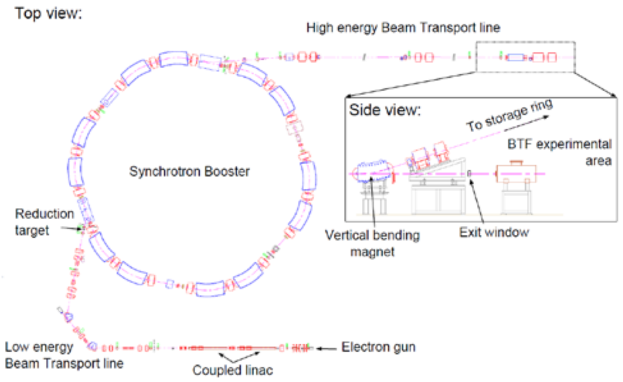

Figure 1: Schematic of the SPS injector and the SLRI-BTF experimental area.

Using the wedge-shape tungsten target that moves at resolution of 10 μm and is installed at LBT [2], the electron test beam intensity is adjustable and well controlled to avoid fluctuation. Having the synchrotron booster as an energy selector, the electron test beam with desired energy can be obtained by setting proper acceleration time of the synchrotron boosters. Due to the ramping pattern, the repetition rates for 1 GeV and 1.2 GeV test beams are 0.5 and 0.33 Hz, respectively. The low multiplicity of electron test beam has been detected with a single plane pixel sensor [3].

Table 1: Test beam parameters at SLRI-BTF.

Parameters	**HBT**
Particles	electron
Energy	Up to 1.2 GeV
Energy spread	0.05% at 1 GeV
Pulse duration	8.5 ns
Repetition rate	0.5 Hz for 1 GeV
	0.33 Hz for 1.2 GeV
Number of electrons per spill	5 x 10^8

PIXEL SENSOR TELESCOPE

In order to perform detection efficiency of a Mono Active Pixel Sensor (MAPS), a pixel sensor telescope has been employed. The telescope is made of seven planes of pALIPIDE (prototype *ALI*CE *PI*xel *De*tector) developed by the ALICE Inner Tracking System (ITS) upgrade project collaboration. A sensor plane comprised of a sensor and a data acquisition board as well as a complete setup of the telescope are depicted in Figure 2. Each sensor plane in the telescope setup is separated by four 2-cm spacers and aligned with center of the beam exit window. The pALIPIDE-1 sensors locates at the first and the last plane while the pALPIDE-2 sensors are at the second to the sixth plane. The middle plane is for a Device Under Test (DUT) or a test sensor. During operation of the telescope, 3-V bias voltage is applied to all but the pALPIDE-1 sensor and the 100 ns TTL signal is used as external trigger signal for the telescope. The EUDAQ framework [4] has been properly installed with the telescope setup.

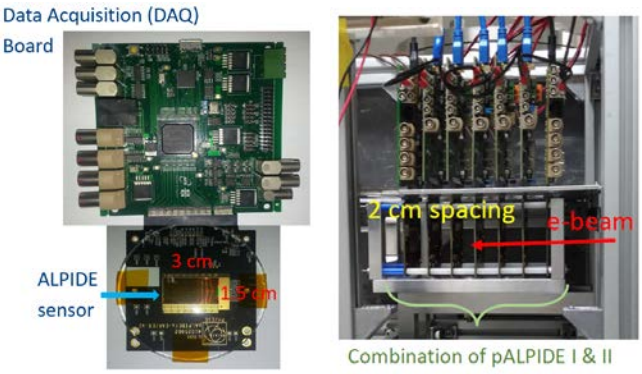

Figure 2: The ALPIDE sensor attached to a data acquisition board (left) and a setup of a pixel sensor telescope with combination of pALPIDE-1 and -2 sensors (right).

DETECTION EFFICIENCY MEASUREMENT

Detection efficiency of the pixel sensors has been investigated with the 1-GeV electron beam and the data are collected over 10^5 events. The test beam intensity is adjusted to be less than 5 clusters per spill. Figure 3 shows the profiles of the test beam detected on each sensor plane with the internal trigger signal of 75 DAC. For this measurement, the average number of clusters detected by DUT is 3.9 clusters per spill while the average cluster size is at 1.75 pixels. The correlation plots of horizontal and vertical positions between the first and other planes are illustrated in Figure 4. The collected data are further analyzed and the detection efficiency are calculated by the EUTelescope framework [5].

The detection efficiency of the test sensor have been studied as a function of internal trigger signal set on the DAQ board and of the number of clusters ranging from 3.9 to 45.4, as shown in Figure 5. It is obvious that the detection efficiency depending on the internal trigger delay of DAQ decreases when the trigger delay increases. According to the required specification of the ALPIDE sensor, the measured detection efficiency of the test senor is larger than 99% as the average number of clusters varies up to 45.4 and the results agree with the requirement.

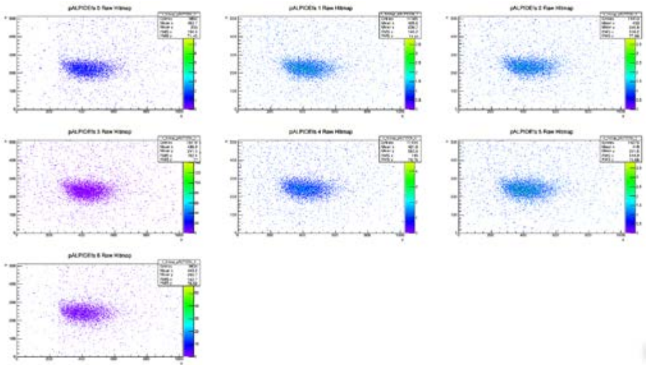

Figure 3: Profiles of the 1-GeV electron test beam detected on each sensor of the beam telescope.

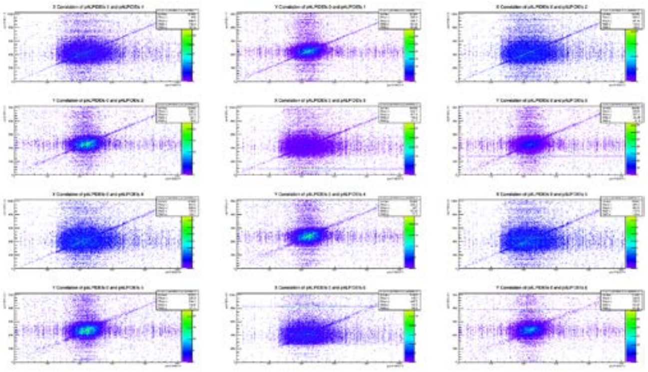

Figure 4: Horizontal and vertical correlation plots between the first and the other sensor planes.

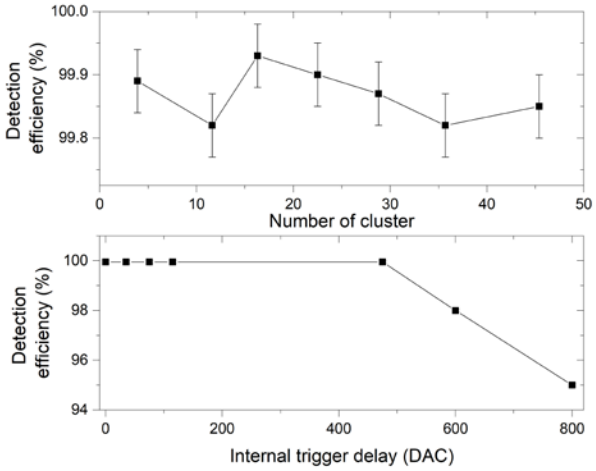

Figure 5: Detection efficiency of the ALPIDE sensor as a function of internal trigger delay signal (bottom) and the number of clusters (top).

UPGRADE OF PIXEL SENSOR TELESCOPE

Due to the limitation of the current telescope setup, it is impossible to study the detection efficiency at edges and corners of the test sensor. A new telescope setup has been installed and ready to operate. Providing flexibility on moving DUT in 2 dimensions, the tracking planes of the new telescope, as shown in Figure 6, are divided into two parts: forward and backward tracking planes. The distance among tracking planes are still 2 cm while DUT is 5.6 cm away from both adjacent planes. Besides, in order to reduce the effect of multiple Coulomb scattering, the current tracking planes will be replaced by new 50 μm thick sensors.

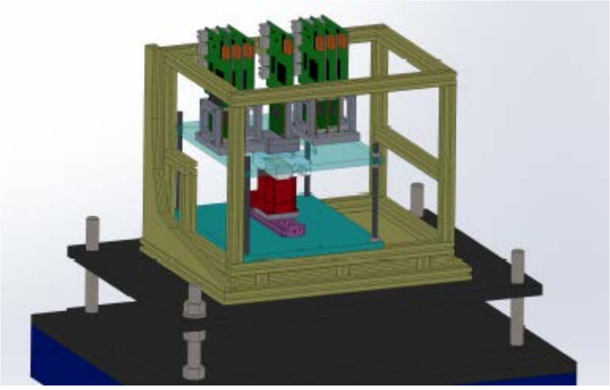

Figure 6: Upgraded station for the 2nd version of a pixel sensor telescope.

TEST BEAM PROPOSAL

In addition to the investigation of the pixel sensor efficiency, SLRI-BTF is also available for testing other types of detectors and instrumentations. SLRI-BTF has received proposals for testing a charged particle detector based on graphene from an international user as well as studying high-energy particle irradiation of scintillating material from domestic users.

SUMMARY

SLRI-BTF has been in operation and providing test beams with desired beam intensity and energy for calibration and testing of high-energy particle detectors and diagnostic instrumentations. The test beam has been employed to investigate the pixel sensor efficiency mounted on the pixel sensor telescope. The detection efficiency of the test pixel sensor has been measured and agrees with design specification. The upgraded beam telescope will be used to further study detection efficiency at different regions of the sensor. Due to the beam time availability, researchers involved in developing particle detectors or interested in using high-energy electron beam for their research are welcome.

ACKNOWLEDGEMENTS

I would like to thank the mechanical system development section and the source, utility maintenance, and operation section for supports during the development and operation of SLRI-BTF.

REFERENCES

[1] K. Kittimanapun, *et. al.*, “Development of the SLRI beam test facility for characterization of monolithic active pixel sensors”, Nucl. Instrum. Methods. Phys. Res. A (2019), https://doi.org/10.1016/j.nima.2019.03.066

[2] K. Kittimanapun, *et. al.*, “Improvement of electron intensity reduction system at SLRI beam test facility”, in *Proc. of International Particle Accelerator Conference, IPAC’17*, Copenhagen, Denmark, May 14-19, 2017, pp. 528-530

[3] K. Kittimanapun, *et. al.*, “Low intensity electron beam measurement at SLRI beam test facility”, in *Proc. of International Particle Accelerator Conference, IPAC’18*, Vancouver, BC, Canada, April 29 - May 4, 2018, pp. 4502-4504

[4] EUDET-type telescope, URL https://telescopes.desy.de

[5] EUTelescope, URL https://eutelescope.web.cern.ch

CONTACT

*Kritsada Kittimanapun, tel: +66-4421-7040 ext 1483; kritsadak@slri.or.th

THE DEVELOPMENT OF VACUUM BRAZING FURNACE AT SIAM PHOTON SOURCE

S. Klinkhieo, S. Duangnil, D. Bumrungkoh, S. Boonsuya, N. Sumano, N. Russamee, and P. Pruekthaisong*

Synchrotron Light Research Institute (Public Organization) 111 University Avenue, Muang District, Nakhon-Ratchasima 30000, Thailand

ABSTRACT

The Vacuum Brazing Furnace (VBF) has been developed by the Synchrotron Light Research Institute (SLRI) in Thailand for carrying out brazing of components (consisting of two or more pieces), and components made of the same and dissimilar materials. Furnace brazing under vacuum is currently the most popular and well accepted method for production of the high quality RF systems, ultra-high vacuum (UHV) components of high energy accelerator and beamline, as well as complicated structure manufacturing. The vacuum furnace with accommodating jobs of 300mm diameter x 500mm long sizes with job weight of 50 kg up to a maximum temperature of 1,200° C at a vacuum of $5x10^{-5}$ torr is designed and fabricated for the first SLRI-VBF prototype. The working principle of brazing process and sub-systems installation are presented. The commissioning and successful brazed components will be also discussed.

INTRODUCTION

Brazing is a welding technique of joining two or more pieces of metal, same or dissimilar compositions, using filler metal that has been melted with a melting temperature above 450° C, but below the melting point of the base metals being joined, and then flowed across and into the joint. This allows "*the molten filler metal to flow via capillary action into the close fitting surfaces of the joint and to form an alloy of the materials at the transition point upon solidification. The base metals/components, do not melt, but they can merge with the molten filler metal by diffusion to form a metallurgical bond that is generally as strong or stronger than the base metals*" [described by The American Welding Society]. The metallurgical properties at the brazed joint depend on the selection of the appropriate filler metal that related to the base metals, and the desired properties of the applications, for example, the brazing can be used to provide a leak tight seal, structural strength, extending section length in piping or tubing materials, etc. [1,2]

The brazing in vacuum is a sophisticated connection method today, it has unique advantages and flexibility for new material connection technology development and complicated structure manufacturing [2]. High vacuum brazing is carried out at high temperature to obtain hermetically sealed joints. The vacuum condition at high temperature results a less residual oxygen to contaminate the work pieces, and improves the minimum distortion properties because all components of the base metal are heated and cooled uniformly. Moreover, the vacuum brazing is widely employed for aviation, aerospace, auto, machinery, electronics, war and civilian industries, etc. It is applied where welding process cannot be used, for example, high quality UHV components of accelerator, and carbide tools which are vacuum compatible and thermally conductive.

The accelerator components made of aluminum and its alloys using welding process have become a very common practice nowadays. However, the fabrication of RF devices and some components of beamline/front-end made of oxygen-free high thermal conductivity (OFHC) copper and stainless steel using welding process is very difficult, and in most of the cases (e.g. welding of copper-stainless steel) it is impossible. The fabrication and joining in such cases is possible using brazing process especially under vacuum. In addition, the modern vacuum brazing technology has extended to the joining of metal to non-metallic components, including glass, ceramic and refractory materials [3]. However, in the first phase, this paper will focus only on the brazing of metals.

In 2017, the Siam Photon Source (SPS), a synchrotron light source operated by the Synchrotron Light Research Institute (SLRI) in Thailand proposed the idea of fabrication of vacuum brazing finance in-house. The main purposes of this project are to: (1) develop knowledge and expertise in vacuum brazing technology, (2) build a low cost prototype of vacuum brazing furnace in the country, (3) reduce the import and preventive maintenance, as well as operating costs, (4) promote and establish the research cooperation in vacuum brazing technology related to the joining metals on high energy accelerator components, and intricate component manufacturing across the nation. The project will be mainly focused on the design and fabrication of vacuum furnace, consisting of heat zone, cooling, temperature control and interlock systems. The brazing parameters so as to obtain high quality brazed joints will be also optimized. The research studies based on the commercial vacuum brazing furnace of BMI-FOURS company type B5-T.

The paper will first report the current status of VBF development project at SLRI, which includes its structure required for design and fabrication, and working steps of vacuum brazing is described in the next Section, followed by the systems installation and commissioning results, and the conclusion given the in last section.

VACUUM BRAZING FURNACE STRUCTURE

The vacuum brazing furnace structure consists of the main vacuum furnace body, heating chamber (hot zone) with the insulator and heating elements, cooling system, and electrical and interlock control systems. The specifications of the vacuum brazing furnace prototype are given in Table 1.

Table 1: The specifications of vacuum brazing furnace prototype at SLRI.

Size W x H x D	300 x 300 x 500 mm.
Max Temperature	1,200° C
Heating Element	Graphite-Molybdenum
Insulator	Graphite
Temp. Ripple	< ± 5° C
Temp. Ramp-Up Rate	≥ 25° C/min
Base Pressure	< 5.0 x 10^{-5} torr
Main Vacuum Pump	Diffusion
Baking Pump	Rotary
Cooling Water Temp.	< 10° C
Cooling Gas	N_2
Hot zone uniformity	< ± 5° C

The final design of VBF prototype is illustrated in Figure 1. The diagram includes the engineering detail drawings of the main brazing furnace and hot zone, vacuum system, heat exchanger, gas quenching, cooling system, power supply, and control system units, respectively.

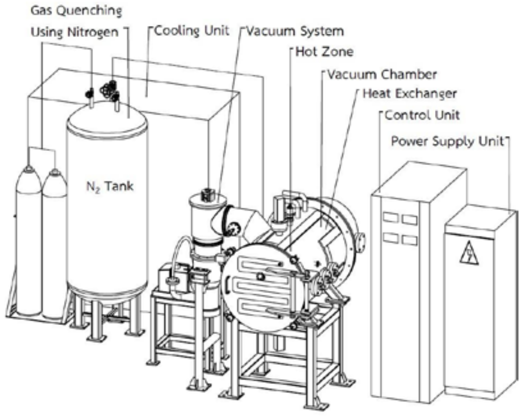

Figure 1: The diagram of vacuum brazing furnace prototype.

Brazing furnace body

The brazing furnace body is horizontal and single chamber heating structure. The principle design of vacuum furnace is based on heating elements and insulation construction material, which depends on the vacuum level requirement, compatibility with the components of base metal and brazing filler materials, temperature requirements, and cooling rate [3]. Generally, the insulation and heating element material are *graphite*, and the refractory metals which are extraordinarily resistant to heat and wear such as *molybdenum*. Graphite is an economical material with lower maintenance requirements. Its purity has studied and improved over the decades, and now is considered for many vacuum brazing applications [3,4].

The furnace can accommodate jobs of 300mm diameter x 500mm long sizes with job weight of 50kgs. The furnace is designed for a maximum temperature of 1,200° C at a vacuum of 5x10^{-5} torr. The brief description of brazed components is given below:

Vacuum system

The main pump is Agilent diffusion pump: VHS-6, with pumping speed: 1,550 l/h, and the baking pump is Agilent dual stage rotary vane pump: PHV75K, will pumping speed: 75 l/h. They are equipped with high vacuum valve, vacuum gauges, and vacuum control system units, respectively. These diffusion and rotary pumps have been employed to obtaining the vacuum of 5x10^{-5} torr inside the brazing furnace chamber.

Heating system

The multi-layers, graphite-molybdenum heating elements and insulator of graphite have been used for temperature control system of the furnace. The closed loop water supply is designed to provide efficient cooling to the system. The heating system includes (i) heating power supply, (ii) heating element, and (iii) temperature control system. The 3 phase 380 VAC 30 KVA power supply SCR type is used in the heating power supply. The closed loop automatic temperature control using PID is implemented according to different control signals, and temperature measuring via a set of thermocouples inside the furnace. The heating elements are 9 molybdenum tubes, which are evenly distributed along hot zone, so as to provide a good hot zone temperature uniformity which is less than ±5° C.

Heat exchanger and cooling system

The heat exchanger is used in vacuum brazing furnace to provide heat transfer. The heat exchanger can protect components being brazed from the heat energy via gas quenching system with flowing of nitrogen or other inert gases. The furnace encloses a cooling system (with cooling water temperature less than 10° C) to cool the work pieces in thermal process for preventing distortion and oxidation attack at the high temperatures in the vacuum furnace during the cooling cycle.

Control system

The operation of the VBF is computer controlled with manual override facility mode. The programmable logic control (PLC) and LabVIEW are integrated together via WorkStation computer to develop the control software and data acquisition systems, and make them operator and user friendly. The working steps and interlock systems are also provided for safe operation of the vacuum furnace.

THE WORKING STEPS OF VACUUM BRAZING

In the vacuum brazing, the joining of two pieces of components is performed when melted filler metal flows into a thin gap or clearance between them, while cooling, it will form a metallurgical bond, and a brazed joint is made [3]. Brazing makes a very strong joint which is stronger than the original base metal pieces without deforming or melting the components [3,4].

The following are the main steps to be followed in vacuum brazing:

Cleaning and washing

A cleaning is essential process of vacuum brazing. The capillary action will work properly if the component surfaces are clean. Typically, the surfaces with contamination of oil, grease, rust, scale or dirt will create a barrier between component surfaces, then result into poor flowing, wetting and spreading of the molten filler metal, while the oxidation due to heating circle in the furnace will result into improper clearance between the components and imperfect joint [3,4].

In order to remove these impurities and oxides, a proper cleaning method is necessary. Generally, most of the impurities can be easily cleaned by physical or chemical methods. In vacuum brazing process all gases are inevitably removed from the area surrounding the components by vacuum pumping; therefore, no reaction or oxidation takes place of the base metals being brazed [3,4].

Joint and clearance

Many types of joints are used in vacuum brazing. However, two basic types, butt and lap types are popularly used. Lap joint provides more strength than butt joints. This is because more area is available for brazing in lap type joint. However, the strength depends not only on brazing area of the surfaces but also on the clearance between the components of the base metal and suitable type of filler metals [4]. The joint strength is reduced if the amount of clearance between the components is either bigger or smaller than a specific value of a particular base metal in given set of conditions. For joining dissimilar metals, the thermal coefficient of expansions must also be considered and taken into account for the proper clearance [4,5]. The proper clearance allows capillary action to work most effectively.

Figure 2, typically, the joint design and proper clearance for brazing of copper-stainless steel of accelerator components at SLRI

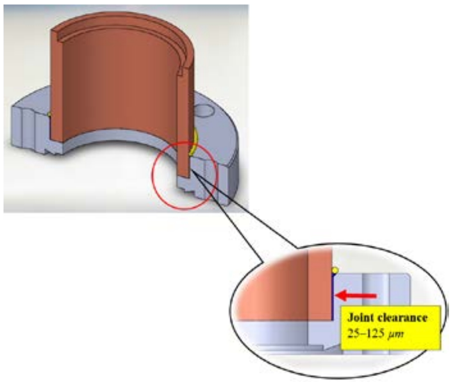

Figure 2: The example of joint design and proper clearance.

Assembly and fixture

Assembly of components requires holding in position. This can be done by using fixtures. Filler metals are cut or formed to the particular sizes, and are placed or attached between the components. It should be ensured that the assembly of the components remain in required position with good alignment throughout the brazing cycle. The common way of doing this is to hold the components together by gravity, and the joints surfaces should keep in horizontal plane for effective working of capillary action. The components after cleaning should immediately assembly and load into the vacuum furnace so that the surfaces are brazed in a good vacuum environment i.e. clean and oxide free condition [4,5].

Figure 3 shows the cleaning, assembly, and holding the components before vacuum brazing process.

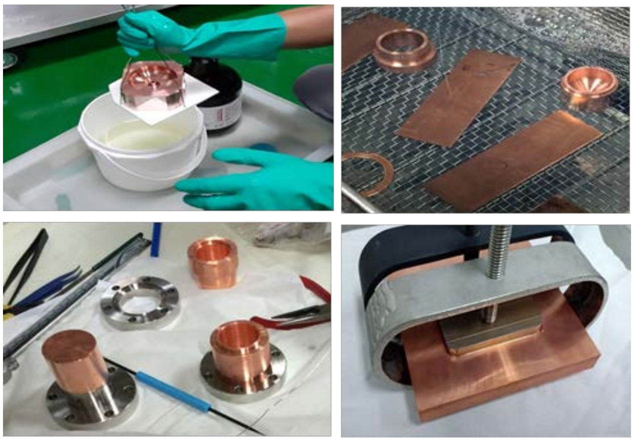

Figure 3: The example of cleaning, assembly and holding the components.

Brazing and heating cycles

Once the components are loaded into the vacuum furnace, the vacuum pumping system and all other systems (e.g. cooling system, power supply) will be checked for starting their proper working. The designed brazing cycle is an important step in the process. The brazing cycle consists of initial pump down, heating ramp, stabilizing soak, heating ramp to brazing temperature and soak, and cool down, respectively.

In order to achieve a high quality brazed joint heating, the components must be uniformly heated, the faster rates are not recommended by reason of the possible distortion of the components, spalling of liquid filler/brazing slurry, and the occurrence of excessive outgassing in the furnace.

All of the above discussions, there are many reasons to say that the vacuum brazing is an effective jointing method today. It has several advantages which are not possible to get in other methods of joining.

INSTALLATION AND COMMISSIONING

The low cost prototype of vacuum brazing furnace has been installed and commissioned at SLRI. The vacuum parts, vacuum furnace, hot zone unit, cooling system, control and power supply units, and other system components related to this prototype both hardware and software, are designed and fabricated in-house by the SLRI engineering teams.

The installation and commissioning works are shown in Figures 4.

Figure 4: The vacuum brazing furnace installation and commissioning at SLRI.

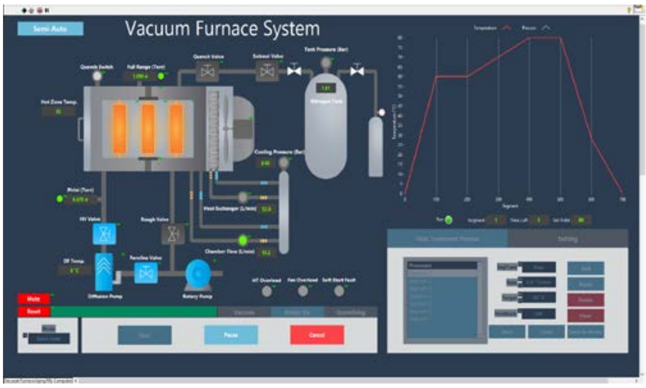

Figure 5: The GUI of control and data acquisition development systems of VBF.

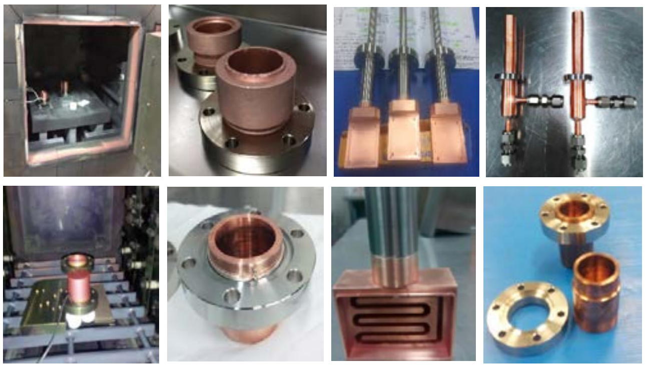

Figure 6: The examples of vacuum brazing of accelerator and beamline components.

The main graphic user interface (GUI) of the control and data acquisition development systems of vacuum brazing furnace will present in Figure 5.

The research also studies on the optimization and selection of appropriate brazing parameters for carrying out high quality copper-copper and copper-stainless steel joints such as surface cleaning and assembly of the components, brazing cycle, proper section of filler metal, and joint clearance design.

The various vacuum components of accelerator and beamline have been brazed successfully using vacuum brazing facility at SLRI which can reduce the import and preventive maintenance, as well as operating costs.

Figure 6 shows the examples of vacuum brazing of accelerator and beamline components e.g. water cooling shutter, fixed mark, safety shutter, water cooled 4-brade slit at the front-end components, etc. These components are explored as better and suitable alternatives to the available components, and some of them are new developments.

CONCLUSION

The vacuum brazing furnace prototype has been designed and fabricated by the engineering team at SLRI, Thailand. The installation and commissioning of the first prototype, as well as vacuum brazing of accelerator and beamline components have been very successfully and effectively done using the vacuum brazing facility available in-house. The vacuum compatible brazing assemblies are leak tested by using Helium leak detector. They show a very impressive results. These detail processes of joining will be highly useful for developing technical expertise in vacuum brazing of UHV compatible accelerator and beamline components at SLRI in the future.

ACKNOWLEDGEMENTS

We would like to thank many colleagues in Technical Support teams of SLRI for their technical assistance, and Mr. Tsai Ming-Hsun from RF Group of NSRRC, Taiwan for sharing his experience, knowledge, and expertise on the vacuum brazing with us. The authors would also like to express their gratitude to Dr. Saroj Rujirawat, Suranaree University of Technology (SUT), for his invaluable suggestions.

REFERENCES

[1] R. M. Nascimento, A.E. Martinelli, A.J Buschinelli, “Review Article: Recent advances in metal-ceramic brazing,” *Ceramica*, 49 (1), 2003, 178-198.

[2] J. Kowalewski and J. Szczurek, “Issues in Vacuum Brazing” *Proc. International Brazing and Soldering Conference*, 2006, 326-333.

[3] R. Singh, K. Yedle, A.K Jain, “Development of Vacuum Brazing Furnace” *Accelerator Component Engineering & Fabrication Centre for Advanced Technology Conference*, 2010, 1- 4.

[4] R. Singh, K.K. Pant, S. Lai, D.P. Yadav, V.K. Raghuvanshi, and G. Mundra "Vacuum Brazing of Accelerator Components", *International. Symposium on Vacuum Science & Technology and its Application for Accelerators*, 2012.

[5] M. Srivastava and B. Sherpa "Review of the High Vacuum Metal-Metal and Metal-Ceramic Brazing Process", *Int. J. of Engineering Research and Applications, ISSN: 2248-9622,* 2014.

CONTACT

*Supat Klinkhieo, tel: +66-44-217040; supat@slri.or.th

ENVIRONMENTAL RADIATION MONITORING SYSTEM AT SLRI

P. Aim-O, M. Sophon and S. Ruengpoonwittaya*

Synchrotron Light Research Institute (Public Organization) 111 University Avenue, Muang District,
Nakhon Ratchasima 30000, Thailand

ABSTRACT

SLRI has set up an environmental radiation area monitoring system consisting of 3 fixed monitors and 4 non-fixed monitors located at 3 different locations, where high radiation dose were expected, at BL1, BL6 and in the control room II. The area monitoring is used to clarify the circumstances of radiation fields, e.g. gamma radiation and neutron radiation. The total dose rate at the different observation points were therefore evaluated. This study leads to estimate the radiation level to provide the radiological protection for radiation workers and users in order to control the radiation exposure level below the dose limit value according to the International Commission on Radiological Protection or ICRP standard.

INTRODUCTION

Siam Photon Source is a type of electron accelerator where electrons travel in the magnetic field near the speed of light and generate high brilliant synchrotron radiation. Synchrotron radiation is an electromagnetic wave which has the photon energies span a wide energy range from infrared to hard X-rays [1].

In normal operation, bunches of high energy electrons of about 1.2 GeV produced by accelerators are injected into an electron storage ring. Gas bremsstrahlung is then generated by interactions of the circulating electrons with the atoms of residual gas in the vacuum chamber of the storage ring. The emitted photons with sufficiently high energies can further produce secondary gamma ray and neutrons by means of photonuclear interactions [2]-[3]. In addition, scattering of these primary photon will interact with the beamline components causing radiation around beamlines and end-stations [5]-[7]. Thus, the radiation monitoring system is highly required and has to be considered for the operation of synchrotron facilities.

There are several techniques available for the measurement of environmental radiation in synchrotron facilities. The active monitoring devices, such as electronic pocket dosimeter and portable gamma spectrometry system, provide new approaches to continuous dose rate measurement [8]. The ionization chambers are typically used to monitor gamma radiation based on its radiation energy [2], [8]. Boron Trifluoride (BF_3) or Helium-3 proportional counters with moderator are used for neutron radiation monitoring [8]. The aim of this work is to estimate the environmental radiation level inside the SLRI experimental hall. The outcome of radiation monitoring will help us to assess the radiation exposed to radiation workers and users while maintaining radiation dose as low as reasonably achievable (ALARA).

Siam Photon Source

At the Siam Photon Source (SPS), the high energy electrons of 1.2 GeV is circulated in the storage ring producing the synchrotron radiation. The maximum current of stored electrons is 150 mA [9]. Three insertion devices are installed in the ring, i.e. an undulator, a 2.4 Tesla multipole wiggler, a 6.5 Tesla super conducting wavelength shifter in order to produce more focused, highly brilliant and intense beam [9]. The SPS storage ring specification is shown in Table 1.

Table 1: SPS storage ring specification

Parameter	Value
Energy	1.2 GeV
Stored current	150 mA
Emittance	41 nm-rad
Lifetime@100 mA	12 hours
Circumference	81.3 m
Injection energy	1.2 GeV

Instruments

In experimental hall of the SPL, the gamma and neutron radiation are monitored through the gamma and neutron detector. The technical specifications for gamma and neutron detectors are given in Table 2.

Table 2: Gamma and neutron detector specifications

	FHT192	FHT 762 Wendi-2
Particle	Photons	Neutrons
Energy range	30 KeV to 7 MeV	Thermal to 5 GeV
Measuring range	100 nSv/h to 1 Sv/h	1 nSv/h to 100 mSv/h
Unit measure	Hp (10)	Hp (10)
Type	Ionization Chamber	Proportional counter
Dead Time	For high dose rate: 6-7 µs	1.8 µs

Three sets of ionization chamber for gamma ray and helium-3 neutron counter are located in the experimental hall nearby the injection area and insertion devices (BL1, BL6) and in the control room II. The area monitor is shown in Figure 1. The ionization chambers detector model FHT 192-10 was used to monitor the gamma dose rate covering energy range from 30 keV to 7 MeV. The principle of ionization chamber is that the ionizing radiation from the source (X- or gamma ray) creates an ionization of the gas atoms. The applied voltage between the anode and cathode causes the negative charges (electrons)are attracted by the anode while the positive charges(ions) by the cathode. An ionizing current is then established which is proportional to the activity of the radiation source.

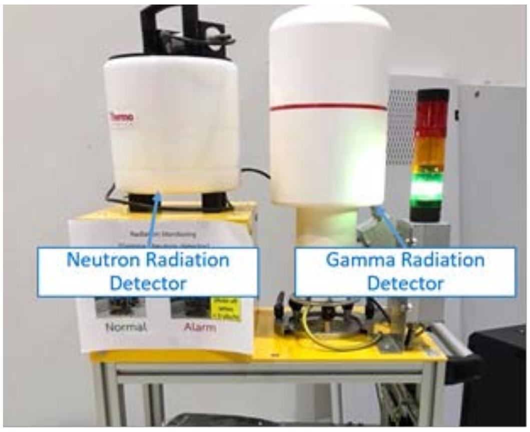

Figure 1: The radiation area monitor

Dose rate

Typically, the radiation dose rate is measured in terms of dose per unit time, micro Sieverts per hour (μSvh^{-1}). A preliminary study on the measurement of gamma and neutron dose rate in the SLRI experimental hall was performed using real-time mode. The radiation dose rate was collected 24 hours/day. Figure 2 shows the radiation dose rate during the service time. The pink line indicates the real-time dose rate, while the green line indicates the 4-hour accumulative dose rate. Fluctuation in the dose rate comes from the injection period.

The radiation dose rate ($\dot{D}$) in μSV/h can be calculated using the following equation:

$$\dot{D} = \frac{\dot{\varphi}A(-\frac{dE}{dx})\Delta x}{\rho A\Delta x} = \dot{\varphi}(-\frac{dE}{\rho dx}) \qquad (1),$$

where$\dot{\varphi}$ is fluence rate (cm^2/s),ρ is density (g/cm^3) and A is area (cm^2).

According to ALARA principle, the dose rate for radiation worker shall not exceed 20 mSv/y or 5 μSv/h based on 2,000 working hours (50 weeks/year x 5 days/week x 8 hours/day). The data (dose rate) from the area monitoring system were collected every second. Therefore, in case of the dose rate is exceed 5 μSv/h, the system will send an alarm for evacuation following SLRI safety regulation.

RESULTS AND DISCUSSION

The radiation dose rate for gamma and neutron at three different locations over the period of 18 days is shown in Figure 3 and 4. The gamma dose rate during the machine study and the normal operation at BL1 are 0.373 μSv/h and 0.198 μSv/h, at BL6 are 0.378 μSv/h and 0.328 μSv/h and at control room II are 0.419 and 0.198 μSv/h (Figure 3). It is clear that during the machine study period, gamma dose rate at each location is fluctuated depending on what machine study is performed. During the normal operation, gamma dose rate at BL6 was the highest due to the reason mentioned above, especially during the injection time. BL6 is also located near the superconducting wavelength shifter in the storage ring which releases some extra gamma ray during the normal operation.

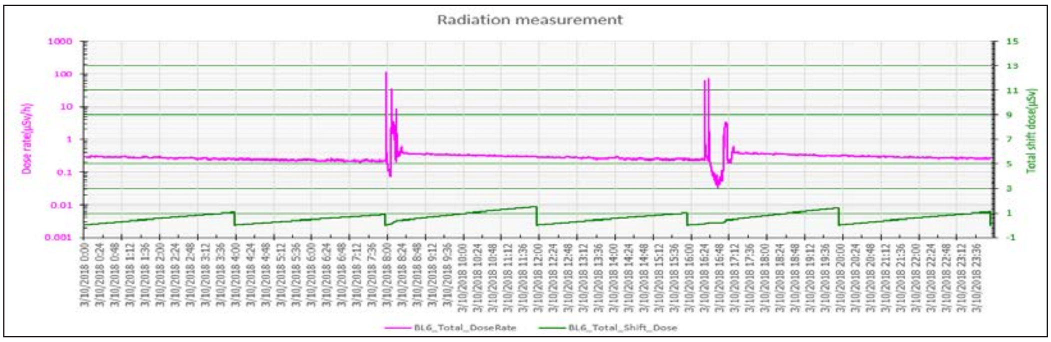

Figure 2: Total dose rate and total shift dose rate from radiation area monitor

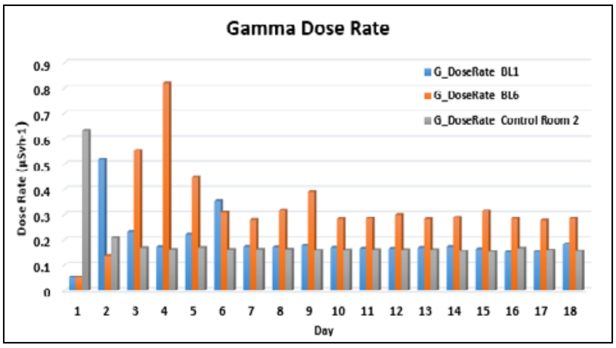

Figure 3: Gamma dose rate measured using ionization chamber.

Neutron dose rate measurement during the machine study and normal operation gives similar results as for gamma dose rate (see Figure 4). During the machine study and normal operation, the neutron dose rate at BL1 are 0.365 µSv/h and 0.104 µSv/h, at BL6 are 0.282 µSv/h and 0.162 µSv/h, while at control room II are 0.235 µSv/h and 0.049 µSv/h.

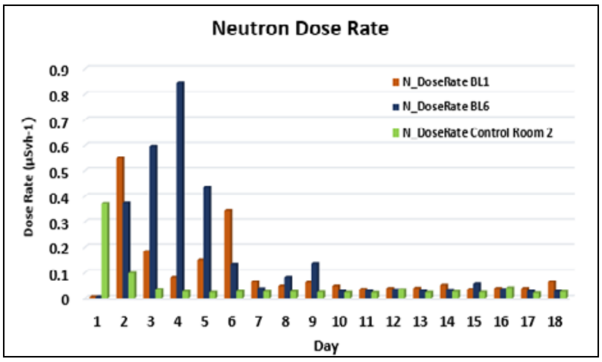

Figure 4: Neutron dose rate measured using He-3 proportional counter.

When considering the total radiation dose rate of gamma and neutron during the machine study and normal operation for this period of study, it is highest at BL6 which are 0.660 µSv/h and 0.311 µSv/h, respectively, due to the abovementioned reason. However, according to the ALARA principle, these numbers are still lower than 5 µSv/h. Therefore, for both machine study and normal operation, it is considered to be safe for radiation workers. However, during the machine study, they are recommended to be not present in the experimental hall.

SUMMARY

The environmental radiation monitoring system has been set up at SLRI to monitor the radiation dose rate at three different major locations. It has been used to study the dose rate for gamma and neutron during the machine study and the normal operation. It has been found that total radiation dose rate for these periods are lower than the safety level for radiation workers. In the near future, for safety reason, more area monitors will be added to increase capability of monitoring radiation dose rate.

ACKNOWLEDGEMENTS

The authors would like to acknowledge the members of Source Utility Maintenance and Operation (SUMO) for data supporting and Dr.Pattanaphong Junphuang for reviewing this work.

REFERENCES

[1] Odenwald, S., & Geyer, A. (2011, July). Mathematical problems featuring radiation effects applications. Link:https://www.nasa.gov/sites/default/files/files/radiation_math.pdf

[2] Ichiki, H., Kawaguchi, T., Ishibashi, K., Ikeda, N., Korenaga, K., & Utsunomiya, Y. (2009). Radiation Monitoring in a Synchrotron Light Source Facility Using Magnetically Levitated Electrode Ionization Chambers. Journal of Nuclear Science and Technology,46(12),1113-1119.Doi:10.3327/jnst.46.1113

[3] ASANO, Y. (2001, March). A Study on Radiation Shielding and Safety Analysis for a Synchrotron Radiation Beamline. Link:http://www.iaea.org/inis/collection/NCLCollectionStore/_Public/32/042/32042690.pdf

[4] MAKOWSKI, C. (2006). Department of Microelectronics and Computer Science. Link: http://jrasrf.desy.de/e86/e575/e605/infoboxContent608/care-thesis-06-004.pdf

[5] LEE, W., POPESCU, R., XIA, Z., EHRLICH, S., & JOB, P. (n.d.). Guidelines for Beamline Radiation Shielding Design at the National Synchrotron Light Source II. Link:https://www.bnl.gov/nsls2/project/reviews/170208_FDR_BMM/files/NSLSII_RelatedDocuments/ShieldingGuidelinesDoc.pdf.

[6] Chouksey, S. (2012). Development of beamline radiation shielding hutch for Indus-2 synchrotron radiation source. Indian Journal of Pure and Applied Physics, 50(11), 782-784.

[7] Birkel, I. (2009). Measurement of Gamma and Neutron Dose from the Operation of the ANKA Storage Ring. Nuclear Technology, 168(1), pp.139-143.

[8] S ez-Vergara, J. (2000). Recent Developments of Passive and Active Detectors used in the Monitoring of External Environmental Radiation. Radiation Protection Dosimetry, 92(1), pp.83-88.

[9] Synchrotron Light Resource Institute. (n.d). Link: http://www.slri.or.th/slri/files/emedia/brochure/2017-10-24 3:24]SLRI_Brochure_English_New.pdf

[10] McGarry, A. (n.d.). Dose Constraints in Occupational Radiation Protection: Regulations and Practices. Link: http://www.icrp.org/docs/Anne McGarry Dose Constraints in Occupational.pdf

CONTACT

*P.Aim-O, Tel: +66-44217040ext1156; pawitra@slri.or.th.

TEN-YEAR SUMMARY OF SLRI

FACILITY DEVELOPMENT

Within the last ten years of the operation, many facility developments and research milestones have been achieved at the Siam Photon Laboratory (SPL). From two beamlines (X-ray Absorption Spectroscopy and X-ray Photolithography) in 2009 to now ten beamlines being fully in-operations, serving more than 300 research projects and 600 users per year. 2011 was one of SLRI's most productive years when Photoemission Spectroscopy, Photoemission Microscopy, Time-Resolved X-ray Absorption, Small-Angle X-ray Scattering, and Micro X-ray Fluorescence beamlines started their user-service operations. SUT-Nanotec-SLRI beamline which was a result from a successful collaboration between SLRI and two other major Thai research entities - National Nanotechnology Center and Suranaree University of Technology - was opened next in 2012. Macromolecule X-ray Crystallography beamline, the first one which utilizes high energy X-ray produced from a superconducting wavelength shifter in SPL, was then opened in 2014 for the protein research community. This was followed by an Infrared Micro-Spectroscopy beamline to serve the vast agricultural and food research communities from both academia and industrial sectors in 2015. Multi-X-ray Technique beamline was opened next by another collaboration of SLRI with Khon Kaen University in 2016 and the currently newest X-ray Tomographic Microscopy beamline was later opened in 2018. ASEAN beamline is currently being constructed and will help to promote the utilization of synchrotron for research in Southeast ASEAN countries.

10th year
SYNCHROTRON
THAILAND
CENTRAL LAB

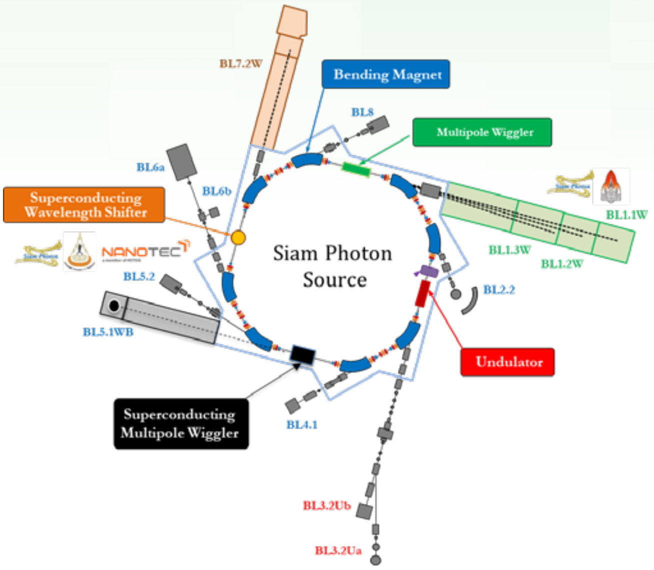

RESEARCH ACTIVITIES

PROMOTING PERMEABILITY-SELECTIVITY ANTI-TRADE-OFF BEHAVIOR IN DEHYDRATION NANOCOMPOSITE MEMBRANES DEVELOPED FROM POLYVINYL ALCOHOL INCORPORATED WITH POLY (2-HYDROXYETHYL METHACRYLATE)-GRAFTED SILICA NANOSPHERES (PVA/PHEMA-GRAFTED SNSS)

*S. Khoonsap [1], S. Rugmai [2], W-S. Hung [3], K-R. Lee [3], S. Klinsrisuk [4] and S. Amnuaypanich [1,4]**
[1]Applied Chemistry Division, Department of Chemistry and Center of Excellence for Innovation in Chemistry (PERCH-CIC), Faculty of Science, Khon Kaen University, Khon Kaen 40002, Thailand
[2] Synchrotron Light Research Institute (Public Organization) 111 University Avenue, Muang District, Nakhon Ratchasima 30000, Thailand
[3] R&D Center for Membrane Technology, Department of Chemical Engineering, Chung Yuan Christian University, Chung-Li 32023, Taiwan
[4] Materials Chemistry Research Center (MCRC-KKU), Faculty of Science, Khon Kaen University, Khon Kaen 40002, Thailand

ABSTRACT

The polymer nanocomposite membranes prepared from polyvinyl alcohol incorporated with poly (2-hydroxyethyl methacrylate) - grafted SiO_2. The pervaporation dehydration of acetone - water solution, increasing of the grafted-PHEMA amount promoted extensively the anti-trade-off behavior as raising temperature. This is because the grafted-PHEMA on SNSs significantly enhanced the water permeability while efficiently limited the permeability of acetone. The characterization of the membrane free volume obtained from PALS suggests clearly that the promoted anti-trade-off behavior in PVA/PHEMA-grafted SNSs nanocomposite membranes were achieved due to a combined effect from the size-selective free volume that provides a molecular sieving for water molecules and the number of corresponding free volume which offers an availability of water-specific transport channels.

INTRODUCTION

Membranes have gained a lot of interests in the separation technology owing to their applicability to separate vast variety of soluble mixtures including the azeotropic, close-boiling point and heat-sensitive mixtures Technically, a separation of binary mixtures by the membranes depends upon the differences in the permeability (*P*) of each component mixture through the membrane which, according to the solution-diffusion model, is a product of the solubility (*S*) and the diffusivity (*D*) [1]. Therefore, the key parameters in affecting the separation performance of membranes are the permeability and a ratio of the permeability of more permeable specie to that of a less permeable one, referred as the selectivity. It is expected that the properties of the membrane materials intrinsically play a pivotal role toward achieving high permeability of the desired specie.

Trade-off between the permeability and the selectivity in the polymer-based membranes is an inherent disadvantage leading to a compromise on the separation performance. The pervaporation, the trade-off in polymer-based membranes is expectedly inevitable. To resolve the trade- off in polymer membranes, inorganic fillers, e.g., zeolites or silica nanoparticles are incorporated with polymer matrix. Inorganic particles incorporated into PVA membranes can serve not only as the cross linker to counter the water swelling but also the molecular sieving to enhance the permeability and selectivity of water. For the nanocomposite membranes, a presence of nano-size particles in polymer matrix alters the free volume hole size as well as the hole size distribution of the membranes consequently both of the permeability and selectivity of water will be improved. As shown experimentally, the anti-trade-off behavior in PVA nanocomposite membranes was promoted as the number of specific molecular sieve (particle loading) increased however the situation can turn into a regular trade-off as the polymeric chains became highly flexible under the elevated temperature and high-water content of feed solution

EXPERIMENTAL

Synthesis of silica Nano spheres (SNSs) and grafting of PHEMA on SNSs

SNSs were synthesized in cyclohexane (ChX)-water biphasic system using amino acid (l-arginine) as weak basic catalyst [2]. PHEMA was grafted on SNSs by the sequential UV-induced graft polymerization [3].

Preparation of PVA membrane filled with PHEMA-grafted SNSs

PVA solution with concentration of 10 wt.% was prepared by dissolving dry PVA powder in DI water at 90 °C under vigorous stirring by a mechanical stirrer. Then a determined amount of PHEMA-grafted SNSs was dispersed in PVA solution and the dispersion was stirred mechanically at 90 °C for another 3 h. To prepare the membrane, PVA/PHEMA-grafted SNSs dispersion was cast on the polyacrylonitrile (PAN) substrate using the casting knife. The cast membrane was then dried at 70 °C in an oven for 2 h. The membranes were prepared at 10 wt.% particle loading using PHEMA-grafted SNSs with different %G of PHEMA grafting.

Characterization

SNSs and PHEMA-grafted SNSs particles were observed through TEM technique. Mechanical and thermal properties were investigated by dynamic mechanical analyzer (DMA) Free volume characteristics of the nanocomposite membranes were studied by Positron Annihilation Lifetime Spectroscopy (PALS) The water sorption selectivity of membranes was determined by HPLC technique and Permeability's of water and acetone through the membrane were investigated by the pervaporation process, the condensed permeate was weighted and analyzed by gas chromatography (GC).

RESULTS AND DISCUSSION

TEM of SNSs and PHEMA-grafted SNSs

As clearly seen, SNSs (Figure 1a) synthesized in the biphasic system were nano-sized spheres and highly uniform. After grafting with PHEMA, both 24G-SNSs (Figure 1b) and 93G-SNSs (Figure1c) remained in discrete spherical particles without apparent aggregates suggesting that PHEMA was evenly grafted on SNSs particle surface. Particle size distributions obtained from TEM images are presented in Figure1d which shows narrow distributions for SNSs as well as PHEMA-grafted SNSs.

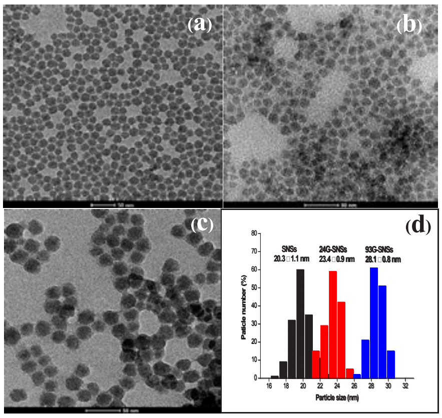

Figure 1: TEM images of (a) SNSs, (b) 24G-SNSs, (c) 93G-SNSs, and (d) particle size distributions obtained from TEM images of particles in (a) to (c).

Dynamic Mechanical Properties of Nanocomposite Membranes

Figure 2 present the results obtained from DMA in terms of the storage moduli (E'). E' of the membranes were relatively large under the glassy state and suddenly declined in the rubbery state. Evidently, inclusion of SNSs caused an improvement of E' in PVA/SNSs membrane compared with unfilled PVA membrane because of the efficient stress transfer arising from a well dispersion of SNSs in PVA matrix. Significant enhancement of E' was progressively increased as increasing amount of the grafted-PHEMA.

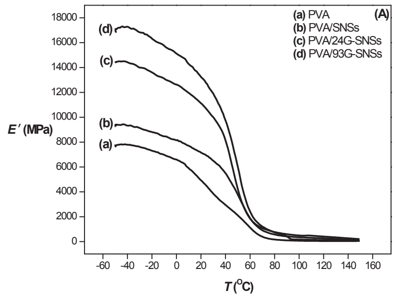

Figure 2: DMA results of the nanocomposite membranes

Water Uptake (W_W) vs. Water Sorption Selectivity (α_s)

A comparison of α_s among different membranes is shown in Figure 3. As can be seen, α_s of all membranes was much larger than unity suggesting preferential sorption of water to acetone by the membranes. Interestingly, unfilled PVA membrane α_s increased at temperatures from 10-30 °C then became declining for temperatures beyond 30 °C In comparison with PVA/SNSs membrane, α_s was profoundly improved for PVA/24G-SNSs and was further enhanced in PVA/93G-SNSs. The cause of unique temperature responding of α_s in PHEMA-grafted SNSs filled membranes is revealed in Figure 4. W_W was monotonically increasing as raising temperature from 10 to 30 °C, W_A was indifferent to a temperature change under the same temperature range before started to increase for temperature > 30 °C. Considering α_s and W_W at the temperature range 10 - 30 °C, the anti-trade-off phenomenon was clearly evidenced particularly for PVA/24G-SNSs and PVA/93G-SNSs membranes where α_s and W_W concomitantly increased with temperature. As raising the temperature above 30 °C, α_s started to decline while W_W maintained its increase thus a regular trade-off behavior took over. Undoubtedly, the grafted-PHEMA on SNSs played an important part in promoting the anti-trade-off behavior by enhancing the water uptake and at the same time limiting the uptake of acetone.

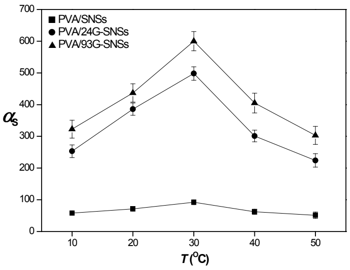

Figure 3: Effect of temperature on the water sorption selectivity (α_s) of the nanocomposite membranes; 90 mol% acetone in aqueous solution as the immersion liquid.

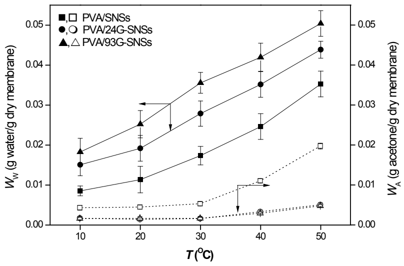

Figure 4: Effect of temperature on water (W_W) and acetone uptakes(W_A) of nanocomposite membranes; 90 mol%acetone in aqueous solution as the immersion liquid.

Water Permeability (P_W) vs. Water Selectivity (α_p)

The permeabilities of PVA/SNSs, PVA/24G-SNSs and PVA/93G-SNSs membranes as shown in Figure 5, α_p of all membranes increased with temperature from 10 °C and reached the maximum at 30 °C before declined at higher temperatures. Noticeably, a temperature dependence of α_p resembled to that of α_s. The grafted-PHEMA on SNSs largely influences the enhancement of α_p as evidenced in PVA/24G-SNSs and PVA/93G-SNSs membranes. A variation of α_p with temperature is directly related to a temperature dependence of P_W and P_A. As presented in Figure 6, for temperature < 30 °C, P_W of the membranes increased with temperature however P_A responded oppositely. For temperature > 30 °C, P_W of the membranes continued to increase and slightly declined as approaching the highest operating temperature while P_A immediately became increasing with temperature. Similar to the sorption behavior, two distinct phenomena are observed, i.e., the anti-trade-off at temperature from 10 to 30 °C where α_p and P_W were concurrently increasing with temperature and a regular trade-off at temperature from 30 to 50 °C where P_W increased with a sacrifice of α_p. As can be seen, the anti-trade-off phenomena was promoted extensively in PVA/24G-SNSs and PVA/93G-SNSs membranes which is obviously resulting from the alteration of the membrane structure owing to the presence of the grafted-PHEMA.

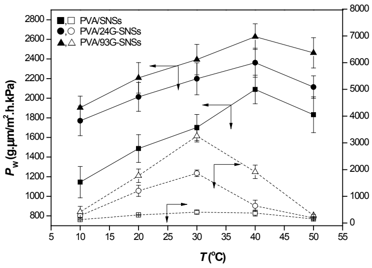

Figure 5: Effect of temperature on water permeability (P_W) and water selectivity (α) of the nanocomposite membranes; 90 mol% acetone in aqueous solution as the feed liquid.

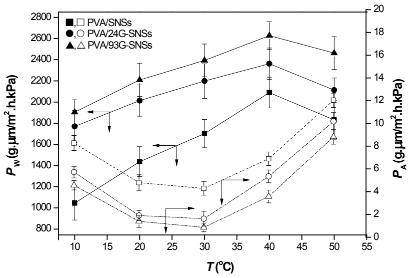

Figure 6: Effect of temperature on water permeability (P_W) and acetone permeability (P_A) of the nanocomposite membranes; 90 mol% acetone in aqueous solution as the feed liquid.

Free Volume Size and Number of Free Volume

As clearly evidenced by the sorption and the pervaporation results, the anti-trade-off behavior of PVA nanocomposite membranes existed under the glassy state. Using PALS technique, the free volume of the nanocomposite membranes can be directly probed as presented in Figure 7 and 8 which report o-Ps lifetime (τ_3) and its relative intensity (I_3) at different temperatures. τ_3 allows the determination of a mean free-volume radius (R_3) and its volume (V_f), while I_3 suggests a relative abundance of the free volume with a mean radius of R_3. Roughly speaking, τ_3 justifies the permissible penetrant size for permeating through the membrane and I_3 indicates the number of such permeating pathways.

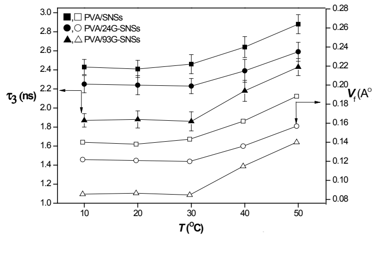

Figure 7: o-Ps lifetime (τ_3) and a volume of free volume (V_f) of the nanocomposite membranes at different temperatures.

Considering τ_3 in Figure 7, τ_3 were relatively constant but for temperatures above 30 °C, it abruptly turned to increasing with temperature. The temperature at the inflection point is in many cases adopted as the glass transition temperature (T_g). For $T < T_g$, V_f of the nanocomposite membranes were constant regardless of temperature raising due to limited mobility of most polymeric chains under the glassy state. In contrast, V_f of the membranes at $T > T_g$ increased monotonically with temperature because polymeric chains are highly mobile under the rubbery state. The grafting of PHEMA on SNSs had a drastic effect in decreasing of V_f both under glassy and rubbery states of the membranes. Generally, for the nanocomposite membranes, nanoparticles are introduced into polymer matrix aiming to disrupt the polymeric chain packing in order to expand the free volume as well as to create additional permeating channels. As demonstrated by DMA result for PVA/PHEMA-grafted SNSs membranes, there existed the region beyond SNSs particle surface where the grafted-PHEMA interpenetrated into the surrounding PVA. Therefore, in this interpenetrating area, the interactions between the grafted-PHEMA and PVA chains can cause a shrinking of the free volume size.

Further analysis of the free volume size was made in term of the τ_3 distributions under different temperatures as presented in Figure 8. Likewise for all membranes, there is the distinctive difference in τ_3 distributions between the membranes under the glassy and rubbery states. τ_3 distributions of the glassy-state membranes were noticeably narrow with a full width at half maximum (FWHM) was in the range of 0.5-0.6 nm; and as increasing temperature, the peak intensity increased. For the rubbery-state membranes, τ_3 possessed broader distributions with FWHM increased to 0.7-1.0 nm and τ_3 distributions had lower intensity as temperature increased. When comparing R_3 of the glassy-state membranes with the kinetic radii of water and acetone molecules which are 0.148 nm and 0.234 nm [4], respectively; it is conceivable that both transports of water and acetone molecules through the glassy PVA/SNSs membrane are unobstructed due to a larger size of free volume. As increasing PHEMA grafting amount on SNSs, acetone molecules, while penetrating through the membrane, increasingly experience a resistance imposing by a size of free volume which is comparable to the acetone's kinetic diameter. However, for water molecules, the resistance is negligible due to a smaller kinetic size of water molecules compared with the size of the free volume. Apparently, the contracted free volume induced by the grafted-PHEMA caused the decreases in the acetone uptake and the acetone permeability in PVA/24G-SNS and PVA/93G-SNSs membranes.

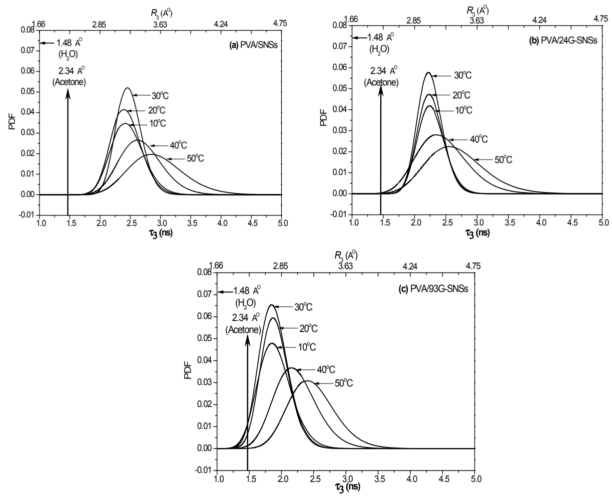

Figure 8: Distributions of τ_3 and free volume radius (R_3) at different temperatures of the nanocomposite membranes.

CONCLUSIONS

The nanocomposite membranes were prepared from PVA filled with PHEMA-grafted SNSs. The tanδ peak temperatures of the membranes suggest the difference regions surrounded SNSs particles depending upon the amount of PHEMA grafting namely the constrained PVA chains in unmodified SNSs, the PVA/grafted-PHEMA interpenetrating region in 24G-SNSs and 93G-SNSs, and the non-penetrating grafted-PHEMA region in 93G-SNSs. The sorption and the pervaporation of water-acetone mixture were performed with the nanocomposite membranes which revealed unique anti-trade-off behaviors for the membranes under the glassy state. The anti-trade-off behavior in the glassy PVA/PHEMA-grafted SNSs membranes was promoted with increasing temperature and the grafting amount of PHEMA however the regular trade-off resumed after the membranes entering the rubbery zone. The free volume characteristic analyzed by PALS indicating that the promoted anti-trade-off behaviors in PVA/24G-SNSs and PVA/93G-SNSs membranes arises from a combined effect of the water-specific free volumes and their increasing number.

ACKNOWLEDGEMENTS

This project is supported by Thailand Research Fund (TRF), Synchrotron Light Research Institute (SLRI) and Khon Kaen University under TRF research scholar program (Grant no. RSA5980075). The partial supports from PERCH-CIC and National Research University Project of Thailand, Office of the Higher Education Commission through Biofuel Cluster of Khon Kaen University are acknowledged (Grant no. NRU59007). S. Khoonsap acknowledges the scholarships from Synchrotron Light Research Institute (SLRI), Thailand (Contract no. 2553/06 GS-53-D01) and the research assistantship from MCRC-KKU.

REFERENCES

[1] J.G. Wijmans, *et al.,* The solution-diffusion model: a review, *J. Membr. Sci.*, 1995, 107, 1-21.

[2] K.D. Hartlen, *et al.,* Facile preparation of highly monodisperse small silica spheres (15 to > 200 nm) suitable for colloidal templating and formation of ordered arrays, *Langmuir.,* 2008, 24, 1714-1720.

[3] S. Khoonsap, *et al.,* Enhancing the grafting of poly(2-hydroxyethyl methacrylate) on silica nanoparticles (SiO_2-*g*-PHEMA) by the sequential UV-induced graft polymerization with a multiple-UV irradiation, *Adv. Powder. Technol.*, 2014, 25, 1304-1310.

[4] T.C. Bowen, *et al.,* Fundamentals and applications of pervaporation through zeolite membranes, *J. Membr. Sci.* 2004, 24, 51-33.

CONTACT

*S. Amnuaypanich; tel:+66-43009700 Ext. 42175; asitti@kku.ac.th

S. Khoonsap; tel:+66-44217040 Ext. 1763; Khoonsap.ti@gmail.com

MAGNETIC FIELD ASSISTED GREEN AND SUSTAINABLE CO_2CONVERSION TO METHANOL OVER 10CU-10FE/ZSM-5 CATALYST

C. Srikkarin[1,2], *W. Umchoo*[1,2], *W. Donplai*[1,2], *Y. Poo-arporn*[3], *M. Charoenpanich*[1,2]
[1]KU-Green Catalysts Group, Department of Chemical Engineering, Faculty of Engineering,
Kasetsart University, 50 Ngam Wong Wan Road, Chatuchak, Bangkok 10900, Thailand
[2]Nanocatalysts and Nanomaterials for Sustainable Energy and Environment Research Network of
NANOTEC, Kasetsart University, 50 Ngam Wong Wan Road, Chatuchak, Bangkok 10900, Thailand
[3]Synchrotron Light Research Institute (Public Organization), 111 University Avenue, Muang District,
Nakhon Ratchasima 30000, Thailand

ABSTRACT

In this work, a selective methanol production via CO_2 hydrogenation was examined over Cu-Fe/ZSM-5 zeolite catalyst in a magnetic field-assisted packed-bed reactor. The CO_2 conversion and methanol selectivity were increased by factors of 1.7 and 2.24 at 220°C, respectivelyat CO_2/H_2 molar ratio of 1:3 over 10Cu-10Fe/ZSM-5 catalyst under magnetic field. It was noted that magnetic field promotes CO_2 adsorption and selective methanol production, leading to the prospectsof a green and sustainable improvement in CO_2 hydrogenation.

INTRODUCTION

The external magnetic field was applied mainly in fluidized-bed reactors to stimulate the movement of magnetic particles, avoiding particles accumulation and channeling [1,2]. However, up to present less available information on magnetic field-assisted catalytic reaction in a fixed bed reactor was reported. Among various metal catalysts, Cu and Fe loaded on ZSM-5 zeolite exhibited significant hydrogenation activityand selectively, promoting the formation of alcohols and C_{2+} hydrocarbons [3,4].

In this work, a conventional packed bed reactor was modified with external magnetic field to promote CO_2 hydrogenation reaction over 10wt.%Cu and 10wt.%Fe loaded on ZSM-5 zeolite (10Cu-10Fe/ZSM-5) catalyst. The effects of reaction temperatures and molar ratio of CO_2/H_2 on CO_2 and methanol production were examined under magnetic field (flux intensity of 27.7mT, N–S orientation) and compared to those obtained without magnetic field.

EXPERIMENTAL

Catalyst preparation

ZSM-5 zeolite was synthesized using sodium silicate solution ($Na_2Si_3O_7$:4wt.%NaOH;27wt.%SiO_2), aluminum nitrate $Al(NO_3)3{\cdot}9H_2O$:98% and tetrapropyl ammonium bromide ($C_{12}H_{28}NBr$ or TPABr:98%). Sodium silicate solution was added to the mixture of TPABr and aluminum nitrate solution, while pH of the mixture was maintained at 10.5. The mixture was kept stirring for 3h and the obtained gel was transferred to a Teflon-lined autoclave and hydrothermally heated at 240°C for 8 h. The solid product was filtered and washed, dried at 110°C for 6 h, and calcined in air at 540°C for 4h.

Then, 10wt.%copper (Cu) and 10wt.%iron (Fe) were loaded onto ZSM-5 zeolite using copper nitrate (Cu $(NO_3)_2{\cdot}3H_2O$:99.95%) and iron nitrate ($Fe(NO_3)_3{\cdot}6H_2O$:98%) as metal precursors via impregnation method. The obtained mixture was dried at 110°C for 6h and calcined in air at 540°C for 4h

Catalysts characterization

N_2 physisorption and X-ray diffraction spectroscopy (XRD) were applied to examine textural properties and crystal structures of ZSM-5 zeolite and 10Cu-10Fe/ZSM-5 zeolite. The structural morphology was analyzed by field emission scanning electron microscopy (FE-SEM) and transmission electron microscopy (TEM). Cu and Fe elements on the catalyst surface were mapped by using energy-dispersive X-ray spectroscopy (EDX). H_2 temperature programmed reduction (H_2-TPR) technique was applied to confirm the reducing temperatures of Cu and Fe catalysts and metal-support interactions.

X-ray absorption near-edge structure (XANES) measurements with time resolved X-ray absorption spectroscopy (TR-XAS) were used to examine Cu and Fe species. Magnetic properties of catalysts were analyzed by using a vibrating sample magnetometer. The desorption behavior of CO_2 over the catalyst was examined under magnetic field using CO_2 temperature programmed desorption (CO_2-TPD) technique.

CO_2 hydrogenation over 10Cu-10F/ZSM-5 zeolite catalyst in a magnetic field-assisted packed bed reactor

Prior to each experiment, 1.0g catalyst was reduced at 480°C for 3h at 1bar with H_2 flow rate of 60ml/min. Then reactant gases (CO_2 and H_2) were introduced to the catalyst bed at a gas hourly space velocity (GHSV) of 12,000$cm^3.gcat^{-1}h^{-1}$ at a total pressure of 10bar. The effects of CO_2/H_2 molar ratios (1:1–1:4) and reaction temperatures (180–260°C) on CO_2 conversion and product selectivity were investigated under the magnetic field orientation of north-to-south (N–S) direction and flux intensity at the catalyst bed of 27.7mT. Effluent gases were analyzed by using gas chromatography.

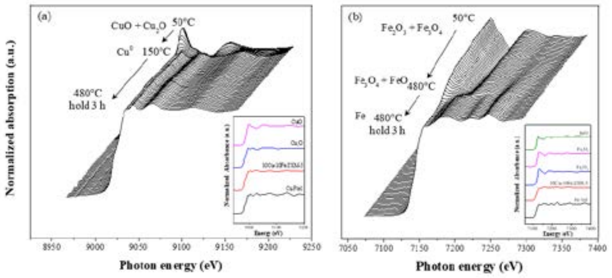

Figure 1: In situ Cu K-edge XANES spectra (a) and Fe K-edge XANES spectra (b) of 10Cu-10Fe/ZSM-5 catalyst reduction from 50°C to 480°C and 180min holding time. Inset shows the spectra of copper and iron standards.

RESULTS AND DISCUSSION

Characteristics of ZSM-5 zeolite and 10Cu-10Fe/ZSM-5 zeolite catalyst

The adsorption isotherm Type II of all catalysts and support indicated the micro pore structure. With Cu and Fe loading (10%each), the pore volume decreased approximately 58%, compared to that of ZSM-5. These metal nanoclusters could possibly penetrate in between ZSM-5 zeolite crystalline particles, leading to a formation of smaller zeolite crystals with CuO and Fe_2O_3 nano clusters finely dispersed on the surface, and partially agglomerated and blocked pores of zeolite support.

From the TPR result, oxides of copper and iron were reduced at 3 reduction temperatures; the first peak temperature at 296°C indicated the simultaneous reduction of CuO to Cu metal and Fe_2O_3 to Fe_3O_4, while the reduction peaks at 515 and 593°C confirmed the transformation of Fe_3O_4 to FeO, and FeO to Fe metal, respectively [5].

The transformation of Cu and Fe oxide species in 10Cu-10Fe/ZSM-5 zeolite catalyst was confirmed by XANES technique after in-situ reduction in the temperature range of 50–480°C with 180min holding time (*Figure 1*). CuO was completely reduced to Cu metal in the temperature range of 150–200°C. In the case of iron oxides, Fe_2O_3 and Fe_3O_4 phases were detected in the reduction temperature range of 50–340°C, while those of Fe_2O_3, Fe_3O_4 and FeO phases, and Fe and FeO phases were detected throughout the reduction temperature range of 340–480°C and at the final temperature of 480°C. These results confirmed that the activeforms of iron oxides on 10Cu-10Fe/ZSM-5 catalyst were mainly the mixed phases of Fe_3O_4 and FeO.

The magnetic properties of the reduced 10Cu-10Fe/ZSM-5 catalyst were significantly enhanced as the bimetallic Fe and Cu exhibited outstanding magnetization with superparamagnetism, whereas the unreduced catalysts were soft magnetic materials.

The CO_2-TPD analysis confirmed two CO_2 desorption peaks on bothwith and without magnetic field conditions. The positions of these desorption peaks were not significantly different, indicating that there was no change in the property of 10Cu-10Fe/ZSM-5 catalyst. However, the amount of CO_2 desorbed under the condition with a magnetic field was approximately 1.22 times lower than that without the use of magnetic field. Similar to the XANES result, the active forms of iron oxides on 10Cu-10Fe/ZSM-5 catalyst prior to CO_2 adsorption process were mainly the mixed phases of metallic Cu, Fe_3O_4 and FeO.

Effect of magnetic field on CO_2 hydrogenation over 10Cu-10Fe/ZSM-5 zeolite catalyst

As shown in Figure 2, the CO_2 conversions increased with the reaction temperature in all CO/H_2 molar ratios. This could be attributed to the fact thatCO_2 hydrogenation reaction has the endothermic nature with the external magnetic field, CO_2 conversions were increased by 1.24, 1.50, and 1.34 times for CO/H_2 molar ratios of 1:1, 1:3, and 1:4, respectively at 260°C. The highest CO_2 conversions were obtained at the molar ratio of 1:3 for all reaction temperatures. This confirmed that the application of external magnetic field help increase the activity of 10Cu-10Fe/ZSM-5 catalyst by means of the improvement of adsorption capacity of reactant molecules and surface reaction over magnetized catalyst.

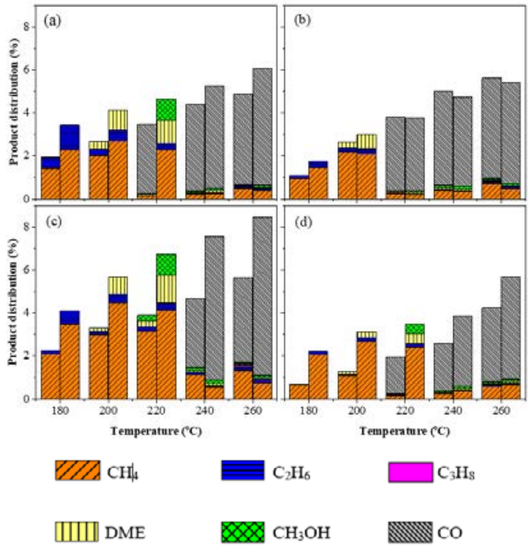

Figure 2: Product distribution from CO_2 hydrogenation over 10Cu-10Fe/ZSM-5 catalyst at C/H_2 molar ratios of (a)1:1, (b)1:2, (c)1:3 and (d)1:4 without magnetic field (first column) and with magnetic field (second column).

The main products from both with and without magnetic field were methane (CH_4), dimethyl ether (DME), methanol (CH_3OH), and carbon monoxide (CO). Considering the product distribution based on CO_2 conversion, CH_3OH selectivity significantly improved under an external magnetic field, and was the highest at CO_2/H_2 molar ratio of 1:3. Under this condition, CH_3OH yield increased by 3.9 times compared to the condition without magnetic field.

At molar ratios of 1:1 and 1:4 under the condition without a magnetic field, $CH_4C_2H_6$, and DME were selectively produced at the temperature lower 220°C. When the reaction temperature higher than 220°C, reversed water-gas shift (RWG) reaction was favored, CO was the main product [6]. When the external magnetic field was applied at 220°C, methanol was produced as the main product with 25 and 10 times higher than those without a magnetic field for CO_2/H_2 molar ratios of 1:1 and 1:4, respectively. This result evidently confirmed the advantages of the external magnetic field for methanol formation and CO retardation.

External magnetic field-induced energy conservation

By means of the energy consumption, the operating temperatures of both the reactions over 10Cu-10Fe/ZSM-5 catalyst with and without magnetic field at the same reaction ratewere compared. It was found that the reaction temperature can be reduced by 53–60°C compared to the base case without magnetic field operated at CO_2/H_2 molar ratios of 1:3. The higher temperature difference led to the higher saving cost per year and the shorter payback period.

CONCLUSION

In this work, the magnetic field-assisted packed bed reactor was applied to promotethe activity together with the selective formation of methanol in CO_2 hydrogenation over Cu-Zn/ZSM-5 catalysts. It was found that CO_2 conversion and CH_3OH selectivity were both improved by factors 1.7 and 2.24 compared to the condition without magnetic field at 220°C. The highest CH_3OH yield wasachieved at CO_2/H_2 molar ratio of 1:3 which increased by factors of 3.9 compared to the condition without a magnetic field. It is therefore noteworthy that the external magnetic field could facilitate a green and sustainable improvement in CO_2 hydrogenation.

ACKNOWLEDGEMENTS

This work was financially supported by the Center of Excellence on Petrochemical and Materials Technology (PETROMAT); the Research Network of NANOTEC (RNN), the Ministry of Science and Technology, Thailand; the Kasetsart University Research and Development Institute (KURDI) and the Thailand Research Fund (TRF) through the Institutional Research Grant (grant no. IRG5980004). The authors would like to thank the Synchrotron Light Research Institute (BL2.2: TR-XAS and BL5.3: Nanotec-XPS) for support in XAS and XPS measurements.

Note: This paper was summarized from the following paper: Catalysis Today 314 (2018)114–121.

REFERENCES

[1] A.A. Kiss et al., Novel efficient process for methanol synthesis by CO_2 hydrogenation, *Chem.Eng.J.*, 2016, 284, 260–269.

[2] M.J. Espin et al.,Effect of particle size polydispersity on the yield stress of magnetofluidized beds as depending on the magnetic field orientation,*Chem. Eng. J.*,2015, 277, 269–285.

[3] O.B. Ayodele et al., Co-synthesis of methanol and methyl formate from CO_2 hydrogenation over oxalate ligand functionalized ZSM-5 supported Cu/ZnO catalyst, *J. CO_2 Util.*,2017, 17, 273–283.

[4] M. Fujiwara, CO_2 hydrogenation for C_{2+} hydrocarbon synthesis over composite catalyst using surface modified HB zeolite,*Appl. Catal. B-Environ.*, 2015, 179, 37–43.

[5] S. Kiatphuengporn et al., Cleaner production of methanol from carbon dioxide over copper and iron supported MCM-41 catalysts using innovative integrated magnetic field-packed bed reactor, *J. Clean. Prod.*, 2017, 142, 1222–1233.

[6] C. Bonura et al., DME production by CO_2 hydrogenation: Key factors affecting the behavior of CuZnZr/ferrierite catalysts,*Catal. Today*, 2017, 281, 337–344.

CONTACT

*Metta Chareonpanich, Tel: +66-2579-2083 ; fengmtc@ku.ac.th

GREEN AND SUSTAINABLE METHANOL PRODUCTION OVER MAGNETIZED FE-CU/CORE-SHELL AND INFILTRATE MESOPOROUS SILICA-ALUMINOSILICATESVIA CO_2 HYDROGENATION

W. Umchoo[1,2], *C. Sriakkarin*[1,2], *W. Donplai*[1,2], *C. Warakulwit*[2], *Y. Poo-arporn*[3], *P. Jantaratana*[4],
T. Witoon[1,2], *M. Charoenpanich*[1,2]
[1]KU-Green Catalysts Group, Department of Chemical Engineering, Faculty of Engineering,
Kasetsart University, 50 Ngam Wong Wan Road, Chatuchak, Bangkok 10900, Thailand
[2]Nanocatalysts and Nanomaterials for Sustainable Energy and Environment Research Network of
NANOTEC, Kasetsart University, 50 Ngam Wong Wan Road, Chatuchak, Bangkok 10900, Thailand
[3]Synchrotron Light Research Institute (Public Organization), 111 University Avenue, Muang District,
Nakhon Ratchasima 30000, Thailand
[4]Department of Physics, Faculty of Science, Kasetsart University, 50 Ngam Wong Wan Road,
Chatuchak, Bangkok 10900, Thailand

ABSTRACT

In this present work, an external magnetic field has been applied to improve catalytic performance in CO_2 hydrogenation. The 10Fe-10Cu over core-shell and infiltrate mesoporous silica-aluminosilicate supports were used as the catalysts and applied under different magnetic flux intensities (0, 20.8mT, 27.7mT) and orientations (north-to-south (N–S), south-to-north (S–N) directions). At magnetic flux intensity of 27. 7mT in N-S direction and temperature of 260°C, the maximum CO_2 conversion was observed over 10Fe-10Cu/infiltrate catalyst. The highest methanol and DME space time yields were obtained at 240°C. These excellent performances could be attributed to the greater adsorption capacities of CO_2 and H_2 reactant gas molecules over the external magnetic field-induced surface-magnetized catalysts.

INTRODUCTION

Hydrogenation reaction is one of the most potential methods for eco-friendly synthesis of sustainable chemicals and fuels from CO_2 [1]. By using this method, methanol, dimethyl ether (DME), and other valuable chemical feedstock can be produced at a relatively low reaction temperature and pressure [1, 2].

In order to improve methanol and DME selectivities from CO_2 hydrogenation, an external magnetic field was applied to a conventional fixed bed reactor [3]. As iron-based catalyst is one of the most active catalysts for CO_2 hydrogenation, where the Cu-based material is a promising catalyst for methanol synthesis due to its low cost, availability, and good performance, the utilization of co-metal, Cu-Fe would therefore help increase both magnetic and catalytic properties of the modified catalyst [4].

In this research, the magnetic field conditions in terms of intensity and orientation affecting the CO_2 conversion and selectivity to methanol over 10Fe-10Cu/core shell and 10Fe-10Cu/infiltrate catalysts were examined.

EXPERIMENTAL

Synthesis of 10Fe-10Cu/core–shell and 10Fe-10Cu/infiltrate mesoporous silica–aluminosilicate catalysts

The core-shell and infiltrate mesoporous silica–aluminosilicate composite supports were synthesized following the processes reported by Chamnankid et al. [5]. Subsequently, 10wt% of Fe and Cu were loaded onto the support using iron nitrate and copper nitrate as the metal precursors. The obtained mixture was dried at 110°C for 6 h and calcined in air at 540°C for 4h.

Magnetic field-assisted CO_2 hydrogenation reaction

In this work, the magnetic field orientation N-S and S-N directions and magnetic flux intensities ±20. 8mT and ±27.7mT were applied [3]. Prior to the CO_2 hydrogenation performance test, 2.0g catalyst was reduced in H_2 atmosphere at 480°C for 3h with H_2 flow rate of 60ml/min. The operating conditions for CO_2 hydrogenation reaction were as follows: CO_2 and H_2 reactant gases ratio, 1:3; a total flow rate, 40ml/min; operating temperatures, 180-260°C; total pressure of 10bar. The reactant gases and products were analyzed by using gas chromatography.

Characterization of textural, chemical and magnetic properties of catalysts

N_2 physisorption was used to examine specific surface area, pore volume, and pore diameter of catalysts. The crystallographic structure of catalysts was examined by X-ray diffraction spectroscopy (XRD). H_2-temperature programmed reduction (H_2-TPR) was used to examine the interaction of Fe and Cu on the supports, and their reducing temperatures. In order to examine Cu and Fe species, X-ray absorption near-edge structure (XANES) measurements were performed using Time resolved X-ray absorption spectroscopy (TR-XAS). Magnetic properties of catalysts were analyzed by using a vibrating sample magnetometer. The CO_2 pulse adsorption was applied to observe the catalyst behavior under magnetic field.

RESULTS AND DISCUSSION

Performance of catalysts under magnetic field

As shown in Figure 1, the highest CO_2 conversions over 10Fe-10Cu/ core–shell and 10Fe-10Cu/infiltrate catalysts at 260°C were 8.32 and 9.10% under magnetic field of 27.7mT in4S-N and 4N-S directions, respectively. In addition, these were 1.69 and 1.91 times greater than that without magnetic field, respectively. With external magnetic field, 10Fe-10Cu/core–shell and 10Fe-10Cu/infiltrate catalysts selectively promoted methanol and DME formation due to the enrichment of magnetized active metals and CO_2 adsorption ability as well.

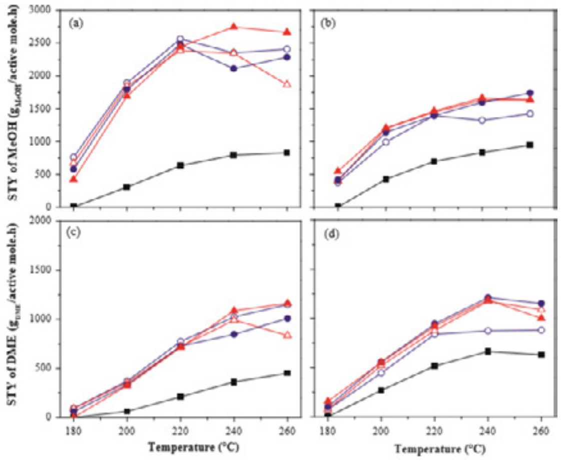

Figure 1: Catalytic performance in terms of CH_3OH and DME space time yield as a function of re action temperature for different magnetic field directions and flux densities over 10Fe-10Cu/core-shell (a and c) and 10Fe-10Cu/infiltrate catalysts (b and d) —■—w/o magnetic field, —○— 2N–S, —△— 2S-N, —●—4N–S, —▲— 4S-N.

Textural and chemical properties of 10Fe-10Cu/core-shell and 10Fe-10Cu/infiltrate catalysts

The uniform mesoporous structures as indicated by type IV isotherm with H1 hysteresis loop were observed in both catalysts [6]. The specific surface area, specific pore volume and average pore size, and metal size of mesoporous silica-aluminosilicate support and the catalysts are listed in Table1. After metal loading, the pore size of10Fe-10Cu/core-shell catalyst was almost identical to that of the support itself, while the larger pore size of 10Fe-10Cu/infiltrate catalyst was decreased due to the partially blockage of mesoporous of the support.

Table 1: Textural properties and the metal size of catalysts.
[a] Calculated from the Scherrer equation.

Catalyst	BET surface area (m^2/g)	Pore volume (cm$_3$/g)	Pore size (nm0	Fe_2O_3 size^a (nm)	CuO size^a (nm)
Core-shell	1516	1.34	2.2, 3.4	-	-
Infiltrate	1812	1.75	2.2, 3.8	-	-
10Fe-10Cu/core-shell	541	0.57	2.2, 3.4	8.9	7.7
10Fe-10Cu/ infiltrate	723	0.83	1.9,3.8	7.6	7.1

Reducibility and magnetic properties of 10Fe-10Cu/core-shell and 10Fe-10Cu/infiltrate catalysts

From H_2-TPR results, the reduction of crystalline CuO phase to Cu metallic and the reduction of Fe_2O_3 to Fe^0($Fe_2O_3 \rightarrow Fe_3O_4 \rightarrow FeO \rightarrow Fe$) were found at temperature ranges of 200–350°C and 350–800°C [7, 8]. At 480°C under H_2 atmosphere, Cu and Fe metals were obtained this result was also confirmed by XANES measurements of the catalysts (Figure 2). Both of the catalysts revealed the reduction of CuO to Cu metal in the temperature range of 150–200°C. Fe_2O_3 and Fe_3O_4 phases were detected in the reduction temperature range of 50–340°C, while those of Fe_2O_3, Fe $_3O_4$ and FeO phases, and Fe and FeO phases, were observed in the reduction temperature range of 340-480°C and also at 480°C, for holding time of 180min.

After the reduction process, the magnetic properties of the reduced 10Fe-10Cu-core-shell and 10Fe-10Cu-infiltrate catalysts were improved as the bimetallic Fe and Cu could indicate excellent magnetization with super paramagnetism, Besides, the saturation of magnetization of 10Fe-1 0 Cu/ core–shell catalyst was higher than that of 10Fe-10Cu-infiltrate catalyst since Fe and Cu atoms aggregated to form bigger cluster sizes on the outer surface of the core-shell support.

Effect of magnetic field for CO_2 and H_2 adsorption abilities

The adsorption ability of CO_2 on both catalysts decreased with increasing the reaction temperature due to exothermic nature of the adsorption process [9]. The adsorption abilities of CO_2 over 10Fe-10Cu/core–shell and 10Fe-10Cu/infiltrate catalysts increased by factors of 1.6-1.8 and 1.3-1.6 under 4S-N and 4N-S orientations, respectively. As the active metal forms of catalysts confirmed by XANES measurements were the mixed phases of metallic Cu, FeO, and Fe. These metal d orbitals could strongly interact with oxygen from CO_2 molecules and thus greatly affected the active surface of magnetized catalyst [10].

In addition, the adsorption capacities of H_2 over 10Fe-10Cu/core-shell and10Fe-10Cu/infiltrate catalysts also increased by factors of 1.1-1.7 and 1.1-1.5, compared to those without magnetic field, respectively. These stronger CO_2 and H_2 adsorptions under magnetic field therefore improve the catalyst performances and methanol and DME productions from CO_2 hydrogenation.

Energy saving under external magnetic field

From the above result, methanol production rate improved by factors of 0.66-0.99 and 0.79-0.94 with 10Fe-10Cu/core-shell and 10Fe-10Cu/infiltrate catalysts, respectively in the temperature range of 220-260°C. The highest energy consumption was 190,751kWh with 4N-S magnetic field condition over 10Fe-10Cu/infiltrate catalyst at 220°C, compared to the cases without magnetic field.

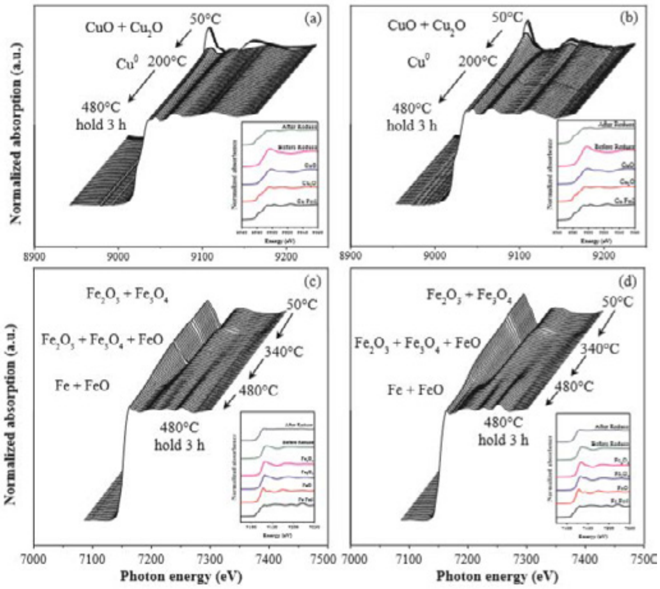

Figure 2: In situ Cu K-edge XANES spectra of (a)10Fe-10Cu/core–shell, and (b)10Fe-10Cu/infiltrate; Fe K-edge XANES spectra of (c)10Fe-10Cu/core-shell, (d)10Fe-10Cu/infiltrate catalysts reduction from 50°C to 480°C and 180min holding time. Inset shows the spectra of copper and iron standards.

CONCLUSION

Application of an external magnetic field successfully improved the catalytic selectivity of CO_2 hydrogenation to methanol and DME over 10Fe-10Cu/core–shell and 10Fe-10Cu/infiltrate catalysts. The highest CO_2 conversion under magnetic field over 10Fe-10Cu/infiltrate catalyst was 20% higher than that without magnetic field, while methanol and DME space time yields at 240°C were 1.2-1.8 and 1.3-2.0 times higher than those without magnetic field. In addition, it was found that the operating temperature has been reduced by 28–30°C (from 260°C) over 10Fe-10Cu/core–shell and 10Fe-10Cu/infiltrate catalysts at the same reaction rate.

ACKNOWLEDGEMENTS

This work was financially supported by the Center of Excellence on Petrochemical and Materials Technology (PETROMAT); the Research Network of NANOTEC (RNN0, the Ministry of Science and Technology, Thailand; the Kasetsart University Research and Development Institute (KURDI) and the Thailand Research Fund (TRF) through the Institutional Research Grant (grant no. IRG5980004). The authors would like to thank the Synchrotron Light Research Institute (BL2.2: TR-XAS and BL5.3: Nanotec-XPS) for support in XAS and XPS measurements.

Note: This paper was summarized from the following paper: Energy Conversion and Management 159 (2018)342–352.

REFERENCES

[1] S. Saeidi et al., Hydrogenation of CO_2 to value-added products-A review and potential future developments,*J CO2 Util*, 2014, 5, 66-81.

[2] A.A. Kiss et al., Novel efficient process for methanol synthesis by CO_2 hydrogenation,*Chem Eng J*, 2016, 284, 260-9.

[3] S. Kiatphuengporn et al. , Magnetic fieldenhanced catalytic CO_2 hydrogenation and selective conversion to light hydrocarbons over Fe/MCM-41 catalysts,*Chem Eng J,* 2016, 306, 866-75.

[4] S.I. Kondo et al., Magnetic analysis of a melt-spun Fe-dilute $Cu60Ag35Fe_5$ alloy,*Phys B*, 2015, 463, 108-13.

[5] B. Chamnankid et al., One-pot synthesis of core-shell silica-aluminosilicate composites:Effect of pH and chitosan addition,*Colloid Surf A Physicochem Eng Asp,* 2011, 380, 319-26.

[6] B. Li et al. , Synthesis, characterization and catalytic performance of high iron content mesoporous Fe-MCM-41, *Micropor Mesopor Mat*, 2012, 15, 277-81.

[7] W. Donphai et al. , Effect of magnetic field on CO_2 conversion over Cu-ZnO/ ZrO_2 catalyst in hydrogenation reaction,*J CO_2 Util*, 2016, 16, 204-11.

[8] S. Kiatphuengporn et al., Cleaner production of methanol from carbon dioxide over copper and iron supported MCM-41 catalysts using innovative integrated magnetic field-packed bed reactor, *J Clean Prod*, 2017, 142, 1222-33.

[9] Z Yong et al., Adsorption of carbon dioxide at high temperature-a review,*Sep Purif Technol*, 2002, 26, 195-205.

[10] P.Y. Lin et al., Effects of magnetic field on catalytic activity of CO oxidation and O_2 adsorption over Ln0.7Sr0.3MnO3, *J Phys Chem*, 1993, 97, 1471-3.

[11] B. Chen et al., High H_2 adsorption in a microporous metal-organic framework with open metal

sites,*Angew Chem,* 2005, 117, 4823-7.
[12] C. Ashman et al., Hydrogen absorption and magnetic moment of Nin clusters,*Chem Phys Lett*, 2003, 368, 257-61.

CONTACT

*Metta Chareonpanich, Tel: + 66-2579-2083; fengmtc@ku.ac.th

STUDY ON THE THERMAL STABILITY OF DIAMOND-LIKE CARBON FILMS BY NEAR-EDGE X-RAY ABSORPTION FINE STRUCTURE

N. Konkhunthot[1], P. Photongkam[2], and P. Wongpanya[1]*
[1]School of Metallurgical Engineering, Institute of Engineering,
Suranaree University of Technology, 111 University Avenue,
Muang District, Nakhon Ratchasima 30000, Thailand
[2]Synchrotron Light Research Institute (Public Organization), 111 University Avenue,
Muang District, Nakhon Ratchasima 30000, Thailand

ABSTRACT

Near-edge X-ray absorption fine structure (NEXAFS) measurement equipped with a vacuum thermal annealing were adopted to study the thermal effects on microstructure transformation of undoped and titanium-doped diamond-like carbon (Ti-doped DLC) films. The results from the C *K*-edge NEXAFS spectra of both in the undoped and Ti-doped DLC films showed not much different feature owing to the low percentage of dopant. The Ti $L_{3,2}$-edge NEXAFS spectra of the Ti-doped DLC films were found to resemble the titanium carbide (TiC) standard material. As the annealing temperature rises, the conversion of the sp^3 to sp^2 carbon-bonding in DLC structure the so-called the graphitization was considerably increased, specifically for the undoped films. In this work, we discovered a vital role in impeding the graphitization process of the TiC phase mainly formed in the Ti-doped DLC structure.

INTRODUCTION

DLC film is a metastable form of amorphous carbon material consisting of a mixture of the sp^2 bonds, sp^3 hybridization, and hydrogen depending on the deposition technique. With the excellent mechanical and chemical properties, such as high hardness and wear resistance, low coefficient of friction, and chemical inertness of DLC film, make it enable to apply in many industrial applications as protective coatings, for example, automobile and mechanical parts, cutting tools, electronic and biomedical components, etc. However, it cannot deny the deterioration of the DLC's properties when it has been used under thermal conditions for a long period of time.

NEXAFS is a powerful technique which is sensitive to local geometrical structure and bonding configuration of C atoms, therefore, it is effective for distinguishing the sp^3 and sp^2 hybridization in the DLC structure. In this study, we demonstrated a guideline for analyzing the thermal stability of the DLC film using the NEXAFS and a vacuum thermal annealing. The absolute $sp^2/(sp^3+sp^2)$ ratios acquired from the C *K*-edge NEXAFS spectra of undoped and Ti-doped DLC films will be compared between undoped and doped samples to assess the phase transformation upon the thermal annealing and discussed here.

EXPERIMENTAL

The undoped and Ti-doped DLC films were fabricated on the *p*-type (100) oriented Si substrates by an in-house pulsed two-filtered cathodic vacuum arc (FCVA) technique located at the BL3.2Ub: PEEM, Synchrotron Light Research Institute, SLRI (Public Organization), Thailand. Prior to fabrication the films, the deposition chamber was pumped to the bass pressure of 2 × 10^{-3} Pa by a turbomolecular pump backed up by a scroll pump. The Ti-doped DLC films were produced with a mixing of the Ti^+ and C^+ plasma generated from an individual cathodic arc source. NEXAFS measurement equipped with a vacuum thermal annealing operated at approximately 10^{-8} Pa were performed at BL3.2Ub: PEEM, SLRI as illustrated in Figure 1. The C K-edge and Ti $L_{3,2}$-edge NEXAFS spectra were carried out in partial electron yield mode to reveal the phase transformation of the DLC films under the thermal annealing in the range of 30-500°C. The photon energy was scanned in an energy range of 440-475 and 275-335 eV for the Ti $L_{3,2}$-edge and C *K*-edge NEXAFS spectra with a scanning step of 0.1 eV.

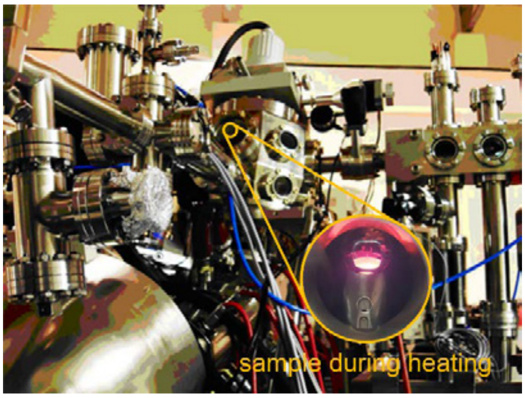

Figure 1: Photograph of the sample during heating at 500 °C along with taking NEXAFS spectrum in PEEM chamber at the BL3.2Ub: PEEM, SLRI.

RESULTS AND DISCUSSION

Local geometrical structure analysis

The microstructures of the undoped and Ti-doped DLC films after thermal annealing in the range of 30-500°C were investigated via the Ti $L_{3,2}$-edge and C *K*-edge NEXAFS spectra as shown in Figure 2 and 3. It is obvious from the Ti $L_{3,2}$-edge NEXAFS spectra that we successfully incorporated the Ti atoms into the DLC structure as confirmed by the presence of the intensity of Ti peaks in Figure 2(b) and (c).The spectral features and positions of the Ti-doped DLC films were similar to those of the titanium carbide (TiC) material standard [1–5] indicating that the Ti atoms added into the DLC films mainly bonded with the C atoms in the form of the TiC phase. The C K-edge NEXAFS spectra of the films consisted of two major regions. The pre-edge resonance located at ~285.4 eV is associated with the C $1s \rightarrow \pi$ *transition from the sp^2(C═C)sites and the sp(C≡C)sites if they present. The broad band region between 288–335 eV is attributable to the over lapping the C $1s \rightarrow \sigma$ *transition at the sp^3(C—C), sp^2(C═C), and sp(C≡C)sites.As seen in Figure 3, the similarity of the spectral features between undoped and Ti-doped DLC films could be observed as long as the percentage of the Ti atoms within the DLC structure is low.

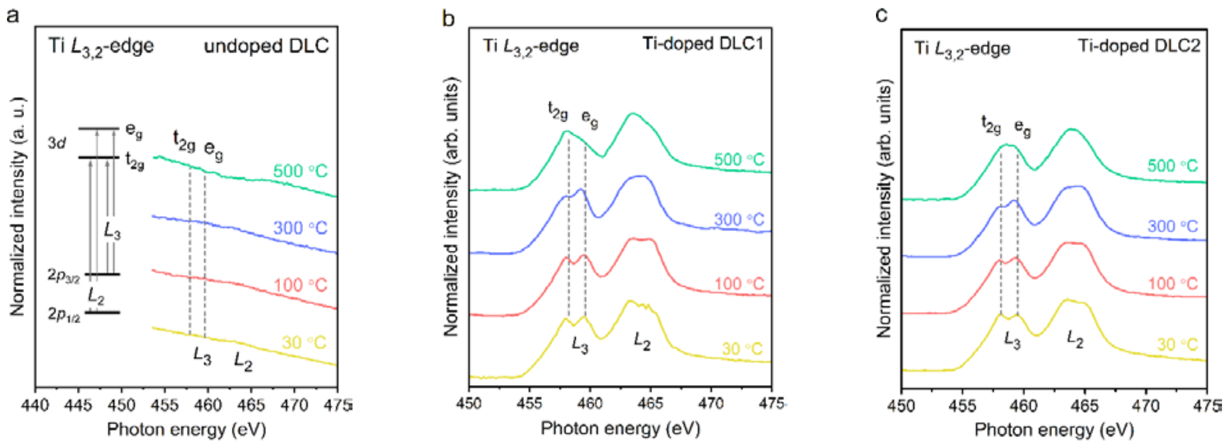

Figure2: Ti $L_{3,2}$-edge NEXAFS spectra of(a)undoped DLC, (b)Ti-doped DLC1, and (c)Ti-doped DLC2 as a function of thermal annealing temperature in the range of 30, 100, 300, and 500 °C, respectively, modified from N. Konkhunthot et al (2019)[9].

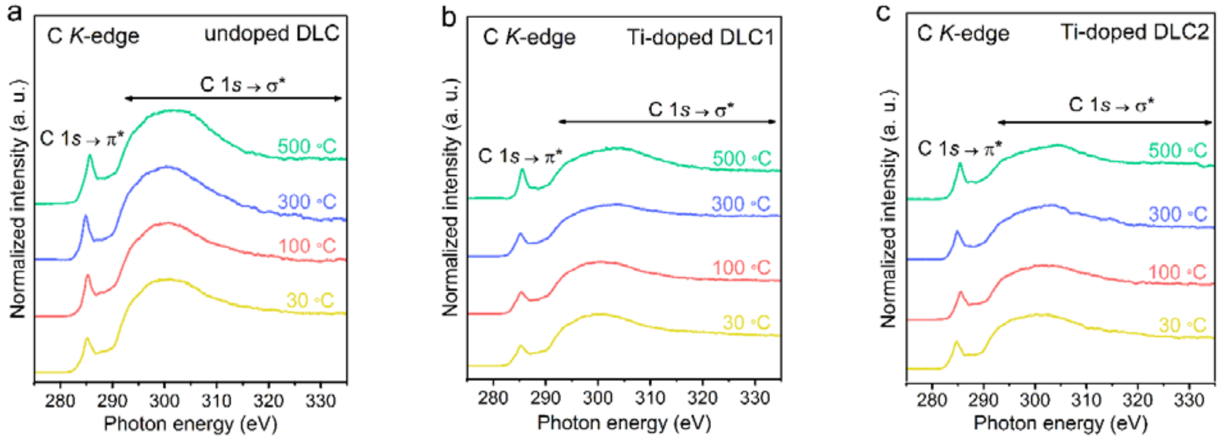

Figure 3 :C K-edge NEXAFS spectra of (a)undoped DLC, (b)Ti-doped DLC1, and (c)Ti-doped DLC2 as a function of thermal annealing temperature in the range of 30, 100, 300, and 500 °C, respectively, modified from N. Konkhunthot et al (2019) [9].

Thermal stability analysis

For quantitative analysis of the graphitization process in the DLC films, we estimated the absolute $sp^2/(sp^3+sp^2)$ ratios of the undoped and Ti-doped DLC films as a function of the annealing temperature by fitting the C K-edge. NEXAFS spectra and comparing with that of a highly oriented pyrolytic graphite (HOPG) standard as demonstrated in Figure 4. As the results, the graphitization process of all the DLC films continuously taken place as the annealing temperature increased. In this study, the Ti-doped DLC films exhibited a lower graphitization rate than the undoped DLC films when the annealing temperature is raised above 100°C. This phenomenon is contributed to the formation of the natural stability (high temperature ~600°C) of the TiC phase impeding the phase transformation [6–8].

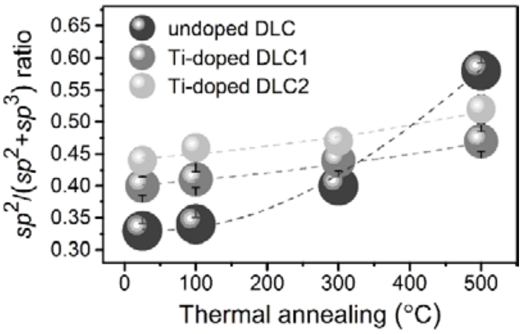

Figure 4: Thermal annealing temperature against the absolute $sp^2/(sp^2+sp^3)$ ratio of undoped DLC, Ti-doped DLC1, and Ti-doped DLC2, respectively, modified from N. Konkhunthot et al (2010) [9].

CONCLUSIONS

The Ti-doped DLC films were successfully fabricated using the simultaneous pulsed two-FCVA technique NEXAFS spectroscopy could identify the presence of the Ti atoms and distinguish the different of the carbon hybridization in the DLC structure which is a quantitative analytical technique for the amorphous carbon films .The thermal stability of the DLC films could be improved by incorporating the small concentration level of the Ti atoms which is in a form of the TiC phase.

ACKNOWLEDGEMENTS

This research is funded by the Thailand Research Fund (TRF) through The Royal Golden Jubilee (RGJ) Ph.D. Programme, Bangkok, Thailand and the Synchrotron Light Research Institute (SLRI), Nakhon Ratchasima, Thailand (Grant number :PHD/0217/2557). The assistance from the staff at the BL3.2Ub: PEEM, SLRI for NEXAFS measurement are acknowledged.

REFERENCES

[1] K .Kanda, K .Fukuda, K .Kidena, R .Imai, M .Niibe, S . Fujimoto, K .Yokota, M .Tagawa, Hyperthermal atomic oxygen beam irradiationeffect on the Ti-containing DLC film, Diam. Relat . Mater . 41 (2014) 4952. https://doi.org/10.1016/j.diamond.2013.10.006.

[2] K. N . Pandiyaraj, J . Heeg, A . Lampka, F . Junge, T . Barfels, M .Wienecke, Y.H .Rhee, H.W .Kim, In vitro cyto and blood compatibility of titanium containing diamondlike carbon prepared by hybrid sputtering method, Plasma Sci . Technol. 14 (2012)829–836, https://doi.org/10.1088/1009-0630/14/9/11.

[3] Q.Z .Wang, F .Zhou, Z.F .Zhou, Y .Yang, C .Yan, C.D . Wang, W.J .Zhang, L.K.Y .Li, I .Bello, S.T .Lee, Influence of Ti content on the structure and tribological properties of Ti-DLC coatings in water lubrication, Diam . Relat . Mater . 25 (2012)163-175, https://doi.org/10.1016/j.diamond.2012.03.005.

[4] P.V .Bharathy, D .Nataraja, P.K .Chu, H.V .Wang, Q . Yang, M.S.R.N .Kiran, J.S .Albero, D .Mangalarai, Effect of titanium incorporation on the structural, mechanical and biocompatible properties of DLC thin films prepared by reactive biased target ion beam deposition method, Appl .Surf .Sci .257 (2010)143–150, https://doi.org/10.1016/j.apsusc.2010.06.052.

[5] Y.J .Jo, T.F .Zhang, M.J .Son, K.H .Kim, Synthesis and electrochemical properties of Ti-doped DLC films by a hybrid PVD/PECVD process, Appl . Surf . Sci 433 (2018)1184-1191, https://doi.org/10.1016/j.apsusc.2017.10.151.

[6] Y.H .Lin, H.D .Lin, K.C .Liu, M.W .Huang, Y.C .Chen, J.R . Chen, H. C . Shih, Annealing effect on the structural, mechanical and electrical properties of titanium doped diamond-like carbon films, Thin Solid Films 518)2009 (1503-1507, https://doi.org/10.1016/j.tsf.2009.09.096.

[7] K. H . Er, M. G . So, Thermal annealing behavior of Si-doped diamond like-carbon films deposited by reactive sputtering, J . Ceram . Process . Res . 11 (2010)760-764.

[8] G .Ma, S .Gong, G .Lin, L .Zhang, G .Sun, A study of structure and properties of Ti doped DLC film by reactive magnetron sputtering with ion implantation, Appl . Surf . Sci . 258 (2012)3045-3050, https://doi.org/10.1016/j.apsusc.2011.11.034.

[9] N . Konkhunthot, P . Photongkam . P . Wongpanya, Improvement of thermal stability, adhesion strength and corrosion performance of diamond-like carbon films with titanium doping,Appl . Surf . Sci . 469 (2019)471-486, https://doi.org/10.1016/j.apsusc.2018.11.028.

CONTACT

*Natthaphong Konkhunthot, tel: +66-44-223000 ; natthaphong.konkhunthot@gmail.com

SLEEM: A TOOL FOR EXPLANATION DE-ALLOYING CORROSION IN MANGANESE ALUMINIUM BRONZE

P. Punburi[1]*, N. Tareelap*[1,*]*, N. Srisukhumbowornchai*[1] *and C. Euaruksaku*[2]
[1]Division of Materials Technology, School of Energy, Environment and Materials, King Mongkut's University of Technology Thonburi, 126 Pracha-Uthit Road, Thungkhru, Bangkok, 10140, Thailand
[2]Synchrotron Light Research Institute (Public Organization), 111 University Avenue, Muang District, Nakhon Ratchasima 30000, Thailand

ABSTRACT

Low energy electron emission microscopy (LEEM) was used to measure local transition energy that was directly correlated to electron work function (EWF) of multiphase manganese-aluminum bronze (MAB) alloys. The transition energy colour mapping distinguished the EWF of multiple phases and clarified that the EWF were in the following order: $EWF_\alpha > EWF_\beta > EWF_\kappa$. The result corresponded to long term corrosion immersion test that de-alloying corrosion takes place at grain boundary of β (lower EWF) phase then propagate into higher EWF α phase.

INTRODUCTION

Manganese Aluminium Bronze (MAB) has multiphase microstructure comprising α phase (Cu-FCC A1), β phase (Cu_2MnAl-FCC L21) and κ intermetallic [1]. De-alloying corrosion is a specific corrosion form that always takes place on Cu alloy because of micro-galvanic effect between α and β phases. The micro-galvanic effect is a result from the differences in chemical composition and electrochemical potential of phases in the alloy. De-alloying corrosion generally starts at the β phase then propagates to α phase. As corrosion involves electron transfer process, electron work function (EWF) can be used to predict corrosion behavior. The EWF is the energy needed to remove electrons out of the metal surface. The EWF increases with corrosion resistance increases [2]. EWF is a relative transition energy which is detected with surface characterization technique. Low energy electron emission microscopy (LEEM) is a high efficiency surface characterization technique which express the transition energy and topographic information simultaneously [3]. Transition energy analysis in this work was performed with Elmitec LEEM-III systemat Beamline 3.2Ub of the Synchrotron Light Research Institute (SLRI), Thailand. The aim of this work is using LEEM to measure local transition energy that is directly related to EWF on multiphase MAB alloy, which helps to explain the corrosion mechanism due to the difference in EWFs.

RESULT

The BSE images of MAB is presented in Figure 1(a). The dark-grey network area is the β phase while light area is a high Cu content α phase. The microstructure after immersion in 0.6M NaCl solution for 6 months is illustrated in Figure 1(b). The region that used to be the β phase now appeared brighter as a result of de-alloying corrosion and cracks are observed throughout the bright areas.

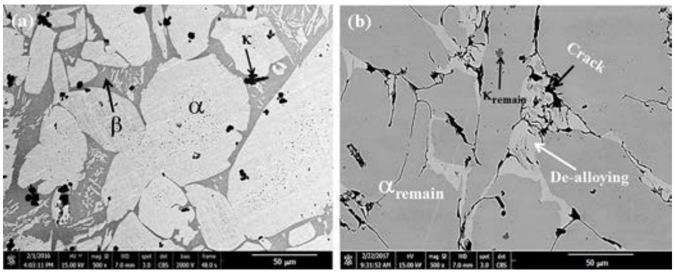

Figure 1: BSE-FESEM images showing the microstructure (a) before and (b) after immersion test in 0.6M NaCl for 6 months [5].

The chemical compositions shown in Table 1 indicates that the de-alloying area is rich with Cu while Al and Mn are decreased significantly. In contrast, the α phase does not change in both appearance and chemical composition after the immersion test. It, therefore, is called α_{remain}. The chemical composition of κ precipitate is also similar to previous because it is embedded in α phase in which indirectly exposure to solution and then, it is called κ_{remain}.

Table 1 Elemental composition analysis (wt.%) by EDX of the sample before and after immersion in 0.6M NaCl for 6 months

	Phase /area	Elemental composition (wt.%)					
		Al	Mn	Fe	Ni	Si	Cu
Before immersion	α	8.84	7.64	1.13	1.37	-	81.02
	β	14.04	10.99	1.95	5.09	-	67.50
	κ	11.29	17.17	58.51	2.88	2.13	2.03
After immersion	α remain	7.58	7.32	1.18	1.10	-	82.82
	de-alloying	0.26	0.64	0.22	0.10	-	98.78
	κ remain	4.73	28.66	57.86	0.51	4.11	4.13

The LEEM image of MAB is displayed in Figure 2(a). There is small contrast between α and β phases;

while, κ precipitate appears darkest and strong contrast against α and β phases. Figure 2(b) is transition energy colour mapping of the area shown in Figure 2(a) using a computer program to detect the LEEM intensity cut-off position at each pixel of the LEEM image stack. Figure 2(c) presents the intensity as a function of Start Voltage (SV) showing the drop at different energies for the α, β phases and κ precipitates. It can be seen that the transition energy are in the order of α>β>κ and thus, similarly, EWFs are in the order of EWF$_{\alpha}$> EWF$_{\beta}$> EWF$_{\kappa}$.

The α phase has the highest transition energy (the highest relative EWF) as shown by light blue to navy-blue in a mapping colour in the range of 1.08–1.12eV. It is because the α phase is a Cu-rich phase of which EWF higher than those of Mn, Al and Fe. The result corresponded to high electrochemical potential of copper that make Cu-rich phase is a high corrosion resistance phase. In contrast, the transition energy of the β phase is in the range of 1.04–1.08 eV and shows up mostly in green colour in the transition energy mapping. The EWF of the β phase is lower than that of the α phase because the β phase contains higher amount of Al and Mn, which have lower EWF in their pure forms [4]. This reason supportsthe observations that the β phase suffers more corrosion incomparison to the α phase. κ precipitates appear to have the lowest transition energy orthe lowest EWF (as shown in Figure 2(b) due to the enrichment of Fe and Mn. However, they were not attacked by de-alloying corrosionthe way the β phase was. This may be because of their smallsizes and the fact that they are not connected to each other to forma large network the same way as the β phase does.

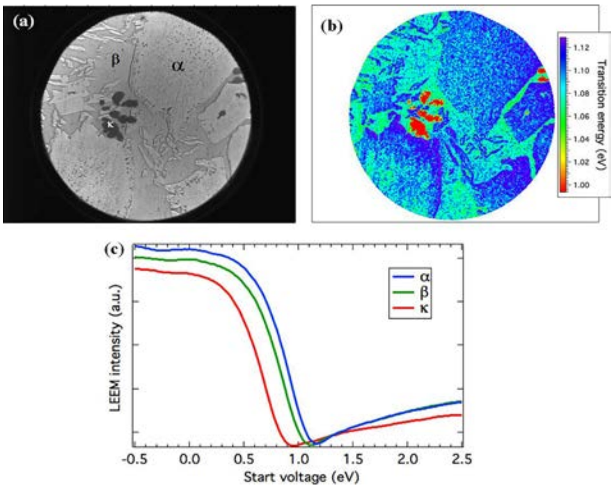

Figure 2: EWF contrast is shown by (a) LEEM image (FOV 75 m); (b) transition mapping of the area in figure (a); and (c) LEEM transition as a function of Start Voltage for α, β phases and κ precipitate [5].

CONCLUSION

EWF mapping created from mirror-mode transition in LEEM could explain corrosion behaviors of MAB cast. The de-alloying corrosion is most severe in the β phase because it has EWF around 0.06 eV lower than that of the α phase. This is because β is Al-rich and Mn-rich. As a result, the β phase releases electrons easily and therefore the corrosion process is enhanced. It is also found that the κ precipitates have the lowest EWF. However, for this case, κ is not to be an essential part of de-alloying corrosion due to its small sizeand not connected to each other. For this reason the de-alloying corrosion beginseverelyon the β phase.

ACKNOWLAGEDEMENT

The authors would like to acknowledge the Royal Thai Navy for providing materials and to thank Professor Supapan Seraphin for a fruitful discussion.

REFERENCES

[1] H. Meigh, " Cast and wrought aluminium bronzes properties, processes and structure" , *IOM Communications Ltd., London*, 2000.

[2] X. C. Huang, H. Lu, D. Y. Li. , " Understanding the corrosion behavior of isomorphous Cu–Ni alloy from its electron work function", *Mater. Chem. Phys.*, Vol. 173, 2016, pp. 238-245.

[3] N. Barrett, J. E. Rault, J. L. Wang, C. Mathieu, A. Locatelli, T. Menteş, M. Niño, S. Fusil, M. Bibes, A. Barthelemy, D. Sando, W. Ren, S. Prosandeev, L. Bellaiche, B. Vilquin, A. Petraru, I. Krug, C. Schneider" Full field electron spectromicroscopy applied to ferroelectric materials" , *J. Appl. Phys.*, Vol.113, 2013, pp. 1-15.

[4] S. Halas," 100 years of work function" , *Mater. sci. - Poland*, vol.24, 2006, pp. 951-966.

[5] P. Punburi, N. Tareelap,N. Srisukhumbowornchai, C. Euaruksakul," Correlation between electron work functions of multiphase Cu-8Mn-8Al and de-alloying corrosion" , *Applied Surface Science,* Vol. 439, 2017, pp.1040-1046.

CONTACT

*Napachat Tareelap, tel: +66-2470-8644;
napachat.tar@kmutt.ac.th

FOURIER TRANSFORM INFRARED SPECTROSCOPY DISCRIMINATES BIOMOLECULAR ALTERATION OF ISOTHIOCYANATE DERIVATIVES TREATMENT IN HEPG2 CELL LINE

P. Pocasap [1], N. Weerapreeyakul [2], K. Thumanu[3]*

[1] Research and Development of Pharmaceuticals Program, Graduate School, Faculty of Pharmaceutical Sciences, Khon Kaen University, 123 Moo 16 Mittapap Road,
Muang District, Khon Kaen 40002, Thailand
[2] Division of Pharmaceutical Chemistry, Faculty of Pharmaceutical Sciences, Khon Kaen University,
123 Moo 16 Mittapap Road, Muang District, Khon Kaen 40002, Thailand
[3] Synchrotron Light Research Institute (Public Organization), 111 University Avenue, Muang District,
Nakhon Ratchasima 30000, Thailand

ABSTRACT

The structure of the isothiocyanates (ITCs) erucin, sulforaphane, erysolin, sulforaphene, and phenethylisothiocyanate were assessed as well as their respective in vitro anticancer activity on the hepatocellular carcinoma cell line HepG2. All of these ITCs induced both apoptotic and necrotic cell death. Principal component analysis (PCA) indicated that the ITCs caused changes in cellular components comparable to vinblastine, not docetaxel. When the discriminating wavenumbers were assigned to the primary spectra, most of the wavenumbers were in the lipid and protein regions. The FTIR data suggests that the ITCs caused cellular component change in the way similar to vinblastine (microtubule depolymerizing agent) than docetaxel (microtubule polymerizing agent), and lipids/proteins are the major biological components that differ between the docetaxel treated group and the other groups. Despite no observable effect on DNA, the ITCs all induced generation of intracellular reactive oxygen species (ROS) and suppressed microtubule polymerization. The variation in sulfur oxidation states and the presence of an aromatic ring on the ITC side chain affected microtubule depolymerization and intracellular ROS generation, leading to apoptotic and necrotic cancer cell death. The summarized result is displayed in Figure 1. Knowing the influences of structural variations of the ITC side chain would be useful for selecting the more potent ITCs (i.e., erysolin) for the design and development of effective chemo preventive agents.

INTRODUCTION

Isothiocyanates (ITCs) are a group of compounds characterized by the presence of an isothiocyanate (N= C=S) moiety on the molecule. In humans, ITCs have been extensively investigated for their health-promoting benefit, especially against cancer.

The various and variable anticancer activities of ITCs have been widely reported. Some of these studies indicated that the impact of structural variations among ITC derivatives on anticancer activity could differ with the mechanism of biological activity and the cell type assessed [1-3]. Never the less, the studies on the anticancer activity of ITCs related to structural variations mainly focus on enzyme induction in phase II metabolism or relevant antioxidant mechanisms [2-4]. There are few, if any, compelling studies demonstrating the relationship between the respective ITC structures and their anticancer effects. Erysolin was more potent than erucin in induction of intracellular ROS as well as increasing cancer cell death in colon cancer cell line HCT116 [8].

In published article of this study, the effect of ITCs on biomolecular alteration were observed using FTIR spectroscopy. PCA as well as unsupervised hierarchical cluster analysis (UHCA) were used to determine the alteration amongst FTIR spectra of different ITC treatment in HepG2 to discriminate their activity in comparison with standard drugs, vinblastine and docetaxel. The impacts of structural variation on cell death inducing activity were investigated via the relationship of sulforaphane analogues with three molecular targets including DNA, reactive oxygen species (ROS), and tubulin in the hepatocellular carcinoma cell line HepG2, and were discussed elsewhere in our work [5]. The interaction of ITCs to these molecular targets could consequently lead to cancer cell death [10]. The knowledge from the study could explain the influence of structural variation of ITC derivatives on the respective chemotherapeutic action; and also provide useful information for developing more effective chemotherapeutic agents through taking advantage of structural modification.

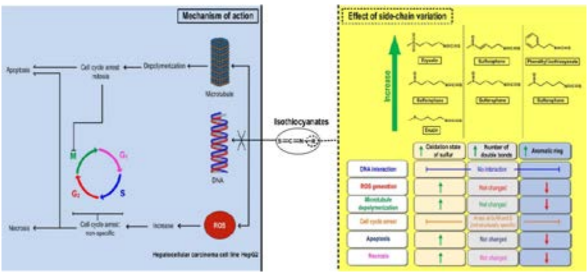

Figure 1: ITCs mechanism of action and the effectof side chain variation in HepG2 cells.

MATERIALS AND METHODS

The treated and untreated HepG2 cells were collected and prepared for spotting on a BaF_2 window as previously described [6]. The spotted cells on the BaF_2 window were analyzed in transfection mode by FTIR spectrometer Bruker Vertex 70 connected to the Bruker Hyperion 2000 microscope (Bruker optic Inc, Ettlingen, Germany), using synchrotron radiation as an IR source. The FTIR spectrometer was equipped with a potassium bromide beam splitter and a MCT (HgCdTe) detector cooled with liquid nitrogen, attached with a PIKE MIRacle (Madison, WI, USA). The scanning range was from 4000-600cm^{-1} with a spectral resolution of 4cm^{-1}. For each spectrum, 64 scans were acquired and averaged using OPUS 6.5 software (Bruker optic Inc, Ettlingen, Germany)

Principal Component Analysis (PCA) (with a spectral range of 3000-2800cm^{-1} and 1800-900cm^{-1}) were performed using Unscrambler® X software (version 10. 1, CAMO Software AS, Oslo, Norway) for identification of any significant variation between data sets. Smoothing the primary spectra were achieved using the Savitzky–Golayalgorithm (with 13 points of smoothing, minimizing the effects of variable baselines) and normalized with extended multiplicative signal correction (EMSC), which normalizes spectra, accounting for differences in sample thickness and correcting for scattering artifacts. Six principal components (PCs) were chosen for analysis. Score plots (2D) and loading plots were used to display the clustering and variations in the data set, respectively.

Unsupervised hierarchical cluster analysis (UHCA) of the FTIR spectral data sets was performed using Ward's algorithm, which utilizes a matrix defining the inter-spectral distances in order to identify the two most similar FTIR spectra.

The spectral distances between all of the remaining spectra and the new clusters were then recalculated. UHCA was performed using OPUS 6.5 software in the spectral regions from 3000-2800cm^{-1} to 1800-900cm^{-1}. The spectral regions were classified as (1) lipid region: 3000-2800cm^{-1}, (2) protein region: 1800-1480cm^{-1}, and (3) nucleic acid region: 1280-900cm^{-1} according to the biological components presented mainly in the region was initiated by adding a reaction mixture and monitored for fluorescent intensity (Ex = 360nm; Em = 420nm). Measurement was analyzed using a Varioskan Flash spectral scanning multimode reader, Thermo Scientific (San Jose, CA, USA). Readings were taken every minute for 1h for a total of 61 readings

RESULTS

Figure 2A shows the primary spectrum of HepG2 treated with sulforaphane compared with the untreated control, vinblastine, and docetaxel (80μm for 24h). The IR spectra could be divided into three main regions according to the major components represented in each region that are lipid, protein and nucleic acid region [6, 7].

PCA is multivariate data analysis technique used to identify spreading and clustering in datasets. It is also used to determine the contribution of variables in this case wavenumber) between samples, differentiating the cell groups. The PCA score plot (Figure 2B) showed that the FTIR primary spectra for all the ITCs (80μm, 24h) could be grouped in the same cluster as the FTIR spectra of the untreated cells, as well as cells treated with vinblastine but not as docetaxel PC1 (x-axis in Figure 2B) explained 91% of the total variance between the docetaxel treated group and the other groups, whereas PC2 (y-axis in Figure 2B) explained the remaining 4% of total variance. The relevant wavenumber of the PCs was then plotted in the PCA correlation loading plot (Figure 2C). The PCA correlation loading plot also indicates the cause of variation in the pattern. The variables (wavenumbers) in the radius between the ellipses are strongly responsible for discriminating the variance. Thus, the wavenumbers displayed between the two ellipses were primarily responsible for the difference between the docetaxel treated group and the other groups. When the discriminating wavenumbers were assigned to the primary spectra (Figure 2A), most of the wavenumbers were in the lipid and protein regions**.**

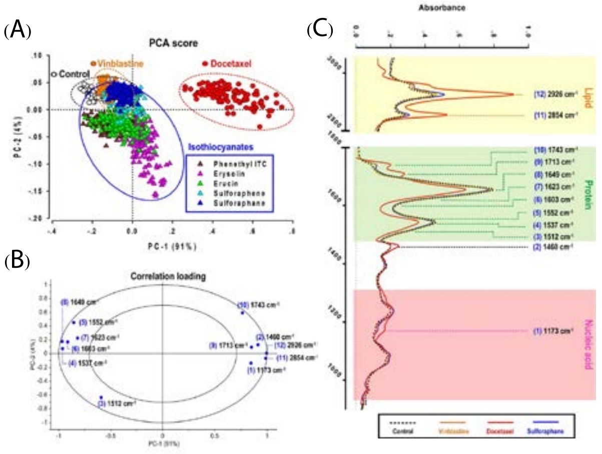

Figure 2: FTIR spectral analysis of HepG2 cells treated with ITCs vs. chemotherapeutic agents (vinblastine and docetaxel) at 80μM for 24h. PCA score plot displayed spectral clustering between control and treated HepG2 cell groups (A). PCA correlation loading plot indicates discriminating wavenumber (B). Primary FTIR spectral overlay with discriminating wavenumber from PCA correlation loading plot of sulforaphane a representative of ITCs (C).

The result suggests that lipids and proteins are the major biological components that differ between the docetaxel treated group and the other groups. In order to confirm the PCA result indicating major differences between the docetaxel treated group and the other groups in lipid and protein components. In order to confirm the PCA result indicating major differences between the docetaxel treated group and the other groups in lipid and protein components, cluster classification of the FTIR spectra based on Ward’ s algorithm was conducted on the three different regions (Figure 2D). It was evident that the spectra for the lipid and protein regions on the right branch (docetaxel) were clearly separated from the other branch (comprising the control, vinblastine, and the ITCs) with heterogeneity scores of 7.5 and 4.5 for the lipid and protein region, respectively. Cluster analysis of the nucleic acid region did not clearly differentiate the docetaxel treated group from the other groups. The right branch containing docetaxel and erucin was separated from the other branches, but the heterogeneity score was lower (1.3), reflecting a non-difference in the nucleic acid region. The result from the PCA analysis was confirmed by cluster analysis where all ITCs were grouped with vinblastine in the lipid and protein regions. Although the results from both the PCA and cluster analyses did not clearly separate the ITC treated group from the vinblastine treated group and the control group, the ITC treated group had an FTIR spectra similar to the vinblastine over against the docetaxel treated group in both the PCA and cluster analyses. The similar cell response reflected by the FTIR analysis after treatment with ITCs compared to vinblastine suggests a similar mechanism of action.

CONCLUSION

In this study, all ITC-treated cells displayed FTIR spectra similar to vinblastine compared to docetaxel as analyzed by PCA and UHCA. The result agrees with the microtubule interaction study because ITCs depolymerized microtubules as did vinblastine, while docetaxel polymerized microtubules. FTIR was demonstrated to be useful in conjunction with other techniques to detect the biological alterationof the treatment sample. In concert with the result form our study described elsewhere [5], these study demonstrated that ITCs exert anticancer activity on HepG2 cells via microtubule depolymerization and ROS generation, which resulted in cell cycle arrest and cell death by both apoptosis and necrosis. The anticancer capabilities of the ITCs were related to variations in their respective side chain. The oxidation state of the sulfur atom and presence of an aromatic ring modified the biological potency against HepG2 cells, whereas there was no effect with the presence of a double bond. Understanding the chemical basis by which ITCs induce apoptosis will be important step in the development of more effective chemotherapeutic treatment strategies using ITCs.

REFERENCES

[1] P. Gupta, B. Kim, S.-H. Kim, S.K. Srivastava, Molecular targets of isothiocyanates incancer: recent advances, Mol. Nutr. Food Res. 58 (2014)1685-1707.

[2] Y. Zhang, P. Talalay, C.G. Cho, G.H. Posner, A major inducer of anticarcinogenicprotective enzymes from broccoli: isolation and elucidation of structure, Proc. Natl.Acad. Sci. U. S. A. 89 (1992)2399-2403.

[3] J. Jakubikova, J. Sedlak, R. Mithen, Y. Bao, Role of PI3K/Akt and MEK/ ERK signalingpathways in sulforaphane- and erucin-induced phase II enzymes and MRP2transcription, G2/M arrest and cell death in Caco-2 cells, Biochem. Pharmacol. 69(2005)1543-1552.

[4] A. Prawan, Y.-S. Keum, T.O. Khor, S. Yu, S. Nair, W. Li, L. Hu, A. -N. T. Kong,Structural influence of isothiocyanates onthe antioxidant response element (ARE)mediated heme oxygenase-1 (HO-1)expression, Pharm. Res. 25 (2008)836-844.

[5] P. Pocasap, N. Weerapreeyakul, K. Thumanu, Structures of isothiocyanates attributed to reactive oxygen species generation and microtubule depolymerization in HepG2 cells, Biomed Pharmacother. 101 (2018)698-709.

[6] C. Junhom, N. Weerapreeyakul, W. Tanthanuch, K. Thumanu, FTIR microspectroscopydefines early drug

resistant human hepatocellular carcinoma (HepG2) cells,Exp. Cell Res. 340 (2016)71-80.

[7] S. Machana, N. Weerapreeyakul, S. Barusrux, K. Thumanu, W. Tanthanuch, FTIR microspectroscopy discriminates anticancer action on human leukemic cells by extracts of *Pinuskesiya*; *Cratoxylumformosum*ssp. *Pruniflorum* and melphalan,Talanta 93 (2012)371-382.

CONTACT

*Natthida Weerapreeyakul: tel 0-4320-2378; natthida@kku.ac.th

A STRUCTURAL STUDY OF BONE CHANGES IN KNEE OSTEOARTHRITIS BY SYNCHROTRON-BASED X-RAY FLUORESCENCE AND X-RAY ABSORPTION SPECTROSCOPY TECHNIQUES

B. Sindhupakorn[1], S. Thienpratharn[1], P. Kidkhunthod[2]
[1]Orthopedic Department, School of Medicine, Medical Institute, Suranaree University of Technology, 111 University Avenue, Muang District, Nakhon Ratchasima 30000, Thailand
[2]Synchrotron Light Research Institute (Public Organization), 111 University Avenue, Muang District, Nakhon Ratchasima 30000, Thailand

ABSTRACT

Osteoarthritis (OA) is a degeneration of articular cartilage and subchondral bone. Our study investigated the changing of biochemical components of cartilage and bone compared between normal and OA people. Using X-ray fluorescence (SR-XRF) and X-ray absorption spectroscopy (XAS) techniquesincluding X-ray absorption near edge structure (XANES) and extended X-ray absorption fine structure (EXAFS). The bone samples were collected from various male and female between 20 and 74 years old. SR-XRF for Ca elements showed a majority three main groups, 20-36 years, 40-60 yearsand over 70 years, respectively. XANES and EXAFS resulted a Ca-amorphous phase when the ages increase.

INTRODUCTION

In osteoarthritis (OA) all of the joint components are involved in the process of degeneration such as synovium, cartilage, calcified cartilage, subchondral bone and trabecular bone [1]. It characterized by articular cartilage degradation which can affect many joints in the body, but is particularly common in weight-bearing joints such as the knee and hip. The loss of cartilage can lead to joint space narrowing, pain, and loss of function and finally leads to the need for total joint replacement. Factors such as previous joint injuries, obesity, the effects of aging on cartilage matrix composition, matrix structure and genetic factors are involved in the pathogenesis of OA. However, the exact pathophysiology remains unclear. Recently, studies in animal models have permitted the evaluation of time dependent histomorphometric changes in articular cartilage relative to those in the subchondral bone plate at disease onset and during progression [2]. The major components in subchondral bone are inorganic component (60-70%) which is calcium and phosphorus, organic component (10%) which is collagen type I, the rest of all is water (10-20%). The inorganic component plays an important role for mechanical strength of the bone [3]. Changes insubchondral bone and trabecular bone were believed to trigger alteration of mechanics and shearing forces in the above cartilage, predisposing the joint to deterioration [4-8]. Studies have been shown in animal studies that subchondral bone changes occur at early stages of OA [9,10] and that alterations to subchondral bone can lead to cartilage degeneration [11,12]. It is well known that changes to the composition of the subchondral bone matrix in OA are associated with alterations in bone microarchitecture [13]. A number of studies have indicated both morphological and biochemical changes in OA bone tissues [14-17]. Subchondral bone changes are important in the etiology of OA. Alteration in subchondral bone remodeling, and followed by bone structure, caused in abnormal load distribution. This may cause or accelerate cartilage damage. Recent studies have shown changes of subchondral bone which may predict changes in articular cartilage [18-21]. The precise role of these changes during initiation and progression is still controversial [22-25]. In this study, synchrotron-based technique.

MATERIALS AND METHODS

1. Femoral condyle bone and cartilage sample collection

Femoral condyle samples were collected from patients between 20 and 74 years old who underwent total knee arthroplasty (TK)and anterior cruciate ligament (ACL) reconstruction with the notchplasty. Exclusion criteria are patients who have inflammatory joint disease, steroid injection prior surgery, high blood calcium and current drug history of bisphosphonate therapy. 13 patient samples were collected with under approval of medical ethics commission, consent of the medical institute of Suranaree University of technology and consent patient form. All the samples were collected from medial condyle of femur with cylindrical osteochondral explants. The size range from 3 to 4 mm height 4-13 mm length. After take bone from the patients, bone was fixed by freeze dried.

2. Structural characteristics: SR-XRF and XANES measurements

The study did at the SUT-NANOTEC-SLRI XAS beamline (BL 5.2) (electron energy of 1.2 GeV; bending magnet; beam current 80-150 mA; 1.1 to 1.7 10^{11} photon s[1]) at the Synchrotron Light Research Institute (SLRI), Nakhon Ratchasima, Thailand. In this study SR-XRF measurements and XANES spectra were conducted in order to obtain the relatively quantitative of calcium (Ca) elements and their chemical and physical state of them in all bone samples. Due to the various sizes of bone samples, the X-ray beam size is optimized for 1mm width x 4mm length at the samples. We used X-ray fluorescence (XRF) at the photon energy of 4240eV which allowed an access to the fluorescence K-lines of Caelements. The SR-XRF spectra were collected, with a dwell time of 60 s, by a Vortex ME4 four-element silicon drift detector. We performed the SR-XRF in air atmosphere (fluorescence detector operated in air). SR-XRF spectra were normalized in order to compare the amount Ca in each sample. XANES and EXAFS spectroscopic techniques at the calcium K-edge use widely to characterize calcium-contented materials especially apatite calcium species in bone. These both spectroscopic techniques do not require a periodicity of materials for determination structures in order to reveal an evidence of novel properties of these such materials i. e. , X-ray diffraction [26, 27]. XANES typically provides the capability to distinguish among crystalline and amorphous Ca species. This special technique requires minimal sample preparation unlike most other structural probes, i. e. infrared spectroscopy. We investigated all human knees samples at Ca K-edge which can deeply address the different calcium structures in each sample. In this study, all XANES spectra were obtained influorescence mode using a Vortex ME4 four-element silicon driftdetector as same as SR-XRF collections. The energy scan was ensured by a fixed exit double crystal Ge(220) monochromator for Ca K-edge (4038.50eV). The energy resolution (ΔE/E) of $2x10^{-4}$ obtained from Ge(220) crystals was used to scan the synchrotron X-ray beam. In order to get sufficient statistics, three scans of XANES measurements and at least six scans for EXAFS collections were preformed prior merging the XANES and EXAFS spectra. The normalized data were analyzed after background subtraction in the pre-edge and post-edge region using the ATHENA software whichis included in an IFEFFIT package [28, 29].

RESULTS AND DISCUSSION

1. Comparison of size of bone samples (WxL)

All femoral condyle samples are shown in Figure 1 as labeled from no. 1 to no. 13, respectively. The samples were collected from male and female patients age between 20 and 74 years old who were underwent TKA and ACL reconstruction.

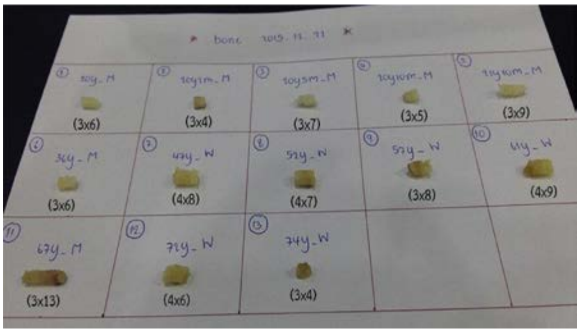

Figure 1: A comparison of studied femoral condyle samples with various ages between 20 and 74 years old who underwent total knee arthroplasty (TKA) and anterior cruciate ligament (ACL) reconstruction with the notchplasty.

2. Normalized SR-XRF at Ca element

Because the SR-XRF intensities are directly proportional to various atomic concentrations in sample. Thus, X-ray fluorescence signal of all samples were normalized with the synchrotron beam current (150 mA - 100 mA) and size of each sample prior comparisons. The excited SR-XRF signals at 4240 eV for Ca elements was illustrated in Figure 2

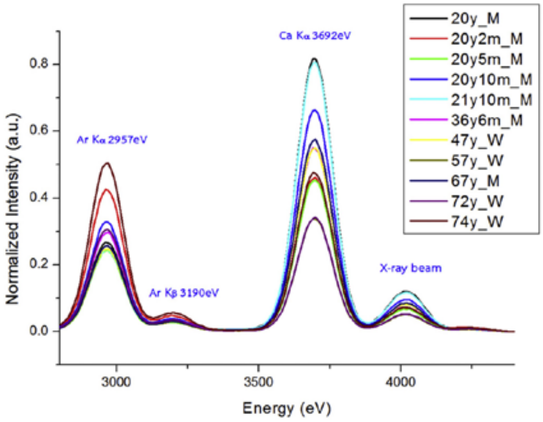

Figure 2: Normalized SR-XRF at Ca elements in all bone samples.

As seen overall in normalized XRF intensities, they can be divided into three main groups, based on their intensities, 20-36 years, 40-60 years and over 70 years, respectively. Consequently, in order to obtained deeper and deeper information of Ca-caused in osteoarthritis, XANES and EXAFS spectra will be further introduced in the next section.

3. Structural characteristic of Ca chemical species by XANES and EXAFS

The XANES spectra at Ca K-edge collected from bone samples and two different standard compounds, Ca3(PO4)2 and Ca5(PO4)3, are presented in Figure 3(a) - (d), respectively.

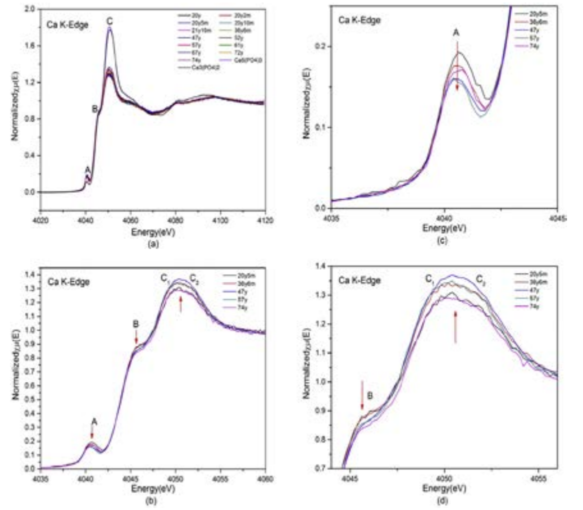

Figure 3: (a)-(d) Normalized XANES spectra at Ca K-edge of all samples.

According to the previous XRF results with three main age groups, XANES spectra ofabout 20 years, 36 years, 47 years, 57 years and 74 years bone samples are focused. Unlike crystalline standard samples, XANES spectra at Ca K-edge of all samples show a poorly crystalline apatite (PCA) at different maturation stages, as seen in broad peaks C1 and C2. As mentioned so far that XANES spectra are commonly used to distinguish between different types of calcium environments invarious Ca-P structure in biological samples [30-32]. In this study, the interpretation of XANES features to electronic transitions of bone samples can be reported with three main regions. The pre-edge region, labeled A, (approximately 4042 eV) is due to transitions from 1s to 3d orbitals or O 2p orbitals [30-32]. Again, a fashion of a slight decrease in intensity is clearly observed with increasing ages. This suggested a different site symmetry of Ca ions in all samples. Moving to higher energies, a shoulder like structure (B) which is assigned to 1s-4s quadrupole-transitions is observed approximately at 4047eV. This transition trends to decrease with increase ages suggesting a lower probability of electron quadruple-transitions, see Figure 3 (d). Finally, as the energy increases, the most intense resonance of the XANES spectra are produced, called whiteline (C1 and C2). The white line is observed with a double peak which is consistent with dipole-electron transitions of 1s to 4p 1/2 and 3/2, respectively. Because dipole-transitions are much more likely than quadruple-transitions, consequently, transitions from 1s to 4p have the highest probability. In addition, features found at higher energies are related to transitions from 1s to higher than 4p unoccupied states or multiple scattering contributions. The relative white line intensities depended on the different Ca stoichiometry in samples [30-32]. In addition, as clearly seen in the white line, C1 and C2, peaks trend to become broader with ages increase. This represents the modification of smaller Ca-O bond length, smaller first shell coordination, as reported [33]. Moreover, this evidence can also imply an existence of more amorphous phases in bone samples as comparing with calcium crystalline standards. To clearly address, EXAFS results at Ca K-edge obtained from 20 years, 36 years, 47 years, 57 years and 74 years bone samples also showed in Figure 4.

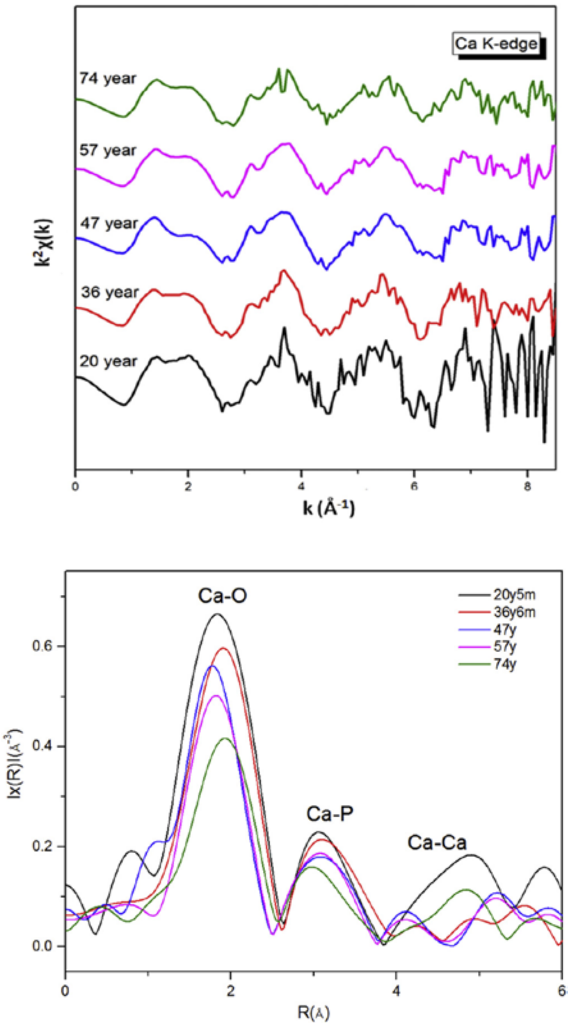

Figure 4: EXAFS spectra, k-space (top) and r-space (bottom), at Ca K-edge of 20 years, 36years, 47 years, 57 years and 74 years bone samples, respectively. (No phase shift correction).

A good agreement between EXAFS data and the previous XANES spectra and other report [33] is presented. This implies a significant signal of Ca-O amorphous phase rather than crystalline Ca structure in bone samples as clearly seen various Ca-O, Ca-P and Ca-Ca distances at different ages in r-space. Moreover, in EXAFS r-space, to the best of our knowledge, the lower intensity, the smaller Ca-ions coordination numbers. Thus, with ages increase, the number of neighboring atoms. This evidence is also supported and consistent with [33] and XANES results.

CONCLUSION

By employing a combination of SR-XRF and XANES and EXAFS at Ca K-edge techniques, a changes evidence in bone structure of osteoarthritis is caused by changes in calcium structures. The SRXRF signals of all bone samples can be used to group ages of patients where three main groups can be clearly identified. A bulk information obtaining from both XANES and EXAFS results shows a fashion of spectra which is related to an electron transitions and structural modification especially around Ca ions at different ages. The increased age is more amorphous phases than younger age. Moreover, the results from this study can be used to predict a chance of knee osteoarthritis occurring in the future.

ACKNOWLEDGEMENTS

This paper is supported by National Research Council of Thailand under grant No.2559A30402245. Many thanks to the SUT-NANOTEC-SLRI Joint Research Facility for awarding XAS beam time and the Suranaree University of Technology hospital is gratefully acknowledged.

REFERENCES

[1] S.R. Goldring, Alteration in periarticular bone and cross talk between Subchondral bone and articular cartilage in osteoarthritis, Ther. Adv. Musculoskelet. Dis. 4 (2012)249-258.

[2] M.B. Goldring, S.R. Goldring, Osteoarthritis, J. Cell Physiol. 213 (2007)626-634.

[3] J. Rhoa, L. Kuhn-Spearingb, P. Ziouposc, Mechanical properties and the hierarchical structure of bone, Med. Eng. Phys. 20 (1998)92-102.

[4] E.L. Radin, R.M. Rose, Role of subchondral bone in the initiation and progression of cartilage damage, Clin. Orthop. Relat. Res. 213 (1986)34-40.

[5] E.L. Radin, R.M. Rose, Role of mechanical factors in pathhogenesis of primaryosteoarthritis, Lancet 299 (1972)519-522.

[6] D.B. Burr, E.L. Radin, Microfractures and microcracks in subchondral bone: arethey relevant to osteoarthrosis? Rheum. Dis.Clin. North. Am. 29 (200)675-685.

[7] D.B. Burr, Anatomy and physiology of the mineralized tissues: role in thepathogenesis of osteoarthrosis, Osteoarthr. Cartil. 12(Suppl A) (2004)520-530.

[8] D.B. Burr, M.A. Gallant, Bone remodelling in osteoarthritis, Nat. Rev. Rheumatol. 8 (2012)665-673.

[9] T. Hayami, M. Pickarski, Y. Zhuo, G.A. Wesolowski, G.A. Rodan, T. Duong le,Characterization of articular cartilage and subchondralbone changes in the ratanterior cruciate ligamenttransection and meniscectomized models of osteoarthritis, Bone 38 (2) (2006)234-243.

[10] H.L.Quasnichka, J.M. Anderson-MacKenzie, A.J. Bailey, Subchondralbone andligament changes precede cartilagedegradation in guinea pig osteoarthritis,Biorheology 43 (3e4)(2006)389e97.

[11] F.C. Ewald, R. Poss, J. Pugh, A.L. Schiller, C.B. Sledge, Hip cartilagesupported bymethacrylate in canine arthroplasty, Clin. Orthop. Relat. Res. 171 (1982)273-279.

[12] A. Lahm, M. Uhl, M. Edlich, C. Erggelet, J. Haberstroh, P.C. Kreuz, Anexperimental canine model for subchondral lesions of theknee joint, Knee 12 (1)(2005)51-55.

[13] G. Li, J. Yin, J. Gao, T.S. Cheng, N.J. Pavlos, C. Zhang, M.H. Zheng, Subchondralbone in osteoarthritis: insight into risk factors and microstructural changes,Arthritis Res. Ther. 15 (6)(2013)223.

[14] P. Dieppe, Osteoarthritis: clinical and researchperspective, Br. J. Rheumatol. 30

[15] M.A. Davies, Epidemiology of osteoarthritis, Clin. Geriatr. Med. 4 (1988)241-255.

[16] T.E. Hardingham, G. Venn, M.T. Bayliss, Chondrocyteresponse in cartilage andin experimentalosteoarthritis, Br. J. Rheumatol. 30 (Suppl. 1)(1991)32-37.

[17] A.J. Hough, Pathology of osteoarthritis, in: W.J. Koopman(Ed.), Arthritis andAllied Conditions, thirteenth ed., Williams and Wilkins, Baltimore, Maryland,1997, pp. 1945-1968.

[18] L. Wachsmuth, K. Engelke, High-resolution imaging of osteoarthritis usingmicrocomputed tomography, Methods Mol. Med. 201 (2004)231-248.

[19] Y.H. Sniekers, H. Weinans, G.J.V.M. van Osch, J.P.T.M. van Leeuwen, Oestrogenis important for maintenance of cartilage and Subchondral bone in a murinemodel of knee osteoarthritis, Arthritis. Res. Ther. 12 (2010)R182.

[20] C. Buckland-Wright, Subchondral bone changes in hand and knee osteoarthritis detected by radiography, Osteoarthr. Cartil. 12 (Suppl A)(2004)S10-S19.

[21] S.M. Botter, G.J.V.M. Van Osch, J.H. Waarsing, J.S. Day, J.A.N. Verhaar,H.P. Pols, J.P.T.M. Van Leeuwen, H. Weinans, Quantificatio of subchondralbone changes in a murine osteoarthritis model using micro-CT, Biorheology43 (2006)379-388.

[22] D.B. Burr, R.B. Martin, M.B. Schaffler, R.D. Jurmain, E.J.

Harner, E.L. Radin,Oesteoarthrosis: sex-specific relationship to osteoporosis, Am. J. Phy. Anthropol. 61 (1983)299-303.

[23] J. Glowacki, S. Hurwitz, T.S. Thornhill, M. Kelly, M.S. LeBoff, Osteoporosis andVitamin-D deficiency among postmenopausal women with osteoarthritis undergoing total hip arthroplasty, J. Bone Jt. Surg. Am. 85 (2003)2371-2377.

[24] M. Sowers, I. Lachance, D. Jamadar, M.C. Hochberg, B. Hollis, M. Crutchfield,M.L. Jannausch, The associations of bone mineral density and bone turnovermarkers with osteoarthritis of the hand and knee in pre- and perimenopausalwomen, Arthritis. Rheum. 42 (1999)483-489.

[25] A. Verstraeten, H. Van Ermen, G. Haghebaert, J. Nijs, P. Geusens, J. Dequeker,Osteoarthrosis retards the development of osteoporosis. Observation of thecoexistence of osteoarthrosis and osteoporosis, Clin. Orthop. Relat. Res. 264(1991)169-177.

[26] D.W. Fu, H.L. Cai, Y. Liu, Q. Ye, W. Zhang, Y. Zhang, X.Y. Chen,G.Giovannetti,M. Capone, J. Li, R.G. Xiong, Diisopropylammonium bromide is a hightemperature molecular ferroelectric crystal, Science 339 (2013)425-428.

[27] D.W. Fu, W. Zhang, R.G. Xiong, The first metaleorganic framework (MOF)ofImazethapyr and its SHG, piezoelectric and ferroelectric properties, DaltonTrans. 30 (2008)3946-3948.

[28] M. Newville, EXAFS analysis using FEFF and FEFFIT, J. Synchrotron Radiat. 8(2001)96-100.

[29] B. Ravel, M. Newville, ATHENA, ARTEMIS, HEPHAESTUS: data analysis for Xray absorption spectroscopy using IFEFFIT, J. Synchrotr. Radiat. 12 (2005)537-541.

[30] K. Asokan, J.C. Jan, J.W. Chiou, W.F. Pong, P.K. Tseng, I.N. Lin, X-rayabsorptionspectroscopy studies of Ba1-xCaxTiO3, J. Synchrotr. Radiat. 8 (2001)839-841.

[31] J. Chaboy, S. Quartieri, X-ray absorption at the Ca K-edge in natural garnetsolid solutions: a full-multiple scattering investigation, Phys. Rev. B 52 (1995)6349-6357.

[32] S.C. Liou, S.Y. Chen, H.Y. Lee, J.S. Bow, Structural characterizationofnano-sizedcalcium deficient apatite powders, Biomaterials 25 (2004)189-196.

[33] D. Eichert, M. Salome, M. Banu, J. Susini, C. Rey, Preliminarycharacterization of calcium chemical environment inapatitic and non-apatitic calcium phosphates of biological interest by XAS, Spectrochim.Acta B 60 (2005)850-858.

CONTACT

*Bura Sindhupakorn, tel: +66-44-223-539; bura@sut.ac.th

DEOXYGENATION OF PALM KERNEL OIL TO JET FUEL-LIKE HYDROCARBONS USING NI-MOS$_2$-BASED CATALYSTS

V. Itthibenchapong[1], A. Srifa[1], R. Kaewmeesri[1], P. Kidkhunthod[2], K. Faungnawakij[1]*
[1] National Nanotechnology Center, 111 Thailand Science Park, Phahon yothin Road,
Klong Luang District, Pathum Thani 12120, Thailand
[2]Synchrotron Light Research Institute (Public Organization), 111 University Avenue,
Muang District, Nakhon Ratchasima 30000, Thailand

ABSTRACT

A palm kernel oil was used as a renewable feedstock to produce jet fuel-like hydrocarbons via the deoxygenation over the Ni-MoS$_2$/γ-Al$_2$O$_3$ catalyst. Synthesized by a liquid processing method with thiourea, the catalyst revealed MoS$_2$ structure with low stacking, while Ni substitution in the MoS$_2$ structure and interaction with the Al$_2$O$_3$ support were determined based on the Ni K-edge XANES and EXAFS results. A high deoxygenation activity was observed with the optimum product yield of approximately 92% and 58%selectivity to C10-C12 hydrocarbons. The flow property of the jet fuel-like hydrocarbons was more desirable than those obtained from palm olein oil-derived fuel(Figure 1).

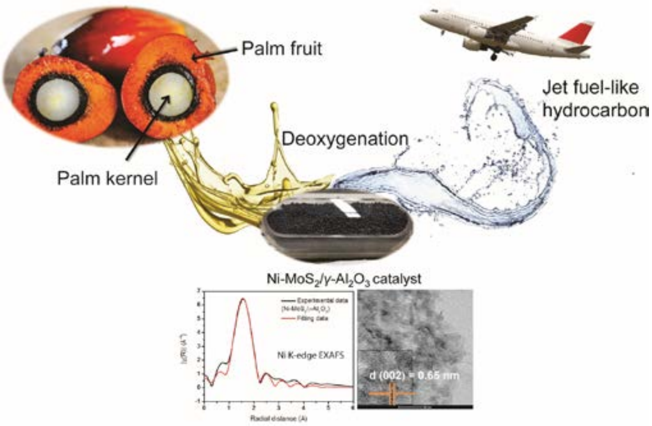

Figure 1: Overview of deoxygenation of palm kernel oil to jet fuel-like hydrocarbons.

INTRODUCTION

Biofuels, such as biodiesel, bioethanol, biogas, and bio-oil, have played an important role as renewable energy for transportation and power generation due to the depletion of fossil fuel. Deoxygenation, which removes oxygenated components from the reactants in the presence of hydrogen gas through hydrodeoxygenation (HDO) and decarbonylation (DCO) and without hydrogen consumption via decarboxylation (DCO$_2$), has been used in various applications including bio-hydrogenated diesel (BHD) or green diesel production and biomass upgrading into valuable chemicals.[1] Co- or Ni-doped MoS$_2$ has been known as the state-of-the-art catalysts for HDO and hydrodesulfurization (HDS) because of their excellent catalytic performance and cost-effective application for large-scale production. The deoxygenation activities of the as-synthesized catalysts were studied using palm kernel oil, which is an abundant source of lauric acid (C12), to produce renewable jet fuel-like hydrocarbons. To provide a simple approach for large-scale preparation, sulfidation by thiourea in a liquid-phase processing will be compatible with a general synthesis method of unsupported and supported metal sulfide catalysts. The exploration of a new potential biojet fuel resource via triglyceride-feedstock conversion could provide a straightforward process for obtaining a high yield and tunable biojet fuel via deoxygenation and further isomerization.

EXPERIMENTAL

The Ni-MoS$_2$/γ-Al$_2$O$_3$ catalyst was prepared by wetness impregnation with a precursor solution based on modification of our previously reported protocol [2] using thiourea as a sulfur agent. The XAS has been employed to study the electronic and local structural information of the materials. The XAS spectra including XANES and EXAFS spectra were acquired at the SUT-NANOTEC-SLRI XAS Beamline (BL5.2) at SLRI. The Mo L3-edge and Ni K-edge spectra were collected in transmission mode using InSb (111) and Ge (220) double crystal monochromator with an energy resolution ($\Delta E/E$) of 2×10^{-4}. The background correction and data fitting of the XANES and EXAFS data were done using the ATHENA and ARTEMIS programs in the IFEFFIT package. [3, 4] Details in other characterization techniques (XRD, XPS, N$_2$-sorption, FTIR and TEM) including the catalytic activity testing and product analysis were reported elsewhere.[5]

DISCUSSION AND SUMMARY

A novel method for metal sulfide preparation using thiourea sulfurization under an inert atmosphere was successfully applied for the synthesis of the Ni-MoS$_2$/γ-Al$_2$O$_3$ catalyst. The XRD results indicated the semi-amorphous nature and small crystallite size of the catalyst and the low stacking and disorder of the MoS$_2$ layers. [6] In addition, the Mo and Ni oxidation state and crystallinity of the bulk Ni-MoS_2/γ-Al_2O_3 material were confirmed by the XANES spectra [7] at Mo L3-edges and Ni K-edges (Figure 2). The Mo L3-edge positions of Mo(0) (standard Mo metal foil, 2520. 0 eV), Mo(IV) (MoS2, 2522. 3 eV) and Mo(VI) (MoO3, α-NiMoO4, 2524. 1 eV)increased with the ionicity of the Mo bonding and electronegativity of the anions. The near-edge and post-edge features of the MoS_2-based compounds exhibited less intense amplitudes (low-k scattering), indicating poor crystallinity in the amorphous phase. Moreover, as seen in Figure2(a), the white line intensity of Ni-MoS_2 became smaller and that of Ni-MoS_2/Al_2O_3 turned into higher when compared with that of MoS2 standard, suggesting an existence of Ni-substitution in both samples. Besides, the Ni K-edge XANES spectra of Ni-MoS_2/γ-Al_2O_3 compared to those of some Ni compounds indicated that the edge energy (at 8345. 6 eV)was between those of the $NiAl_2O_4$(8346. 1eV), NiO(8345.9 eV), and NiS_2(8339.4 eV) standards, as shown in Figure2(b). These results confirmed the presence of both Ni-S and Ni-O bonds, which may arise at the metal-support interface between Ni and MoS_2 and alumina, respectively. Based on the different post-edge features, unlike those in NiO and NiS_2 standards, this result also suggested the substitution of Ni into the MoS_2 and MoS_2/Al_2O_3 structures which is consistent with the observed Mo L3-edge XANES results.

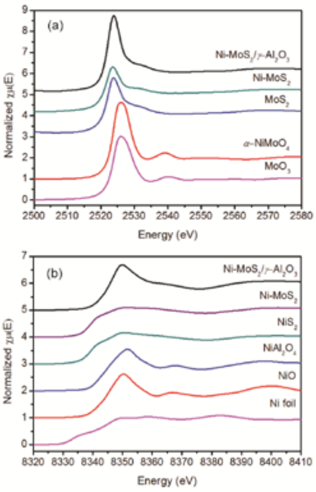

Figure 2: (a) XANES spectra at Mo L_3-edges of Ni-MoS_2/γ-Al_2O_3 compared to those of Mo compounds and (b) XANES spectra at Ni K-edges of Ni-MoS_2/Al_2O_3 compared to those of Ni compounds.

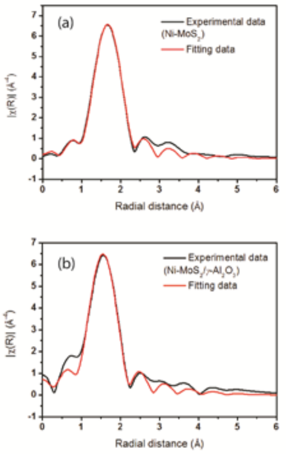

Figure 3: Measured EXAFS data with the best fitting at the Ni K-edge for the Ni-MoS_2 and Ni-MoS_2/γ-Al_2O_3 samples.

In order to clarify the Ni-substitution in samples, the EXAFS data at Ni K-edge is necessarily employed. The measured EXAFS spectra (black line) and the best fitting (red line) at Ni K-edge for the Ni-MoS_2 and Ni-MoS_2/Al_2O_3 samples are shown in Figure3(in real space). The fitting parameters are listed in elsewhere.[5] The mean Ni-S and Ni-S/Ni-O coordination numbers and bonding distances around the Ni atoms in the MoS_2 and MoS_2/Al_2O_3 samples were 4. 78(2)and 1. 68(1)/3. 40(2) and 2. 223(4)Å and 2. 204(1)/2. 025(3) Å, respectively. These EXAFS results confirmed Ni substitution into the MoS_2 and MoS_2/Al_2O_3 structures, which is consistent with the reported XANES results. The metal doping in the based catalysts, i.e. Ni or Co doping in MoS_2[2,8] has been confirmed as the promoting effect to improve catalytic deoxygenation performance by modification of the electronic and geometric surface structure of the catalytic active sites via defects e.g. S-vacancies in MoS_2.[8]

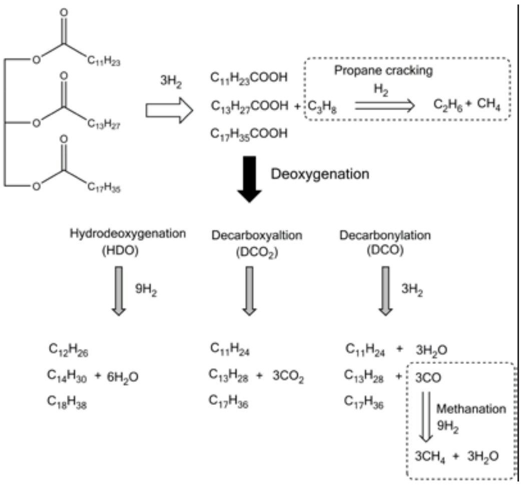

Figure 4: Proposed catalytic palm kernel oil conversion via deoxygenation into jet diesel-like hydrocarbons.

The catalytic performance for the deoxygenation of palm kernel oil was studied as an alternative approach for the production of jet fuel-like hydrocarbons. The proposed reaction pathway was shown in Figure 4. A high HDO activity, which was the major pathway for deoxygenation, was observed a high H_2 pressure was applied at 300 °C with a long contact time (low LHSV) between the reactants and the catalyst. The promotion of DCO_2 and DCO occurred as the reaction temperature increased and with a short resident time (fast LHSV). The side reactions, such as cracking and methanation, occurred at high temperatures, such as 330 °C. The optimum product yield was approximately 92%, which was primarily from the HDO product (~60%) with 58%selectivity to C10-C12 for the jet fuel-like hydrocarbons under the following conditions: 330 °C, H_2 pressure of 50 bar, LHSV of 1 h^{-1}, and H_2/oil ratio of 1000 N(cm^3 cm^{-3}). The conversion of palm kernel oil was >99% under various operational conditions in the current study (i. e. , reaction temperature, LHSV, and H_2 pressure). Therefore, the selectivity to C10-C12 alkanes in the liquid product remained at approximately 58%, corresponding to the amount of lauric acid in the palm kernel oil feedstock. In addition, the catalytic activities of the different oil feedstock (i.e., palm kernel oil and palm olein oil) based on the yield contributed by the high HDO product selectivity were similar (result not shown). Therefore, the fatty acid chain did not significantly affect the deoxygenation performance over the Ni-MoS_2/γ-Al_2O_3 catalyst under the studied conditions. Depending on the product composition, the liquid biofuel from palm kernel oil consisted of jet fuel-like hydrocarbons, and product from palm olein oil consisted of diesel-like hydrocarbons. The differences in heating value and cold flow property of biofuel products from the two feedstock were in association with the composition of the alkanes based on their fatty acid origins.(Table 1) The medium chain alkanes (i.e., C10-C12) in the product obtained from palm kernel oil improved the cloud point (6.2 °C) and pour point (-3.0 °C) while maintaining an excellent high heating value of 46.6 MJ kg^{-1} comparable to the green diesel from palm olein. Typically, the commercial jet fuels contain additives to keep low freezing point, cloud point and pour point, leading to excellent cold flow properties at actual working conditions as seen in Table 1. The fuel property and chemical composition of the additive-free jet fuel-like hydrocarbons in this work could be suitable for blending with fossil jet or diesel range fuel. The isomerization of the developed fuel can also be applicable to improve its cold flow property.

Table 1: Heating values and cold flow properties of liquid products obtained from palm kernel oil, palm olein oil, and commercial jet fuels.

Feedstock	HHV (MJ kg^{-1})	Cloud point (°C)	Pour point (°C)	Remark
Palm kernel oil	46.6	6.2	-3.0	The present work
Palm olein oil	46.0	22.1	19.0	The present work
POSF-2827 (Jet A type)[9]	n/a	-48.0	-52.5	Commercial Jet fuel, with additives
Jet A-1 type [10]	43.5	-52	n/a	Commercial Jet fuel, with additives

ACKNOWLEDGMENTS

This work was supported by the National Nanotechnology Center (NANOTEC)under National Science and Technology Development Agency (NSTDA)and the Thailand Research Fund (TRF), Thailand under contract no. TRG5880192 and RSA5580055. The XAS and XPS experiments were performed at the BL-5.2 SUT-NANOTEC-SLRI XAS Beamline and the SUT-NANOTEC-SLRI XPS, respectively.

REFERENCES

[1] A. Srifa, K. Faungnawakij, V. Itthibenchapong, N. Viriya-Empikul, T. Charinpanitkul, S. Assabumrungrat, "Production of bio-hydrogenated diesel by catalytic hydrotreating of palm oil over NiMoS_2/γ-Al_2O_3 catalyst, *Bioresour. Technol.*, vol. 158, pp. 81-90, 2014.

[2] V. Itthibenchapong, C. Ratanatawanate, M. Oura, K. Faungnawakij, "A facile and low-cost synthesis of MoS_2 for hydrodeoxygenation of phenol", *Catal. Commun.*, vol. 68, pp. 31-35, 2015.

[3] M. Newville, "EXAFS analysis using FEFF and FEFFIT", *J. Synchrotron Radiat.*, vol. 8. pp. 96-100, 2001.

[4] B. Ravel, M. Newville, "ATHENA, ARTEMIS, HEPHAESTUS: data analysis for X-ray absorption spectroscopy using IFEFFIT", *J. Synchrotron Radiat.*, vol. 12, pp. 537-541, 2015.

[5] V.Itthibenchapong, A.Srifa, R.Kaewmeesri, P.Kidkhunthod, K.Faungnawakij, "Deoxygenation of palm kernel oil to jet fuel-like hydrocarbons using Ni-MoS_2/γ-Al_2O_3catalysts",*Energy Convers.Manag.,* vol. 134, pp. 188-196, 2017.

[6] R.R.Chianelli, E. B. Pecoraro, T. A. J. P.Deneufville, "Molybdenum disulfide in the poorly crystalline "Rag" structure", *Science,*vol. 203, pp. 1105-1107, 1979.

[7] V.R. Surisetty, Y. Hu, A.K. Dalai, J. Kozinski, “Structural characterization and catalytic performance of alkali (K) and metal (Co and Rh)-promoted MoS_2 catalysts for higher alcohols synthesis”, *Appl. Catal., A*, vol. 392,pp.166-172, 2011.

[8] J. V. Lauritsena, J. Kibsgaard, G. H.Olesen, P. G. Moses, B.Hinnemann, S. Helveg, J. K. Nørskov, B. S. Clausen, H.Topsøe, E.Lægsgaard, F. Besenbacher,“Location and coordination of promoter atoms in Co- and Ni-promoted MoS_2-based hydrotreating catalysts”, *J. Catal.*,vol. 249,pp. 220-233, 2007.

[9] S. Zabarnick, N. Widmor, “Studies of jet fuel freezing by differential scanning calorimetry”, *Energy Fuels*, vol. 15, pp. 1447-1453, 2001.

[10] C.J. Chuck, J. Donnelly, “The compatibility of potential bioderived fuels with Jet A-1 aviation kerosene”, *Appl. Energy*, vol. 118, pp. 83-91, 2014.

CONTACT

*Vorranutch Itthibenchapong, tel: +66-2564-7100 ext. 6615; vorranutch@nanotec.or.th

FABRICATION OF POLYMER BASED MICRONEEDLES USING MICROINJECTION MOULDING

P. Janphuang[1*], *M. Laebuab*[2], *P. Leuasoongnoena*[1], *P. Taweewatb*[2], *S. Suphachiaraphana*[1]
[1] Synchrotron Light Research Institute (Public Organization), 111 University Avenue,
Muang District, Nakhon Ratchasima 30000, Thailand
[2]Thai-German Institute, 700/1 Moo 1 Amata Nakorn Industrial Estate, Bangna Trad Road,
Muang District, Chonburi 20000, Thailand

ABSTRACT

We present the development of sharp tipped plastic hollow microneedles fabricated using microinjection moulding. Unlike traditional approaches of injection moulding process, three mould inserts were used to form the sharp tip of microneedles. The injection moulding parameters including clamping force, temperature, injection pressure and velocity were characterized in order to obtain the optimum reproducibility. Sharp tipped and hollow microneedles, made of biocompatible polymethyl methacrylate (PMMA), with a round tip radius of 50 µm and 500 µm in height have been realized by microinjection moulding process demonstrating the potential of a low cost, high production efficiency, and suitable for mass production.In addition, polymer based sharp tipped microneedles fabricated using X-ray LIGA has been proposed.

INTRODUCTION

Currently, transdermal drug delivery (TDD)is one of a convenient way to deliver medicine into the subcutaneous tissues without drawbacks such as pain and digestive system disorders [1]. To achieve this, the drug is injected through the outermost layer of skin, Stratum Corneum (SC), from where it diffuses into the blood vessels of the deeper dermal skin layer through microneedle conduits. Since there are no nerves in SC layer, thus, this method is pain-free in comparison to hypodermic needle [2].

The MNs are typically designed in arrays in order to improve the surface contact with the skin. Various types of MNs yield have been developed, including coated MNs enable drug on the surface of the needles, hollow MNs for drug infusion, and dissolving MNs encapsulated drug and release after insertion [3].In recent years, polymers based MNs is of great interest. Most of polymers have high toughness and biocompatible enabling polymers based MNs to avoid crack and hardly induce side effect during their insertion into the skin. Injection molding is one of a promising process in which melt materials, mostly polymer, is forced to flow under high pressure through a plunger into a mold cavity, where it solidifies and then ejected to produce a replicated structure on the surface. Thus, mould based fabrication technique could further reduce the manufacturing cost and is suitable for mass production.

DESIGN AND FABRICATION

In order to successfully fabricate MNs by microinjection moulding process, guidelines for the design of a runner system and a detailed description on the flow analysis of molten polymer into the cavity were carried out by FE simulation in Moldex3D.

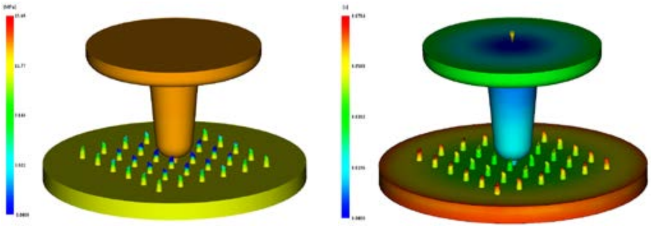

Figure 1: Simulated results of (a) injection pressure loaded to the designed runners and the mould insert and (b) molten PMMA filled in the cavity.

The designed microneedle patch consists of 36 microneedles, occupying approximately 500 mm^2. Considering the skin deformation, the MNs shank length is limited to 300 – 400 µm. However, it can be assumed that the entire needle shank will not penetrate into the skin since the human skin is very flexible. Thus, the length of the MNs in this work is defined to be 500 µm.

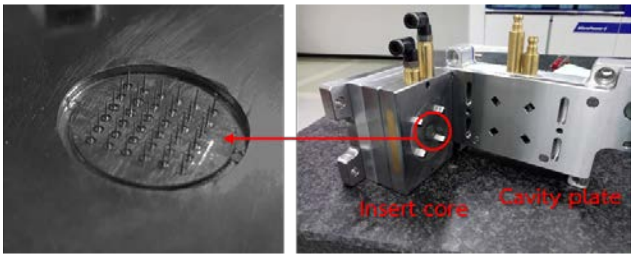

Fig. 2. Fabricated mould insert and cavity (a) upper mould insert with pins (b) microneedles cavities(lower mould insert).

The runner optimization analysis is first performed in order to define the size and the number of gates, and the injection pressure applied to the cavity. In simulation, polymer melt temperature (T_p = 230 °C), mould temperature (T_m = 50 °C), holding pressure (P_h = 60 MPa), and injection flow (V_i = 9 ccm/s) were kept constant (to the values recommended by the manufacturer). The simulated results revealed that one point gate, with diameter of 5 mm, was sufficient for the injection of molten PPMA, as shown in Fig. 1. More than 90% of MNs cavities were fulfilled by the molten PMMA in 0.1 seconds using injection pressure of about 16 MPa, as illustrated in Fig. 1(b).

A three-mould-insert system were designed in this work since it makes both filling and demoulding process much easier in order to achieve sharp tipped and hollow microneedles [4]. The upper mould insert (fig. 2(a) was composed of 36 pins, fabricated using mechanical milling, installed to form the lumen structure in microneedles. The cavities in the lower mould insert and the pin alignment holes on the third mould insert were fabricated using Micro Electrical Discharge Machining (μ-EDM)and the whole microneedle mould was made of high temperature alloy (SKD11) in order to enhance the corrosion resistance and wear resistance with less thermal expansion stress.

MICROINJECTION MOULDING

The microinjection mould insert was carefully aligned inside the mould base through the alignment pins and the mould guide to ensure proper matching of the cavities. The mould insert and mould based were then installed into the MircroPower-5t microinjection moulding machine, as shown in Fig. 3, to investigate the capability of microinjection moulding process for the production of microstructure.

Figure 3: Optical images of (a) MicroPower-5t microinjection moulding machine and (b) the installed microneedle mould.

The machine temperature was set at 230 °C to maintain the PMMA in the molten state. The shot size of 1 ccm was selected. Using large shot size (greater than 1 ccm), flush will occur. The clamping force was 5 tons (5000 kg) and the injection pressure was found to be 120 MPa. Both of these parameters are close to the maximum capacity of the MicroPower-5t. Complete polymer based microneedle patch fabricated using microinjection moulding is illustrated in Fig. 4.

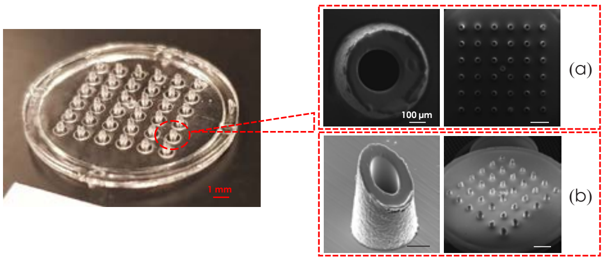

Figure 4: The fabricated microneedle using microinjection moulding technique. The right figures indicate the SEM image of microneedles, (a) top view and (b) side view.

FABRICATION OF MICRONEEDLES USING X-Ray LITHOGRAPHY

In this section, fabrication of the microneedle using x-ray lithography has been study. The PMMA was doubly exposed with x-ray radiation from synchrotron radiation at SLRI. The sharp tipped of the microneedle was created using inclined technique. 750 µm thick of PMMA sheet was firstly exposed (fig. 5(a)) forming the vertical needle. In second exposure, the substrate was tilted for 30° in order to create the sharp tipped needlesas shown in fig. 5(b). After development, it was found that the needle shape was initiatively formed on the PMMA (fig. 5(c)). However,the sharp tipped structure wasnot completed. The exposure time, deep x-ray exposure angle (exposure of an inclined plane), and a gap between the gold absorber mask and PPMA, are ongoing for the optimization of fabricated microneedle using X-ray lithography.

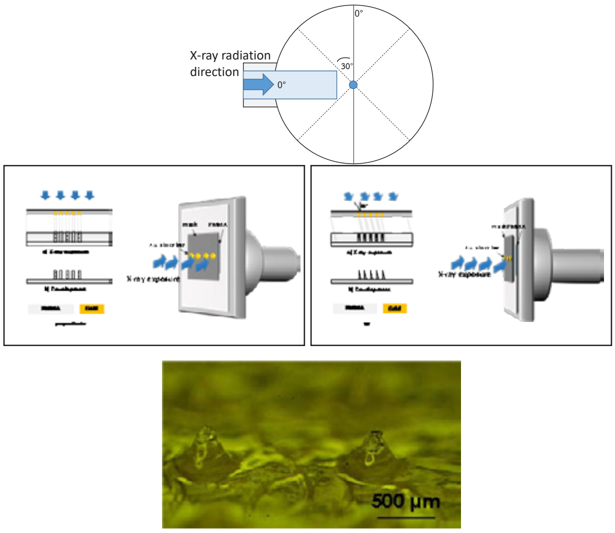

(c)

Figure 5: The fabrication of microneedle using X-ray lithography; (a) schematic diagram of first exposure (b) the second step to create the sharp tipped needles (c) the fabricated microneedles.

REFERNCES

[1] G. Ma, C. Wu,"Microneedle, bio-microneedle and bio-inspired microneedle: a review",*J Control Release*, 251:11–23, 2017.

[2] S. Indermun, R. Luttge, Y.E. Choonara, et al., "Current advances in the fabrication of microneedles for transdermal delivery",*J Control Release*, 185:130–8, 2014.

[3] E. Larrañeta, R.E.M Lutton, A.D. Woolfson, R.F. Donnelly,"Microneedle arrays as transdermal and intradermal drug delivery systems:materials science, manufacture and commercial development",*Mater Sci Eng Rep*, 104:1–32, 2016.

[4] K.L. Yung, Y. Xu, Ch. Kang, et al., "Sharp tipped plastic hollow microneedle array by microinjection mould", *J. Micromech. Microeng*, 22: 015016, 2012.

CONTECT

*Pattanaphong Janphuang, tel: +66-4421-7040 ext. 1433; Pattanaphong@slri.or.th

SYNCHROTRON X-RAY ABSORPTION SPECTROSCOPY STUDY OF LOCAL STRUCTURE IN STRONTIUM-DOPED HYDROXYAPATITE

A. Bootchanont[1], W. Sailuam[2], S. Sutikulsombat[3,4], L. Temprom[4], N. Chanlek[5],*
P. Kidkhunthod[5], P. Suwanna[4], R. Yimnirun[2]
[1]Division of Physics, Faculty of Science and Technology, Rajamangala University of Technology
Thanyaburi, 39 Moo 1, Khlong Luang District, Pathumthani 12110, Thailand
[2]School of Physics, Institute of Science, Suranaree University of Technology, and COE-NANOTEC-SUT
on Advanced Functional Nanomaterials, 111 University Avenue,
Muang District, Nakhon Ratchasima 30000, Thailand
[3]Materials Science and Nanotechnology Program, Faculty of Science,
Khon Kaen University, 123 Moo 16 Mittapap Road, Muang District, Khon Kaen 40002, Thailand
[4]Department of Materials Science, Faculty of Science, Kasetsart University,
50 Ngam Wong Wan Road, Chatuchak, Bangkok 10900, Thailand
[5] Synchrotron Light Research Institute (Public Organization), 111 University Avenue, Muang District,
Nakhon Ratchasima 30000, Thailand

ABSTRACT

Sr-doped hydroxyapatite (HAp) materials were prepared by a sol-gel method and their overall structure, investigated by X-ray diffraction, showed a mixture of hydroxyapatite and β-calcium phosphate (TCP)) crystals. The Sr*L3*-edge XANES spectra were measured and compared with simulated XANES spectra obtained from the FEFF8. 2 program in conjunction with first-principles calculations by density functional theory (DFT). Based on the good agreement between the experimental and calculated local environment results, the conclusion could be drawn that Sr substitutes on the hydroxyapatite Ca1 site close to the phosphate (-PO_4) group capable of bonding with living osseous tissues, while the substitution of Sr^{2+} cations at the other sites was unlikely in bone-based compounds.

INTRODUCTION

Bone, the major structure present in a human body, serves as mechanical support for the body and as the major storage of calcium and phosphate ions necessary for a wide variety of metabolic functions [1]. Osteoporosis, a disease of the bones, is viewed as a major public health issue. The problem of osteoporotic bone has widely been studied for better treatment of osteoporosis patients**.** The most important dysfunctions in natural bone are an imbalance of bone building, bone resorption predomination, and bone density reduction over time. One of the most widely used medicines in the treatment of osteoporosis is strontium ranelate or a strontium (II)salt of ranelic acid, which is used orally in the form of drugs [2-4].

The addition of strontium (Sr^{2+}) to osteoporosis patients is believed to lead to an activity of new bone tissue. This includes stimulation of the Wn/β-catenin signaling pathway [4], which affects the self-regeneration of stem cells and shows anti-fracture efficacy for osteoporosis treatment. Therefore, strontium is key to osteoporosis treatment.

In recent research, scientists believe that the Sr^{2+} cations substitute on Ca^{2+} sites in biological apatites. Therefore, the localization of Sr^{2+} cations in bone-based materials has widely been investigated [2-9]. However, each region of the biological bone is a rather complex structure. The dysfunctions of bone in osteoporosis patients are caused by Ca-deficiency in $Ca_5(PO_4)_3(OH)$crystals. Hydroxyapatite includes two types of calcium cations, referred to as Ca1 and Ca2. The atoms of calcium Ca1 are located at the edges of a hexagonal unit cell, near the Ca around -PO_4 group capable of bonding with living osseous tissues and associated with strong bones [10-13], while the atoms of calcium Ca_2 form equilateral triangles with the column of structural hydroxyl groups in the middle [14]. Generally, it is well known that the hydroxyl (-OH) groups are highly reactive and exhibit antibacterial behavior [15,16]. Because -OH groups can oxidize the cell wall of bacteria, which will be terminated**.** In recent research, the Zn^{2+} modified-HAp was found to enhance the antibacterial properties such as S**.** aureus, S. epidermidis, and P. aeruginosa [16,17]. A few years later, researchers found that Zn^{2+} substitute on Ca around -OH group of HAp [18,19]. Therefore, it is possible that the Ca around -OH group of HAp have impact on the antibacterial properties. However, the Sr^{2+} substitution modifies their thermal stability, solubility, textural properties, and surface reactivity**.** Therefore, local sites of Sr^{2+} contribute to both increased activations of the new bone tissue and reduced fracture risk [2,3].

In this work, we focus on identifying the local site of Sr^{2+} on hydroxyapatite material by employing a synchrotron-based X-ray Absorption Spectroscopy technique, which is associated with the excitation of core electrons to unoccupied states, and exhibits the interference of backscattering with neighboring atoms. Thus, information about the local arrangement of atoms around the absorbing atoms can be obtained from this technique, which is suitable for fingerprint investigations of complex, inhomogeneous materials.

EXPERIMENTAL

Hydroxyapatite powders were synthesized by a sol-gel method. High purity calcium nitrate tetrahydrate($Ca(NO_3)_2$. 4H2O, QRèC), di-ammonium hydrogen phosphate, ($(NH_4)_2HPO_4$, QRèC), and strontium acetate ($Sr(CH_3COO)_2$, SIGMA ALDRICH) were used as starting materials. The materials were weighed according to the Ca:Sr:P mole ratio of 9:1:6. Calcium nitrate tetrahydrate was first dissolved in ethanol, after then Sr precursors were added by 5 mol% of Ca (called as Ca solution). Di-ammonium hydrogen phosphate was separately dissolved in deionized water (called as P solution). Both solutions were quickly mixed until the gel was formed. The gel was set at room temperature for 24 hours and then was dried at 80 °C. The dried powders were calcined at a temperature of 600 °C for 2 h with 5°C/ min heating rates [17,20]. The global structure was investigated by the X-ray diffraction technique. XRD patterns were scanned in 2θ range of 20°-60° with a 0.02° steps and CuKα radiation was used.

The local structure was investigated at ambient temperature using Synchrotron X-ray Absorption Spectroscopy (SXAS) measurement at BL5.2 of the Siam Photon Laboratory, Synchrotron Light Research Institute (SLRI), Thailand (with electron energy of 1.2 GeV and beam current 80-120 mA). The synchrotron X-ray beam with energy step of 0.20 eV was provided to excite the electrons in Sr*L3*-edge. The Sr*L3*-edge X-ray Absorption Near-Edge Structure (XANES) spectra were obtained in florescence mode.

COMPUTATIONAL

Density functional theory (DFT) calculations were employed to obtain first-principles predictions of the defect stability. All calculations employed the generalized gradient approximation (GGA) exchange-correlation functional and projector-augmented wave (PAW) pseudopotentials as implemented in the Vienna Ab Initio Simulation Package (VASP). For HAp structure, the cutoff for plane wave expansions was 520 eV. For geometry and cell optimizations of bulk structures, k-point setting by Monkhrost-Pack scheme grid k-point as a 5 x 5 x 5 mesh and a common unit cell size containing 44 atoms (10 Ca atoms, 6 P atoms, and 28 O atoms) were used. For β-TCP structure, the cutoff for plane wave expansions was 260 eV. Energies and forces were converged to 0.0001 eV per atom and 0.001 eV/Å, respectively. For geometry and cell optimizations of the bulk structures, k-point setting by Monkhrost-Pack scheme grid k-point as a 1 x 1 x 1 mesh and a common unit cell size containing 276 atoms (66 Ca atoms, 42 P atoms, and 168 O atoms) were used.

RESULTS AND DISCUSSION

X-ray diffraction patterns of Sr-doped hydroxyapatite (HAp), as shown in Figure 1, indicated the mixture of the hydroxyapatite and the beta-$Ca_3(PO_4)_2$(β-TCP) phases, which could be matched with JCPDS file No. 74-0566 and 09-0169, respectively. These compound phases represent calcium phosphate-based bones in human body. In addition, Sr compounds were not observed as separated phase, an indication of a complete substitution of Sr in the prepared materials. It should be noted here that XRD measurements generally show direct evidence for the periodic atomic structure of crystals which measure the average spacing between planes of atoms. Therefore, the XRD results show an overview of the crystal structure of the compounds present in the material. If Sr is substituting in Ca sites of HAp, it will slightly affect XRD data. However, this slight change will only lead to the changes in the lattice parameters, it will not permit the direct identification of the location of the substituted lattices. The XAS measurements were employed to obtain this local site information.

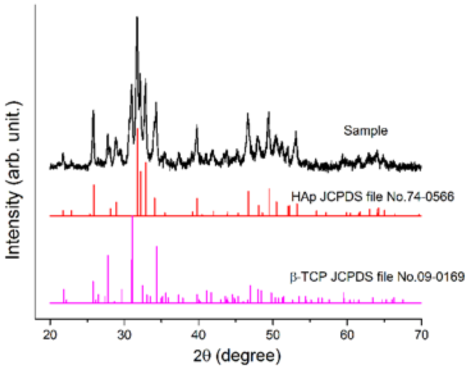

Figure 1: XRD pattern of Sr-doped hydroxyapatite material.

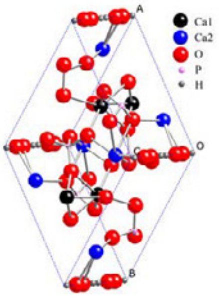

Figure 2: Crystal structure of hydroxyapatite (Hap) material.

Generally, X-ray Absorption Near-Edge Structure (XANES) measures the excitation of core electrons to unoccupied conduction states, and exhibits oscillations associated with spherical electron waves that scatter from neighboring atoms. Thus information about the local arrangement of atoms around the absorbing atoms can be obtained [21-26]. Figure 2 shows the crystal structure of hydroxyapatite with different local sites of Ca. Structural models of Sr in Ca1 and Ca2 site of hydroxyapatite crystal (a= 9.41898, c= 6.88119) [27] are represented with black and blue balls, respectively. Both sites are surrounded by 8-fold oxygen coordination with different distances. The crystal structure of β-TCP (a=10.4352, c=37.4029) [28] with different local sites of Ca is shown in Figure 3. The Ca1, Ca2 and Ca3 sites are surrounded by 8-fold oxygen coordination and the Ca4 and Ca5 are surrounded by 6-fold and 9-fold oxygen coordination, respectively. To ensure the structural stability, the crystal structures of Sr-substituted HAp were first obtained by DFT calculations with the GGA approximation used in each case, as described earlier. The Sr*L3*-edge XANES simulated spectra were then obtained using the FEFF8.2 code.

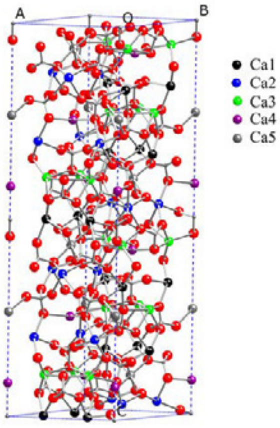

Figure 3: Crystal structure of β-Ca3(PO4)2 material.

The normalized Sr *L3*-edge XANES spectra of Sr-doped hydroxyapatite powders and the corresponding simulated XANES spectra are shown in Figure 4. Several key features can be observed in the measured Sr*L3*-edge XANES spectra. First of all, the absorption edge (as indicated by a solid vertical line) clearly indicates that the oxidation number of Sr corresponds to Sr^{2+} (with the absorption edge matching that of SrCO3). From a qualitative comparison between the measured and simulated spectra, the features (indicated by arrows) of the simulated XANES spectra at around 1953 eV and 1968 eV, suggest that Sr substitutes on Ca1 site of HAp. Since the local sites of Ca1 are close to -PO_4 group and Ca2 are close to -OH group, this implies that the substituting Sr atoms are surrounded by -PO4 groups in HAp structure.

As shown in Figure 5, the simulated Sr*L3*-edge XANES spectra with Sr substitution in β-TCP structure indicate that the Sr^{2+} cations substitute on Ca1, Ca2 and Ca3 sites, which have 8-fold oxygen coordination with different distances, similar to Ca1 and Ca2 sites in hydroxyapatite. The results show that the simulated spectral features of Sr in β-TCP structure do not match with the measured spectra. It should be noted that the difference between the data and simulations points to the fact that the presumed local substitution sites in the simulation do not reflect the actual substitution sites in the structure. These results clearly indicate that the features of the measured XANES spectra are consistent with the calculation of Sr^{2+} cations on Ca1 site of HAp structure, while they are inconsistent with calculations of Sr^{2+} cations on Ca2 sites of HAp structure and the whole sites of β-TCP structure in bone-based compounds. The simulated spectral features of Sr in β-TCP structure and Ca2 in HAp structure do not match with measured spectra. On the other hand, the simulated result of Sr on Ca1 site in HAp structures shows a good match with the measured spectra, as shown by the arrows in Figure 4. The finding from this work can possibly be linked to the dysfunctions of bone in osteoporosis patients which is caused by Ca in Ca1 site of HAp. The Sr-based drug substituting on Ca can contribute to creation of the network of bonding with living osseous tissues and to reduction of fracture risk [12]. This makes it possible for Sr around -PO_4 group to stimulate and repair the linked dysfunctional bones, resulting in stronger bones.

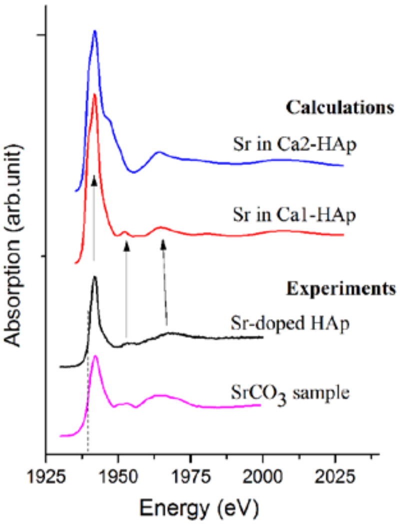

Figure 4: The normalized Sr L3-edge XANES spectra of Sr doped hydroxyapatite sample; experimental and calculated spectra, showing Sr substitutes on Ca1 and Ca2 sites in hydroxyapatite.

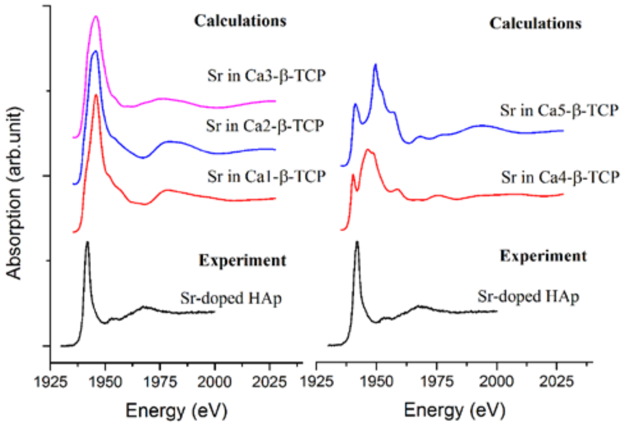

Figure 5: The normalized Sr L3-edge XANES spectra of Sr doped hydroxyapatite sample; experimental and calculated spectra, showing Sr substitutes on Ca1, Ca2, Ca3, Ca4 and Ca5 sites in β-TCP crystal.

CONCLUSION

The structural investigations of Sr-doped hydroxyapatite have been carried out by using XRD and synchrotron XAS techniques. The XRD results showed the mixed phase of hydroxyapatite and β-Calcium phosphate. The Sr L3-edge XANES spectra were measured and these data compared with simulation of XANES spectra obtained by using first principles density functional simulations of electronic and atomic structure along with spectra calculations done by the FEFF8.2 program. The XAS results clearly indicated the substitution of Sr^{2+} ions on Ca1 site of HAp structure close to PO_4 group, while the substitution of Sr^{2+} cations at the other sites was unlikely in bone-based compounds.

ACKNOWLEDGMENTS

The computing resources were provided by Computational Materials Physics Project, SLRI, Thailand. This work was supported by Rajamangala University of Technology Thanyaburi. The authors are thankful to Asst. Prof. Dr. Michael F. Smith of School of Physics, Institute of Science, Suranaree University of Technology, Thailand for help with technical and English editing.

REFERENCES

[1] S. V. Dorozhkin and M. Epple, Biological and Medical Significance of Calcium Phosphates, Chem. Int. Ed. 41 (2002)3130 -3146.

[2] D. Bazin, M. Daudon, Ch. Chappard, J. J. Rehr, D. Thiaudiere and S. Reguer, The status of strontium in biological apatite: an XANES investigation, J. Syn. Rad., 18 (2011)912-918.

[3] D. Bazin, A. Dessombz, C. Nguyen, H. K. Ea, F. Liote, J. J. Rehr, Ch. Chappard, S. Rouziere, D. Thiaudiere, S. Reguerand M.Daudon, The status of strontium in biological apatite: an XANES/EXAFS investigation, J. Syn. Rad. 21 (2014)136-142.

[4] J. Abert, C. Bergmann, H. Fischer, Wet chemical synthesis of strontium-substituted hydroxyapatite and its influence on the mechanical and biological properties, Ceram. Int. 40 (2014)9195-9203.

[5] K. L. Wong , C. T. Wong, W. C. Liu, H. B. Pan, M. K. Fong, W. M. Lam, W. L. Cheung, W. M. Tang, K. Y. Chiu, K. D. K. Luk and W. W. Lu, Mechanical properties and in vitro response of strontium-containing hydroxyapatite/polyetheretherketone composites, Biomaterials. 30 2009 3810-3817.

[6] T. Kokubo, H-M Kim and M. Kawashita, Novel bioactive materials with different mechanical properties, Biomaterials. 24 (2003)2161-75.

[7] J. Terra, E. Rodrigues Dourado, Jean-Guillaume Eon, Donald E. Ellis, G. Gonzalez and A. Malta Rossi, The structure of strontium-doped hydroxyapatite: an experimental and theoretical study, Phys. Chem. Chem. Phys. 11 (2009)568-577.

[8] L. Sopyan, C. M. Mardziah, A. R. Toibah, S. Ramesh, Synthesis of Strontium-doped Hydroxyapatite Powder via Sol-Gel Method, Adv. Mater. Res. 47-50 (2008)928-931.

[9] C. M. Mardziah, I. Sopyan and S. Ramesh, Strontium-Doped Hydroxyapatite Nanopowder via Sol-Gel Method: Effect of Strontium Concentration and Calcination Temperature on Phase Behavior, Trends Biomater. Artif. Organs. 23 (2009)105-113.

[10] M. Vallet-Reg and J. Marıa Gonza´lez-Calbet, Calcium phosphates as substitution of bone tissues, Sol. State Chem. 32 (2004)1-31.

[11] I. Manjubala, M. Sivakumar, R.V. Sureshkumar and T.P. Sastry, Bioactivity and osseointegration study of calcium phosphate ceramic of different chemical composition, J. Biomed. Mater. Res. 63 (2002)200-8.

[12] J-HoPark, D-Y Lee, K-T Oh, Y-K Lee, K-M Kim, K-N Kim, Bioactivity of calcium phosphate coatings prepared by electrodeposition in a modified simulated body fluid, Mater. Lett. 60 (2006)2573-2577.

[13] Y. Zhu, Q. Liu, P. Xu, L. Li, H. Jiang and Y. Bai, Bioactivity of calcium phosphate bioceramic coating fabricated by laser cladding, Laser Phys. Lett., 13 (2016)5.

[14] Joanna Kolmas, EwaGroszyk, and DagmaraKwiatkowska-Różycka, Substituted Hydroxyapatites with Antibacterial Properties, BioMed. Research Inter., 2014 (2014)178123.

[15] H.S. Ragab, F.A. Ibrahim, F. Abdallah, A. Al-Ghamdi., F. El-Tantawy, N. Radwan, and F. Yakuphanoglu, Synthesis and in vitro antibacterial properties of hydroxyapatite nanoparticles, Pharm. Biol. Sci. 9 (2014)77-85.

[16] M. C. Dodd, H-P E. Kohler and U. von Gunten,

Oxidation of Antibacterial Compounds by Ozone and Hydroxyl Radical: Elimination of Biological Activity during Aqueous Ozonation Processes, Environ. Sci. Technol., 43 (2009)2498-2504.

[17] L. Temprom, S. L. Seet, P. Tippayawat, P. Suwanna, Bioactivity, Cytotoxicity and Antibacterial Evaluation of Undoped, Zn-doped, Sr-Doped, and Zn/Sr-codoped Hydroxyapatites Synthesized by a Sol-Gel Method, Chiang Mai J. Sci. 43 (2016)1-11.

[18] K. Matsunaga, H. Murata, T. Mizoguchi, A. Nakahira, Mechanism of incorporation of zinc into hydroxyapatite, ActaBiomaterialia, 6 (2010)2289-2293.

[19] Yuanzhi Tang, Helen F. Chappell, Martin T. Dove, Richard J. Reeder and Young J. Lee, Zinc incorporation into hydroxylapatite, Biomaterials, 30 (2009)2864-2872.

[20] K. P. Sanosh, Min-Cheol Chu, A. Balakrishnan, T. N. Kim, Seong-Jai Cho, Preparation and characterization of nano-hydroxyapatite powder using sol-gel technique, Bullet. Mater. Sci. 32 (2009)465-470.

[21] J. J. Rehr and R. C. Albers, Theoretical approaches to x-ray absorption fine structure, Rev. Mod. Phys. 72 (2000)3.

[22] L. Hedin and S. Lundqvist, Explicit local exchange-correlation potentials, Solid State Phys. 23 (1969)1.

[23] C. Laulhé, F. Hippert, J. Kreisel, M. Maglione, A. Simon, J. L. Hazemann and V. Nassif, EXAFS study of lead-free relaxor ferroelectric BaTi1−xZrxO3 at the Zr K edge, Phys. Rev. B, 74 (2006)014106.

[24] A. Bootchanont, J. Jutimoosik, S. Chandarak, M. Unruan, P. Kidkhunthod, W. Klysubun, S.Rujirawat, R. Yimnirun, R. Guo and A. Bhalla, Synchrotron X-ray Absorption Spectroscopy Study of Local Structure Transformation Behavior in Perovskite Ba(Ti,Zr)O3 System, J. Alloys. Compd. 616, (2014)430-435.

[25] A. Bootchanont, N. Triamnak, S. Rujirawat, R. Yimnirun, D. P. Cann, R. Guo, and A. Bhalla, Local structure and evolution of relaxor behavior in BaTiO3-Bi(Zn0.5Ti0.5) O3 ceramics, Ceram. Int. 40, (2014)14555-14562.

[26] A. Bootchanont, S. Rujirawat, R. Yimnirun, R., R. Guo and A. Bhalla, Local structure study of phase transition behavior in Ba (Ti,Sn)O3 perovskite by X-rayabsorption fine structure, Ceram. Int. 42, (2016)8151-8154.

[27] L.I. Ardanova, E.I. Getman, S.N. Loboda, V.V. Prisedsky, T.V. Tkachenko, V.I. Marchenko, V.P. Antonovich, N.A. Chivireva, K.A. Chebishev, A.S. Lyashenko, Inorganic Chem. 49 (2010)10687-10693.

[28] Y. Masatomo, S. Atsushi, K. Takashi, H. Akinori, Crystal structure analysis of β-tricalcium phosphate Ca3(PO4)2 by neutron powder diffraction, J. Solid State Chem. 175 (2003)272-277.

CONTACT

* Atipong Bootchanont, tel: +66-849550910; atipong_b@rmutt.ac.th

X-RAY ABSORPTION SPECTROSCOPY INVESTIGATION OF RELATIONSHIP BETWEEN MAGNESIUM VACANCY AND MAGNETIC PROPERTIES OF MAGNESIUM OXIDE POWDER

A. Khamkongkaeo[1], W. Klysubun[2], T. Boonchuduang[1], W. Sailuam[2],
P. Sriwattana[3], T. Phetrattanarangsi[1], K. Srimongkon[4], B. Sakkomolsri[5],
A. Pimsawat[5,6,7], S. Daengsakul[5,6,7], P. Kidkhunthod[2], A. Bootchanont[8], B. Lohwongwatana[1]*
[1]Innovative Metals Research Unit, Faculty of Engineering, Chulalongkorn University,
254 Phayathai Road, Pathumwan, 10330 Thailand
[2] Synchrotron Light Research Institute (Public Organization), 111 University Avenue,
Muang District, Nakhon Ratchasima 30000, Thailand
[3]International school of Nano-Engineering (ISE), Chulalongkorn University,
254 Phayathai Road, Pathumwan, 10330 Thailand
[4]Department of Applied Physics, Faculty of Engineering, Rajamangala University of Technology ISAN (Khon Kaen Campus), 150 Sirchan Road, Muang District, Khon Kaen 40000, Thailand
[5]Department of Physics, Faculty of Science, Khon Kaen University, Thailand
[6]Nanotec-KKU Center of Excellence on Advanced Nanomaterials for Energy Production and Storage, KhonKaenUniversity, 123 Moo 16 Mittapap Road, Muang District, Khon Kaen 40002, Thailand
[7]The Integrated Nanotechnology Research Center, Khon Kaen University, 123 Moo 16 Mittapap Road, Muang District, Khon Kaen 40002, Thailand
[8]Division of Physics, Faculty of Science and Technology, Rajamangala University of Technology Thanyaburi, 39 Moo 1, Khlong Luang District, Pathumthani 12110, Thailand

ABSTRACT

This paper reports on the ferromagnetism of MgO powder and degraded powder at room temperature. The $Mg(OH)_2$ was calcined at 450°C for 5 h. The calcined powder was separated into two batches (i) kept in vacuum sealed (MgO-F) and (ii) kept at ambient environment (at 45-55% relative humidity) for 2 days (MgO-D). The samples were characterized by XRD, VSM, XANES and EXAFS. The results confirmed that MgO phase in MgO-F. Both $Mg(OH)_2$ and MgO compositions were found in MgO-D. The origin of ferromagnetism at room temperature of MgO-F and MgO-D is attributed to the Mg vacancies in the MgO structure that revealed and verified by XAS results.

INTRODUCTION

Magnesium oxide (MgO) is an advanced metal oxide that exhibits a much larger tunneling magnetoresistance (TMR) ratio due to its wide band gap [1] and diamagnetic behavior [2-4]. However, some articles have reported that MgO exhibits ferromagnetism at room temperature[5, 6]; this could lead to a change in the efficiency of tunneling barrier. In 2005, Coey reported [7] the contradiction of the widely accepted localized or band theory magnetism via four material systems exhibiting d^0 ferromagnetism. The magnetization of the material caused by the absence of metallic atoms in the structure resulted in the unpaired electrons in oxygen atoms nearby to couple each other and form a magnetic inducing region inside the bulk material [8, 9]. Both theoretical and experimental procedures have been conducted to pinpoint the origin of the d^0 ferromagnetic behavior in MgO in relation to the density of defects and impurities in the structure, but still to date there are no concrete evidence to proof such relationship [10, 11].

In this work, commercial $Mg(OH)_2$ powder (>95%purity, Hi Media Laboratories Pvt. Ltd, India) was used as a starting material to obtain MgO powder that contained a certain level of defect in the cubic structure. Commercial MgO powder (99.99% purity, Sigma-Aldrich Co. LLC.) was studied in comparison to investigate the local structure using XAS including XANES and EXAFS to gain better insight regarding the relationship between the local structure and the ferromagnetism of MgO.

MATERIALS AND METHODS

MgO powders preparation

In the preparation of MgO powders, commercial $Mg(OH)_2$ powder was used as a raw material. The elemental composition of the raw material was analyzed by XRF. The commercial $Mg(OH)_2$ powder consists of Mg (41.50 wt%), Ca (0.20 wt%), S (0.15 wt%), with a minute amount of Cl, Si, Fe, Sr, Br (ppm) and light elements (i.e. O and H) for balance. Commercial $Mg(OH)_2$ powder was calcined at 450 °C for 5 h in air. The calcined powder was separated into two batches (i) the powder that kept in vacuum sealed bag (MgO-F) and (ii) the powder that kept at ambient environment (30-32 °C at 45-55% relative humidity) for 2 days (MgO-D).

Structural characterizations

The MgO-F and MgO-D were characterized by XRD. XANES and EXAFS measurement were carried out in the fluorescence-yield mode at BL8:XAS beamline at the Synchrotron Light Research Institute (SLRI). The spectra were recorded at room temperature in a photonenergy region of the Mg K-edge. The photon energies were scanned by a Beryl $(10\bar{1}0)$double crystal monochromator and calibrated against the K-edge of Mg metal (1303 eV) using Mg foil. The storage ring was operated at energy of 1.2 GeV with electron currents decaying from 110 mA to 70 mA. The absorption was determined by I_f/I_0 and normalized using the ATHENA software [12]. The normalization procedure was described elsewhere [13] as well as in the Athena Users' Manual [12]. The EXAFS data were processed using a Fourier transformation procedure in the Artemis software[12] with the following parameters: Hanning window, k range of 2.5 $Å^{-1}$and 7 $Å^{-1}$, k^3 weight, dk= 1 $Å^{-1}$ and Rbkg= 1.

Magnetic measurement

Magnetic properties of all samples were studied at room temperature with a vibrating sample magnetometer (VersaLabTM-3 Tesla, Cryogen-free, Quantum Design, Inc., USA) by varying applied field ±1.6 x 10^5 A/m.

Computational methodology

First principles density functional theory (DFT) calculations with the generalized gradient approximations (GGA) as the exchange correlation (XC) functional [14] was employed to understand the origin of ferromagnetism in $Mg(OH)_2$. The ultrasoft pseudopotentials with the projector augmented wave method as implemented in the VASP package [15] were used. A typical $Mg(OH)_2$ bulk unit cell consists of 5 atoms. A 2 x 2 x 2 supercell containing 80 atoms of host $Mg(OH)_2$ was used to study various vacancies. The plane wave expansions (up to 520 eV) and the k-point samplingof the Brillouin zone for density of state (DOS) were used for basisset. Moreover, 6 x 6 x 6 Monkhorst-Pack scheme was used in this work [16]. The calculations were converged when the acting forces on each atom was less than 0. 1 meV/Å; such parameters corresponded to the total energies convergence of ~0.1 meV/atom.

RESULTS AND DISCUSSION

Crystal structures

XRD patterns of the MgO-F and the MgO-D were shown in Figure 1. The diffraction peaks of the MgO-F were indexed as only the cubic structure of MgO. The same result, not shown here, was found for the commercial MgO powder. On the other hand, the MgO-D displayed both MgO and $Mg(OH)_2$. The $Mg(OH)_2$ in the MgO-D was likely due to MgO that has highly hygroscopic reaction [17] with humidity in ambient environment.

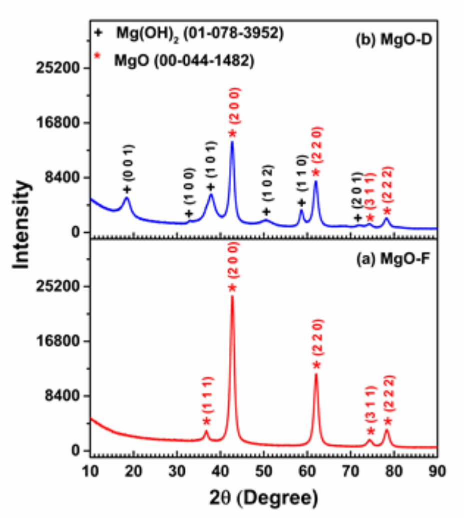

Figure 1: XRD of (a)MgO-F and (b)MgO-D.

Magnetic behavior

Figure 2, the ***M-H*** curves of the commercial $Mg(OH)_2$ powder, MgO-F and MgO-D showed ferromagnetic behavior while only diamagnetic behavior was occurred in the MgO-C. The commercial $Mg(OH)_2$ powder exhibited the largest amplitude of ***M-H*** curve. Although the MgO-D contained both $Mg(OH)_2$ and MgO, its specific magnetization value was quite different from our previous work[18]. This may be attributed to the different ratios of MgO and $Mg(OH)_2$ compositions.

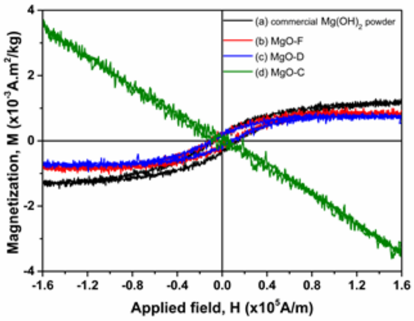

*Figure 2: **M-H** curves at room temperature for (a) commercial $Mg(OH)_2$ powder, (b) MgO-F, (c) MgO-D and (d) MgO-C.*

XANES study

The normalized XANES spectra for those samples were shown in Figure 3. The XANES feature of MgO-F and MgO-D resembled that of MgO-C. This observation was in good agreement with XANES feature of MgO reported by Yoshida et al. [19]. The comparative studied on the fraction of MgO that was formed by the dehydration of $Mg(OH)_2$ related to the estimations by XANES and XRD. The absorption edge (E_0) by taking a maximum of first derivative of MgO-F and MgO-D were in good agreement with MgO-C which corresponded to Mg^{2+}. The characteristic peaks, labeled by A, B, C and D were clearly observed. The peak A in Mg K-edge spectra was attributed to the 1s electrons transition to an unoccupied bound 3p-like state [19, 20]. However, the energy shift of peak A, towards higher energy, was observed in the following sequence: MgO-C, MgO-F and MgO-D. This was the indication that valence states of the three samples were actually different. Finally, EXAFS data revealed the origin of such difference which was related to the coordination number of the second nearest neighbor of MgO.

EXAFS study

Figure 4 showed Fourier transformin the R-space of MgK-edge EXAFS spectra of all samples. The strong peaks observed at 1.61 Å and 2.60 Å corresponded to the Mg-O and Mg-Mg coordinations, respectively. MgO has a cubic structure, in which each Mg atom is surrounded by six O atoms in the first neighbor shell, and twelve Mg atoms in the second nearest neighbor shell. For hexagonal $Mg(OH)_2$, the first shell coordination is similar to that of the cubic MgO, but the second shell has only six Mg atoms. The EXAFS features of MgO-F and MgO-D was similar to MgO-C, except that their amplitudes were significantly lower. The reduction ofpeak amplitude suggested the MgO-F and MgO-D had lower crystallinity than the MgO-C. This could be understood by the EXAFS equation [13].

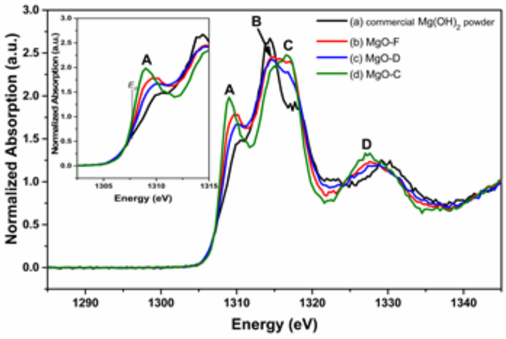

Figure 4: The Fourier transform of EXAFS spectra at Mg K-edge in R-space for (a) commercial $Mg(OH)_2$ powder, (b) MgO-F, (c) MgO-D and (d) MgO-C.

The EXAFS fitting was carried out using the Artemis software. The best fit parameters were given in Table 1. From the fitting results, the numbers of O Mg atoms in MgO phase of MgO-F and MgO-D were smaller than the perfect cubic MgO model. In addition, the EXAFS fitting shown that the numbers of O and Mg atoms in the first and second shells of commercial $Mg(OH)_2$ powder were lower than those found for MgO-D.

Table 1: The parameters from the EXAFS fitted data.

Sample	Composition	Shell	N	σ^2	R (Å)	R-factor
Commercial $Mg(OH)_2$ powder	$Mg(OH)_2$	Mg-O Mg-Mg	4.7 ± 0.9 4.7 ± 0.8	0.001 ± 0.004 0.001 ± 0.006	2.008 ± 0.006 3.037 ± 0.011	0.008
MgO-F	MgO	Mg-O Mg-Mg	5.1 ± 0.9 7.6 ± 1.4	0.003 ± 0.001 0.001 ± 0.001	2.054 ± 0.016 2.971 ± 0.022	0.005
MgO-D	MgO	Mg-O Mg-Mg	5.6 ± 0.3 9.3 ± 0.8	0.002 ± 0.001 0.009 ± 0.002	2.037 ± 0.005 2.984 ± 0.009	0.003
	$Mg(OH)_2$	Mg-O Mg-Mg	5.7 ± 0.5 5.6 ± 0.6	0.006 ± 0.002 0.001 ± 0.002	2.061 ± 0.008 2.969 ± 0.010	
MgO-C	MgO	Mg-O Mg-Mg	6 12	0.001 ± 0.001 0.0003 ± 0.0009	2.076 ± 0.021 2.960 ± 0.024	0.006

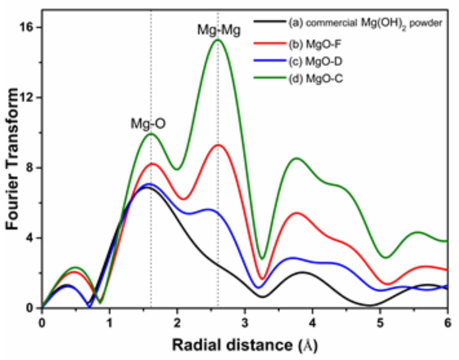

Figure 3: Normalized XANES spectra at Mg K-edge for (a) commercial $Mg(OH)_2$ powder, (b) MgO-F, (c) MgO-D and (d) MgO-C. Inset graph is a zoom view showing edge shift towards higher energy.

Therefore, we concluded that these samples have some Mg vacancies and O vacancies in MgO and $Mg(OH)_2$ structures, which were probably the cause of ferromagnetism. Although the data on the second nearest neighbor of Mg K-edge in our experiment has lower precision, could have some effect on the result, due to short k range for EXAFS refinement. The EXAFS fitting of the first and second nearest neighbors of MgO structure is in good agreement with the defect that observed by XANES spectra.

Density of state of $Mg(OH)_2$

Figure 5 showed the total density of states of (a)perfect $Mg(OH)_2$bulk, (b) neutral Mg vacancy (V_{Mg}^{0}), (c) single charged Mg vacancy(V_{Mg}^{1+}), (d) closed Mg vacancy (V_{Mg}^{2+}) and (e)neutral O vacancy (V_{O}^{0}). A single Mg and O vacancy in

$Mg(OH)_2$ were focused. The neutral Mg or O vacancy were formed by removing one Mg atom or O atom, leading to the vacancy concentration of 2.5%. Adding one and two electrons to the center of the neutral Mg vacancy simulate the single charged Mg vacancy and closed Mg vacancy. The magnetization value of perfect $Mg(OH)_2$ bulk was 0 μ_B while neutral Mg vacancy, single charged Mg vacancy and closed Mg vacancy gave the magnetization values around 2 μ_B, 1 μ_B and 0 μ_B, respectively. However, at oxygen vacancy, the magnetization is zero (shown in Figure 5(e)). The DFT calculations indicates that the Mg vacancy in $Mg(OH)_2$ is the origin of magnetic behavior. This mechanism is similar to the origin of ferromagnetism in MgO [2].

In our EXAFS experiment, MgO-C has Mg that is surrounded by six O atoms and twelve Mg atoms at the first and second nearest neighbors. The spin outer shell electrons of Mg 3s orbitals and O 2p orbitals were fully occupied therefore the total magnetic moment of the commercial MgO powder was zero. This observation corresponds to the diamagnetic behavior of this sample. On the other hand, non-zero magnetic moment of MgO-F that has only MgO composition was observed. We believed that the ferromagnetism in this sample was caused by the induction of magnetic moment from the 2p orbitals of the nearest O atoms surrounding the Mg vacancies. The evidence of Mg vacancies was confirmed by the EXAFS result. Although the MgO-D consisted of MgO and $Mg(OH)_2$ compositions, the magnetic behavior and specific magnetization value were very much similar to the MgO-F. The Mg vacancies at Mg site of MgO and $Mg(OH)_2$ played an important role for magnetic behavior of the MgO-D.

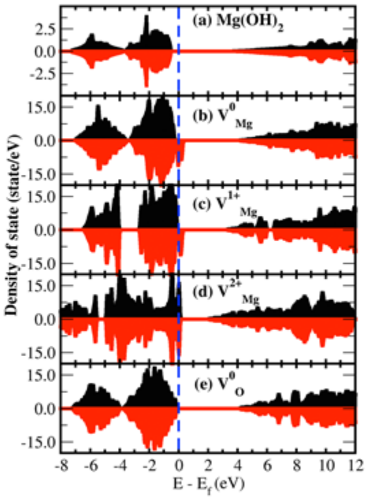

Figure 5: Total density of state of (a)Pure $Mg(OH)_2$, (b)neutral charged Mg vacancy (V_{Mg}^{0}), (c) single charged Mg vacancy (V_{Mg}^{1+}), (d) closed shell Mg vacancy (V_{Mg}^{2+}) and (e)neutral charged O vacancy (V_{O}^{0}).

In our EXAFS experiment, MgO- C has Mg that is surrounded by six O atoms and twelve Mg atoms at the first and second nearest neighbors. The spin outer shell electrons of Mg 3s orbitals and O 2p orbitals were fully occupied therefore the total magnetic moment of the commercial MgO powder was zero. This observation corresponds to the diamagnetic behavior of this sample. On the other hand, non-zero magnetic moment of MgO-F that has only MgO composition was observed. We believed that the ferromagnetism in this sample was caused by the induction of magnetic moment from the 2p orbitals of the nearest O atoms surrounding the Mg vacancies. The evidence of Mg vacancies was confirmed by the EXAFS result. Although the MgO-D consisted of MgO and $Mg(OH)_2$ compositions, the magnetic behavior and specific magnetizationvalue were very much similar to the MgO-F. The Mg vacancies at Mg site of MgO and $Mg(OH)_2$ played an important role for magnetic behavior of the MgO-D.

CONCLUSION

MgO powder was prepared by a thermal decomposition method using commercial $Mg(OH)_2$ powder as a starting material. The raw material was then calcined at 450 °C for 5 h in air to obtain MgO powder. The degraded powder was observed with 45.5% of $Mg(OH)_2$ and 54.5%of MgO compositions after keeping at ambient environment (30-32 °C at 45-55% relative humidity) for 2 days. Magnetic properties of all samples except commercial MgO powder exhibited ferromagnetic behavior at room temperature. Ferromagnetismin these samples caused by the induction of magnetic moment from the 2p orbitals of the nearest O atoms surrounding the Mg vacancies. The evidence of Mg vacancies was addressed by XAS data.

ACKNOWLEDGEMENTS

The authors would like to thank Department of Physics, Khon Kaen University for providing the VSM and XRD facilities. We thank the Synchrotron Light Research Institute (Public Organization), BL8: XAS, Nakhon Ratchasima, Thailand for providing XAS facility. We gratefully acknowledge Computing resources provided by Computational Materials Physics Project, SLRI, Thailand for magnetization calculation. This work is supported by Rachadapisek Sompote Fund for Postdoctoral Fellowship, Chulalongkorn University, Thailand.

REFERENCES

[1] V. Harnchana, A.T. Hindmarch, A.P. Brown, R.M. Brydson, C.H. Marrows, "TEM investigation of MgO thin films for magnetic tunnel junction application", *J Phys Conf Ser.*, vol. 241, pp. 012039, (2010).

[2] F.-G. Kuang, S.-Y. Kang, X-Y. Kuang, Q-F. Chen, "An ab initio study on the electronic and magnetic properties

of MgO with intrinsic defects", *RSC ADV.*, vol. 4, pp. 51366-51373, 2014.

[3] N.K. Useinov, D.A. Petukhov, L.R. Tagirov, "Tunnel magnetoresistance in asymmetric double-barrier magnetic tunnel junctions", *J Magn Magn Mater.*, vol. 373, pp. 27-29, (2015).

[4] B. B. Singh, S. Chaudhary, D. K. Pandya, " Tunneling behavior in ion-assist ion-beam sputtered CoFe/MgO/NiFe magnetic tunnel junctions", *Mater Res Bull.*, vol. 47, pp. 3786-3790, 2012.

[5] D. Chhikara, K.M.K. Srivatsa, S.K. Muthusamy, "On the synthesis and characterization of ZnO/MgO nanocomposite by thermal evaporation technique", *Solid State Sci.*, vol. 37, pp. 108-113, 2014.

[6] S. Phokha, J. Klinkaewnarong, S. Hunpratub, K. Boonserm, E. Swatsitang, S. Maensiri, "Ferromagnetism in Fe-doped MgO nanoparticles", *J Mater Sci Mater Electron.*, vol. 27, pp. 33-39, 2015.

[7] J.M.D. Coey, "d^0 ferromagnetism", *Solid State Sci.*, vol. 7, pp. 660-667, 2005.

[8] C. Peng, Y. Liang, K. Wang, Y. Zhang, G. Zhao, Y. Wang, "Possible Origin of Ferromagnetism in an Undoped ZnO d^0 Semiconductor", *J Phys Chem C*, vol. 116, pp. 9709-9715, 2012.

[9] T. Uchino, T. Yoko, "Symmetry and nonstoichiometry as possible origins of ferromagnetism in nanoscale oxides", *Phys Rev B.*, vol. 85, pp. 012407, 2012.

[10] J. Li, Y. Jiang, Y. Li, D. Yang, Y. Xu, M. Yan, "Origin of room temperature ferromagnetism in MgO films", *Appl Phys Lett.*, vol. 102, pp. 072406, 2013.

[11] J. Li, Y. Jiang, G. Bai, T. Ma, D. Yang, Y. Du, M. Yan, "Room temperature ferromagnetism of amorphous MgO films prepared by pulsed laser deposition", *Appl Phys A.*, vol. 115, pp. 997-1001, 2013.

[12] B. Ravel, M. Newville, "ATHENA, ARTEMIS, HEPHAESTUS: data analysis for X-ray absorption spectroscopy using IFEFFIT", *J Synchrotron Radiat.*, vol. 12, pp. 537-541, 2005. [13]S. Calvin, XAFS for Everyone, (2013).

[14] J.P. Perdew, K. Burke, M. Ernzerhof, "Generalized Gradient Approximation Made Simple", *Phys Rev Lett.*, vol. 77, pp. 3865-3868, 1996.

[15] G. Kresse, J. Furthmüller, "Efficiency of ab-initio total energy calculations for metals and semiconductors using a plane-wave basis set", *Comp Mater Sci.*, vol. 6, pp. 15-50, 1996.

[16]D.J. Chadi, "Special points for Brillouin-zone integrations", *Phys Rev B.*, vol. 16, pp. 1746-1747, 1977.

[17] P. Jo-Yong, L. Yun-Jo, J. Ki-Won, B. Jin-Ook, Y.D. Jae, "Chemical Synthesis and Characterization of Highly Oil Dispersed MgO Nanoparticles", *J Ind Eng Chem*, vol. 12, pp. 882-887, 2006.

[18] H. Aritani, H. Yamada, T. Yamamoto, T. Tanaka, S. Imamura, "XANES study of Li-MgO and Li-La_2O_3-MgO catalysts for oxidative coupling of methane", *J Synchrotron Radiat.*, vol. 8, pp. 593-595, 2001.

[19] T. Yoshida, T. Tanaka, H. Yoshida, S. Takenaka, T. Funabiki, S. Yoshida, T. Murata, "A XANES study on the dehydration process of magnesium hydroxide", *Physica B: Condensed Matter*, vol. 208, pp. 581-582, 1995.

[20] L. Dien, P. Mingsheng, T. Murata, "Coordination and local structure of magnesium in silicate minerals and glasses; Mg K-edge XANES study", *The Canadian Mineralogist*, vol. 39, pp. 199-206, 1999.

CONTACT

*Boonrat Lohwongwatana, tel: + 66- 81- 343- 8886; boonrat@gmail.com

TEN-YEAR SUMMARY OF SLRI

RESEARCH AT SLRI

For the last ten years SPL has been one of the main platforms for scientific research collaborations in Thailand and in Southeast Asia. Advanced material characterization techniques provided by the synchrotron have let people from the same and different fields to be in contact and initiate collaborations. Because the economy of many ASEAN countries including Thailand relies heavily on agriculture and food production, researchers in these fields are one of the first to utilize the capability of SPL develop new scientific knowledge and technology that make strong impacts. Scientific papers related to the production of rice, starch, and meats are constantly published by users and beamline scientists of SLRI over the years. For example, micro-spot infrared spectroscopy was used to map different nutrients in meat of local chicken and how fungal diseases spread in some plants. Studies of super-food such as Thai mushroom and many herbal medicines are also actively performed where researchers employ synchrotron techniques to try to understand the active ingredients in them. A few of the researches have shown evidence in the bioactivities which may be used to tackle serious illness such as cancer and Alzheimer disease. On the other end of the spectrum, scientists who study key materials in Thai industrial economy like metals and polymers used SAXS, XAS, XPS, and PEEM techniques either to develop new products or to find out the root cause of problems in production lines. Furthermore, synchrotron characterization of advanced materials used for novel electronic devices like photovoltaics, batteries and transistors at SPL were published in many major scientific journals. Synchrotron techniques are also used for applications on forensic science and cultural heritage research.

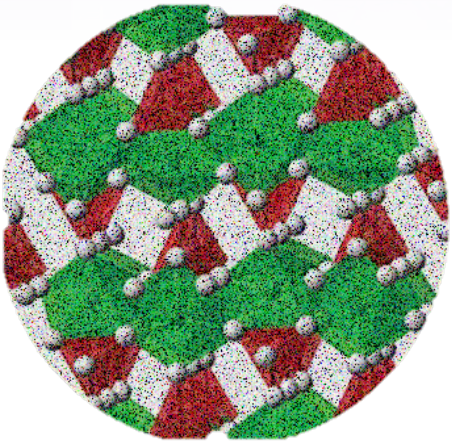

INDUSTRIAL APPLICATIONS

CHITOSAN-ZINC CHELATE VACCINE TO STIMULATEPLANT IMMUNITY AGAINST PLANT DISEASES

Chitosan is a natural polymer extracted from chitin found in the shells of shrimps and crabs as well as squid pens, etc. At present, chitosan has attracted increasing interest in agriculture applications due to its remarkable bioactivity and biodegradable properties which are non-toxic to the bio-system. Chitosan's anti-microbial and defense booster performances are utilized with the goals of controlling plant diseases before they can cause more serious economic damages and inhibiting or delaying the spread of the diseases.

The Synchrotron Light Research Institute (Public Organization) has conducted a research for Green Innovative Bio-technology Co., Ltd. to develop a formula of chitosan-zinc chelate plant vaccine to stimulate plant immunity against plant diseases. In this formula, plant vaccine with nanoscale structure of Chitosan surrounding zinc and lysine amino acid to maximize plant absorption of nutrients and amino acids. The resulting product is a high-potential plant vaccine with the unique properties of chitosan together with minerals and lysine which are essential to plant growth. The vaccine can be used to protect crops from plant diseases and to remedy crops that have already been affected by microbes, insects and mineral deficiency.

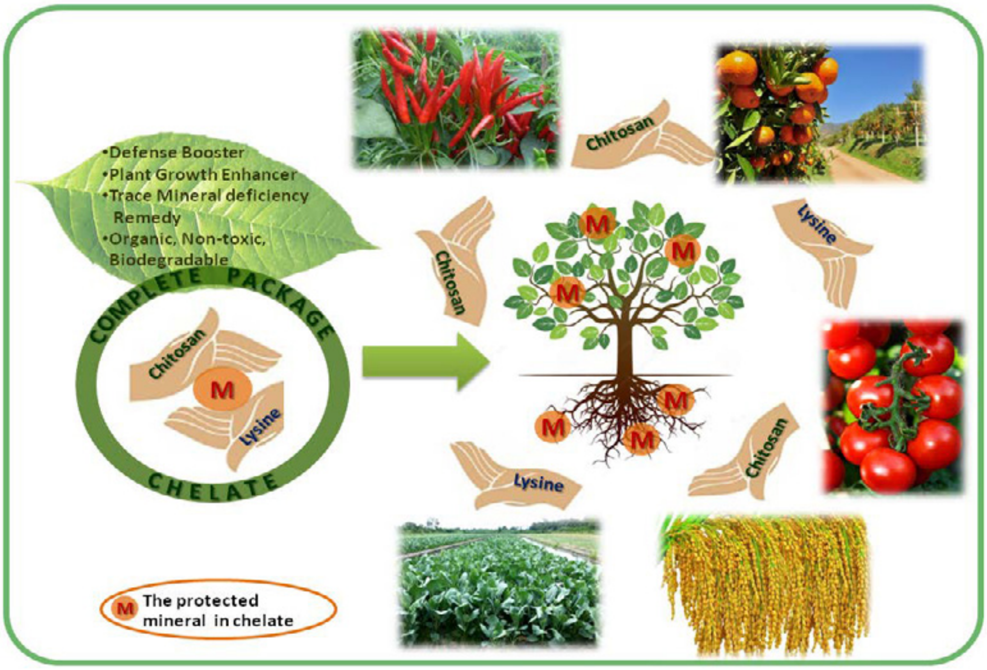

W. Kiatponglarp, P. Kitkhuntod, B. Maikhuntod,
Synchrotron Light Research Institute (Public Organization)

and *Green Innovative Bio-technology Co.,Ltd.*

STRUCTURE AND COMPOSITION OF CASSAVA WASTES

The Synchrotron Light Research Institute (Public Organization) had conducted a research for Ratchasima Green Energy Co., Ltd. involving a test of the structure, composition and characteristics of cassava wastes to identify a way to utilize cassava wastes as functional food. The research found the composition of cassava wastes to be 45-50% carbohydrate, 2-3% protein, 0-1% fat and 10-15% fiber (dry weight). Most fibers found in cassava wastes are insoluble fibers of the hemicellulose, cellulose and lignin types which are beneficial for the excretory system. They can also absorb fat from food, decrease sugar absorption and enhance weight loss by absorbing water into the digestive tract and making one feel easily full. Since fibers help relieve constipation the risk of colonic carcinoma is also reduced. In addition, cassava wastes contain a large amount of carbohydrate which can be processed into carbohydrate with fiber-like attributes but has better health benefit than consuming natural fibers. This is because the microorganisms in colons can feed on them, therefore, promoting the growth and functioning of useful bacteria in the colon by producing short chain fatty acid that is active in inhibiting carcinoma cell growth, fighting infection and enriching the immunity system as well as strengthening intestine lining, defending colonic carcinoma and boosting the immunity against diseases.

Therefore, cassava wastes can be processed into high-quality fibers. This research produces a new and innovative type of health food which can add more value to waste materials and to the company's profit. The product also creates additional value to Thailand's food and agricultural products by exporting them and generating more national income.

W. Kiatponglarp,
Synchrotron Light Research Institute (Public Organization),

P. Rawangsap,
Ratchasima Green Energy Co., Ltd.

USE OF PHOSPHATE REPLACERS IN CRYOGENIC FROZEN WHITE SHRIMP PRODUCTS

King Mongkut's University of Technology North Bangkok, in collaboration with Thailand Institute of Scientific and Technological Research, studied the use of carbohydrate compounds as phosphate replacers in cryogenic frozen white shrimp products and conducted a joint research with the Synchrotron Light Research Institute (Public Organization) in assessing the absorption and distribution of phosphate replacers in cryogenic frozen white shrimps with the FTIR Microspectroscopy technique. It was found that sorbitol, a type of sugar alcohol, can satisfactory penetrate and diffuseinto shrimp meat, therefore, increasing its ability to carry more water and inhibit protein denaturingdue tocryogenic freezing. The use of sorbitol helps to improve the quality of shrimp texture during the processing steps of cryogenic freezing storage, defrosting and heating. Therefore, the use of sorbitol as phosphate replacer can solve the problem of phosphate residues which will provide a solution to the problem of trade barriers faced by relevant industries, particularly the seafood processing industry.

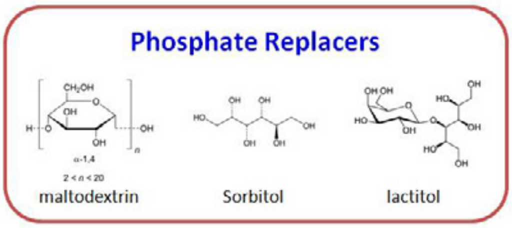

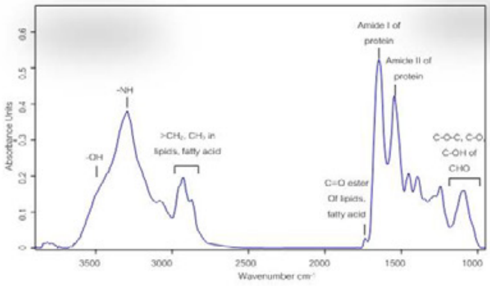

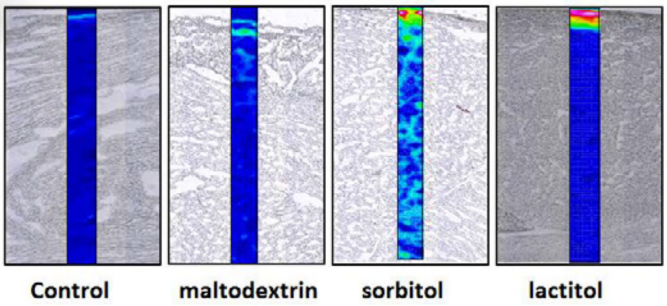

W. Kiatponglarp and C. Uthaisa,
Synchrotron Light Research Institute (Public Organization);

S. Wallapa,
Thailand Institute of Scientific and Technological Research;

N. Bussayasoros and W. Rangsartthong,
King Mongkut's University of Technology North Bangkok

TEN-YEAR SUMMARY OF SLRI

TECHNOLOGY and KNOWLEDGE TRANSFERS

Over the years of building the facilities to serve synchrotron users, SLRI engineers kept developing their skills of scientific equipment manufacturing. Many engineering know-hows have been transferred to both in-house and collaborative research and developments - from vacuum brazing and thin-film coating developed by the vacuum engineering team in collaboration with Astronomical Research Institute to prototyping medical linac for cancer treatment by the accelerator physicists and electronic Braille reader for people with visual impairment by electronic engineers working at the X-ray photolithography beamline. SLRI has already started many projects with research groups from private sectors to help pushing R&D with impacts to the economy.

In term of knowledge transfer and human resource development, SLRI has hosted several workshops and trainings annually to introduce various synchrotron techniques to newcomers and to build research community and network. Each workshops and trainings target different groups such as ASEAN synchrotron science camp which focuses on university students and young scientists, ASEAN workshops on particular techniques which aim to grad students and potential users. Not only academic sector, SLRI has also approached industrial one in order to help developing their products, solving problems and enhance their competitiveness in global market.

APPRECIATIONS

It could be undeniably said that SLRI is currently one of the most successful regional hubs for knowledge and technology exchanges in Southeast Asia. SPL is a small synchrotron but with highly appreciated helps from experts from around the world that put people together and push the community toward existence in the international research playing field.

Australian Synchrotron | diamond | ESRF | NSRRC | SPring-8 | SOLEIL SYNCHROTRON | SSRF Shanghai Synchrotron Radiation Facility

USER STATISTICS

SLRI BEAMTIME SERVICES, USER STATISTICS AND RESEARCH OUTCOMES

S. Wannapaiboon, P. Kidkhunthod, S. Tonghom, S. Rodthai, W. Chanthawat, and A. Saesong
Synchrotron Light Research Institute (Public Organization), 111 University Avenue, Muang District, Nakhon Ratchasima 30000, Thailand

ABSTRACT

Annually, Synchrotron Light Research Institute supports academic users from various disciplines to access synchrotron facilities without a service charge. Users are requested to submit the beamtime proposals via the online application system. The submitted proposals are then reviewed by the SLRI proposal review committee for scientific merit and beneficial applications prior to the beamtime allocation. A variety of research cluster proposals have been granted resulting in the high number of peer-reviewed publications with high quality as shown in the statistics. In addition, SLRI provides workshops, technical trainings, and outreach programs for users to improve their knowledge and scientific skills on synchrotron techniques. Moreover, SLRI annually organized the Annual User Meeting (AUM) to receive the feedback from users and to strengthen the SLRI user community.

SLRI BEAMTIME SERVICES

Synchrotron Light Research Institute (SLRI) provides synchrotron-based characterization techniques and complimentary facilities to researchers in various research fields including materials science, chemistry, physics, engineering, life science, earth science, and environmental science. SLRI supports academic users from universities and governmental institutes to access synchrotron facilities without a service charge. The users are expected to publish their obtained scientific knowledge and results as research publications. Not only the academia, SLRI also provides beamtime services and problem-based consultancy for private and industrial sectors, in which some fees may be applied.

Generally, SLRI operates the beamtime services in two periods each year, namely the 1st period starting from January to May and the 2nd period from September to December. Access to synchrotron beamlines at SLRI is approved through the beamtime proposals which are technically reviewed by the SLRI proposal review committee (PRC) and the responsible beamline manager (BLM) for the scientific merit and to ensure the research quality contributing to scientific advancement. Proposals for beamtime application are requested to submit online via http://beamapp.slri.or.th. In beamtime proposals, users are expected to describe the scientific background of the research project, the requested beamline, and the experimental plan. Moreover, the description of samples including their chemical and biological hazard and the corresponding safety instruction are required. Users may request the preferred date of experiment to be conducted at SLRI. After the evaluation of beamtime proposals, the beamtime services are scheduled by the responsible beamline managers. Subsequently, the User Service Division officially informs the beamtime allocation to users. Then, users are requested to confirm the allocated beamtime and the lists of participants with the User Service Division prior to visiting SLRI. In 2019, SLRI facilitates the financial support (*i.e.* local transportation and accommodation) for some national and ASEAN users, who have applied for SLRI grants and whose beamtime proposals are rated in the high ranking by the PRC. To support all current and prospective users, staffs of the User Service Division are the first point of contact for information, questions and requests concerning beamtime application process, policies for beamtime services, logistical transportation, and accommodation. Once the users arrive at SLRI, please check-in at the user lounge and proceed for the safety instruction and sample checking with the staffs of the Safety Division. After that, users will receive the SLRI access card and the personal dosimeter for working at the beamlines.

USER STATISTICS & RESEARCH OUTCOMES

SLRI facilitates synchrotron-based techniques for academic users from various disciplines through the beamtime proposal applications. Since the first beamline was publicly opened for external users in 2003, the number of users is significantly increased with respect to the number of service beamlines. Since 2017, there are totally 10 beamlines with 12 experimental end-stations available for beamtime services. Hence, the number of academic users accessing SLRI from fiscal year 2016 to 2019 is ranged between 400 and 500 users (Figure 1). The gradual increase of the total number of users from 2016 to 2019 is observed due to the addition of three fulltime-operated beamlines (*i.e.* BL1.1W, BL1.2W and BL4) and the well-established user communities of the other beamlines. Interestingly, the higher contribution of ASEAN and international users are significantly noticed from 2016 to 2019. Especially, there are 62 ASEAN users (*ca.* 13%) and 46 international users (*ca.* 9.5%) using synchrotron facilities at SLRI in 2019 (Figure 1).

Considering the number of principal investigators (PIs) from 2016 to 2019 (Figure 2), both new and continued users are increased annually. The ratio of continued users/new users is gradually expanded highlighting the enhancement of well-established user community at SLRI.

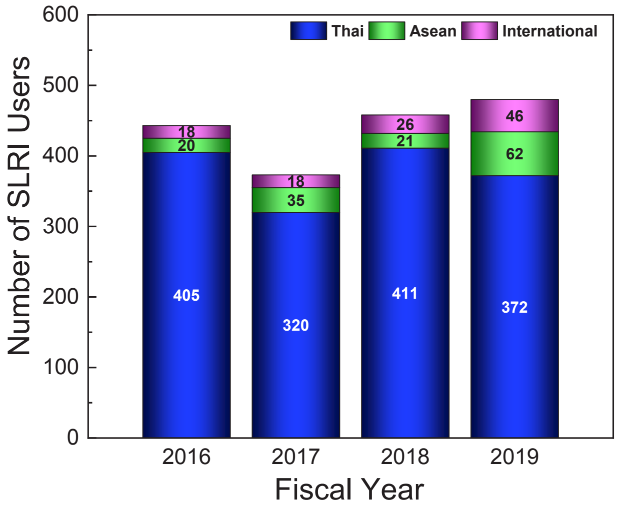

Figure 1: Number of academic users accessing SLRI for beamtime services in fiscal year 2016 to 2019 separated by a classification of country of professional affiliation.

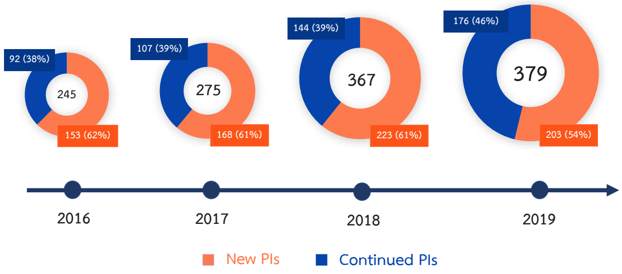

Figure 2: Number of principal investigators (PIs) in fiscal year 2016 to 2019 categorized as new PIs (orange) and continued PIs (blue), respectively. Note that, the number shown herein is the total summation of the number of PIs at each beamline. Hence, the double counting as well as multiple counting may be included.

Regarding to the 553 beamtime proposals in fiscal year 2019 (Figure 3), materials science and engineering reveals the highest contribution (221 proposals, 40%). Moreover, the beamtime proposals of surface, interface, and thin films (11%), biological and life science (11%), and chemistry (10%) also show the large fraction. This information reflects the user community of SLRI.

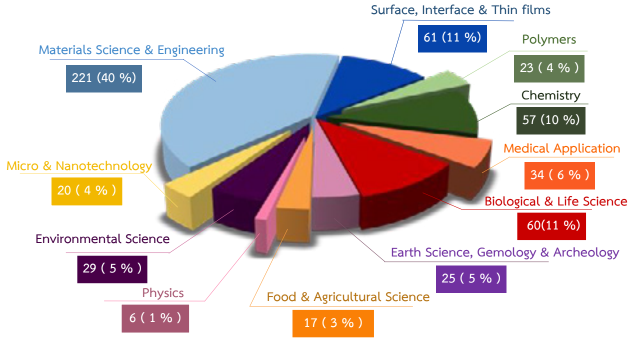

Figure 3: Number of beamtime proposals in fiscal year 2019 separated by research clusters.

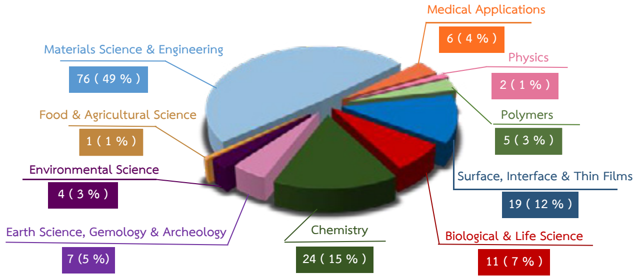

Figure 4: Number of peer-reviewed research publications in fiscal year 2019 separated by research clusters.

One of the important measurable outputs of SLRI is the number and quality of peer-reviewed publications. The number of publications has continuously increased from 2006 and eventually reached over 130 publications per year since 2017. In fiscal year 2019, there are 155 publications reported the utilization of synchrotron techniques at SLRI in their research works. Insight into the research clusters of the SLRI publications (Figure 4), the materials science and engineering cluster reveals the highest contribution (76 articles, 49%), following by chemistry (24 articles, 15%), surface interface and thin films (19 articles, 12%) and biological and life science (11 articles, 7%), respectively. Note that, the distribution of peer-reviewed publications separated by research clusters is rather correlated with the distribution of beamtime proposals. Regarding to the quality of peer-reviewed publications obtained in fiscal year 2019 (Figure 5), 98 articles (55%) are ranked in the first journal quartile (Q1). In addition, 49 articles (27%) are ranked in the second journal quartile (Q2). This obtained information indicates both the standard quality of beamline facilities and scientific advancement provided at SLRI.

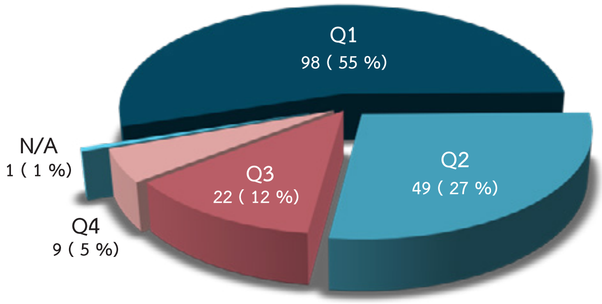

Figure 5: Number of peer-reviewed research publications in fiscal year 2019 separated by research journal quartile.

SLRI USER SERVICE ACTIVITIES

The user activities which have been annually organized by the User Service Division are categorized into 3 main groups, namely 1) outreach programs, 2) workshops and trainings, and 3) user meeting and conference. The main purpose of these activities is to strengthen experimental and analytical skills for users and to support users to achieve such high-quality data and publishable results. The SLRI user service activities are lists in detail below:

1) Outreach programs
- ASEAN Synchrotron Science Camp (annually)
- Synchrotron Science Camp for Science Teacher (annually)
- Synchrotron Radiation Applications (SRA) (circumstance)

2) Workshops and trainings
- ASEAN workshops on synchrotron-based techniques
- Experimental training for SLRI users

3) User meeting and conference
- SLRI Annual User Meeting (AUM)
- ASIAN Conference on X-ray Absorption Spectroscopy 2019 (ACXAS2019)

All these aspects remain a key role to enhance the success of SLRI.

Figure 6: Examples of SLRI user service activities.

REFERENCES

[1] Online Beamtime Application System
http://beamapp.slri.or.th

CONTACT INFORMATION

User Service Division, Business Development and Strategic Department
Tel: +66-44-217040 ext. 1602-1605
Email: userservice@slri.or.th
Website: www.slri.or.th

EDITORIAL BOARD:

DESIGN & LAYOUT

Tewarit Panpian

Synchrotron Light Research Institute (Public Organization)
Sirindhornwitchothai Building
111 University Avenue, Muang, Nakhon Ratchasima, 30000
Post Address: PO. Box 93 Nakhon Ratchasima 30000 THAILAND
Phone: +66-44-217-040 ext. 1602-1603
Fax: +66-44-217-047
E-mail: userservice@slri.or.th